UNDERSTANDING THE CHANGES IN WINDS AND PRECIPITATION OVER SOUTH ASIA: OBSERVATIONS, PROJECTIONS, AND LIMITATIONS

PANKAJ UPADHYAYA

CENTRE FOR ATMOSPHERIC SCIENCES
INDIAN INSTITUTE OF TECHNOLOGY DELHI
APRIL 2026

© Indian Institute of Technology Delhi (IITD), New Delhi, 2026

Understanding the Changes in Winds and Precipitation over South Asia: Observations, Projections, and Limitations

by

Pankaj Upadhyaya

Centre for Atmospheric Sciences

Submitted

In Fulfillment of the Requirements of the Degree of

Doctor of Philosophy

To The



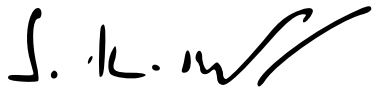
Indian Institute of Technology Delhi

– April 2026 –

Dedicated to Aama

Certificate

This is to certify that the thesis entitled "**Understanding the Changes in Winds and Precipitation over South Asia: Observations, Projections, and Limitations**" being submitted by **Mr. Pankaj Upadhyaya** to the Indian Institute of Technology Delhi for the award of the degree of **DOCTOR OF PHILOSOPHY** is a record of original bonafide research carried out by him. He worked under our supervision and has fulfilled the requirements for the submission of this thesis. The results contained in this thesis have not been submitted in part or full to any other university or institute for the award of any degree or diploma.



SAROJ KANTA MISHRA

Professor, Centre for Atmospheric Sciences

Principal Investigator, DST Centre of Excellence for Climate Information

Indian Institute of Technology Delhi



SANDEEP SAHANY

Head, Climate Projections and Extremes Branch

Centre for Climate Research Singapore

Acknowledgment

I would first like to express my sincere gratitude to my supervisors, Dr. S. K. Mishra and Dr. Sandeep Sahany, for their invaluable guidance, encouragement, and support throughout my doctoral journey. Their mentorship has profoundly shaped my scientific thinking, work ethic, and approach to research. I am deeply thankful for their patience, trust, and the intellectual freedom they provided, which allowed me to learn, explore, and grow as a researcher.

I extend my heartfelt thanks to Dr. John T. Fasullo at NCAR, whose collaboration and guidance have greatly enriched this work. I am also grateful to the members of my SRC committee for their constructive feedback and encouragement at various stages of my research. I sincerely acknowledge the Department of Science and Technology, Government of India, for awarding me the DST INSPIRE Fellowship, which supported my PhD research.

I dedicate this thesis to Aama, whose love, care, warmth, and unwavering faith have been the foundation of all my achievements; her pride in my smallest successes continues to inspire me every day. I owe my deepest gratitude to my parents, who have been my pillars of strength and the reason behind everything I am today. Pita, being my first teacher, instilled in me discipline and perseverance; and Mummy, with her simplicity, resilience, and tireless care, has always motivated me to strive for good.

My heartfelt appreciation goes to Swati and Lata, whose unconditional love and support have brought comfort and strength during difficult times. I am profoundly grateful to Bhinaju, whose patience, kindness, and positivity have been a constant source of strength and encouragement through every challenge. I also fondly remember Indra Da, who made my childhood special; his affection and care

remain deeply cherished. My little niece, Eebu, is a bundle of joy and light in my life. Her laughter and warmth inspire me to be happy.

I sincerely appreciate Pankaj for his constant motivation and meaningful friendship, from deep conversations to everyday reflections. I am also deeply thankful to my friend Nisha, who has listened to my countless rants with great patience and continues to inspire me with her wisdom and discipline. My heartfelt thanks go to Alvina, who has always been my go-to person through the chaos of Delhi—from long conversations and shared laughter to discussions on academic realities over chai and dinner outings. I also thank Bijit for his support through many of life's challenging moments. I am deeply grateful to Nikki for being a caring and supportive friend throughout this journey.

I am deeply thankful to Popat Sir and Nisha Ma'am, whose guidance as guardians since the beginning has shaped my growth. I am equally grateful to my wonderful labmates and friends — Debi, Sandeep, Ashish, Akhil, Saurav, Anirudh — for their cooperation, positivity, and camaraderie. They have been my family away from home, sharing endless banters over chai, laughter, and encouragement through long lab hours and challenging times.

I also thank Kamal Da and Binoy Mama, whose belief in me made many struggles easier to face, and Chetan, whose affection fill me with hope and purpose. I also thank Prabal and Hriday for their support throughout this journey.

I feel extremely fortunate to have shared my journey with all these wonderful people. My perceptions, philosophies, and understanding of life — and of myself — have taken shape through their presence.

Place: New Delhi

Date: 10 April 2026

Pankaj Upadhyaya

Abstract

Beyond the global consensus on climate change, understanding its regional manifestations is essential for informed policy and effective decision-making. Yet the regions most vulnerable to climate impacts often lack robust and actionable climate information. South Asia exemplifies this challenge: home to over one-fifth of the global population, it faces multiple vulnerabilities arising from strong socioeconomic dependence on climate-sensitive sectors, complex land–ocean–atmosphere interactions, and limited model reliability at regional scales. Successive generations of climate models have produced inconsistent, at times contradictory, projections, underscoring the need for improved physical understanding and reliable detection of human-induced changes. Confidence in future projections depends on how well models reproduce historical changes, but reported changes in South Asian winds and precipitation remain uncertain due to observational gaps, limited agreement on underlying drivers, and the difficulty of separating forced signals from internal variability and model uncertainty. With growing availability of long-term observations, large-ensemble (LE) simulations, and an increasingly distinguishable forced signal, it is now possible to evaluate model performance with greater confidence.

Leveraging these developments, this thesis examines how winds and precipitation over South Asia have changed in past, how they may evolve through the twenty-first century, and how reliably current models simulate these changes. Winds and precipitation represent distinct yet interconnected facets of the climate system: models explicitly simulate winds with higher fidelity, while precipitation, represented through implicit sub-grid parameterizations, exposes structural and

parameter uncertainties. Together, they provide an integrated perspective on the robust and fragile elements of model performance.

Historical analyses using multiple observations and large-ensemble (LE) simulations reveal a robust weakening of the continental subtropical westerlies (STWs), a key circulation feature whose role in South Asia's climate has been under-recognized, since the late twentieth century. This weakening originates from aerosol- and land-use land-cover (LULC)-driven surface cooling over northwestern South Asia, which reduces the zonal pressure gradient against a greenhouse-gas-(GHG-) warmed Arabian Peninsula, producing a differential warming pattern that deflects and slows the continental winds. In contrast to winds, the observed changes in precipitation—drying over the Indo-Gangetic Plain and increased precipitation in north-western and peninsular regions—are not simulated neither by CMIP nor LE models, reflecting persistent deficiencies in parameterizations governing convection, cloud microphysics, and aerosol–cloud interactions.

Future projections indicate a transition in the forcing regime. As aerosol emissions decline, their earlier cooling effect no longer masks GHG warming, allowing GHGs and LULC changes to emerge as the dominant drivers of circulation. These forcings strengthen near-surface winds over large parts of South Asia and increase the wind-energy potential, extending favourable regions beyond the present onshore resourceful regions. However, the realizable wind-energy potential remains constrained by uncertainties in irrigation representation and by socio-economic factors such as urbanization, land-use competition, and rising electricity demand.

In contrast, precipitation projections remain highly uncertain. Perturbed-parameter ensemble analyses and targeted numerical experiments demonstrate that small variations in parameter choices that govern convective and cloud-related processes can reverse the sign of regional precipitation change—even under

identical SST forcing, indicating that conventional SST-based attribution assumptions may not hold regionally. These sensitivities arise from the competing effects of convective heating and SST-forced response, which modulate precipitation most strongly along the margins of deep convection and in nearby secondary convective regions, where drying signals to warming commonly emerge. These regions include the Maritime Continent, Africa, and South America, which are equally vulnerable to climate-change-related uncertainties. This parameter-driven uncertainty exceeds internal variability and partly explains the divergent and often self-contradictory precipitation projections reported across successive model generations, even though global-mean precipitation responses to warming remain comparatively robust.

Together, the findings show that wind changes can be more robustly attributed and projected, whereas precipitation response remains uncertain because precipitation depends on parameterized convection and sub-grid processes that models cannot implicitly simulate, unlike winds, which are simulated by solving momentum equations. The thesis highlights the need for improved representation of sub-grid processes, strengthened regional customization, expanded use of coordinated LEs, greater integration of AI/ML approaches to refine uncertain parameterizations as immediate priorities, alongside longer-term progress toward kilometre-scale modelling to enhance the credibility of regional climate information for South Asia.

सारांश

वैश्विक सहमति से परे, जलवायु परिवर्तन की क्षेत्रीय अभिव्यक्तियों को समझना सूचित नीति और प्रभावी निर्णय लेने के लिए महत्वपूर्ण है। फिर भी, जलवायु प्रभावों के प्रति सबसे अधिक संवेदनशील क्षेत्रों में अक्सर मजबूत और कार्रवाई योग्य जलवायु जानकारी की कमी होती है। दक्षिण एशिया इस चुनौती का एक मज़बूत उदाहरण है: यह वैश्विक आबादी के पांचवें हिस्से से अधिक का घर है, और यह जलवायु-संवेदनशील क्षेत्रों पर मजबूत सामाजिक-आर्थिक निर्भरता, जटिल स्थल–महासागर–वायुमंडल अंतःक्रियाओं, और क्षेत्रीय पैमाने पर सीमित मॉडल विश्वसनीयता से उत्पन्न कमजोरी की कई परतों का सामना करता है। जलवायु मॉडलों की लगातार पीढ़ियों ने असंगत, और कभी-कभी, विरोधाभासी अनुमान दिए हैं, जो बेहतर भौतिक समझ और मानव-जनित परिवर्तनों का विश्वसनीय पता लगाने की आवश्यकता को रेखांकित करता है। भविष्य के अनुमानों में विश्वास इस बात पर निर्भर करता है कि मॉडल प्रेक्षित ऐतिहासिक परिवर्तनों को कितनी अच्छी तरह से अभिरूपण करते हैं। फिर भी, दक्षिण एशियाई हवाओं और वर्षा में रिपोर्ट किए गए ऐतिहासिक परिवर्तन अनिश्चित बने हुए हैं, जो अवलोकनों में अंतराल, उनके अंतर्निहित चालकों पर सीमित सहमति, और आंतरिक परिवर्तनशीलता (Internal Variability) और मॉडल अनिश्चितता से बाहरी रूप से मजबूर संकेतों को अलग करने में लगातार कठिनाई को दर्शाते हैं। दीर्घकालिक अवलोकनों, बड़े-एन्सेम्बल (Large Ensemble) अभिरूपण की बढ़ती उपलब्धता, और आंतरिक परिवर्तनशीलता से अधिक स्पष्ट रूप से भेद्य बाह्य बलित संकेतों की उपलब्धता के साथ, अब वास्तविक परिवर्तनों के संदर्भ में मॉडल प्रदर्शन का अधिक निश्चित मूल्यांकन संभव हो गया है।

इन हालिया प्रगतियों का लाभ उठाते हुए, यह शोधप्रबंध दक्षिण एशिया में पवन और वर्षा के ऐतिहासिक परिवर्तनों, उनके इक्कीसवीं सदी के दौरान संभावित परिवर्तन, तथा वर्तमान मॉडलों की इन परिवर्तनों के अभिरूपण में विश्वसनीयता का मूल्यांकन करता है। पवन और वर्षा, क्षेत्रीय जलवायु प्रणाली के भिन्न किंतु परस्पर संबंधित घटक हैं। पवनें बड़े पैमाने पर गतिकीय प्रतिक्रियाओं को अभिव्यक्त करती हैं, जिन्हें मॉडल अपेक्षाकृत उच्च सटीकता से प्रत्यक्ष रूप से अभिरूपित कर सकते हैं; जबकि वर्षा, जो उप-ग्रिड-

स्केल (sub-grid-scale) प्रक्रियाओं द्वारा नियंत्रित होती है और जिन्हें पैरामीटराइजेशन (parameterization) के माध्यम से निरूपित किया जाता है, मॉडल की संरचनात्मक (structural) तथा पैरामीटर-सम्बंधी (parameter-related) अनिश्चितताओं को उजागर करती है। दोनों मिलकर मॉडल प्रदर्शन के सुदृढ़ तथा नाजुक पक्षों पर एक समेकित दृष्टिकोण प्रदान करते हैं।

ऐतिहासिक विश्लेषण — बहुविध प्रेक्षणों और बड़े-संग्रह (Large-Ensemble; LE) अभिरूपणों के उपयोग से — यह बताते हैं कि बीसवीं शताब्दी के उत्तरार्ध से महाद्वीपीय उप-उष्णकटिबंधीय पश्चिमी पवनों (Subtropical Westerlies; STWs) में एक स्पष्ट और दृढ़ क्षीणता हुई है। यह एक प्रमुख संचरणीय विशेषता है जिसकी दक्षिण एशिया की जलवायु में भूमिका पहले अपेक्षाकृत कम मानी गयी थी। यह क्षीणता मुख्यतः उत्तर-पश्चिमी दक्षिण एशिया पर एरोसॉल और भूमि-उपयोग/भूमि-आवरण (LULC) प्रेरित सतही शीतलन से उत्पन्न होती है, जो हरितगृह-गैस (GHG)-प्रेरित उष्मन के सापेक्ष क्षेत्रीय रूप से दाब प्रवणता (zonal pressure gradient) को कम कर देती है — परिणामतः एक असमान ऊष्मन पैटर्न बनता है जो महाद्वीपीय प्रवाह को विचलित और धीमा कर देता है।

पवनों के विपरीत, अवलोकित वर्षा-परिवर्तन — जिसमें इंडो-गंगा मैदान में शुष्कन, और उत्तर-पश्चिम तथा प्रायद्वीपीय क्षेत्रों में वर्षा में वृद्धि शामिल है — को न तो CMIP मॉडल और न ही बड़े-संग्रह अभिरूपण सटीक रूप से अभिरूपित कर पाते हैं। यह संवहन, बादल सूक्ष्मभौतिकी और एरोसॉल–बादल अंतःक्रियाओं को नियंत्रित करने वाले पैरामीटराइजेशन में बने लगातार दोषों को दर्शाता है।

भविष्य के जलवायु प्रक्षेपण यह संकेत देते हैं कि प्रेरण (forcing) व्यवस्था में बदलाव आ रहा है। जैसे-जैसे एरोसॉल उत्सर्जन घटता है, उनका पूर्व का शीतलन प्रभाव अब हरितगृह-गैस उष्मन को छिपा नहीं पाता, और परिणामतः हरितगृह-गैस तथा LULC परिवर्तन संचरण के प्रमुख चालक के रूप में उभरते हैं। ये प्रेरक दक्षिण एशिया के बड़े भागों में निकट-सतही पवनों को सशक्त करते हैं और पवन-ऊर्जा संभाव्यता को बढ़ाते हैं, जिससे वर्तमान तटीय-आधारित संसाधन क्षेत्रों से परे अनुकूल क्षेत्र विस्तारित होते दिखते हैं। हालांकि, व्यावहारिक (realizable) पवन-ऊर्जा क्षमता सिंचाई के अभिरूपण में अनिश्चितताओं और शहरीकरण, भूमि-उपयोग प्रतियोगिता तथा बढ़ती विद्युत मांग जैसे सामाजिक-आर्थिक कारकों द्वारा सीमित बनी रहती है।

वर्षा के प्रक्षेपण इसके विपरीत अत्यधिक अनिश्चित बने हुए हैं। परिवर्तित-पैरामीटर संग्रह (Perturbed-Parameter Ensembles; PPE) के विश्लेषण और लक्षित संख्यात्मक प्रयोग यह दर्शाते हैं कि संवहन एवं बादल-सम्बन्धी प्रक्रियाओं को नियंत्रित करने वाले पैरामीटर विकल्पों में सूक्ष्म परिवर्तन भी क्षेत्रीय वर्षा परिवर्तन के संकेत का चिह्न उलट सकते हैं — यहाँ तक कि समान SST-प्रेरण के अन्तर्गत भी — जो बताता है कि पारंपरिक SST-आधारित कारण-निर्धारण मान्यताएँ क्षेत्रीय स्तर पर सदा लागू नहीं रहतीं। ये संवेदनशीलताएँ संवहनी ऊष्मन और SST-प्रेरित प्रतिक्रिया के प्रतिस्पर्धी प्रभावों से उत्पन्न होती हैं, जो गहरे संवहन के किनारों तथा निकटवर्ती द्वितीयक संवहनी क्षेत्रों में वर्षा को सबसे अधिक नियंत्रित करते हैं—यही वे क्षेत्र हैं जहाँ तापन के प्रति शुष्क संकेत सामान्यतः उभरते हैं। इन क्षेत्रों में समुद्री-महाद्वीपीय क्षेत्र (Maritime Continent), अफ्रीका और दक्षिण अमेरिका भी सम्मिलित हैं, जो जलवायु-परिवर्तन सम्बन्धी अनिश्चितताओं के प्रति समान रूप से संवेदनशील हैं। यह पैरामीटर-चालित अनिश्चितता आंतरिक परिवर्तनशीलता से भी अधिक है और यह भागिक रूप से उन परस्पर भिन्न तथा कई बार स्वविरोधी वर्षा प्रक्षेपणों की व्याख्या करती है जो लगातार विकसित होती मॉडल-पीढ़ियों में रिपोर्ट किए गए हैं—हालाँकि वैश्विक-औसत (global-mean) वर्षा की प्रतिक्रिया अपेक्षाकृत सुदृढ़ बनी हुई है।

समेकित रूप से, निष्कर्ष यह दिखाते हैं कि पवन परिवर्तन अधिक दृढ़ता से कारणनिर्धार्य (attributable) और प्रक्षेप्य (projectable) हैं, जबकि वर्षा-प्रतिक्रिया अनिश्चित बनी रहती है क्योंकि वर्षा पैरामीटराइज्ड संवहन एवं उप-ग्रिड प्रक्रियाओं पर निर्भर है जिन्हें मॉडल अनायास अभिरूपित नहीं कर सकते—इसके विपरीत पवनों का अभिरूपण गति समीकरणों को हल करके किया जाता है। यह शोध उप-ग्रिड प्रक्रियाओं के बेहतर निरूपण, क्षेत्रीय अनुरूपन (regional customization) के सशक्तिकरण, समन्वित बड़े-संग्रहों के प्रयोग का विस्तार, तथा अनिश्चित पैरामीटराइजेशनों को परिष्कृत करने हेतु AI/ML तरीकों के समेकन को तात्कालिक प्राथमिकताएँ बताता है; साथ ही लंबी अवधि के लिये किलोमीटर-स्तरीय मॉडलिंग की ओर प्रगति क्षेत्रीय जलवायु सूचना की विश्वसनीयता बढ़ाने के लिये आवश्यक है।

List of Contents

Certificate i
Acknowledgment ii
Abstract iv
List of Contents x
List of Figures xiii
List of Tables xvi
List of Acronyms xvii

1. Introduction **1**
1.1 Background. 3
1.2 Rationale and Knowledge Gaps 6
1.3 Scientific Objectives and Analytical Approach. 9
1.4 Methodological Overview 11
1.5 Structure of the Thesis 13

2. Changes in Winds and Precipitation over South Asia: Observed Changes **15**
2.1 Introduction 16
2.2 Data, Models, and Analytical Methods. 21
2.2.1 Observation and Reanalysis Data. 21
2.2.2 Model Data 22
2.3 Observed Changes in Winds over South Asia 26
2.3.1 Sea-level Pressure and Temperature as Causal Drivers 32
2.3.2 Simulated Forced Response – Insights from Les 36
2.4 Attribution of Changes to External Forcings: Insights from SF Experiments. 40
2.4.1 Role of Internal Variability 45
2.4.2 Individual Forcing Contributions and Non-Linear Interactions 50
2.4.3 Simulated Changes from CMIP and its Attribution using DAMIP 53
2.5 Weakening of STWs in the Context of Monsoon Low-level Jet Shift 55
2.6 Surface Wind Changes and Implications for WPP 58
2.7 Observed Changes in Precipitation 61
2.7.1 Mechanism: Causal Links to Changes in Circulation. 64
2.7.2 Simulated Precipitation Changes – Insights from CESM2LE, MPI-GE, CMIP6. 70
2.7.3 Model Uncertainty as a Challenge to Precipitation Simulation 71

2.8 Summary, Limitations, and Directions for Future Research . . . 73
3. Changes in Winds and Precipitation over South Asia: Future Projections 76
3.1 Introduction . . . 77
3.2 Data, Models, and Analytical Methods. . . . 83
3.2.1 Wind Power Calculation. . . . 86
3.3 Changes in Monsoon Winds . . . 89
3.4 Projected Changes in Near-Surface Winds . . . 91
3.5 Attribution – Insights from SF simulations . . . 94
3.6 Thermodynamic and Pressure Responses. . . . 99
3.7 Land-Use and Irrigation Controls . . . 105
3.8 Scenario and Model Dependence of Wind Projections. . . . 108
3.9 Future WEP and Socio-Economic Constraints . . . 113
3.10 Projected Changes in Precipitation. . . . 115
3.11 Summary, Limitations, and Directions for Future Research. . . . 118
4. Modeling Limitations: Diagnosing the Uncertainty in Precipitation Changes 122
4.1 Introduction. . . . 123
4.2 Data, Models, and Analytical Methods . . . 127
4.2.1 Perturbed Parameter Ensemble Simulations . . . 127
4.2.2 CMIP6 and AMIP Experiments . . . 131
4.2.3 Selection of Wet and Dry Regions . . . 133
4.3 Precipitation Response to SST Warming in PPE Simulations . . . 133
4.4 Precipitation Response to SST in Targeted Parameter Experiments . . . 138
4.5 Role of Internal Variability . . . 142
4.6 Drivers of Regional Precipitation Uncertainty . . . 146
4.7 Limits to Confidence in Future Precipitation Projections . . . 149
4.8 Summary, Limitations, and Directions for Future Research. . . . 152
5. Summary and Future Scope 156
5.1 Overview . . . 157
5.2 Synthesis of Key Findings. . . . 159
5.3 Scientific Contributions and Methodological Advances. . . . 162
5.4 Limitations of the Thesis. . . . 164
5.5 Future Scope . . . 166
5.6 Concluding Remarks. . . . 170

Bibliography 173
List of Publications. 194
Biographical Sketch 195

List of Figures

1.1 Precipitation Projections for South Asia from six IPCC assessments 5

2.1 Climatology and trends of monsoon winds at 850 hPa. 25

2.2 The time series of area-averaged windspeed over the NWI (20-30N, 60-80E). . 27

2.3 Climatology and trends of zonal and meridional winds 28

2.4 The time series of westerly index defined as area-averaged zonal windspeed over the NWI (20-30N, 60-80E) 30

2.5 The vertical structure of zonal circulation and its trend over the period 31

2.6 Climatology and trends of sea level pressure (SLP), winds at 850hPa, and near-surface temperature (TS) 33

2.7 Climatology and trends of winds at 850 hPa from CESM2-LE 35

2.8 Climatology and Trends of SLP, and TS from ALL forcing CESM2-LE simulations. 37

2.9 Climatology and trends of winds at 850 hPa from MPI-ESM GE. 39

2.10 Trends of SLP from Single Forcing Large Ensemble (SF-LE) simulations of CESM2. 42

2.11 Trends of TS from SF-LE simulations of CESM2 44

2.12 Trends of Westerly Index from reanalyses, CESM2-LE and SF simulations . . . 46

2.13 Trends of area averaged SLP and TS from reanalyses, CESM2-LE, and SF simulations. 47

2.14 Trends of wind speed at 850 hPa in SF-LE simulations of CESM2 49

2.15 Non-linearity in response of the wind speed to individual forcings at 850 hPa. 51

2.16 Trends of wind speed at 850 hPa, SLP, and TS from CMIP6 simulation. 52

2.17 The multimodel mean (MMM) trends of wind speed at 850 hPa in Single Forcing (SF) DAMIP simulations 54

2.18 Climatology and shifts in the horizontal and vertical position of the Somali Jet over the last four decades. 56

2.19 Shifts in the Somali Jet at 850 hPa over the last eight decades. 57

2.20 Trends of near-surface winds and Wind Power Potential (WPP). 59

2.21 Climatology and trends of precipitation. 61

2.22 Time evolution of precipitation. 62

2.23 Climatology and trends of convergence/divergence and vorticity. 63

2.24 Climatology and trends of vertical velocity (w) and vorticity. 64
2.25 Climatology and trends of Moisture Flux Convergence (MFC). 66
2.26 Climatology and trends of specific humidity and temperature over NWI. . . . 67
2.27 Climatology and trends of Convective Available Potential Energy (CAPE) from ERA5. 69
2.28 Model fidelity in simulating the past changes in precipitation 71
3.1 Power curve for GE 2.5 MW turbine. 89
3.2 Climatology and trends of monsoon winds at 850 hPa. 90
3.3 Climatology and change in near-surface winds in CESM2-LE simulations in the coming decades. 93
3.4 Trends of near-surface wind speed in SF-LE simulations of CESM2. 96
3.5 Comparative role of anthropogenic aerosol emission. 97
3.6 Trends of TS and SLP in SF-LE simulations of CESM2 98
3.7 Trends of TS and SLP in CESM2-LE simulations. 100
3.8 Climatology of mean temperature and its zonal gradient at 850 hPa, and the trend in zonal temperature gradient 101
3.9 Zonal temperature anomaly and its trend 102
3.10 Seasonal mean zonal circulation and trend in the pressure-latitude plane averaged over the region between 8°N and 25°N 103
3.11 Trends of TS and SLP in (SF-LE) simulations of CESM2. 104
3.12 Percentage changes in land cover types in the future under scenario SSP3-7.0 . 106
3.13 Climatology and trend of surface energy fluxes. 107
3.14 Trends of near-surface wind speed in CESM2-LE simulations. 109
3.15 Trends of near-surface wind speed in CESM large ensembles. 110
3.16 Trend and standard deviation of near-surface winds in CMIP6 multi-model simulations for the future. 112
3.17 Climatology and trends of wind energy potential (WEP) in CESM2-LE simulations in the coming decades. 113
3.18 Projected changes in precipitation at the end of the 21st century (2065–2099) relative to the historical period from different climate model ensembles. 116
3.19 Area-averaged precipitation projections at multiple spatial scales for the late 21st century (2065–2099) relative to the historical baseline (1980–2014). . . 117
4.1 Performance evaluation of different cases of model simulation using CESM CAM5. 131

4.2 Effect of warming sea surface temperatures on precipitation patterns in the PPE simulations 134

4.3 Effect of warming sea surface temperatures on average and zonal precipitation in the PPE simulations. 136

4.4 Variability in effect of warming sea surface temperatures (SSTs) on precipitation response in the PPE simulations. 137

4.5 Modified tropical SSTs. 138

4.6 Effect of warming sea surface temperatures on precipitation patterns in the targeted parameter experiment. 140

4.7 Uncertainty in the effect of warming SSTs on precipitation patterns in the targeted parameter experiment. 141

4.8 Comparison of the impact of warming SSTs on JJAS precipitation in multidecadal and seasonal experiments. 143

4.9 Effect of warming SSTs on precipitation patterns across the global in the targeted parameter experiment. 144

4.10 Effect of warming SSTs on average and zonal precipitation in the targeted Parameter experiment. 145

4.11 Effect of warming SSTs on convective heating in the targeted parameter experiment. 147

4.12 Uncertainty in precipitation response from AMIP and future projections from CMIP6. 149

4.13 Effect of SSTs warming on precipitation in the AMIP and end of the century projections from CMIP6 simulations. 151

List of Tables

2.1 CMIP6 and DAMIP Models used in the chapter 23

3.1 Details of CMIP6 models used in the analysis 85

4.1 Description of targeted numerical experiments. 130

4.2 Details of CMIP6 Models used in the chapter. 132

List of Acronyms

AER	Aerosol Forcing
ALL	All Forcings
AMIP	Atmospheric Model Intercomparison Project
AR	Assessment Report (of IPCC)
BMB	Biomass Burning Forcing
CAM	Community Atmosphere Model
CAPE	Convective Available Potential Energy
CESM	Community Earth System Model
CESM2-LE	Community Earth System Model Version 2 Large Ensemble
CESM2-SF-LE	CESM2 Single Forcing Large Ensemble
CMIP	Coupled Model Intercomparison Project
DAMIP	Detection and Attribution Model Intercomparison Project
EE	Everything Else
EM	Ensemble Mean
ENSO	El Niño–Southern Oscillation
ERA5	ECMWF Reanalysis Version 5
FAR	First Assessment Report (IPCC)
GCM	General Circulation Model
GHG	Greenhouse Gas
GPCP	Global Precipitation Climatology Project

IGP	Indo-Gangetic Plain
IMD	India Meteorological Department
IO	Indian Ocean
IOD	Indian Ocean Dipole
IPO	Interdecadal Pacific Oscillation
IPCC	Intergovernmental Panel on Climate Change
ITCZ	Intertropical Convergence Zone
LE	Large Ensemble
LLJ	Low-Level Jet
LULC	Land-Use/Land-Cover Change
MERRA2	Modern-Era Retrospective Analysis for Research and Applications, Version 2
MFC	Moisture Flux Convergence
MMM	Multi-Model Mean
MPI-ESM-GE	Max Planck Institute Earth System Model Great Ensemble
NAT	Natural Forcing
NCEP–NCAR	National Centers for Environmental Prediction / NCAR
NH	Northern Hemisphere
NSW	Near-Surface Winds
NWI	Northwest India
PD	Present Day
PI	Pre-Industrial

PPE	Perturbed-Parameter Ensemble
RCP	Representative Concentration Pathway
RMSE	Root Mean Square Error
SAR	Second Assessment Report (IPCC)
SASM	South Asian Summer Monsoon
SF	Single Forcing
SH	Southern Hemisphere
SLP	Sea-Level Pressure
SMILE	Single-Model Initial Condition Large Ensemble
SRES	Special Report on Emission Scenarios
SSP	Shared Socioeconomic Pathway
SST	Sea Surface Temperature
SST4K	+4 K SST Warming Experiment
STWs	Subtropical Westerlies
TAR	Third Assessment Report (IPCC)
TOA	Top of Atmosphere
TP	Tibetan Plateau
TS	Surface Temperature
WEP	Wind Energy Potential
WI	Western India
WPP	Wind Power Potential

Chapter 1: Introduction

Chapter 1

Introduction

Human-induced climate change is now unequivocal, with anthropogenic greenhouse gases (GHGs) driving long-term warming and significant changes in global circulation and the hydrological cycle (IPCC 2021). Global mean temperature has risen by about 1.1 °C since the late nineteenth century, accompanied by robust signals such as a weakened Walker circulation (Vecchi et al. 2006), a poleward expansion of the Hadley cell (Lu et al. 2007), and a thermodynamically intensified hydrological cycle (Held and Soden 2006). These global-scale responses provide the broader physical context within which regional climate change unfolds, and their expression is especially pronounced and critical in vulnerable regions such as South Asia.

The South Asian climate system represents one of the most physically dynamic and socially significant components of the global atmosphere. Spanning from the arid subtropics of western Asia to the humid tropics of the Indian Ocean (IO), it sustains nearly a quarter of the world's population and underpins critical sectors such as agriculture, water resources, and renewable energy. Given this dependence, even modest shifts or changes in winds or precipitation can have disproportionate effects on food security, energy systems, and disaster risk across the region, underscoring the socio-economic vulnerability of South Asia. At its heart

lies the seasonal reversal of winds and associated precipitation known collectively as the South Asian monsoon—a coupled ocean–atmosphere–land system that redistributes heat and moisture across the eastern hemisphere. In recent decades, the strength and regional expression of these winds and precipitation have changed appreciably, shaped by both external forcing and internal atmospheric–oceanic fluctuations. Understanding the causes and consequences of these changes is not merely an academic pursuit but a prerequisite for societal resilience in a region where livelihoods strongly depend on the climate (Mishra et al. 2023).

1.1 Background

The South Asian hydroclimate is governed by a delicate balance between large-scale circulation and regional thermodynamics. The seasonal southwesterly winds transport moisture from the tropical IO to the subcontinent, sustaining continental precipitation and modulating surface energy fluxes (Webster et al. 1998). Superimposed upon these low-level flows are the subtropical westerlies, which extend eastward from the Arabian Peninsula and Central Asia across the Indo-Gangetic Plain (IGP), influencing moisture transport and regional temperature gradients (Rodwell and Hoskins 2001). These interacting circulation systems—cross-equatorial flow, low-level jets, subtropical westerlies, and deep convective heating—reflect the complexity of the South Asian climate system, which is influenced simultaneously by local forcings (such as aerosols, irrigation, and land-use change), regional feedbacks, and remote modes of variability such as El-Niño Southern Oscillation (ENSO) and the Indian Ocean Dipole (IOD) (Turner and Annamalai 2012). Together, these systems form an interconnected circulation structure that links tropical and subtropical flow regimes (Krishnamurti and Bhalme 1976). Small

shifts in their strength or position can therefore have disproportionate impacts on hydrology, ecosystems, and regional economies.

Over the last century, human activity has emerged as a dominant force reshaping the regional climate. Rapid population growth, urban expansion, industrial emissions, and agricultural intensification have altered atmospheric composition and land-surface characteristics. Greenhouse gas–driven warming has modified land–ocean temperature gradients and enhanced the moisture-holding capacity of the troposphere (Held and Soden 2006). Meanwhile, aerosols from industrial and household sources have reduced surface solar radiation and modified boundary-layer structure (Li et al. 2016b; Ramanathan et al. 2005; Ramanathan and Carmichael 2008), and largescale irrigation, deforestation, and land-use change have altered albedo, surface roughness, and evapotranspiration, influencing near-surface winds (NWS) and the hydrological response (Cook et al. 2015). These forcings interact across scales, producing spatially heterogeneous circulation and precipitation changes across South Asia.

Remote oceanic and continental influences further modulate the regional climate. Sea-surface temperature anomalies across the Indo-Pacific basin, including ENSO and the IOD, strongly affect large-scale flow patterns and moisture transport into South Asia (Krishnamurthy and Goswami 2000; Saji et al. 1999). The IO has warmed faster than the global mean, altering vertical stability and regional precipitation patterns (Roxy et al. 2015). Warming over West and Central Asia influences pressure gradients and the strength of the subtropical westerlies, particularly during the pre-summer season (Dong et al. 2022; Singh et al. 2022). These interactions complicate attribution efforts by linking local responses to remote modes of internal variability.

Despite advances in global climate models, projections for South Asia remain inconsistent across generations of climate models and IPCC assessments, with

substantial disagreement in both the magnitude and distribution of future precipitation (Mishra et al. 2023). This inconsistency is illustrated in Figure 1.1, which show how successive assessment reports have produced inconsistent, at times, self-contradictory projections for precipitation over the region. Such discrepancies highlight the need for credible, physically grounded regional assessments and underscore the practical challenges faced by policymakers in regions with limited observational and institutional capacity.

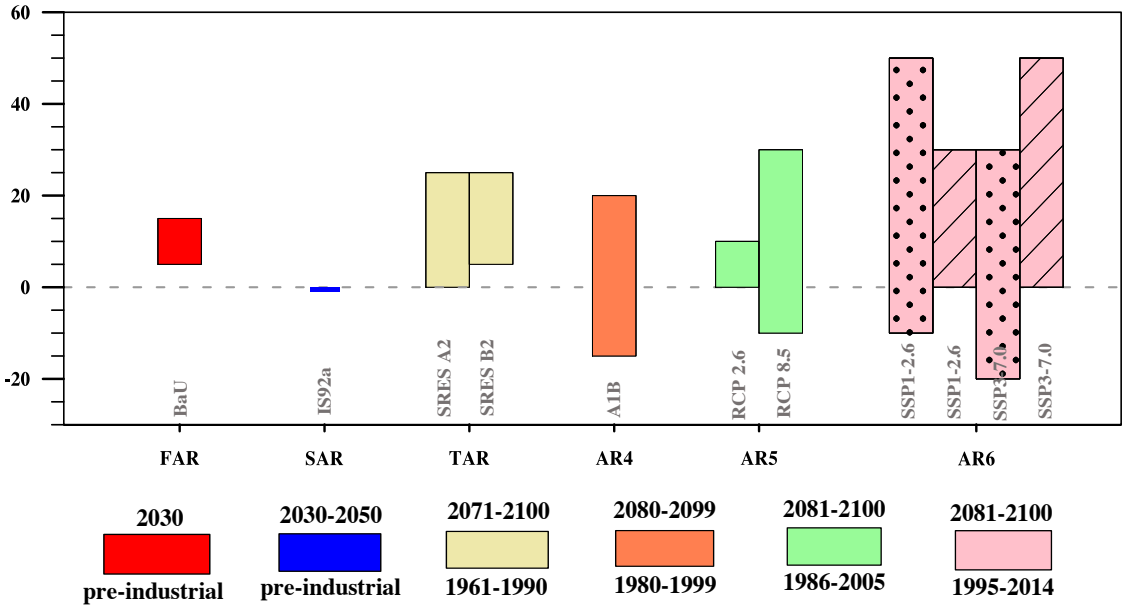


Figure 1.1 | Precipitation Projections for South Asia from six IPCC assessments. Projected precipitation changes from the six IPCC reports for different emission scenarios — FAR for BaU, Second Assessment Report (SAR) for IS92a, Third Assessment Report (TAR) for SRES A2 and B2, Assessment Report Four (AR4) for SRES A1B, Assessment Report Five (AR5) for RCP2.6 and RCP8.5, and AR6 for SSP1–2.6 and SSP3–7.0. Projections are shown for annual mean precipitation from all the reports except for FAR (summer), SAR (summer) and AR6 (winter (stippled) and summer (hatched)) for which seasonal precipitation projections are presented. The precipitation projections are presented in terms of percentage change in the projected period (mentioned above the key) with respect to the base period (mentioned below the key) except for SAR for which it is only available in absolute scale (mm per day). (refer Mishra et al., 2023)

Beyond its scientific importance, the question carries profound societal relevance. Changes in winds and precipitation determine agricultural productivity, water availability, and the feasibility of renewable energy expansion—cornerstones of sustainable development in a region with limited adaptive capacity. As South Asia pursues ambitious targets for climate-resilient growth, the reliability of future projections becomes critical for planning energy infrastructure, irrigation strategies, and long-term climate adaptation. Understanding how the region's winds and precipitation are changing—why, and with what degree of confidence—therefore constitutes both a scientific necessity and a policy imperative.

1.2 Rationale and Knowledge Gaps

Climate models, while indispensable for understanding and projecting regional climate change, exhibit systematic biases in regional climate simulation. For instance, models exhibit up to 100% bias in simulating precipitation over South Asia (Anand et al. 2018; Jain et al. 2019). Winds are explicitly resolved, but precipitation depends strongly on parameterized processes such as deep convection, cloud microphysics, and aerosol–cloud interactions, all of which differ substantially across models (Mishra, 2009). These deficiencies in process representation are widely recognized as major contributors to the inter-model spread in regional hydroclimate simulations (Knutti and Sedláček 2013). These differences propagate into the simulated hydroclimate response and contribute to the wide spread in regional precipitation projections. The challenge is compounded by the difficulty of separating externally forced responses from internal variability associated with ENSO, the IOD, and other coupled modes, which can dominate multi-decadal anomalies in winds and precipitation. Large-ensemble studies further show that internal variability alone can generate regional anomalies comparable to or larger

than forced signals, especially in the tropics (Deser et al. 2020). These challenges are particularly acute over South Asia, where steep orography, strong land–sea thermal gradients, and intense aerosol loading amplify model biases in both circulation and precipitation (Guilbert et al. 2023; Wang et al. 2021b). As a result, even when models reproduce large-scale changes reasonably well, their regional manifestation often diverge in both magnitude and spatial pattern.

A second challenge concerns the combined influence of multiple external forcings. Greenhouse gases enhance land–ocean temperature contrasts and increase atmospheric moisture content, strengthening the thermodynamic component of the hydrological cycle (Held and Soden 2006). Aerosols impose strong regional radiative perturbations that cool the land surface, suppress boundary-layer development, and weaken near-surface pressure gradients (Bollasina et al. 2011; Ramanathan and Carmichael 2008). Land-use change and irrigation further modify surface fluxes by altering albedo, evapotranspiration, and stability, contributing to locally intensified circulation and moisture anomalies (Cook et al. 2015). Over South Asia, extremely high aerosol concentrations, large-scale irrigation in the IGP, and rapid land-use transitions produce regionally unique responses that most global models struggle to simulate accurately (Bollasina et al. 2011; Singh et al. 2019). These forcings act through distinct but interacting pathways, often masking or amplifying one another's effects and producing regionally heterogeneous outcomes. Quantifying their relative and combined contributions remains difficult because observational records are short or spatially sparse, and models differ substantially in how they represent aerosol–radiation interactions, aerosol–cloud processes, and land-surface feedbacks, including irrigation (Xie et al. 2015).

Third, while internal variability has long been recognized as a confounding factor, its magnitude and structure have only recently become quantifiable through large-ensemble (LE) simulations. Earlier approaches relied on long control runs to

approximate variability, but LEs, which average across dozens of realizations under identical external conditions, now enable direct estimation of the forced response and its uncertainty envelope. Large-ensemble experiments have demonstrated that internal variability alone—arising from unforced coupled interactions—can generate multi-decadal anomalies in circulation and precipitation that rival or exceed externally forced signals (Deser et al. 2020; Maher et al. 2021). Over South Asia, these fluctuations arise from the combined effects of ENSO, the IOD, the Pacific Decadal Oscillation, and Atlantic multidecadal modes, each modulating land–ocean gradients, moisture transport, and the structure of ascent (Krishnamurthy and Goswami 2000; Wang et al. 2021a). Yet few studies have systematically applied this framework to South Asia, where competing forcings and strong variability make signal detection especially difficult. As a result, internal variability remains a dominant and irreducible source of uncertainty in both observed changes and projected changes.

Finally, even when externally forced responses can be identified, the reliability of regional projections remains constrained by structural and parametric uncertainty. Multi-model ensembles, such as Coupled Model Intercomparison Project (CMIP), provide valuable intercomparisons but often conflate differences arising from model design, tuning, and parameterization choices due to representations of key physical processes, especially convection, cloud microphysics, and aerosol–radiation interactions (Collins et al. 2011; Zhou et al. 2020). These discrepancies produce a wide spread in projected precipitation over South Asia, often exceeding the magnitude of the ensemble mean signal, with inconsistencies persisting across successive IPCC assessments (Mishra et al. 2023). This challenge is compounded by uncertainty related to future aerosol emissions and land-use trajectories.

In summary, the central knowledge gaps concern (i) incomplete attribution of observed changes, (ii) limited confidence in projections due to model deficiencies, and (iii) inadequate diagnosis of the processes that generate unacceptably large inter-model differences. Addressing these deficiencies requires a framework that couples physical understanding with methodological rigor—an approach that forms the guiding motivation of this thesis.

1.3 Scientific Objectives and Analytical Approach

The overarching aim of this thesis is to advance understanding of how winds and precipitation over South Asia are changing under anthropogenic influence, by integrating observational evidence with physically interpretable model analyses. This aim is supported by three specific objectives that together address the past, future, and uncertain aspects of regional climate change. The first objective is to identify and assess robust observed changes in winds and precipitation over South Asia and attribute them to externally forced responses where physical evidence and model fidelity permit. Building on this, the second objective is to evaluate future projections of these variables under evolving external forcings and socio-economic pathways, with particular attention to uncertainties linked to emissions scenarios, land-use policies, and model representation. The third objective is to diagnose model uncertainty in precipitation responses to warming, examining how parameter choices contribute to inter-model differences and what these differences imply for both attribution and projection.

Each objective corresponds to a core analytical component of the thesis—respectively addressing the historical, future, and uncertainty dimensions of South Asian climate change.

To achieve these objectives, the thesis adopts a multi-tiered analytical strategy that integrates observations, reanalyses, and a hierarchy of model ensembles. The first tier employs observational and reanalysis datasets to quantify historical trends and their spatial coherence, focusing on circulation and hydroclimate variables such as winds, sea-level pressure, temperature, and precipitation. Statistical attribution is supported by the use of large-ensemble and single-forcing simulations that separate externally forced signals from internal variability. The second tier extends this framework to future projections using coordinated ensemble experiments under multiple emissions scenarios. By comparing LEs, single-forcing experiments, and multi-model datasets (CMIP6) (Eyring et al. 2016), the analysis evaluates the consistency and divergence of simulated responses. The third tier employs perturbed-parameter ensembles (PPEs) and targeted numerical experiments to diagnose how uncertainties in model physics propagate into precipitation projections, identifying the dominant parameters and processes responsible for spread across models.

Throughout these analyses, the emphasis remains on physical interpretability along with statistical rigor. Circulation changes are linked to thermodynamic drivers—such as temperature gradients and pressure anomalies—while precipitation changes are examined in relation to dynamical convergence, convective instability, and moisture fluxes. This physically grounded approach ensures that statistical significance is supported by causal understanding. The use of ensemble-based frameworks further allows quantification of uncertainty across different levels: internal variability within a single model, structural differences between models, and parametric sensitivity within a model family. Collectively, these methods enable a holistic evaluation of the reliability and mechanisms of South Asian climate change.

1.4 Methodological Overview

While detailed methodologies are presented in subsequent chapters, it is useful here to outline the conceptual logic that underpins the analytical design. The thesis rests on the integration of three complementary strands of evidence:

(i) Multi-dataset synthesis of observations and reanalyses.

A diverse suite of atmospheric reanalyses and gridded observational datasets provides the empirical foundation for assessing historical changes. These products, derived from independent assimilation systems and observational networks, allow detection of consistent features across data sources and offer an estimate of observational uncertainty. Reanalysis fields such as 850 hPa winds, sea-level pressure, surface temperature, and moisture flux are used to infer dynamical and thermodynamic adjustments, while high-resolution precipitation datasets characterize hydroclimatic changes. Agreement among independent datasets is treated as evidence of robustness. This component primarily supports the first objective by providing the empirical basis for detecting historical changes and assessing their spatial coherence across independent datasets.

(ii) Ensemble-based isolation of forced responses.

To attribute observed trends to external drivers, the thesis utilizes coordinated model ensembles that quantify the forced signal and its spread. LEs average across multiple realizations under identical external conditions to suppress uncorrelated internal variability, yielding a best estimate of the externally forced response. Single-forcing large ensembles (SF-LEs) (Simpson et al. 2023) further decompose this response into contributions from individual forcings—GHGs, aerosols, LULC change, and others—by allowing each to evolve independently. These experiments provide a physically consistent framework for attribution and for assessing how different drivers interact to produce the observed patterns of change. These

ensemble experiments contribute to both first objective, by separating forced signals from internal variability, and second objective, by evaluating future changes under evolving external forcings; they also enable the applied assessment of wind-energy potential by linking circulation changes to changes in NWS.

(iii) Diagnosis of model uncertainty through perturbed-parameter ensembles. Recognizing that even the most advanced models differ in their internal physics, the thesis employs a PPE of the CESM CAM6 (Eidhammer et al. 2024) atmospheric model to quantify how parameter choices influence precipitation responses to surface warming. By systematically varying parameters controlling convection, cloud microphysics, and turbulence, the PPE reveals the sensitivity of precipitation to model formulation. Comparisons with multi-model and atmosphere-only experiments (AMIP, CMIP6) establish how parameter uncertainty within a single model relates to structural uncertainty across models. This framework connects model design with projection confidence, providing a mechanistic explanation for the inter-model spread in precipitation simulations. This tier directly advances third objective by diagnosing how parameter and structural differences shape precipitation responses and by clarifying the physical sources of inter-model divergence.

The integration of these three approaches—observations, ensemble simulations, and uncertainty diagnosis—creates a tiered methodological architecture that advances from empirical detection to robust attribution and, finally, to diagnostic evaluation of model fidelity. By combining physical interpretation with statistical rigor, the approach bridges the gap between understanding what has changed, anticipating what will change, and assessing how reliably those changes can be projected.

1.5 Structure of the Thesis

The thesis is organized into five chapters that together follows a logical progression from empirical detection to projection, uncertainty diagnosis, and synthesis. The sequence is conceptual rather than descriptive: each chapter builds upon the previous to develop an increasingly integrative understanding of South Asian climate change.

- **Chapter 2** establishes the observational foundation by identifying robust changes in winds and precipitation over South Asia during the recent decades, attributing them to external forcings where supported by evidence. It reveals a pronounced weakening of the continental subtropical westerlies, linked to aerosol- and land-use-induced cooling and reduced meridional pressure gradients, and discusses the associated redistribution of precipitation and model fidelity in simulating these changes.

- **Chapter 3** extends the analysis to the twenty-first century, evaluating projected changes under multiple emissions and socio-economic scenarios. It shows a transition from aerosol-driven weakening to greenhouse-gas- and land-use-dominated strengthening of circulation, alongside persistent uncertainty in precipitation projections. The chapter also explores implications for regional wind-energy potential, connecting physical change to societal relevance.

- **Chapter 4** addresses the origins of model uncertainty by examining how parameter and structural differences govern precipitation responses to warming. Through perturbed-parameter ensembles and multi-model comparisons, it demonstrates that parameter choices alone can reverse the sign of regional precipitation change, highlighting the central role of model physics in shaping projection spread.

- **Chapter 5** synthesizes the findings, articulating the broader implications for regional climate science and policy. It underscores that while circulation responses to external forcing are relatively robust, precipitation projections remain limited by parameterization uncertainty and model fidelity, and it outlines pathways for improving both physical understanding and modelling approaches.

Together, these chapters form a coherent narrative that progresses from understanding *what* has changed, to anticipating *what may change*, and finally to diagnosing *how confidently those changes can be simulated*. The thesis thus offers an integrative assessment of the evolving climate over South Asia, linking observational evidence, model-based attribution, and process-level diagnosis within a single conceptual framework.

This thesis adopts a rigorous scientific and methodological approach to investigate how anthropogenic forcings are reshaping winds and precipitation over South Asia. It treats the region as both a sentinel and a testbed for examining the combined effects of GHGs, aerosols, LULC changes, and internal variability, and emphasizes the value of ensemble-based and process-aware approaches for constraining regional climate behavior. At its core, the thesis addresses a central challenge in regional climate science: identifying robust physical signals of change despite the influence of internal variability and uncertainties in model representation. The chapters that follow apply this framework to quantify observed changes, diagnose the physical drivers of those changes, assess the reliability of projections, and evaluate the sources of uncertainty that shape confidence in the future evolution of South Asian winds and precipitation.

Chapter 2: Changes in Winds and Precipitation over South Asia: Observed Changes

Chapter 2

Changes in Winds and Precipitation over South Asia: Observed Changes

2.1 Introduction

The atmospheric circulation over South Asia is shaped by multiple interacting wind systems that couple the tropical and subtropical atmosphere and control the region's hydroclimate. Among these, the southwesterly monsoon winds dominate as the main conveyor of moisture to the subcontinent, regulating regional precipitation and supporting the livelihoods of nearly one-fourth of the global population. Another key feature in the lower troposphere is the subtropical westerlies (STWs), which originate over Central Asia and the Arabian Peninsula and extend eastward across the IGP as part of the continental branch of the monsoon flow (Singh et al. 2022) (Fig. 2.1a). Prevailing poleward of 20°N, these westerlies influence monsoon dynamics through horizontal wind shear, modulate large-scale moisture transport, and play an important role in determining the wind energy potential of South Asian countries (Gao et al. 2018).

A central theme of this thesis is the contrasting robustness of circulation and precipitation responses to warming. Large-scale winds are explicitly resolved in climate models and are dynamically constrained by pressure gradients and energy balance, which makes their long-term changes comparatively robust across

observations and models. Precipitation, in contrast, depends strongly on parameterized sub-grid processes such as convection and cloud microphysics, leading to substantially larger uncertainty in both historical trends and future projections. Understanding this contrast between circulation and precipitation responses provides a useful framework for interpreting hydroclimatic changes across South Asia.

Existing studies present mixed evidence regarding the direction and magnitude of wind trends across South Asia. While changes in the southwesterly monsoon circulation have been extensively investigated (Bollasina et al. 2011; Chung and Ramanathan 2006; Jin and Wang 2017; Ramanathan et al. 2005; Roxy et al. 2015; Turner and Annamalai 2012; Wang et al. 2013), changes in the STWs have received relatively little attention. Several analyses report a weakening of surface winds over the continental landmass linked to Indian Ocean warming (Gao et al. 2018) and an associated decline in 850 hPa winds related to rising surface pressure over the Tibetan Plateau (Singh et al. 2022). In contrast, low-level monsoon winds over the ocean have been reported to strengthen, driven by a reinforced Walker circulation over the western Pacific that enhances cross-equatorial westerlies across the Indian Ocean (Joseph et al. 2024). Other studies find a weakening of these cross-equatorial winds (Swapna et al. 2014) or a poleward shift of the low-level jet with implications for the distribution of precipitation across South Asia (Li et al. 2023). Despite a long history of monsoon research, inconsistencies remain in both the magnitude and spatial structure of wind changes, and their attribution to external forcing continues to pose a major challenge.

Despite the relatively robust dynamical constraints on winds, precipitation responses remain substantially more uncertain because they depend on both large-scale circulation and parameterized sub-grid processes. Winds are explicitly resolved in models, but precipitation is parameterized, which introduces large

biases and weak agreement with observations. Given its importance for agriculture, water resources, and disaster management in South Asia, understanding why precipitation trends differ between models and observations is crucial. Over the past eight decades, observations indicate a persistent decline in precipitation over the monsoon trough and east-central India (Bollasina et al. 2011; Roxy et al. 2015; Salzmann and Cherian 2015), whereas in recent decades, central and northwestern India have experienced partial trend reversals with localized increases (Jin and Wang 2017; Joseph et al. 2024; Rajesh and Goswami 2023; Singh et al. 2022). While these trends are largely consistent across multiple observational products, climate models fail to reproduce them (Guilbert et al. 2023; Guo et al. 2015; Saha et al. 2014; Salzmann and Cherian 2015). The large model–observation discrepancy arises from the parameterization of convection and cloud microphysics and from the incomplete treatment of aerosol–cloud interactions. Combined with the obscuring influence of internal variability, this creates substantial challenges for attributing observed precipitation changes to specific external drivers (Sarojini et al. 2016).

The South Asian climate is controlled by an intricate interplay of natural variability and external forcing, with anthropogenic influences becoming increasingly dominant in recent decades (Huang et al. 2020a). Global warming driven by GHGs produces widespread temperature increases, but its regional expression is strongly shaped by the combined influence of aerosols, LULC change, and oceanic variability (Singh et al. 2019). Rapid industrialization, urbanization, and agricultural intensification across South Asia have increased emissions of aerosols from industry, transport, and household activities, while large-scale irrigation and land conversion have modified surface albedo, roughness, and energy fluxes (Cook et al. 2015; Singh et al. 2018). Together, these forcings reshape the land–sea thermal contrast and atmospheric stability, altering both circulation and precipitation.

Although GHGs are relatively well mixed, their impacts exhibit strong hemispheric asymmetry, with the Northern Hemisphere showing amplified warming (Friedman et al. 2013). In South Asia, this background warming is further modulated by aerosol loading and LULC changes that produce heterogeneous responses. Anthropogenic aerosols, particularly sulfates and black carbon, alter the regional energy balance by scattering and absorbing solar radiation, leading to surface cooling and atmospheric dimming (Lau and Kim 2017; Ramanathan et al. 2005). This cooling has masked part of the greenhouse-gas-induced warming signal (Lau et al. 2017) and weakened the land–sea thermal gradient that drives monsoon circulation. At the same time, LULC change and irrigation alter surface fluxes and boundary-layer processes, further modifying atmospheric stability and the distribution of convection (Shepherd 2014; Singh et al. 2018).

Beyond local processes, remote influences also modulate South Asian circulation. The subtropical belt between 25° and 40° N, where the STWs originate, has undergone anomalous warming in recent decades (Dong et al. 2022; Teng et al. 2022). Basin-scale warming of the Indian Ocean (Chung and Ramanathan 2006), western Pacific (Li et al. 2017), and Atlantic (Li et al. 2008, 2016a), as well as enhanced heating over the Tibetan Plateau (Luo et al. 2024) and broader subtropical circulation changes (Chen et al. 2024), all exert significant remote control on South Asian winds and precipitation. The relative importance of these influences remains uncertain, as they operate through coupled feedbacks and can reinforce or offset one another (Monerie et al. 2022).

The co-existence of multiple competing forcings—GHG-induced warming, aerosol-induced cooling, and LULC-driven land–atmosphere feedbacks—creates a complex forcing landscape that complicates the attribution of observed regional trends (Bollasina et al. 2011; Lau and Kim 2017; Monerie et al. 2022). Isolating externally forced signals is further complicated by internal variability, which can

amplify or obscure forced responses on interannual to multidecadal timescales (Huang et al. 2020a). Historically, long pre-industrial control simulations were used to approximate the magnitude of internal variability, but the advent of LE simulations now allows direct quantification of the forced response by averaging across multiple realizations under identical external conditions.

Recent advances in SF-LE experiments have made it possible to isolate the individual and combined effects of different external drivers, such as GHGs, aerosols, and LULC, by allowing only one forcing to evolve while others remain fixed at pre-industrial levels (Deser et al. 2020; Maher et al. 2021; Simpson et al. 2023). These frameworks provide a powerful tool for diagnosing the forced component of climate change and for quantifying the magnitude of internal variability. Yet systematic investigations using these approaches remain sparse for the South Asian region, despite its climatic importance and sensitivity to anthropogenic modification.

Considering these scientific and methodological challenges, this chapter investigates the historical changes in winds and precipitation over South Asia, emphasizing the changes in winds over the continental land and its hydroclimatic consequences. By combining observations, reanalyses, and multi-ensemble simulations, it seeks to delineate the physical mechanisms underlying these changes, identify the relative contributions of key external forcings, and evaluate the fidelity of models in reproducing the observed trends. In particular, the chapter highlights the contrasting robustness of circulation and precipitation responses: while large-scale winds are dynamically constrained and relatively consistently simulated across models, precipitation remains more uncertain because it depends on parameterized sub-grid processes. This synthesis forms the basis for understanding the externally forced nature of South Asian climate and establishes a foundation for the projection and uncertainty analyses presented in the subsequent chapter.

2.2 Data, Models, and Analytical Methods

The analysis in this chapter combines a broad suite of observational and modeling resources to characterize how winds and precipitation over South Asia have changed since 1980 and to identify the dominant physical drivers of those changes.

2.2.1 Observation and Reanalysis Data

Three state-of-the-art atmospheric reanalyses: ERA5 (Hersbach et al. 2020), NCEP–NCAR (Kalnay et al. 1996), and MERRA-2 (Gelaro et al. 2017), serve as the foundation for diagnosing the circulation and thermodynamic structure associated with South Asian winds and precipitation. ERA5, developed using the advanced Integrated Forecasting System of the European Centre for Medium-Range Weather Forecasts, provides hourly data on a 0.25° × 0.25° grid, offering unprecedented spatial detail and improved representation of hydrometeorological processes compared to earlier reanalyses. Its modern assimilation framework integrates a wide range of in-situ and satellite observations, ensuring greater consistency in energy and water budgets during the satellite era. The NCEP–NCAR reanalysis, although coarser at 2.5° × 2.5°, extends further back in time to the mid-twentieth century, providing a long-term historical baseline against which more recent datasets can be compared. The MERRA-2 product, developed by NASA, incorporates aerosol–radiation and aerosol–cloud interactions and achieves a spatial resolution of 0.5° × 0.625°, allowing improved representation of radiative feedbacks. Using all three datasets enables the detection of robust and common features across independent assimilation systems and provides an estimate of structural uncertainty inherent to reanalyses. All variables—winds, sea-level pressure (SLP), and near-surface temperature (TS)—are bilinearly interpolated to a common 0.25° grid for direct comparison. Agreement in the sign, spatial structure, and significance

of trends among these datasets is treated as a measure of confidence in the robustness of detected changes.

Precipitation changes are examined using the high-resolution 0.25° × 0.25° gridded dataset from the India Meteorological Department (IMD) (Rajeevan et al. 2008) and the 2.5° × 2.5° Global Precipitation Climatology Project (GPCP) (Adler et al. 2003). The IMD dataset, based on over 7 000 rain-gauge stations, provides reliable spatial detail over land, while GPCP complements it with global oceanic coverage. Long-term context is derived from the Climate Research Unit (CRU) (Harris 2013) dataset (1901–2020), which enables examination of century-scale variability. All precipitation analyses are restricted to the June–September (JJAS) season, corresponding to the active South Asian monsoon, and the 1980–2020 period when both satellite and reanalysis data are most reliable.

2.2.2 Model Data

To attribute observed changes to specific forcings and to distinguish them from natural variability, this study utilizes several coordinated model ensembles. A central tenet of modern climate science is the use of climate model simulations to separate the human-induced forced climate signal from the background of internal variability. The Community Earth System Model version 2 Large Ensemble (CESM2-LE) (Rodgers et al. 2021) provides 100 realizations of the climate system under identical forcings but different initial conditions. The simulations cover 1850–2100 with historical forcings (1850–2014) followed by the SSP3–7.0 scenario (2015–2100). Fifty members are analyzed for the 1980–2020 period at 1° resolution to examine ensemble-mean (EM) trends in 850 hPa wind speed, SLP, and TS. The LE frameworks are particularly powerful in detecting transient forced signals amidst chaotic variability (Deser et al. 2020; Maher et al. 2021) and have been widely used

to explore uncertainties in temperature and precipitation trends (Díaz et al. 2021) (Díaz et al., 2021), monsoon behaviour (Zhou et al. 2020), and extremes (Pendergrass et al. 2019).

Model	Resolution	Reference
ACCESS-CM2	192×144	(Ziehn et al. 2020)
ACCESS-ESM1-5	192x145	(Ziehn et al. 2020)
BCC-CSM2-MR	320×160	(Wu et al. 2019)
CanESM5	128×64	(Swart et al. 2019)
CNRM-CM6-1	256×128	(Voldoire et al. 2019)
FGOALS-g3	180×80	(Li et al. 2020)
GFDL-ESM4	288×180	(Dunne et al. 2020)
HadGEM3-GC31-LL	192×144	(Andrews et al. 2019)
IPSL-CM6A-LR	144×143	(Boucher et al. 2020)
MIROC6	256×128	(Tatebe et al. 2019)
MRI-ESM2-0	320×160	(Yukimoto et al. 2019)
NorESM2-LM	144×96	(Seland et al. 2020)

Table 2.1 | CMIP6 and DAMIP Models used in this chapter. Details of the CMIP6 models employed for the detection and attribution of wind changes, along with their horizontal resolution, are provided. The all-forcing simulations representing the total historical forcing are taken from CMIP6, while the corresponding single-forcing experiments—greenhouse gas (GHG), anthropogenic aerosol (AER), and natural forcing (NAT)—following the all-but-one approach, are obtained from DAMIP.

To further diagnose the contributions of individual forcings, SF-LE simulations from CESM2 are employed (Simpson et al. 2023). In these experiments, only one forcing evolves historically while others are fixed at 1850 levels. Simulations include anthropogenic aerosols (AER, 20 members), biomass-burning aerosols (BMB, 15 members), greenhouse gases (GHGs, 15 members), and a

composite "Everything Else" (EE, 15 members) that encompasses solar variability, volcanic aerosols, ozone, and LULC. The LULC forcing shows a persistent upward trend and is emphasized among EE results due to its strong influence on regional climate. Each simulation spans 1850–2050, offering long temporal coverage for attribution analyses.

In addition to CESM2 experiments, historical and scenario simulations from the Max Planck Institute Grand Ensemble (MPI-ESM GE) (Olonscheck et al. 2023) are examined. These runs extend from 1850–2014 for historical forcings and 2015–2100 under SSP3–7.0, with continuous analysis for 1980–2020. The atmospheric component has a horizontal resolution of ~1.8° with 47 vertical levels, while the ocean model operates at ~1.5° with 40 levels, ensuring balanced representation of air–sea coupling. Finally, a 12-model multi-model mean (MMM) from CMIP6 (Eyring et al. 2016) and complementary DAMIP single-forcing simulations (Gillett et al. 2016) are analyzed to evaluate model structural diversity (see Table 1 for model details). The DAMIP includes simulations driven separately by AER, GHG, and natural forcings (NAT). All model outputs are interpolated to a 1° × 1° grid before calculating ensemble means and trends for 1980–2020.

Together, these observational and modeling resources provide a unified framework for diagnosing the observed evolution of South Asian winds and precipitation, quantifying externally forced changes, and isolating the contributions of specific anthropogenic drivers. This multi-dataset, multi-model approach ensures that subsequent analyses rest on a physically consistent and statistically defensible foundation.

In this thesis, the term subtropical westerlies (STWs) refers to lower-tropospheric (850 hPa) westerly flow over continental South Asia and is used consistently to describe the continental branch of the monsoon circulation. A Westerly Index (WI), defined as the mean 850 hPa zonal wind over 20°–30° N and

60°–80° E, is used to quantify the strength of the STWs. The term near-surface westerlies (NSWs) refers to winds at approximately 100m height, primarily considered in the context of wind-energy applications. Other diagnostics include Moisture Flux Convergence (MFC), vertical-velocity profiles, Convective Available Potential Energy (CAPE), and zonal temperature anomaly gradients between the Arabian Sea and the Indian subcontinent.

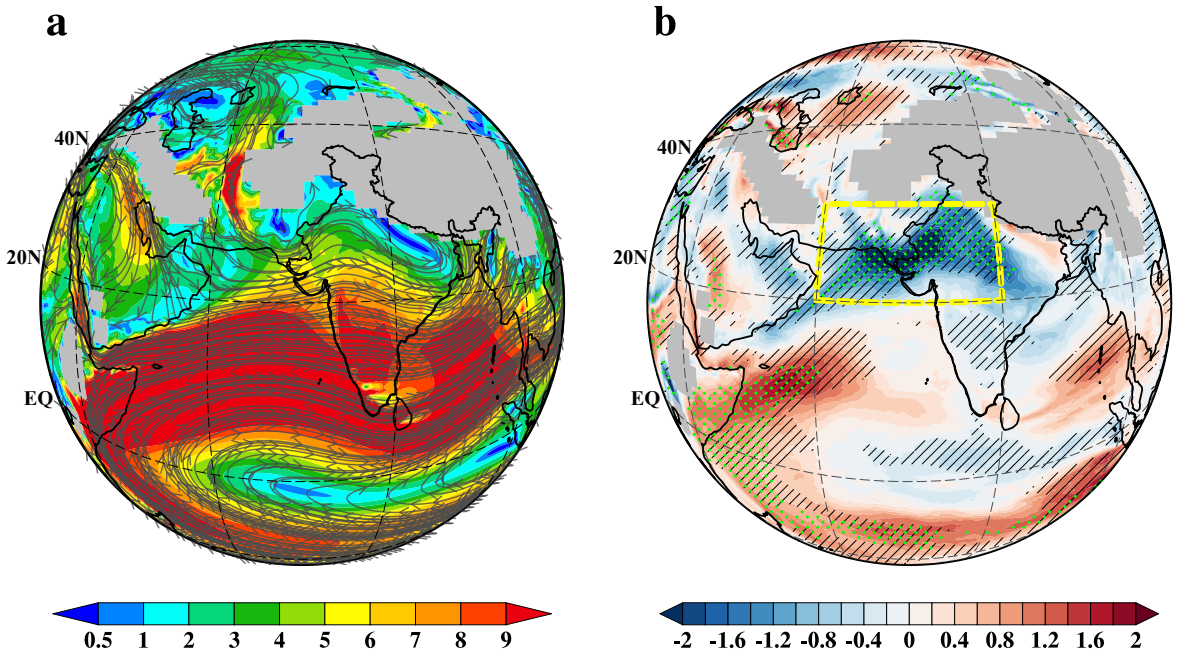


Figure 2.1 | Climatology and trends of monsoon winds at 850 hPa. a Climatology (m sec^{-1}) and **b** trends (m sec^{-1} per 41 years) of wind speed at 850 hPa during the Indian Summer Monsoon months (June-September) over 41 years (1980-2020). The shaded background in **a** is the mean wind speed from three data sets (ERA5, NCEP-NCAR, and MERRA2). The overlaid streamlines in **a** represent the climatological winds. The shaded background in **b** is the trend in ERA5; the stippling represents the regions where the trends exceed a 99% statistically significant level, and the hatching represents the regions where the sign of the trend agrees in all three datasets.

Trends are estimated using the Theil–Sen median-slope estimator, a robust measure insensitive to outliers, and statistical significance is assessed with the non-parametric Mann–Kendall test. All changes are expressed per 41 years (1980–2020), unless stated explicitly. To estimate forced response, trends are computed after

averaging across the ensemble members to derive the ensemble mean. To estimate the ensemble spread the trends are calculated for each member and the standard error is calculated across these individual trends from the ensemble mean. Consistency among reanalyses and ensemble means is taken as evidence of a robust change.

2.3 Observed Changes in Winds over South Asia

The climatological structure of the South Asian summer monsoon at 850 hPa (Fig. 2.1a) reveals the defining features of the large-scale low-level circulation that governs the seasonal transport of heat and moisture across the region. During boreal summer, strong thermal contrasts between the warm continental landmass and the relatively cooler surrounding oceans generate intense pressure gradients that drive the monsoon flow. At the heart of this system lies a powerful cross-equatorial current that forms near 50°E, known as the Somali Jet. This jet originates in the Southern Hemisphere and crosses the equator, curving northeastward as it traverses the Arabian Sea before turning eastward toward the Indian subcontinent. The jet acts as the primary conduit for moisture-laden air from the tropical Indian Ocean into South Asia, fuelling the convective core of the monsoon.

Poleward of this moist oceanic flow lies a broad zone of westerlies extending from the Arabian Peninsula and Iran across Pakistan into northern India. These westerlies, referred to as the STWs, constitute the continental branch of the monsoon's low-level circulation. They advect drier air from arid western Asia and feed directly into the monsoon trough—a zone of persistent low pressure and deep convection stretching from Pakistan to the Bay of Bengal. The convergence of the dry STWs with the humid southwesterlies over the trough establishes the monsoon's main ascent region and defines the geographical extent of precipitation

across the subcontinent. The two branches therefore function as an interconnected dynamical system that couples the tropical and subtropical atmosphere. The cross-equatorial southwesterlies serve as the main moisture supply mechanism, while the STWs regulate the inland penetration of this moist air and modulate the spatial structure of precipitation.

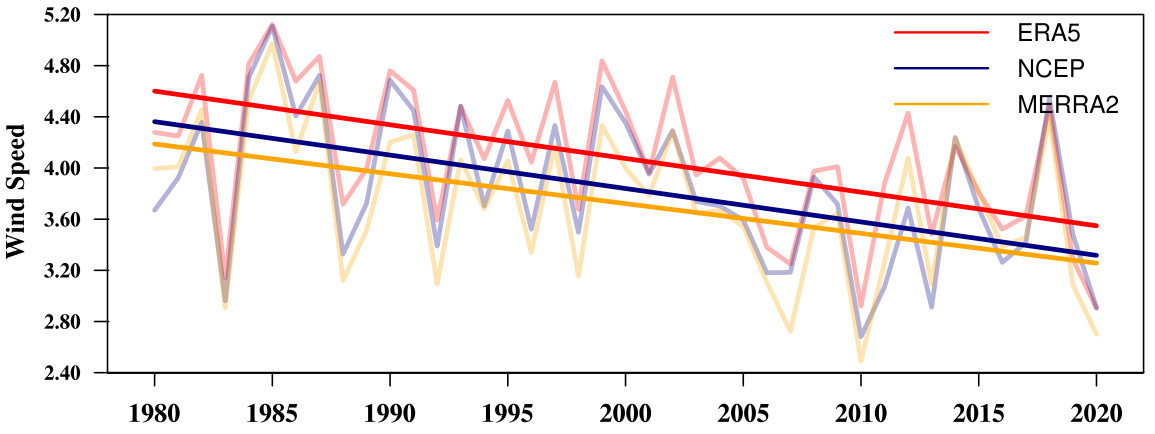


Figure 2.2 | The time series of area-averaged windspeed (m sec^{-1}) over the yellow box (20°-30°N, 60°-80°E). The straight line is the fitted trend using linear regression, where slope is obtained from Theil-Sen estimator. The results are calculated for a common grid resolution of 0.25 x 0.25.

The analysis of lower-tropospheric winds from three independent reanalysis datasets demonstrates that this coupled system has undergone a substantial change in recent decades (Fig. 2.1b). All datasets consistently indicate a statistically significant weakening of 850 hPa winds over the continental regions of South Asia since 1980. The most pronounced reduction occurs in latitudes 20°–30° N and longitudes 60°–80° E, which corresponds to the core zone of the STWs. Over this region, wind speeds have declined by approximately 1 m sec^{-1} across all reanalyses, equivalent to a reduction of more than 25 percent relative to the climatological mean (Fig. 2.2). The coherence of this weakening across independent datasets and varying assimilation systems underlines the robustness of the signal.

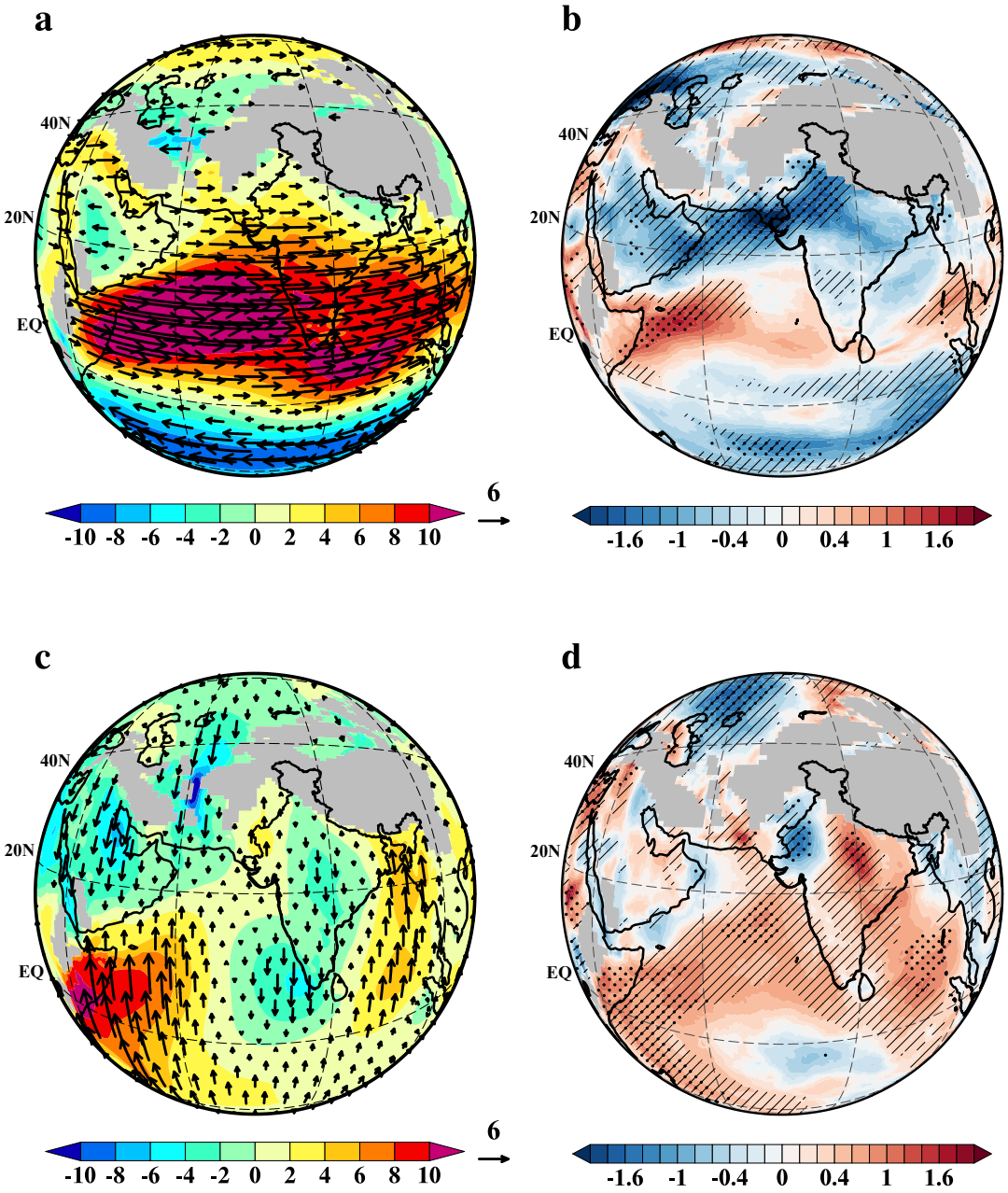


Figure 2.3 | Climatology and trends of zonal and meridional winds. a Climatology and **b** trends of u-component of the 850 hPa horizontal wind speed (m sec^{-1}) during the Indian Summer Monsoon months (June-September) over 41 years (1980-2020). The climatology shown in **a** is the mean of three data sets (ERA5, NCEP-NCAR, and MERRA2). The shaded background in **b** is the trend in ERA5 (m sec^{-1} per 41 years); the stippling represents the regions where the trend exceeds 99% statistically significant level, and the hatching represents the regions where the sign of the trend agrees in all the three datasets. **c,d,** Same as **a,b**, but for v-component of the 850 hPa horizontal winds. The results are calculated for a common grid resolution of 0.25 x 0.25.

In contrast, the southwesterly monsoon winds over the oceanic domain exhibit a modest but coherent strengthening. This intensification extends along the entire length of the cross-equatorial low-level jet, including the Southern Hemisphere branch, with the most prominent increase occurring near the Horn of Africa. Such a pattern reflects a redistribution of momentum within the coupled monsoon system rather than a uniform decline. The continental circulation has weakened, while the oceanic branch has marginally intensified, signifying that the land and ocean components are responding differently to external forcing. Similar patterns have been noted in other observational and modelling studies that report a weakening of the large-scale monsoon circulation under anthropogenic forcing but with regionally heterogeneous signatures (Bollasina et al. 2011; Chung and Ramanathan 2006; Jin and Wang 2017; Turner and Annamalai 2012).

To understand the nature of these changes more precisely, the zonal and meridional components of the 850 hPa winds were examined separately (Fig. 2.3). Over the South Asian landmass and northern Arabian Sea, the climatological circulation is dominated by the zonal component, whereas strong meridional cross-equatorial flow defines the Somali Jet over the western Arabian Sea.

The analysis shows that the overall weakening of winds across the continental regions and northern Arabian Sea is primarily due to a reduction in the westerly (zonal) component. In contrast, the strengthening over the ocean is largely associated with an enhancement of the meridional (northward) component, except near the western Arabian Sea where the increase in the zonal component contributes more substantially. Over central India, a slight increase in the meridional flow is observed, but this is outweighed by the decline in the zonal component, leading to a net reduction in the resultant wind magnitude. This decomposition confirms that the weakening of the monsoon circulation over land is driven mainly by the decline

in the zonal westerlies, which are dynamically linked to the subtropical pressure gradients over the region.

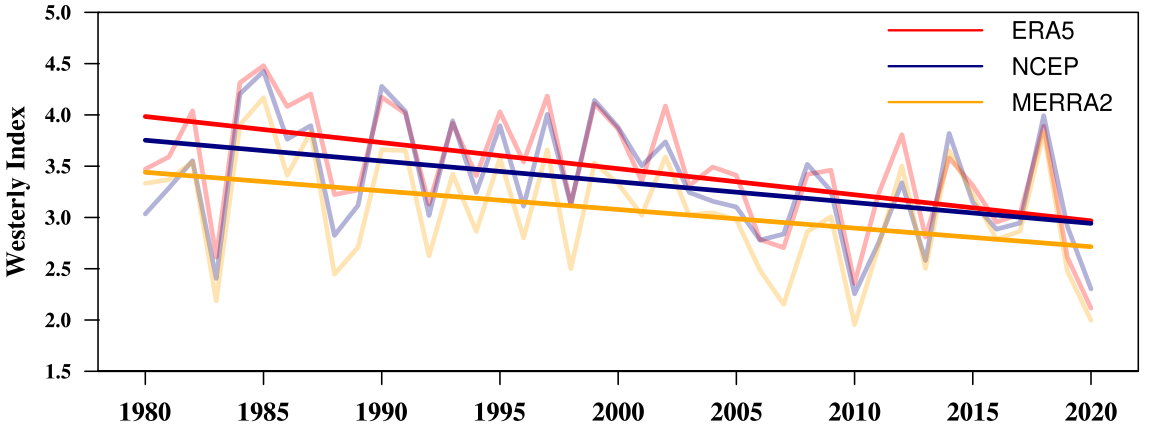


Figure 2.4 | The time series of westerly index (m sec^{-1}) defined as area-averaged zonal windspeed over the yellow box (20-30N 60-80E). The straight line is the fitted trend using linear regression, where slope is obtained from Theil-Sen estimator. The results are calculated for a common grid resolution of 0.25 x 0.25.

To quantify the magnitude and temporal evolution of this weakening, a WI was constructed as the area-averaged 850 hPa zonal wind over the domain 20°–30° N, 60°–80° E—representing the core of the subtropical westerly belt (Fig. 2.4). The index exhibits a persistent and statistically significant downward trend across all reanalyses. Over the 1980–2020 period, the WI decreased by approximately 1.04 m sec^{-1} in ERA5, 0.83 m sec^{-1} in NCEP–NCAR, and 0.74 m sec^{-1} in MERRA-2. This steady decline is significant at the 99 percent confidence level and indicates a coherent regional weakening spanning Pakistan, northwestern India, and adjoining areas of Afghanistan and Bangladesh. The agreement among datasets provides compelling evidence that the decline of the westerlies is a region-wide feature rather than a data artifact.

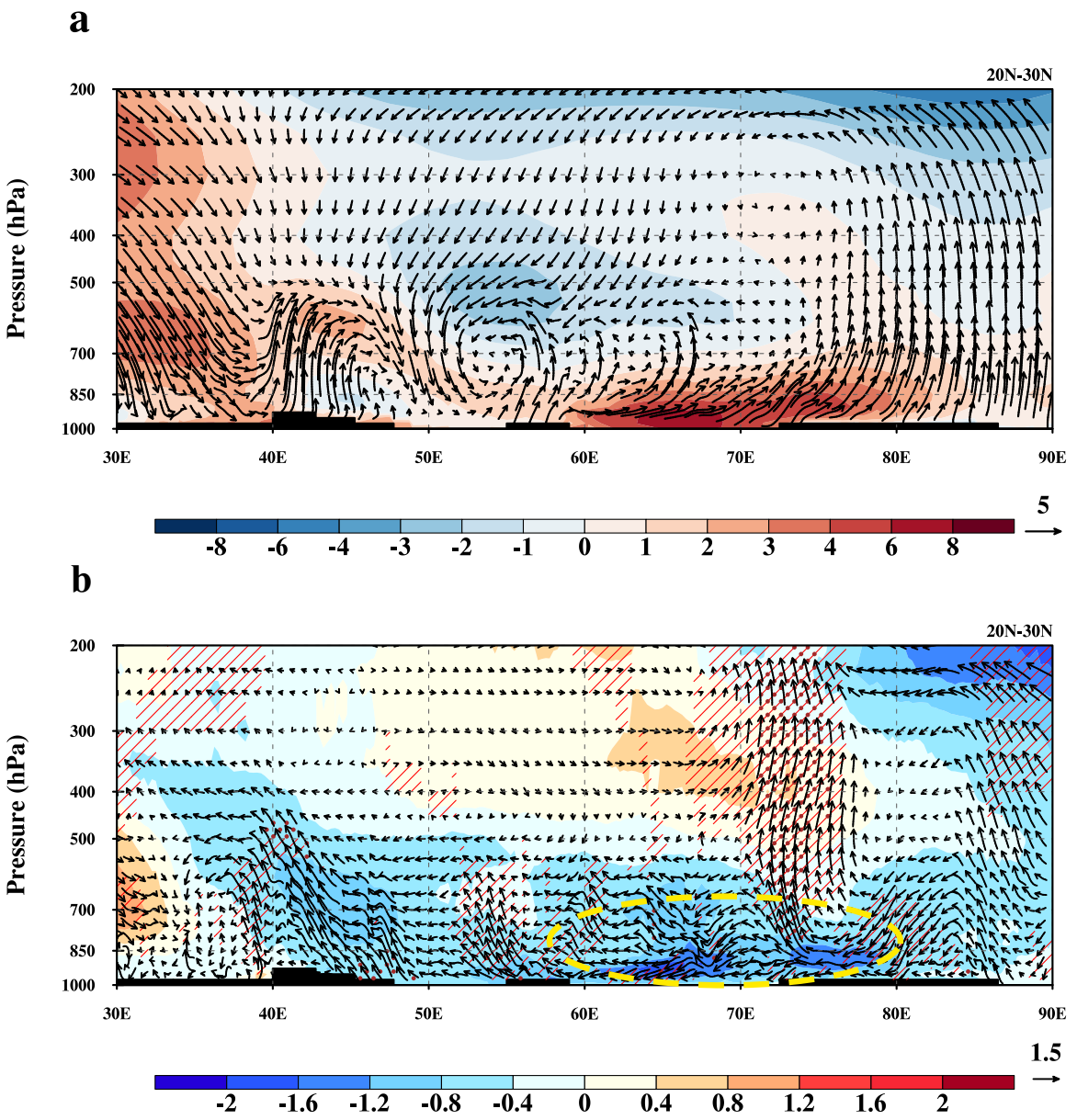


Figure 2.5 | The vertical structure of zonal circulation and its trend over the period. a The climatology, **b** the trend of zonal circulation (resultant of u and omega scaled by 10^2) averaged from 20N to 30N. The climatology shown in **a** is the mean of three data sets (ERA5, NCEP-NCAR, and MERRA2) and the shaded background is the zonal component (u) of the wind speed (m sec^{-1}). The shaded background in **b** is the trend of 'u' (m sec^{-1} per 41 years) in ERA5; the stippling represents the regions where the trend exceeds 99% statistically significant level, and the hatching represents the regions where all the three datasets agree in sign. The area of interest is marked with yellow ellipse. The results are calculated for a common grid resolution of 0.25 x 0.25.

The vertical structure of the wind change, examined through longitude–pressure cross-sections averaged between 20° and 30° N (Fig. 2.5), reveals that the reduction in zonal wind component (u) is not confined to the surface or boundary layer but extends vertically throughout the lower and mid-troposphere, reaching up to approximately 700 hPa. The weakening is accompanied by enhanced upward motion over northwestern South Asia and a corresponding reduction in subsidence over the Arabian Peninsula. This vertical coherence underscores that the observed change represents a large-scale dynamical adjustment rather than the result of local frictional or boundary-layer processes. It reflects a fundamental alteration in the thermal and pressure gradients that maintain the continental circulation.

The evidence from multiple reanalyses points to a systematic and spatially coherent decline of the STWs and a shift in the balance between the land and ocean branches of the monsoon. The weakening of the STWs emerges as a defining dynamical feature of the recent decades, with implications that extend beyond regional circulation patterns to influence monsoon precipitation, atmospheric energetics, and the surface wind resources of South Asia. These changes, as will be shown in the following sections, are part of a broader, externally forced reorganization of the South Asian monsoon system under ongoing climate change.

2.3.1 Sea-level Pressure and Temperature as Causal Drivers

In order to investigate the physical basis for the weakening of the STWs across South Asia, the SLP trends for the period 1980–2020 were examined in detail. According to the geostrophic wind relationship, the strength of the horizontal wind is directly proportional to the horizontal pressure gradient; hence, any reduction in pressure contrast between two regions inevitably weakens the winds flowing between them.

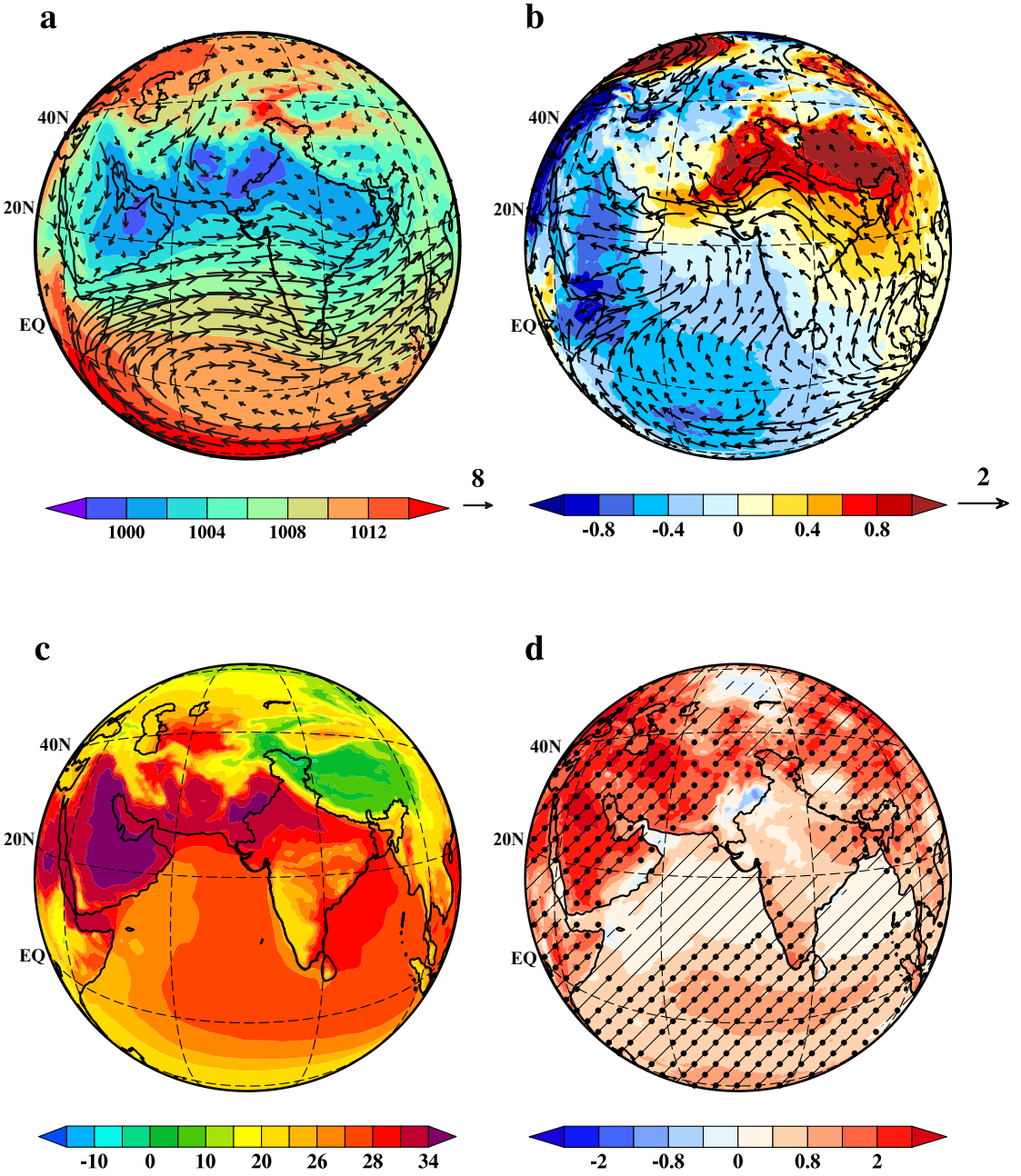


Figure 2.6 | Climatology and trends of sea level pressure (SLP) (hPa per 41 years), winds at 850hPa, and TS (ºC per 41 years). **a** Climatology and **b** the trends of SLP (underlying shading) during the Indian Summer Monsoon months (June-September) over 41 years (1980-2020). The overlaid wind vectors in **a** represent the climatological mean winds. The climatology shown in **a** is the mean of three data sets (ERA5, NCEP-NCAR, and MERRA2). The overlaid vectors and shaded background in **b** are the trends of winds and SLP, respectively, in ERA5. **c** Same as SLP in **a** but for TS. The shaded background in **d** is the trend of TS in ERA5; the stippling represents the regions where the trends exceed a 99% statistically significant level, and the hatching represents the regions where the sign of the trend agrees in all three datasets. The results are calculated for a common grid resolution of 0.25 x 0.25.

The mean SLP during the summer monsoon season displays a well-defined spatial pattern, with a characteristic low centered over northwestern South Asia and extending eastward across Pakistan and the IGP to the head of the Bay of Bengal (Fig. 2.6a). This continental low-pressure zone forms the monsoon trough, a key dynamical feature of the system. South of this trough, high pressure dominates the southern Indian Ocean, maintaining the strong meridional gradient that drives the monsoon flow.

The trend in SLP derived from ERA5 for the last four decades (Fig. 2.6b) reveals a distinct pattern of pressure change. Pressure has increased by approximately 0.4–1.0 hPa along the monsoon trough and its peripheral regions, including northwestern India, Pakistan, and adjoining areas of Afghanistan. In contrast, a decline of about 0.6 hPa is observed over the Arabian Peninsula and central Asia. The coexistence of positive SLP anomalies over the continental region and negative anomalies to the west effectively flattens the zonal pressure gradient that sustains the low-level westerlies. As a result, the winds that typically flow eastward across the subcontinent have weakened and partially deflected toward the Arabian Peninsula. The overlaid wind vectors in Fig. 2.6b clearly depict this westward deflection of the flow, indicating a weakening of the STWs.

In addition to the substantial changes in SLP over the land, a slight decrease in pressure is observed over the western equatorial Indian Ocean, most likely due to oceanic warming, which enhances local convection and deepens the thermal low. This pressure decrease contributes to a strengthening of the cross-equatorial flow from the Southern Hemisphere, which, upon crossing the equator, turns westward downstream toward the Arabian Peninsula. Thus, while the continental branch of the circulation has weakened, the oceanic branch has simultaneously intensified.

The spatial pattern of SLP change is physically consistent with the underlying pattern of differential heating across the region. The Arabian Peninsula has

undergone exceptional warming exceeding 2 °C, resulting in a significant reduction in surface pressure (Fig. 2.6d). In contrast, northwestern India and Pakistan have experienced comparatively weak warming or even slight cooling in certain areas, particularly within the IGP, despite the broader hemispheric warming trend. This asymmetry in surface temperature has effectively reduced the land–sea thermal contrast that historically underpins the monsoon circulation. The thermal weakening over the subcontinent raises surface pressure, while strong warming and resultant pressure falls over the Arabian Peninsula act to diminish the zonal gradient. The combined influence of these opposing anomalies weakens the geostrophic forcing of the STWs and weakens their strength.

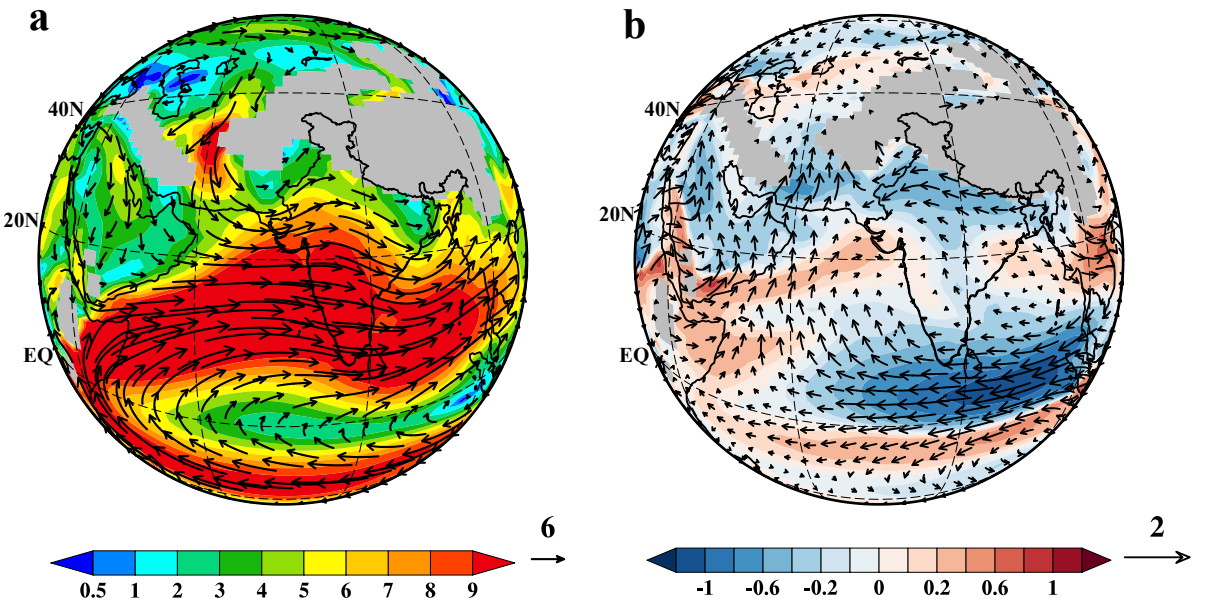


Figure 2.7 | Climatology and trends of winds at 850 hPa from CESM2-LE. **a** Climatology (m sec^{-1}) and **b** trends (m sec^{-1} per 41 years) of the wind speed at 850 hPa during Indian Summer Monsoon months (June-September) over 41 years (1980-2020) from all forcing CESM2-LE. The climatology shown in **a** is the ensemble mean wind speed of 50 ensemble members and the shaded background in **b** is the trend in the ensemble mean wind speed. The vector winds represent the direction of the winds – **a** climatology, and **b** trends in the ensemble mean.

In summary, the observed changes in SLP and TS reflect enhanced warming and pressure reduction over the western deserts and oceanic regions, limited warming and pressure rise over the northern Indian landmass, and consequent flattening of the zonal pressure gradient. This thermodynamic restructuring provides a direct and physically grounded explanation for the decline in the strength of the STWs and the anomalous westward redirection of low-level flow.

2.3.2 Simulated Forced Response – Insights from LEs

The climate system responds to a combination of externally forced changes and unforced internal variability that arises from coupled atmosphere–ocean dynamics. The LE simulations provide a framework to distinguish between these two components. In an LE, many realizations are produced under identical external forcings but with perturbed initial conditions; averaging across members suppresses uncorrelated internal variability, leaving the EM as an estimate of the externally forced response (Deser et al. 2020; Frankcombe et al. 2018). The spread among ensemble members represents the range of internal variability about this forced signal (Simpson et al. 2025). Recent coordinated initiatives, such as LESFMIP (Smith et al. 2022), emphasize that large ensemble sizes (≈ 30–50 members) are required to robustly extract regional-scale forced signals, particularly for atmospheric circulation changes where the signal-to-noise ratio is low. Hence, the ensemble mean (EM) of the CESM2 Large Ensemble provides an estimate of the externally forced response by averaging out internal variability across multiple realizations. Individual ensemble members represent different realizations of internal variability, and their spread quantifies its magnitude. This separation is essential for interpreting regional circulation changes and assessing the robustness and confidence of projected climate responses.

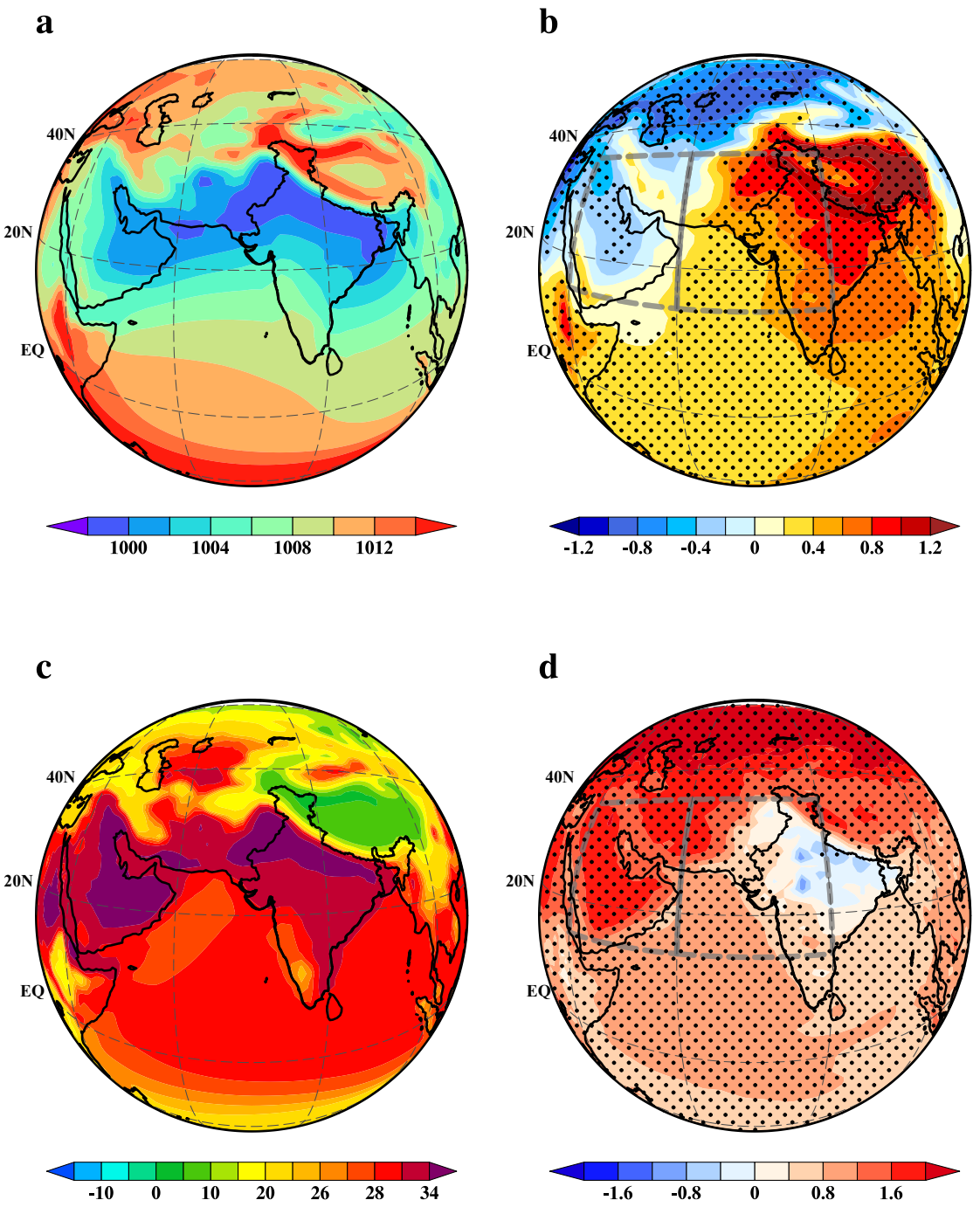


Figure 2.8 | Climatology and Trends of SLP (hPa per 41 years), and TS (ºC per 41 years) from ALL forcing CESM2-LE simulations. a Climatology **b** Trends of ensemble mean SLP, during the Indian Summer Monsoon months (June-September) for 1980-2020 from 50-membered CESM2-LE simulations. The stippling represents the regions where the trends exceed 99% statistically significant level. **c, d** Same as **a, b** but for TS. The rectangular boxes in **b** and **d** are used for area-average calculations in the analysis of Fig. 2.13.

An estimate of the forced climate response to all external forcings is estimated from the EM trends of the CESM2-LE (referred to as ALL in the following sections; see methods). The simulated response of winds is largely consistent with the observed trends in the South Asian region; however, the pattern of change over land is spatially broader and weaker in magnitude (0.2–0.6 m sec^{-1}) compared to the reanalysis data (Fig. 2.7b). This represents a simulated weakening that is approximately 50–60% smaller than the observed trends in the reanalyses. Similar to the reanalyses, anomalous easterly winds along the monsoon trough region are also simulated (Fig. 2.7b). The WI in ALL simulations shows a weakening trend smaller than the observed (not shown). Overall, the large-scale pattern of weakening is reproduced across ensemble members, indicating a forced signal despite the reduced amplitude relative to observations.

The trends in SLP from all-forcing CESM2-LE model simulation are shown in Fig. 2.8b, where widespread positive trends of 0.4-1.0 hPa over the South Asian region and significant negative trends of 0.2-1.0 hPa over the Arabian Peninsula and central Asian region are simulated, consistent with the observed changes in SLP. Further, the simulated cooling of the IGP (~0.6^{o}C), and the lack of significant warming in northwestern South Asia, amidst widespread warming of more than 1^{o}C in neighbouring regions, are consistent with observations. Moreover, the model also simulates a substantial warming (~1.4^{o}C) of the Arabian Peninsula and the Iranian Plateau (Fig. 2.8c). Close agreement in the simulated and observed patterns of surface pressure and temperature reinforces that the model captures the large-scale thermodynamic gradients that underpin the weakening of the STWs.

The ALL CESM2-LE simulations largely capture the nuances of the observed changes, providing confidence in using the more granular SF simulations to isolate the drivers of wind changes over South Asia. Therefore, we leverage the CESM2-SF-LE to pinpoint the specific drivers of the observed weakening of the STWs.

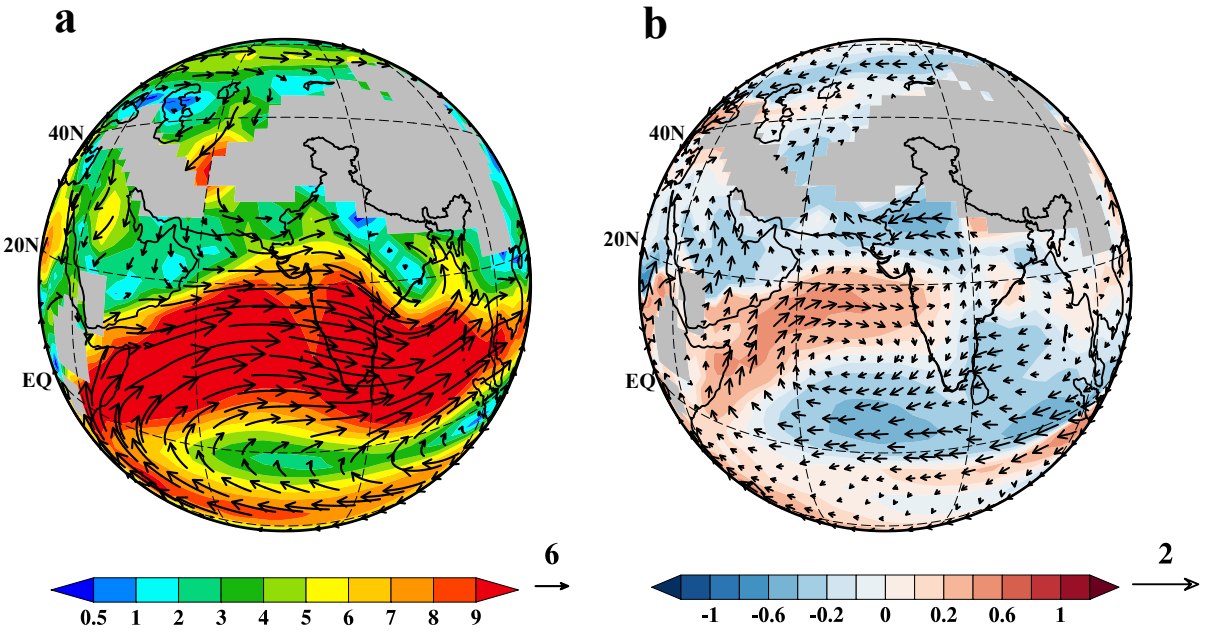


Figure 2.9 | Climatology and trends of winds at 850 hPa from MPI-ESM GE. a Climatology (m sec^{-1}) and b, trends (m sec^{-1} per 41 years) of the wind speed at 850 hPa during Indian Summer Monsoon months (June-September) over 41 years (1980-2020) from all forcing MPI-ESM GE. The climatology shown in a is the ensemble mean wind speed of 50 ensemble members and the shaded background in b is the trend in the same. The vector winds represent the direction of the winds – a climatology, and b trends in the ensemble mean.

We further explore the 50-member Grand Ensemble simulation of MPI-ESM to verify the results and investigate inter-model differences in reproducing observed trends. In the EM, wind speed is simulated to decrease by 0.2–0.4 m sec^{-1} in northwestern South Asia, which, while being less than the magnitude of the reduction in CESM2-LE exhibits a similar pattern of change (Fig. 2.9b). The time evolution of WI also shows a marginal weakening (~0.19 m sec^{-1}) in zonal wind component (u) over the region (not shown). Thus, while the forced responses estimated in two large ensembles exhibit some differences in terms of magnitude, there is a general agreement in the patterns of change. The simulated pressure and temperature trends by EM of MPI-ESM GE also show similar pattern of changes as that of the CESM2-LE.

2.4 Attribution of Changes to External Forcings: Insights from SF Experiments

The co-existence of multiple external forcings—GHG, AER, and LULC—along with natural variability, presents a significant challenge in attributing the observed regional climate trends. To disentangle these influences, SF-LE simulations from CESM2 were employed. These simulations provide a powerful and direct framework for isolating the effects of individual forcing agents. Each experiment evolves one external forcing while keeping others fixed at pre-industrial levels, thereby allowing the direct quantification of its contribution to the observed changes. This design enables a systematic decomposition of the overall response into the separate influences of AER, GHG, BMB aerosols, and LULC changes. By construction, ensemble averaging suppresses internal variability, yielding a clearer estimate of the forced response. This single-forcing large ensemble framework (e.g., Deser et al. 2020; Simpson et al. 2023) enables physically consistent attribution. Comparing the sum of individual responses with the all-forcing case also helps assess nonlinear interactions among forcings.

Among all the external forcings examined, anthropogenic aerosols emerge as the dominant driver of the observed weakening of the STWs. During 1980–2020, the aerosol-only simulation reveals widespread surface cooling of about 0.4–1.0 °C over South Asia, with the strongest anomalies over the IGP (Fig. 2.11a). This cooling leads to a robust increase in SLP of approximately 0.2–0.6 hPa over the same region, where a climatological low-pressure system typically resides during the summer monsoon (Fig. 2.10a). The underlying process—commonly referred to as the "dimming" mechanism (Bollasina et al. 2011; Ramanathan et al. 2005)—arises because aerosols scatter and absorb incoming solar radiation, reducing the net amount of shortwave energy reaching the surface. Over heavily polluted regions such as northern India,

this persistent reduction in surface insolation has lowered daytime temperatures and suppressed boundary-layer turbulence. The resulting surface cooling raises surface pressure and acts to weaken the meridional and zonal pressure gradients that sustain the monsoon flow.

This aerosol-induced dimming has effectively masked a portion of the greenhouse gas–driven warming that would otherwise have occurred. As a result, the Indian subcontinent has warmed at a slower rate than the global average, with the IGP showing particularly subdued warming relative to nearby oceanic and desert regions. This response reflects the weakening of the land–sea pressure gradient described earlier with observations. This mechanism directly links human-induced air pollution to the dynamical weakening of the monsoon circulation and provides a clear physical explanation for the observed decline in westerly strength.

LULC changes, incorporated within the "Everything Else" (EE) forcing, reinforce this aerosol effect and contribute substantially to the overall pressure anomalies (Fig. 2.10b). The EE simulation shows a moderate increase in SLP across central and southern India, extending the aerosol-induced high-pressure anomaly. The corresponding TS response exhibits localized cooling, particularly over irrigated and urbanized regions. These signals are consistent with known effects of large-scale irrigation, which enhances latent heat flux and evapotranspiration, thereby lowering surface temperature and increasing surface humidity. Over the IGP, the extensive expansion of irrigated agriculture in recent decades has produced precisely these effects, altering the local energy balance and sustaining a higher surface pressure anomaly during the monsoon season. Similarly, rapid urbanization and land conversion in northern India have modified albedo and roughness length, further altering the regional energy distribution. The combined outcome is a weakening of the pressure gradient between the Indian subcontinent and the Arabian Peninsula.

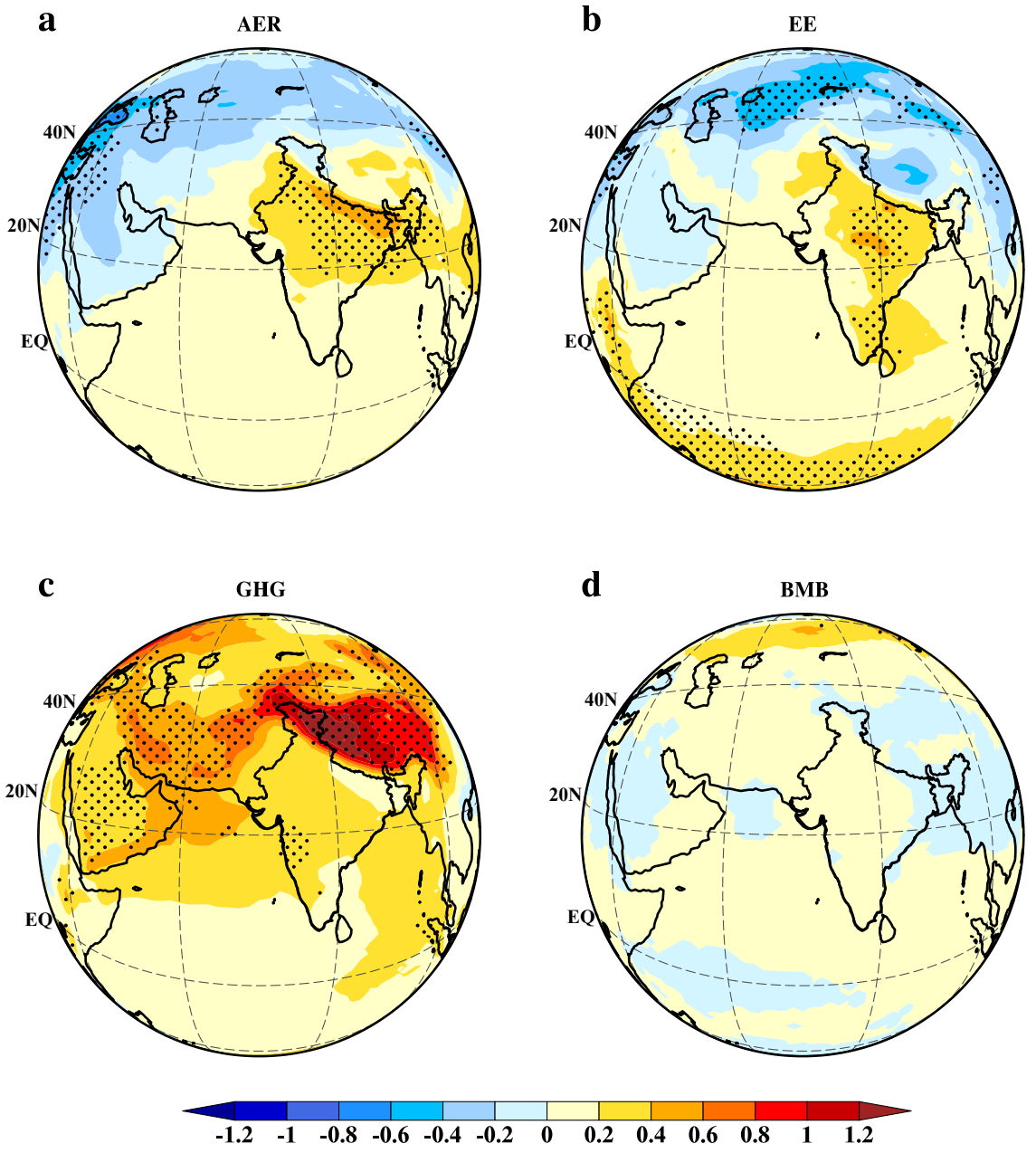


Figure 2.10 | Trends of SLP from Single Forcing Large Ensemble (SF-LE) simulations of CESM2. Trends of the SLP (hPa per 41 years) during the Indian Summer Monsoon months (June-September) for 1980-2020 from CESM2 SF-LE for the four individual forcings – a Anthropogenic Aerosols (AER), b Everything Else (EE), c Greenhouse Gases (GHG), and d Biomass Burning Aerosols (BMB) (see methods). Trends are calculated for ensemble mean of 20 ensemble members for AER (a) and 15 ensemble members for other forcings (b-d); the stippling represents the regions where the trends exceed 99% statistically significant level.

The EE forcing also contributes indirectly to the warming of the Arabian Peninsula and the Iranian Plateau (Fig. 2.11b), regions that strongly influence the meridional pressure gradient driving the STWs. Together, the aerosol and LULC forcings create a distinct pattern of land–sea thermal contrast reduction—cooling and pressure rise over India, coupled with warming and pressure fall to the west. The weakening of this gradient represents the key dynamical pathway through which these forcings exert their influence on the large-scale monsoon circulation.

GHGs are the primary global driver of climate change, but their regional influence over South Asia is complex and often modulated by aerosols and land-surface processes. The GHG-only simulation reveals widespread warming exceeding 1 °C across most of India and the Indian Ocean (Fig. 2.11c). However, this warming is largely counteracted by the aerosol-induced cooling, resulting in muted observed warming over the landmass. The combined effect—GHG-driven warming masked by aerosol dimming—is central to understanding the regional monsoon response. Under GHG-only forcing, SLP decreases significantly over the Arabian Peninsula and Central Asia due to strong surface warming in these regions (Fig. 2.10c). Over northern India, however, the model shows a weak increase in SLP of about 0.2–0.4 hPa. This counterintuitive result likely arises from increased atmospheric heating due to enhanced precipitation and latent heat release, which offsets the surface warming's tendency to lower pressure. The net effect is a heterogeneous pressure response: pressure rises modestly over northern India but declines sharply to the west. This pattern mirrors the observed weakening of zonal and meridional pressure gradients, though with a smaller magnitude than that driven by aerosols and LULC. Thus, GHGs shape the broad weakening pattern but cannot account for its full amplitude. Instead, the regional outcome reflects the interplay between GHG-induced warming and aerosol-induced cooling.

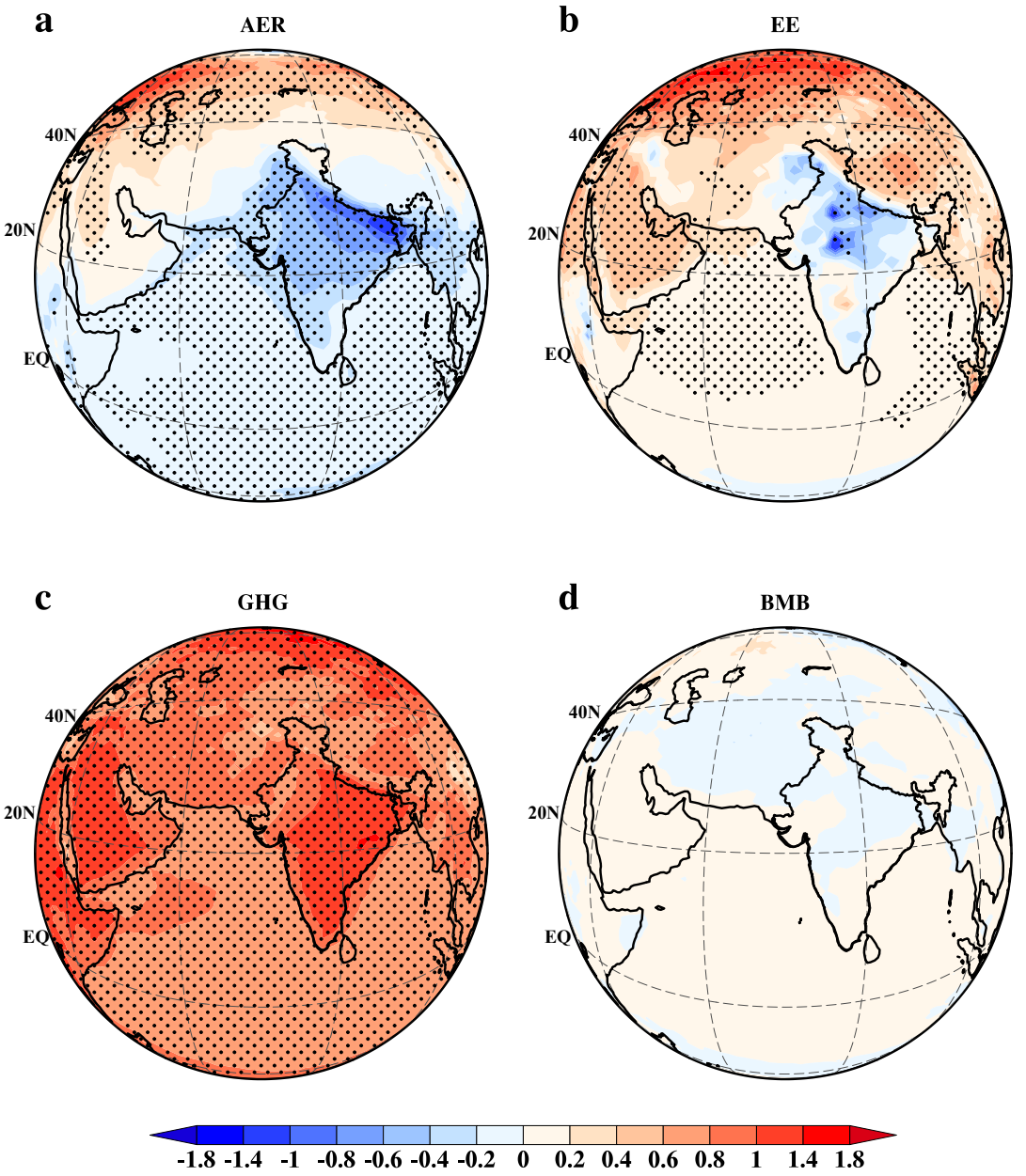


Figure 2.11 | Trends of TS (ºC per 41 years) from Single Forcing Large Ensemble (SF-LE) simulations of CESM2. Trends of the TS (ºC per 41 years) during the Indian Summer Monsoon months (June-September) for 1980-2020 from CESM2 SF-LE for the four individual forcings – a Anthropogenic Aerosols (AER), b Everything Else (EE), c Greenhouse Gases (GHG), and d Biomass Burning Aerosols (BMB) (see methods). Trends are calculated for ensemble mean of 20 ensemble members for AER (a) and 15 ensemble members for other forcings (b-d); the stippling represents the regions where the trends exceed 99% statistically significant level

BMB play a comparatively minor role in the South Asian circulation response (Fig. 2.10d and 2.11d). Their direct radiative impact is limited, as emissions over the subcontinent are relatively smaller compared to industrial aerosol sources. Nonetheless, BMB can exert important remote influences through their effect on the tropical Indian Ocean. Recent studies (Tian et al. 2023) have shown that changes in BMB emissions over Africa and South America have contributed to the enhanced warming of the tropical Indian Ocean. In the CESM2 simulations, this process manifests as a slight decrease in SLP over the western Indian Ocean, consistent with local SST increases. Although this effect indirectly strengthens the cross-equatorial flow, it does not significantly alter the continental circulation. Hence, while BMB aerosols modulate oceanic conditions, their contribution to the weakening of the STWs is negligible.

2.4.1 Role of Internal Variability

Internal variability refers to natural, unforced fluctuations within the climate system that can manifest on a range of timescales, from interannual to multidecadal (Deser et al. 2020). Because a single observational record represents just one possible realization of climate history, separating the human-caused signal from this natural noise is a significant challenge. LE climate model simulations, such as the CESM2-LE, are specifically designed to overcome this by producing many simulations with the same external forcings but different initial conditions. By averaging across these many members, the forced climate signal can be robustly isolated from the random fluctuations of internal variability, while the spread of the ensemble quantifies the magnitude of this variability (Frankcombe et al. 2018).

Here we analyze observed trends in the WI, SLP, and TS against the changes from individual members as well as the EM of the large ensemble simulation to

determine if the changes are a forced response or due to internal variability. This approach focuses on the key regions of northwestern South Asia and the Arabian Peninsula, as their combined temperature and pressure gradients are the primary driver of the STWs. The range of internal variability estimated by two standard error (the black error bar) in the 50-membered total forcing simulations.

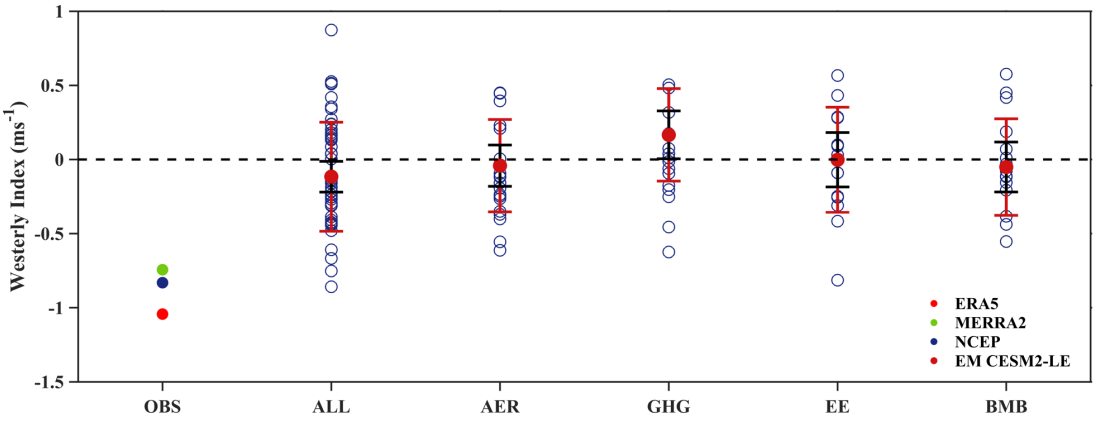


Figure 2.12 | Trends of Westerly Index from reanalyses, CESM2-LE and SF simulations. Trends of westerly index (m sec^{-1} per 41 years) during Indian Summer Monsoon months (June-September) over 41 years (1980-2020) from the three reanalyses, all forcing, and single forcing simulations of CESM2 LE. For the model simulations, trends from individual members are represented with open markers and the ensemble mean trends are marked with the filled markers. The black error bars represent the two-standard error (i.e. $\boldsymbol{2\sigma/\sqrt{N}}$), where $\boldsymbol{\sigma}$ is the standard deviation of the trends from individual members and N is the number of ensemble members. The red error bars represent $\boldsymbol{2\sigma}$ range.

A comparison of observed trend in WI as those from ensemble members of CESM2-LE ALL-forcing simulations highlights a discrepancy in magnitude. While the reanalyses show a pronounced weakening of the WI, with trends falling at approximately −0.8 to −1.0 m sec^{-1} over the 41-year period, the EM trend of the CESM2-LE is significantly smaller at (−0.12±0.05) m sec^{-1} (Fig. 2.12). The fact that the observed trends fall at the lower end of the ensemble spread indicates that the model simulations systematically underestimate the magnitude of the weakening of the westerlies. This suggests two possibilities: either the model's sensitivity to the external forcings is too weak, or the observed trend has been amplified by an

unforced, low-frequency mode of natural variability that the models did not capture. This finding underscores a critical area of model deficiency that warrants further investigation.

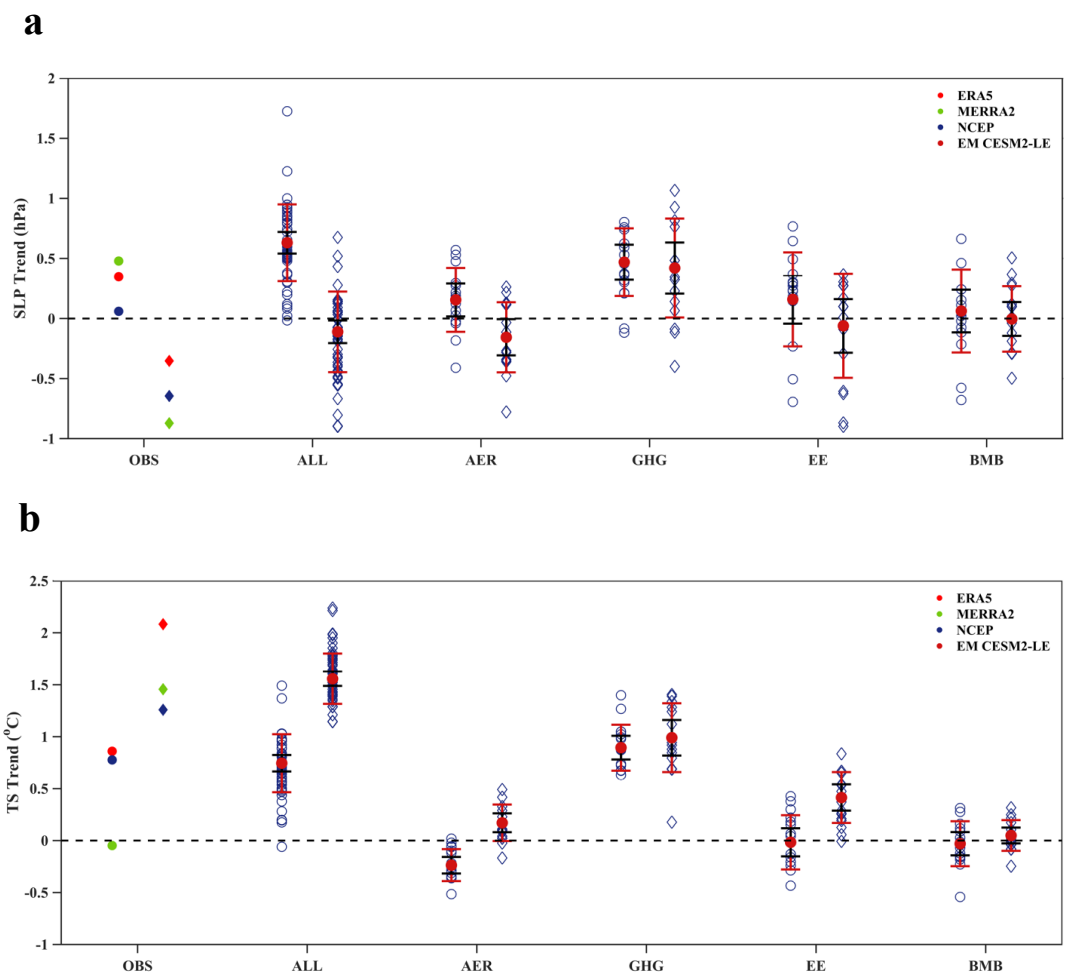


Figure 2.13 | Trends of area averaged SLP and TS from reanalyses, CESM2-LE, and SF simulations. Trends of **a** SLP (hPa per 41 years) and **b** TS (°C per 41 years) area-averaged over the northwestern South Asia and Arabian Peninsula during Indian Summer Monsoon months (June-September) over 41 years (1980-2020) from the three reanalyses, all forcing, and single forcing simulations of CESM2-LE. The circles represent trends for the first region bounded by (40E-60E) and, whereas the diamonds represent the second region bounded by (60E-80E) both in the latitudinal belt (15N-35N) (please see the rectangular boxes marked in Fig. 3). The trends are calculated only for the land after masking out the ocean. For the model simulations, trends from individual members are represented with open markers and the ensemble mean trends are marked with the filled markers. The black error bars represent the two-standard error (i.e. $\boldsymbol{2\sigma/\sqrt{N}}$), where $\boldsymbol{\sigma}$ is the standard deviation of the trends from individual members and N is the number of ensemble members. The red error bars represent $\boldsymbol{2\sigma}$ range.

The trends of the area-averaged SLP are shown for two representative boxes (Fig. 2.8) in the latitudinal belt (15°N-35°N), over the Arabian Peninsula and northwestern South Asia bounded by (40°E-60°E) and (60°E-80°E), respectively (Fig. 2.13a). The EM trend in SLP over northwestern South Asia is (0.63 ±0.04) hPa, and that over the Arabian Peninsula is (-0.11±0.05) hPa, for which the mean trend in reanalyses are 0.3 hPa and -0.62 hPa, respectively. The trends from the reanalyses fall beyond the range of internal variability estimated by two standard error (the black error bar) in the 50-membered total forcing simulations. This implies that the observed trends in SLP cannot be explained by internal variability alone and hence the changes are forced responses due to external forcings. Moreover, the trends from reanalyses, particularly ERA5, fall within the ensemble spread represented by the two-standard deviation (the red error bars) in all forcing simulation, which suggest that the trends in model simulations are consistent with the observed trends and remain within expected internal variability bounds.

The area averaged EM trend in TS over the northwestern South Asia is (0.74 ±0.04) ^{o}C and that over the Arabian Peninsula is (1.5±0.03) ^{o}C in total forcing simulations (Fig. 2.13b), while the mean trend in reanalyses are 0.53 ^{o}C and 1.6 ^{o}C, respectively. Similar to SLP, the observed changes in TS fall beyond the range of internal variability implying a robust forced signal (Fig. 2.13b). The range of internal variability and ensemble spread in TS is generally smaller compared to SLP, indicating lesser uncertainty in simulating the changes in temperature than pressure in model simulations. Therefore, the similarity between the changes from reanalyses and EM of CESM2-LE simulations suggests that the model simulations are capturing the main causes behind the observed weakening of monsoon winds, decreases in SLP gradient, and associated patterns of warming and large-scale circulation changes.

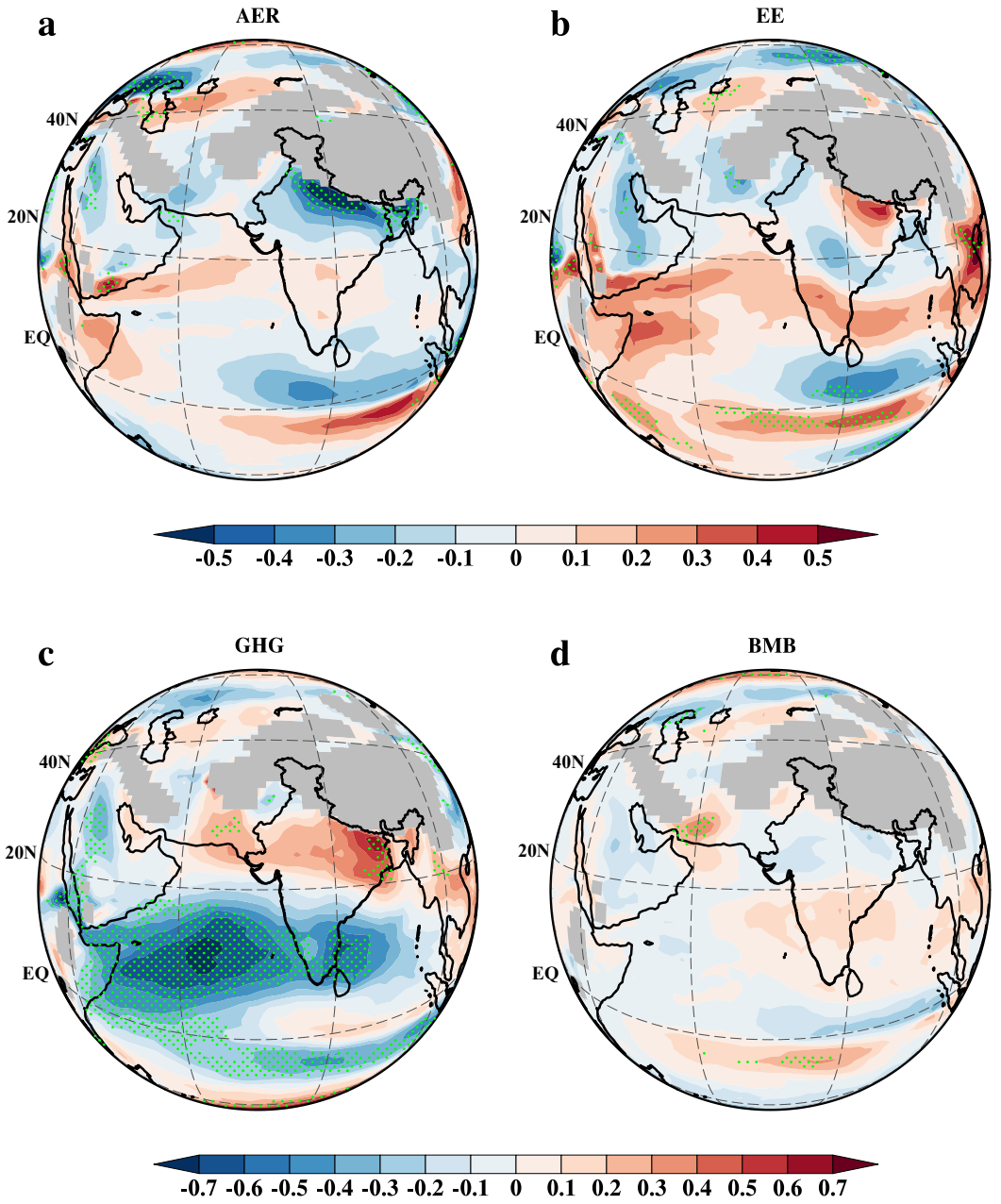


Figure 2.14 | Trends of wind speed at 850 hPa in Single Forcing Large Ensemble (SF-LE) simulations of CESM2 (m sec^{-1} per 41 years). Trends of the wind speed at 850 hPa during Indian Summer Monsoon months (June-September) over 41 years (1980-2020) from CESM2 SF-LE for four individual forcings – a Anthropogenic aerosols (AER), b Everything Else (EE), and c Greenhouse gases (GHG), and d Biomass burning aerosols (BMB) (see methods). Trends are calculated for the ensemble mean of 20 ensemble members for a AER and b-d, 15 ensemble members for other forcings; the stippling represents the regions where the trends exceed 95% statistically significant level.

2.4.2 Individual Forcing Contributions and Non-Linear Interactions

An analysis of the CESM2 single-forcing simulations provides clear insight into how individual external drivers contribute to the weakening of winds over South Asia. The results indicate that the observed decline arises from the combined influence of multiple forcings, each exerting distinct, and in some cases opposing, regional effects.

Anthropogenic aerosols play the dominant role. The aerosol-only simulations closely match the total forcing experiments and account for most of the observed weakening. Aerosol-induced surface cooling leads to an increase in SLP over the Indian landmass (Fig. 2.14a), reducing the land–sea pressure gradient and weakening winds, particularly along the monsoon trough. Land-use and land-cover changes, which dominate the "Everything Else" forcing, provide a secondary but significant contribution. These changes further enhance SLP over central and southern India, reinforcing the aerosol-induced pressure anomaly (Fig. 2.14b). The LULC forcing increases steadily throughout the period, unlike other EE components such as solar or volcanic influences, which show episodic variations and cannot explain the long-term trend.

GHGs exert a more spatially complex influence. While they cause widespread warming, the model shows modest strengthening of winds along 20°–30° N (Fig. 2.14c), a response overwhelmed by the aerosol-induced reduction. GHGs also drive a marked weakening of winds over the northern and equatorial Indian Ocean, consistent with strong oceanic warming and associated stability increases. Biomass-burning aerosols make only a minor contribution. Their direct effects on regional circulation are weak, and their indirect impacts—such as changes in tropical ocean heating—do not significantly alter continental winds.

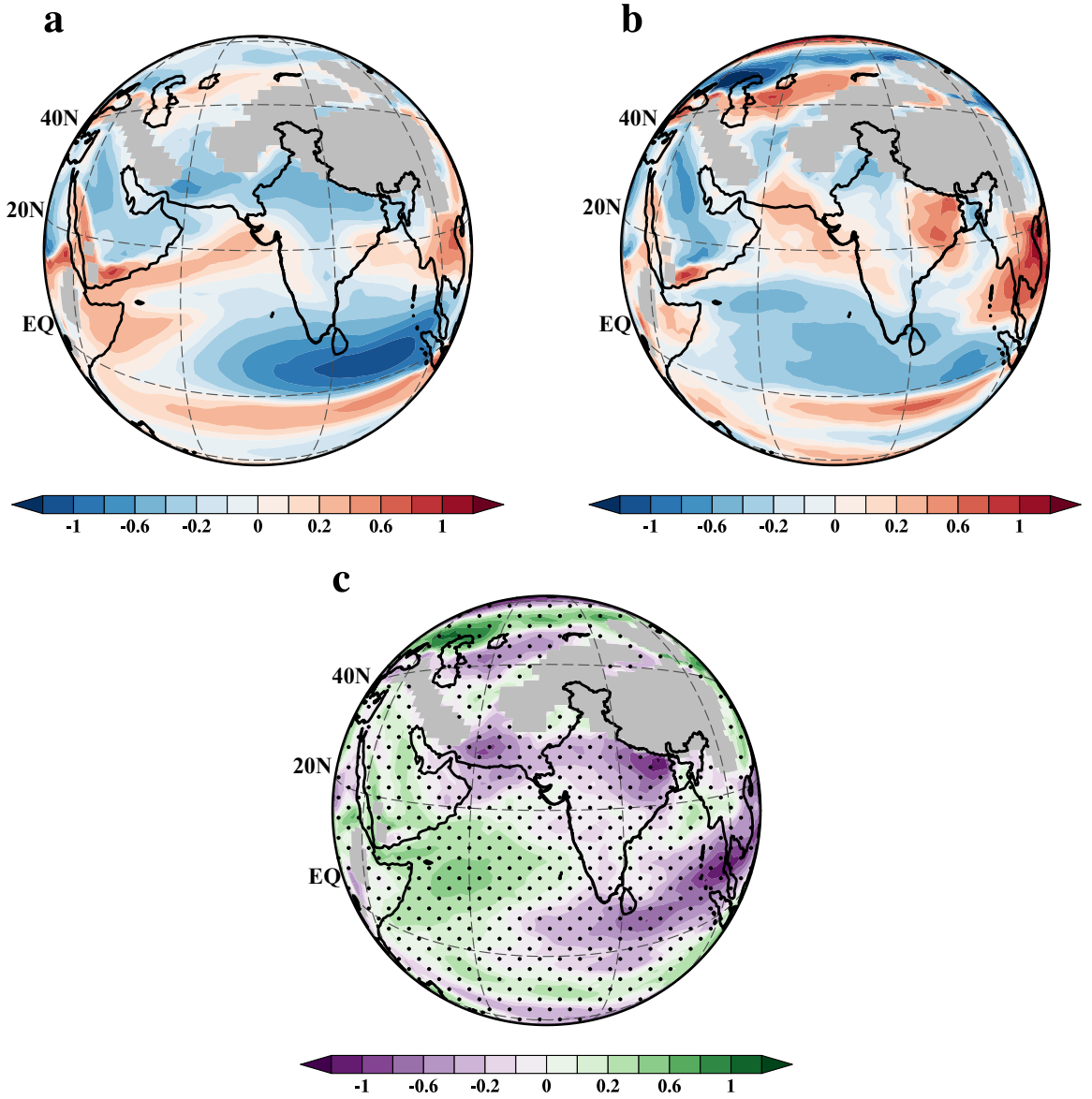


Figure 2.15 | Non-linearity in response of the wind speed to individual forcings at 850 hPa. Trends of ensemble mean **a** wind speed from all forcing CESM2 SF-LE, **b** sum of the trends of ensemble mean wind speed from individual forcings shown in Fig. 2.14, and **c** the difference a – b between the two. The stippling represents the regions where the difference exceed 99% statistically significant level.

A comparison of the total-forcing and summed single-forcing responses underscores the importance of non-linear interactions. The all-forcing response (Fig. 2.15a) exceeds the linear sum of individual responses (Fig. 2.15b), particularly over northwestern South Asia and the western Arabian Sea, where the difference is

statistically significant. These results indicate that interactions among forcings—especially between aerosols and GHGs—modify cloud–radiation and surface temperature feedbacks, amplifying the total response. Such coupling implies that linear superposition underestimates the true forced signal.

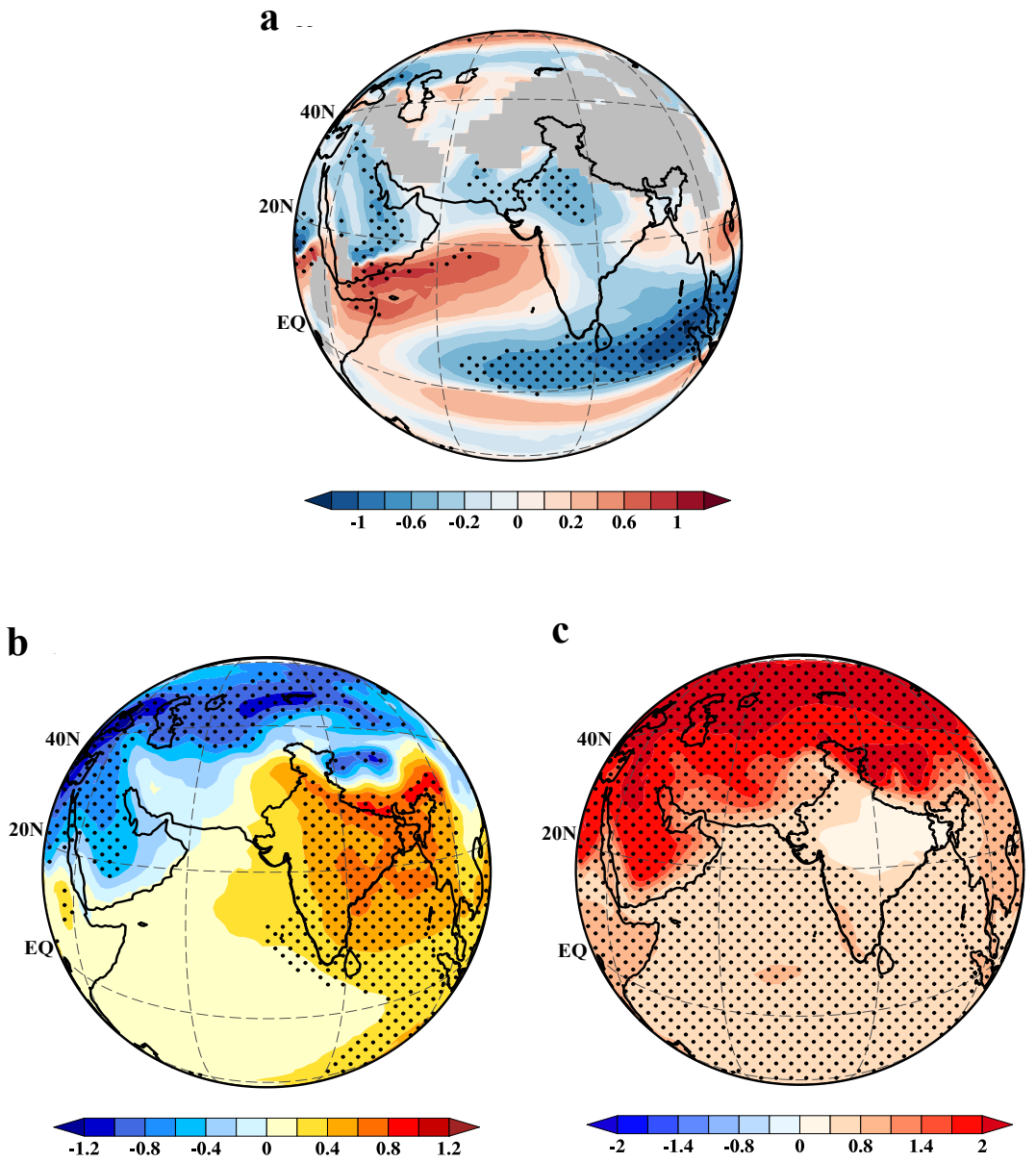


Figure 2.16 | Trends of wind speed at 850 hPa (m sec^{-1} per 41 years), SLP (hPa per 41 years), and TS (ºC per 41 years) from CMIP6 simulation. Trends of ensemble mean **a** wind speed at 850 hPa, **b** SLP, **c** and TS during the Indian Summer Monsoon months (June-September) for 1980-2020 from 12 models of CMIP6 all-forcing simulations. The stippling represents the regions where the trends exceed 99% statistically significant level.

Despite these complexities, the underlying thermodynamic drivers remain consistent: surface cooling and pressure rise over the subcontinent, coupled with warming and pressure decline over the Arabian Peninsula, have jointly reduced the meridional pressure gradient and weakened the STWs. The coherence between model results and reanalyses confirms that the observed changes in SLP and TS represent a robust forced response, beyond the range of internal variability, and can be confidently attributed to anthropogenic climate change.

2.4.3 Simulated Changes from CMIP and their Attribution using DAMIP

To further substantiate the results from the CESM2-LE simulations, all-forcing simulations from CMIP6 (ALL CMIP6) and complementary single-forcing experiments from 12 models participating in DAMIP were analyzed (see Methods and Table 1). The MMM trends in wind speed, SLP, and TS show consistency with both reanalyses and LE results (Fig. 2.16). The MMM indicates a clear reduction in lower-tropospheric wind speed of about 0.2–0.4 m sec^{-1} over northwestern South Asia, accompanied by a notable SLP rise of 0.4–0.6 hPa along the monsoon trough and a corresponding decline of 0.4–0.6 hPa over the Arabian Peninsula. These patterns collectively point to a weakening of the zonal pressure gradient and, consequently, of the STWs. The temperature change pattern simulated by the models also aligns with observations: temperatures over northern and central India remain largely unchanged, while pronounced warming exceeding 1.4 °C occurs over the Arabian Peninsula and central Asia. This spatial asymmetry in heating and pressure response reinforces the physical mechanism identified in the CESM2-LE results—namely, that differential land–sea and west–east thermal gradients have led to a systematic weakening of the monsoon's continental circulation.

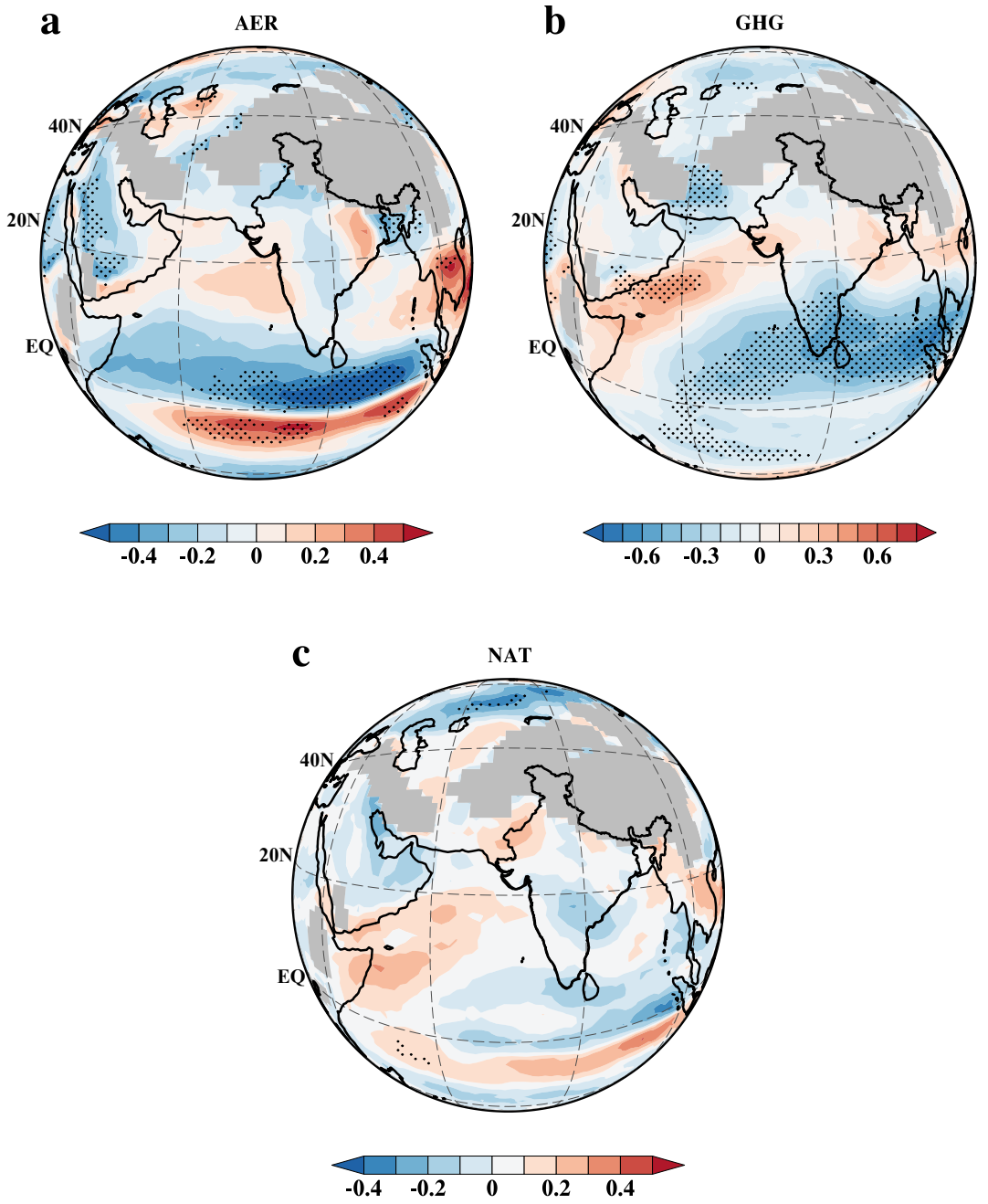


Figure 2.17 | The multimodel mean (MMM) trends of wind speed at 850 hPa in Single Forcing (SF) DAMIP simulations (m sec^{-1} per 41 years). Trends of the wind speed at 850 hPa during Indian Summer Monsoon months (June-September) over 41 years (1980-2020) from DAMIP6 for three individual forcings – **a** Anthropogenic aerosol emission (AER), **b** Greenhouse gases (GHG), and **c** Natural Variability (NAT) (see methods). Trends are calculated for multi model mean (MMM) of 12 models; the stippling represents the regions where the trends exceed 95% statistically significant level.

The agreement across multiple models provides additional confidence in the robustness of these findings. The analysis of single-forcing simulations from the CMIP6/DAMIP models also underscores the primary role of aerosols in the wind weakening, while finding that the contributions from GHGs and natural variability (NAT) are not significant (Fig. 2.17). A marginal weakening of winds in the monsoon trough region in AER simulations hints to be contributing to the overall weakening in ALL CMIP6 simulations; however, with an overall underestimation. The GHGs and NAT induced changes in wind speed are not significant and are in contrast to the simulated changes in ALL simulations almost over the entire Indian subcontinent. However, the strength of the weakening of winds in ALL simulations is significantly greater than in AER simulations, which may be partly because of unaccounted contributions from LULC changes and partly because of non-linearity in the combined effects of the external forcings.

2.5 Weakening of STWs in the Context of Monsoon Low-level Jet Shift

Analysis of reanalyses suggests that the Somali Jet, which represents the primary oceanic component of the monsoon circulation, has largely maintained its position and intensity through recent decades. In the JJAS climatology (Fig. 2.18a), the jet core is located between 5°N and 10°N, with maximum wind speeds exceeding 12 m sec^{-1}. Examination of the jet axis, defined as the latitude of peak 850 hPa wind speed, shows minimal meridional displacement since 1980. Both ERA5 and MERRA-2 indicate that the axis has remained nearly stationary or shifted marginally southward by about 1° near 70°–75° E (Fig. 2.18b). Thus, the weakening of the STWs has occurred without any corresponding structural shift in the low-level jet that dominates the oceanic branch of the monsoon.

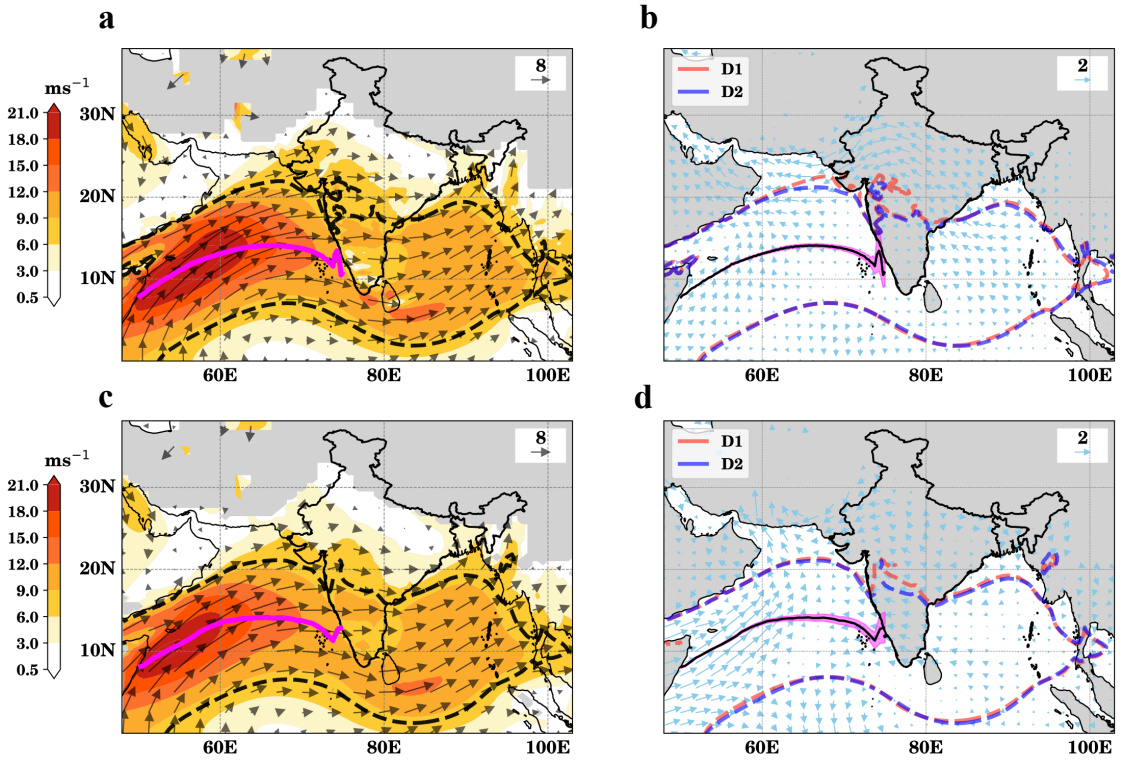


Figure 2.18 | Climatology and shifts in the horizontal and vertical position of the Somali Jet over the last four decades. a. Climatology of winds at 850 hPa from 1980-2022 for June through September (JJAS). The meridional extent of the jet is depicted by the contour of 8 m s^{-1} (black dashed contour). The axis of the jet is defined as the contour of maximum wind speed, denoted by a pink line. **b.** The contour of the meridional extent of the jet for the first (D1, red dashed contour) (1980-1989) and last (D2) (2011-2020), blue dashed contour) decade, along with the mean climatological position of the axis of the jet (black line), is shown. The interannual variability (one standard deviation) in the location of the axis of the jet is indicated with pink shading. **c, d** Same as a, b but for MERRA2 dataset.

Extending the analysis back to 1940 reveals a modest but consistent southward shift of approximately 1.5°, along with a slight weakening of the jet's maximum speed (Fig. 2.19). These trends, although statistically significant, are small in magnitude and do not suggest any substantial displacement of the low-level jet. Contrary to earlier suggestions of a systematic northward migration (Sandeep and Ajayamohan 2015), the longer record indicates that the Somali Jet has remained broadly stationary, with no robust evidence of poleward shift. This stability implies

that the observed weakening of the STWs over land is not dynamically linked to changes in the position or strength of the oceanic jet.

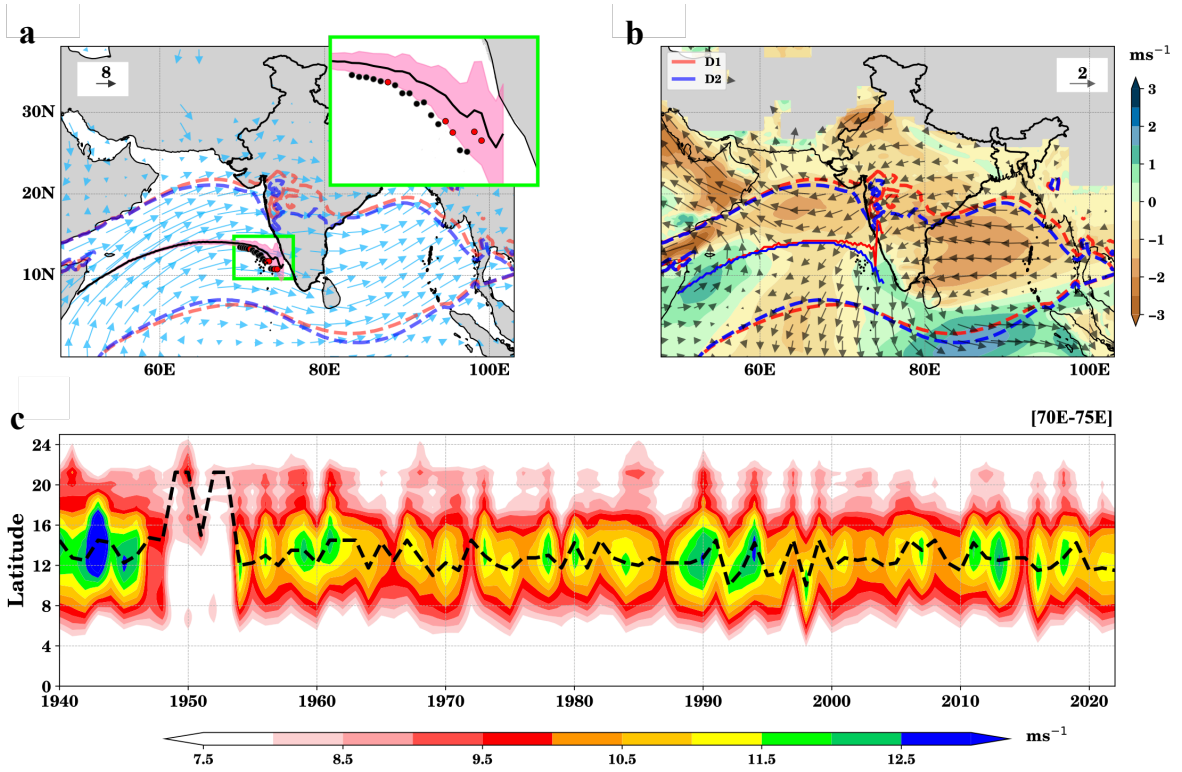


Figure 2.19 | Shifts in the Somali Jet at 850 hPa over the last eight decades. a. The contour plot of the meridional extent of the jet for the first (D1) (1940-1949) and last (D2) (2010-2019) decade, along with the mean climatological position of the axis of the jet. The interannual variability (one standard deviation) in the location of the axis of the jet is indicated with pink shading. The green box marks the location of a significant shift in the jet. The inset image is the expanded view of the green box. The black filled circles depict locations where there is a significant shift in the location of the axis of the jet. The red filled circles depict the locations, where there are significant shift in the axis of the jet, but the trend is within the interannual variability of the jet. **b.** The difference in winds from the last decade (D2) (2010-2019) to the first decade (D1) (1940-1949), with the meridional extent of the jet from each decade depicted separately, along with the axis of the jet from the respective decade. **c.** The time evolution of wind speed across the latitudes is represented as the Hovemöller diagram averaged over the eastern Arabian Sea (70E-75E), where the trends are significant. The latitude of maximum wind speed is denoted using the black dashed line.

The differing responses of the two systems reflect their distinct physical controls. The Somali Jet is primarily governed by cross-equatorial sea surface temperature gradients and large-scale Hadley circulation adjustments, whereas the

STWs are shaped by land–atmosphere thermal contrasts, aerosol forcing, and orographic influences. While greenhouse-gas-driven ocean warming has slightly strengthened the cross-equatorial flow, aerosol- and land-use-induced surface cooling over the subcontinent has weakened the continental branch. The contrasting responses of these two regimes underscore that the decline in STWs arises from regional thermodynamic and radiative imbalances rather than from a shift in the low-level jet itself.

This context establishes that the weakening of the STWs is an independent feature of the evolving monsoon circulation. The Somali Jet's quasi-stationary behaviour rules out the possibility that the continental slowdown is compensated by an oceanic intensification or migration. Instead, both observational and model evidence point to a decoupling of the land and ocean branches of the monsoon, each responding to different aspects of external forcing. Although the long-term behaviour of the jet appears stable, its subtle variations warrant closer investigation in future work to assess whether small-scale or transient changes may influence the broader circulation response.

2.6 Surface Wind Changes and Implications for WPP

The observed weakening of the STWs is not an isolated phenomenon confined to a single atmospheric layer but rather a part of a larger-scale circulation change that extends to the near-surface (Fig. 2.5b). Over the last four decades (1980–2020), near-surface wind speed (10m height) in South Asia has significantly weakened, particularly over Northwestern India (NWI) and southern Pakistan (Fig. 2.20a). In these regions, wind speed has decreased by approximately 1 m sec^{-1}, representing a substantial reduction of ~30% with respect to the climatological mean. This robust

trend, consistently observed across three independent reanalysis datasets, confirms a significant, large-scale change in regional wind patterns.

This decline in wind speed has profound implications for the region's renewable energy landscape, as wind power density is proportional to the cube of wind speed ($P \propto V^3$). The observed wind weakening translates directly into a substantial decline in onshore wind power potential. To quantify this, an analysis using an industrial wind power curve (discussed the detailed methodology and technical details in Chapter 3) shows a decrease in wind power of up to 300 MW over the key wind-power potential regions of northwestern and southwestern India (Fig. 2.20b). Other parts of India, where mean wind power production is lower, experienced insignificant changes.

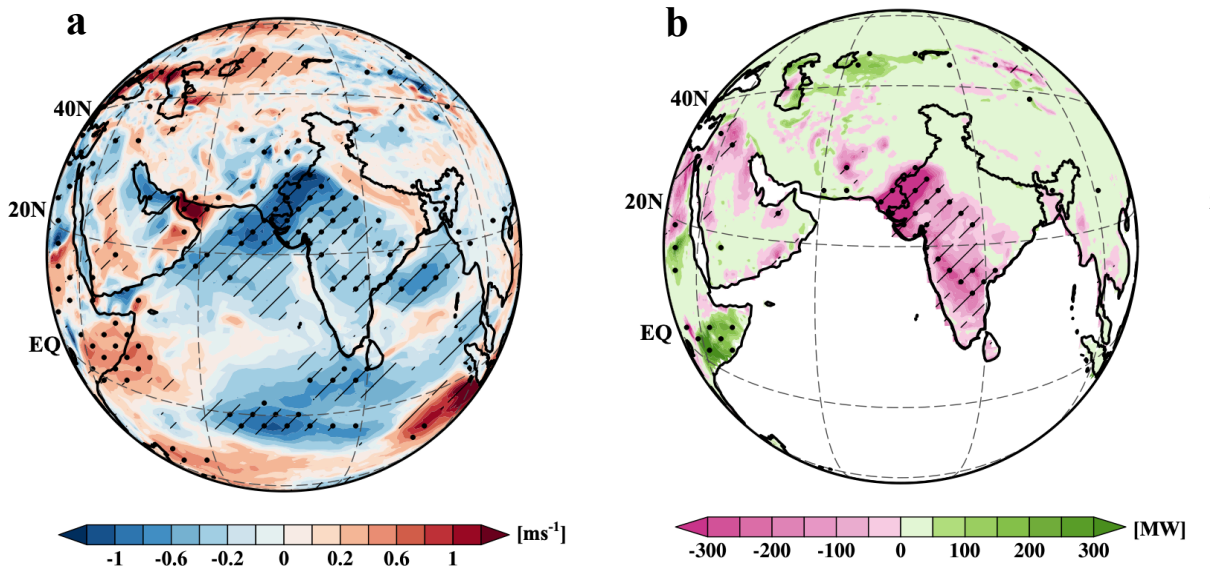


Figure 2.20 | Trends of near-surface winds (m sec^{-1} per 41 years) and Wind Power Potential (WPP) MW/grid per 41 years. **a** Trends (m sec^{-1} per 41 years) of near-surface (10m) wind speed during the Indian Summer Monsoon months (June-September) over 41 years (1980-2020) from the three reanalyses. The shaded background is the trend in ERA5; the stippling represents the regions where the trends exceed a 99% statistically significant level, and the hatching represents the regions where the sign of the trend agrees in all three datasets. **b** Same as **a**, but for WPP.

The economic and policy implications of this decline are crucial for India, a leading country in wind energy production in South Asia. Over 63% of the total annual wind energy is generated during the spring and summer months, highlighting the critical dependence of the sector on the prevailing southwesterly monsoon winds (Gao et al. 2018). The production is concentrated in western and southern states like Gujarat, Rajasthan, Maharashtra, and Tamil Nadu due to their favorable wind resources. This observed decline in wind power potential presents a direct conflict between the impacts of climate change and national and global commitments to expand renewable energy capacity. It underscores a crucial challenge for policymakers in the region as they plan for future energy mitigation and adaptation strategies.

The findings caution policymakers, government, and private agencies about the potential changes in the wind energy resources of South Asia that may unfold in the time to come. At a crucial juncture of migration from non-renewable to renewable energy to meet the region's ever-rising energy demands, the past and future changes in these wind energy resources are to be kept at the center stage for formulating policies to optimize the economic return from the large-scale investments that are being made in its development. A discussion on the future impact of climate change on wind power potential of South Asia, its attribution, and implications using LE simulations are presented in the chapter 3 of the thesis.

While the preceding analysis focused on historical wind changes and their implications for wind energy, such circulation changes also have important consequences for regional hydroclimate. The South Asian monsoon is a coupled system in which lower-tropospheric winds govern moisture transport, convergence, and the distribution of precipitation, so any sustained weakening or reorganization is expected to leave a clear imprint on precipitation. To assess this hydrological response, we now examine long-term precipitation changes over South Asia.

Reliable observations from the early twentieth century enable a century-scale assessment, and recent changes are interpreted alongside the circulation changes in the last few decades.

2.7 Observed Changes in Precipitation

The observed trend in precipitation from 1901 to 2020 shows distinct spatial and temporal variations (Fig. 2.21), with some components evolving monotonically and others modulated by multidecadal oscillations (Fig. 2.22). Spatially, three broad regimes emerge. The most prominent feature is a persistent decline in precipitation over central-eastern India—part of the monsoon core region—which has exhibited a long-term downward trend since about 1940. The mean decrease of ~ 2 mm day^{-1} per 81 years corresponds to 20–25 percent of the climatological mean. This region, located within the IGP, is the "rice bowl" of South Asia and depends heavily on monsoon precipitation for agricultural productivity.

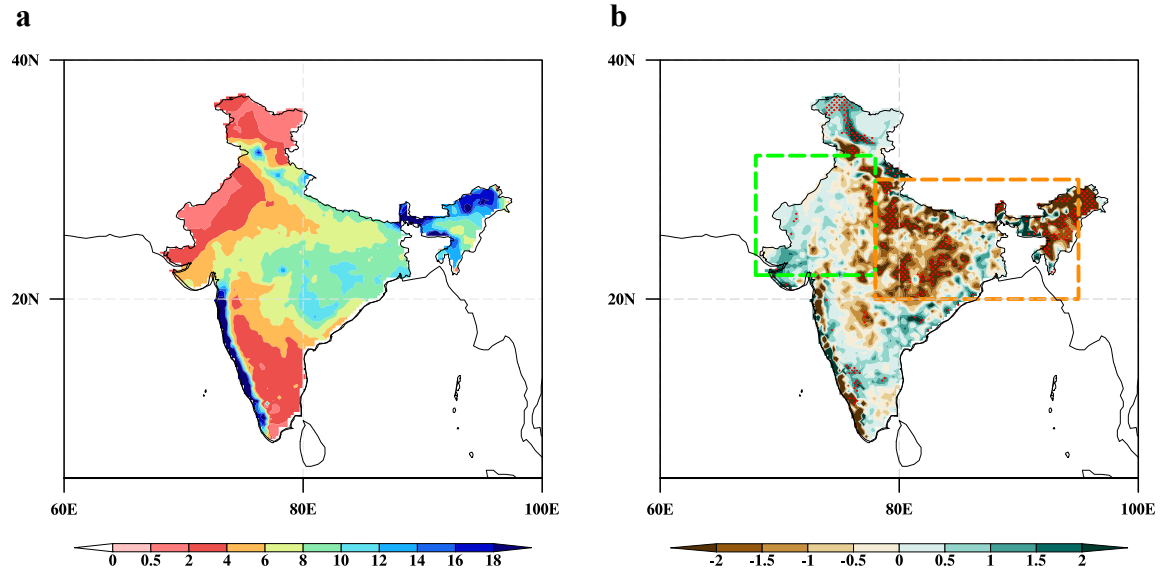


Figure 2.21 | Climatology and trends of precipitation (mm day^{-1}). a Climatology and b trends of the precipitation from gridded data by India Meteorological Department (IMD) during the Indian Summer Monsoon months (June-September) over 41 years (1940-2020). The stippling represents the regions, where the trends exceed 95% statistically significant level. c,d, Same as a,b, but for precipitation from GPCP data.

In contrast, north-western South Asia, including Pakistan and adjoining regions of India, shows a marked increase in precipitation during the past four decades. Although the century-scale increase is small, the post-1980 rise approaches 30%, representing one of the most significant regional hydroclimatic shifts in the observational record. Smaller yet coherent increases are also seen along the eastern coast and the Western Ghats.

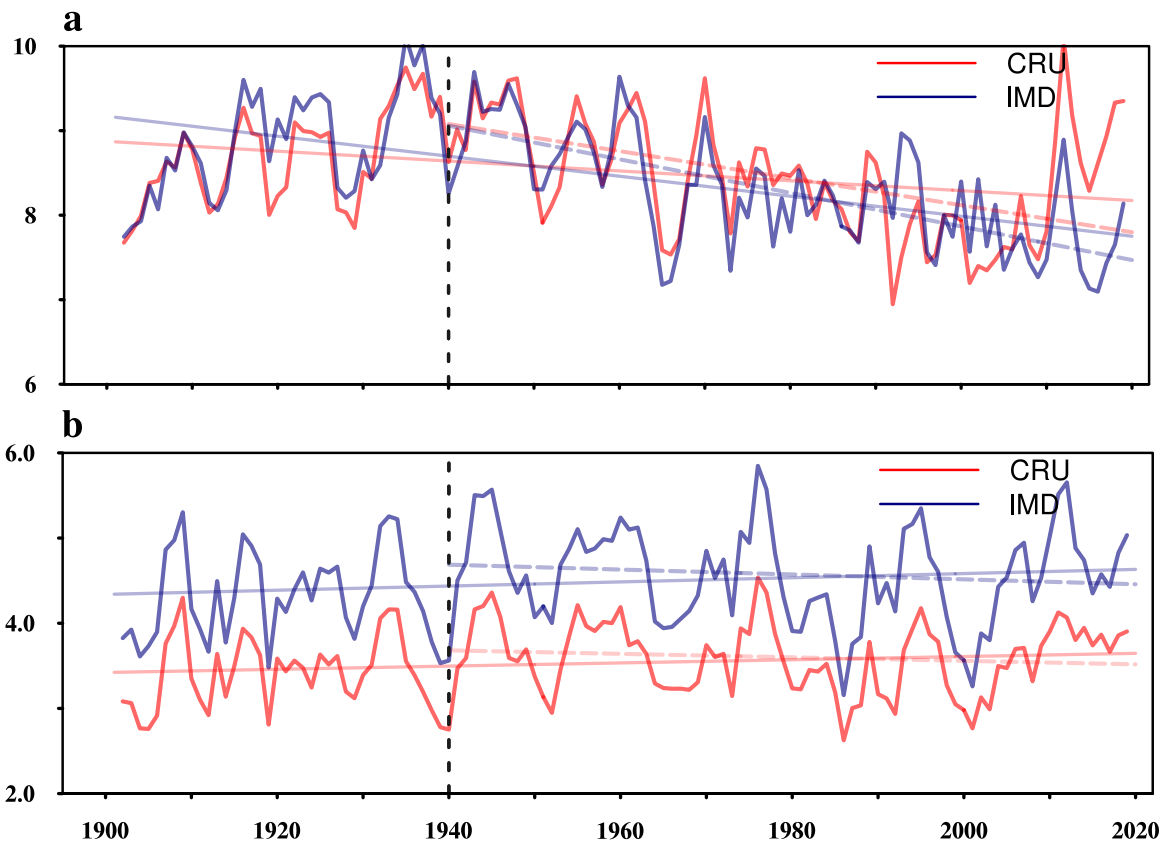


Figure 2.22 | Time evolution of precipitation. a Time series of area-averaged precipitation (mm day^{-1}) over IGP region (orange box) from gridded data by India Meteorological Department (IMD) and Climate Research Data (CRU) during the Indian Summer Monsoon months (June-September) from 1900 to 2020. **b** Same as a but for precipitation over the NWI region (green box).

These uneven changes pose a serious challenge for South Asia's agrarian economy. The IGP, with its dense population and irrigation-dependent agriculture, now faces water stress, while the semi-arid northwest is experiencing

unprecedented wetting and a higher incidence of short-duration extreme events. The resulting imbalance—deficits in one region and surpluses in another—underscores the need to understand the physical drivers that have reorganized the monsoon precipitation system.

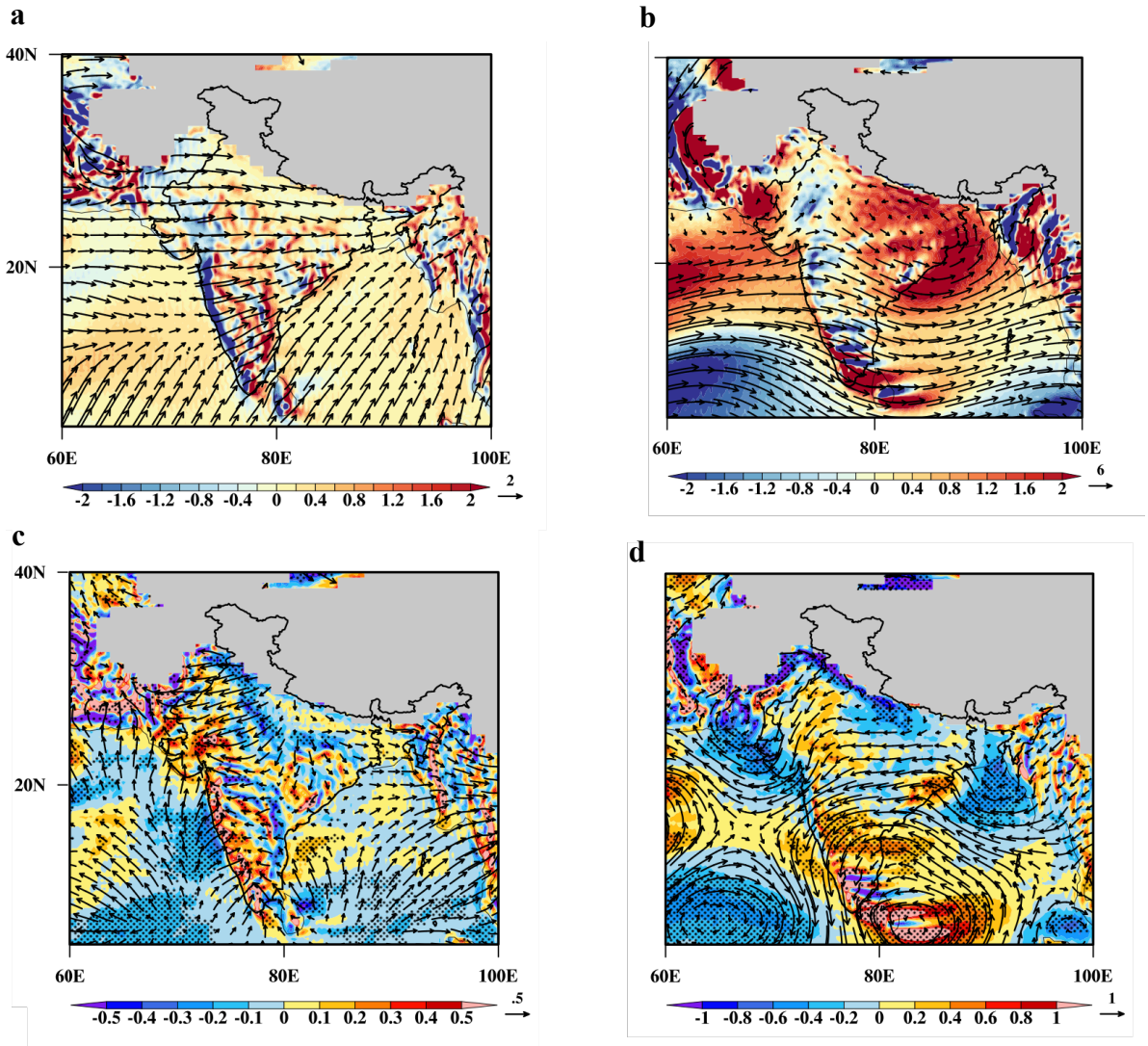


Figure 2.23 | Climatology and trends of convergence/divergence and vorticity. a Climatology (s^{-1}) and **c** trends (s^{-1} per 41 years) of the convergence/divergence from ERA5 data during the Indian Summer Monsoon months (June-September) over 41 years (1940-2020). The stippling represents the regions, where the trends exceed 95% statistically significant level. **b, d** Same as a, c, but for vorticity.

2.7.1 Mechanism: Causal Links to Changes in Circulation

The regional redistribution of precipitation is dynamically consistent with the weakening and westward deflection of the STWs. Changes in the background circulation, captured through divergence and vorticity trends, show a reorganization of ascent and convergence patterns that mirrors the spatial structure of precipitation change.

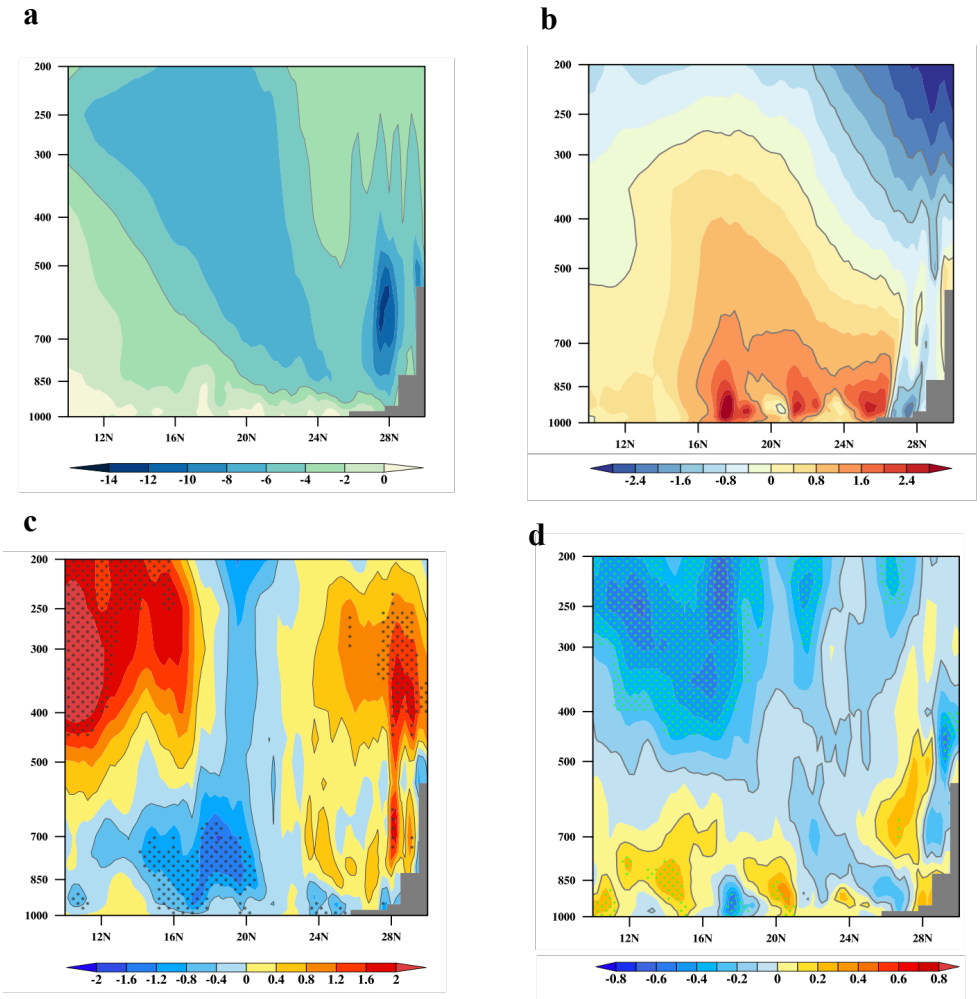


Figure 2.24 | Climatology and trends of vertical velocity (w) and vorticity. a Climatology (Pa s^{-1}) and **c** trends (Pa s^{-1} per 41 years) of the vertical velocity (w) and vorticity from ERA5 data in latitude -pressure cross section over the Indian longitudes during the Indian Summer Monsoon months (June-September) over 41 years (1940-2020). The stippling represents the regions, where the trends exceed 95% statistically significant level. **b, d,** Same as a, c, but for vorticity (s^{-1}).

The ERA5 reveal that the eastern IGP—climatologically a zone of strong low-level convergence and cyclonic vorticity—has transitioned toward weaker convergence and increasing divergence (Fig. 2.23). Meanwhile, convergence has strengthened over north-western and peninsular India, as well as the eastern coast near 20° N and the western Arabian Sea. Regions that have become more convergent exhibit enhanced cyclonic vorticity and rising motion, coinciding with observed precipitation increases; areas that have become divergent show anticyclonic tendencies and reduced precipitation.

The changes in vertical velocity and vorticity in the meridional cross section averaged over the Indian longitude (70-90E) indicates that the ascending motion over the IGP and eastern Indian regions (24N-28N) during summer has decreased substantially in the past, whereas it has increased in the southern flank of the regions between 26N-20N along with increase in cyclonic vorticity in the lower troposphere (Fig. 2.24). These changes in vertical motion and analogous changes in vorticity are coincident with the decrease and increase in precipitation over IGP and peninsular India, respectively. Moreover, the moisture flux convergence (MFC) over the region also shows trends that corroborate with the trends in precipitation (Fig. 2.25). While the MFC has increased over the northwestern South Asia, it has decreased substantially over the IGP regions and with some marginal increase over the peninsular India. The changes in vertical distribution of the MFC, over the IGP regions shows that the decrease has been all throughout the over troposphere (Fig. 2.25d).

The increase in precipitation over northwestern South Asia has received considerable attention in recent years, particularly in light of the unprecedented extreme rainfall events in the region (Arshad et al. 2025). Although it has been extensively examined (Joseph et al. 2024; Li et al. 2023; Rajesh and Goswami 2023), its underlying causes remain debated. In our earlier discussion, we established its

mechanistic connection to large-scale changes in vorticity and convergence/divergence fields; however, additional processes appear to be at play.

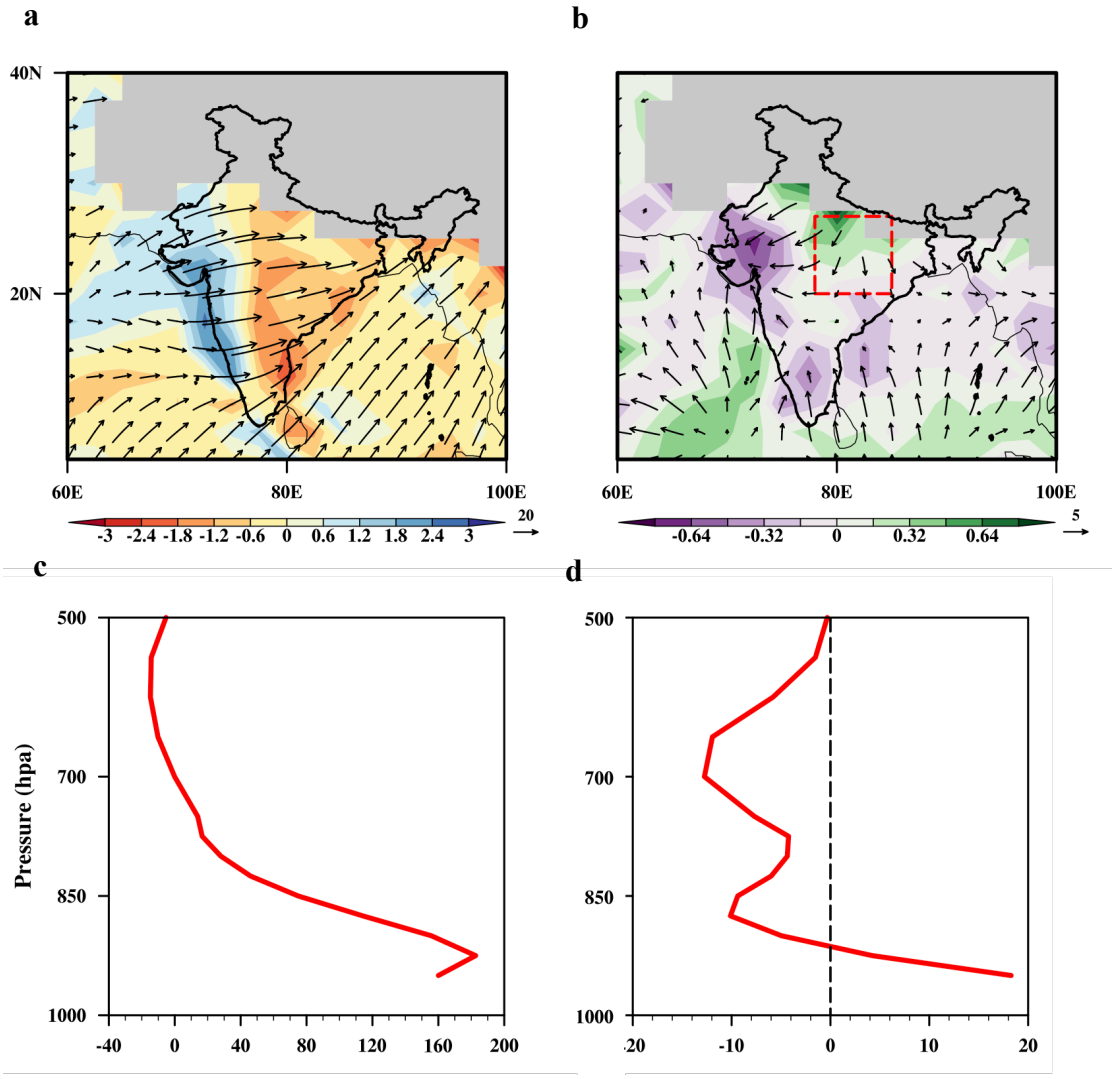


Figure 2.25 | Climatology and trends of Moisture Flux Convergence (MFC). a Climatology and **b** trends of the Moisture Flux Convergence (MFC) from ERA5 data during the Indian Summer Monsoon months (June-September) over 41 years (1940-2020). The ERA5 data is regridded to the resolution of 2.5X2.5 to smoothen the MFC field. **c,d,** Climatology and trends of area-averaged MFC at pressure levels over monsoon trough region (red box of b).

The time evolution of area-averaged precipitation over this region reveals that the increase has not been monotonic, unlike the more consistent rise over the IGP and eastern India. Instead, it exhibits multi-decadal variability, with a more

pronounced upward trend emerging after the early 21st century (Fig. 2.22b). Considering these recent shifts, it is essential to examine the possible link between enhanced precipitation and the concurrent weakening of the STWs over northwestern South Asia. This connection is plausible, as STWs are the predominant summer winds over this region and can substantially influence the local moisture balance and convective environment.

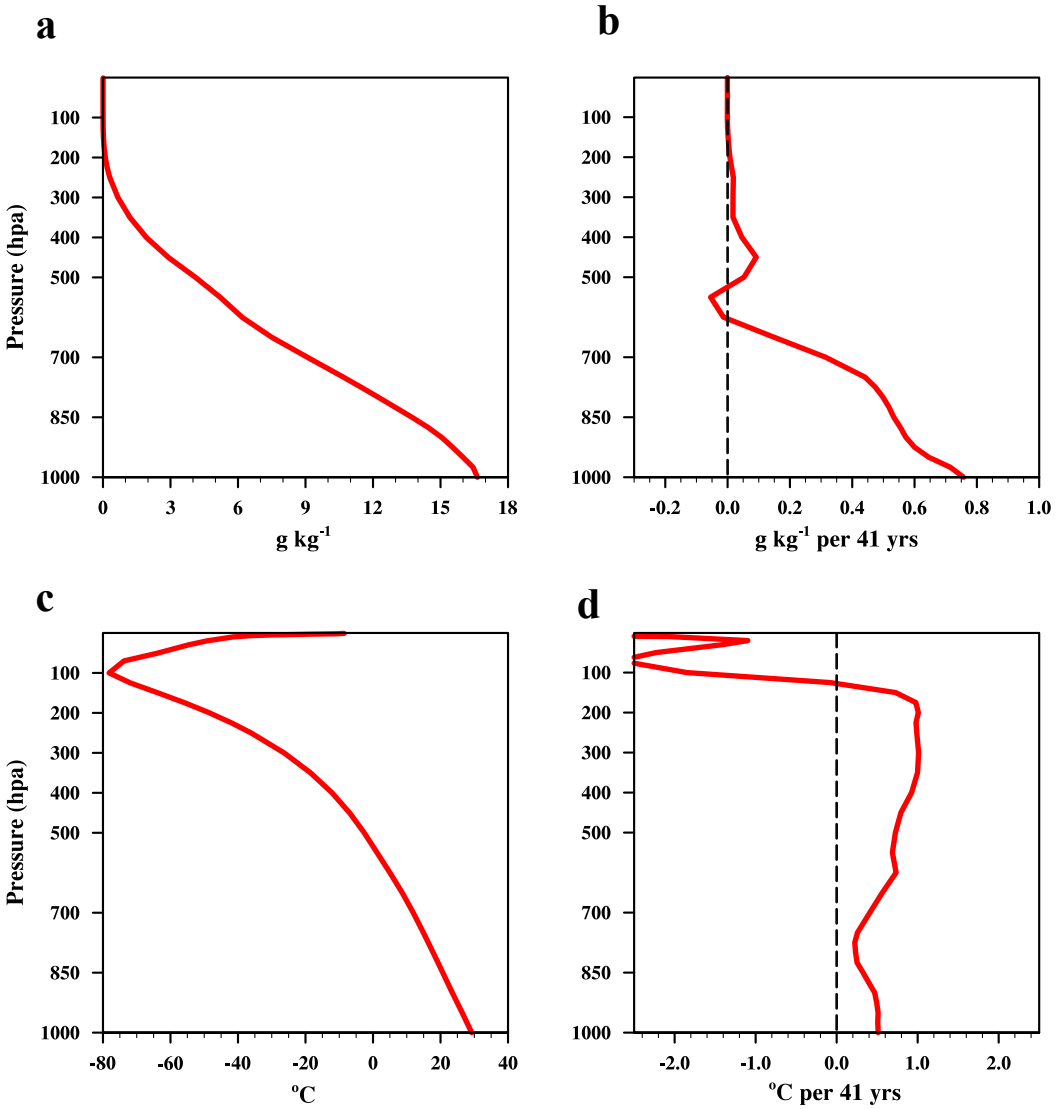


Figure 2.26 | Climatology and trends of specific humidity and temperature over NWI. **a** Climatology and **b** trends of area-averaged specific humidity at pressure levels over NWI region. **c, d** Same as a, b but for temperature.

The STWs are dry westerlies originating over western and central Asia that traverse the narrow corridor between the Hindukush and Zagros mountain ranges before merging with the moist south-westerlies across the IGP, where the climatological monsoon trough lies. The vertical profiles of specific humidity and temperature (Fig. 2.26) reveal a progressive increase in moisture content from upper to lower levels, with the maximum loading in the lower troposphere (Fig. 2.26b) over NWI. Although temperatures have risen slightly in the upper troposphere, with minimal change near the surface (Fig. 2.26d), this modest stabilization appears to be offset by increased lower-tropospheric humidity, which enhances convective instability. Trends in CAPE further support this inference, showing a striking ~30% increase over northwestern South Asia (Fig. 2.27b).

When downstream winds weaken relative to upstream winds, the resulting imbalance leads to air mass convergence, favoring ascent and moisture accumulation. The observed deceleration of westerlies along the monsoon trough, together with their strengthening over the upstream Arabian Sea, likely promotes such speed convergence, contributing to enhanced moisture loading in the lower atmosphere. Additionally, reduced intrusion of dry air from central and western Asia—linked to the weakening of STWs—has created a more conducive environment for deep convection and increased precipitation. Similar increases in rainfall over northwestern India have been reported in other studies (Li et al. 2023; Rajesh and Goswami 2023; Singh et al. 2022), with proposed mechanisms including the westward expansion of the Indian Ocean warm pool and ITCZ (Rajesh and Goswami 2023), rising surface pressure over the TP (Singh et al. 2022), and the poleward shift of the low-level jet (Li et al. 2023). A comprehensive synthesis encompassing these potential drivers, along with the STW-related mechanism discussed here, is essential for developing a more complete understanding of the evolving precipitation regime in northwestern South Asia.

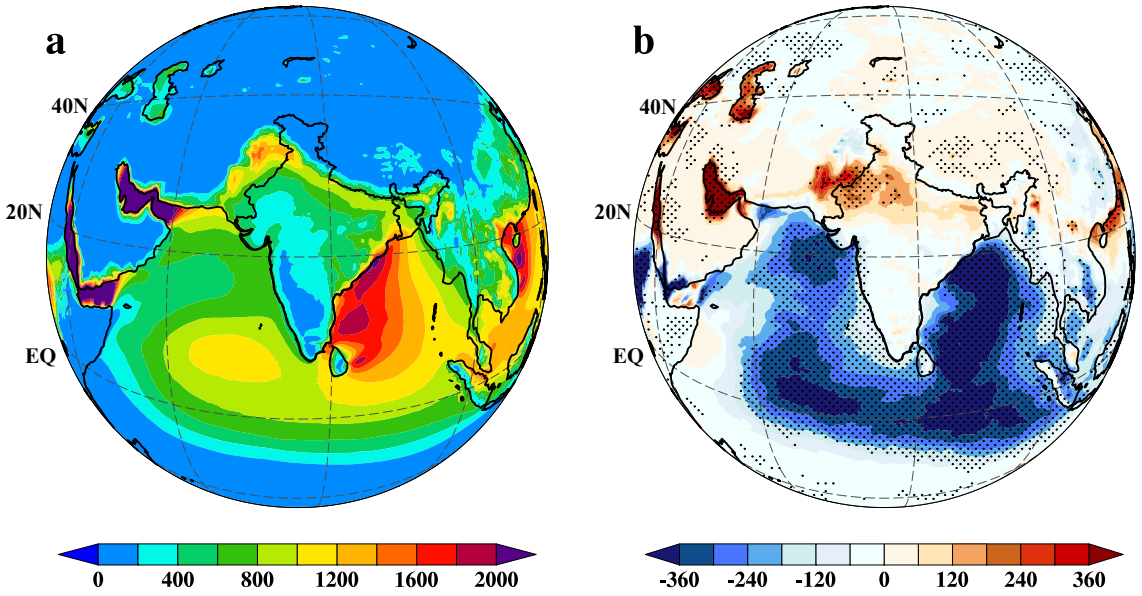


Figure 2.27 | Climatology and trends of Convective Available Potential Energy (CAPE) from ERA5. a Climatology (J kg^{-1}) and **b** trends of CAPE (J kg^{-1} per 41 years) during the Indian Summer Monsoon months (June-September) over 41 years (1980-2020) from ERA5. The stippling represents the regions, where the trends exceed 95% statistically significant level.

While winds are explicitly resolved in climate models and therefore simulated with a higher degree of reliability, precipitation is parameterized and remains highly uncertain in its response to external forcings because it depends on convection, cloud microphysics, and land–atmosphere feedbacks that differ substantially across models. This contrast is central to interpreting regional hydroclimate change: circulation adjustments can often be diagnosed with confidence, whereas precipitation responses may diverge widely even under similar forcing conditions. Having established the more robust aspects of wind changes, we now turn to precipitation and evaluate how well current models reproduce its historical changes. To do so, we analyze past changes simulated by a suite of modeling systems—single-model large ensembles and multi-model ensembles—and assess their fidelity relative to the observed patterns.

2.7.2 Simulated Precipitation Changes – Insights from CESM2LE, MPI-GE, and CMIP6

The trend in EM of 50 ensemble members of CESM2 shows a wide-spread increase in precipitation all across South Asia accompanied by a decrease over the east Asia and maritime continent regions (Fig. 2.28c). The simulated EM trend is not consistent with the observed trend and cannot explain the past changes. We have also analyzed the precipitation changes from EM of 100 ensemble members of the MPI-GE, which shows very different changes from the changes simulated by EM of CESM2-LE (Fig. 2.28d). There is some agreement in simulated precipitation changes between the two suits of large ensembles over the IGP regions and over the Eastern Asian region, however the difference in simulated magnitude of changes are distinct. The simulated changes are mostly opposite to the observed changes and therefore the observed changes cannot be explained alone as the impact of external forcings. It also suggests that the role of internal variability in past precipitation changes is crucial and entails a further investigation. In addition, the lack of consistency across ensemble frameworks indicates substantial model-dependent responses, highlighting structural uncertainties in simulating regional precipitation patterns.

We have further analyzed the precipitation simulation from 40 CMIP6 models (refer Table 4.2 for model details). The trends in MMM precipitation of these models show marginal changes in precipitation over the South Asian region, with increase in precipitation over the western ghats and foothills of Himalayan region (Fig. 2.28e). Notably, the MMM trend from CMIP6 shows similar changes as that are simulated by the CESM2LE, however with lesser magnitudes. Overall, both single-model large ensembles and multi-model ensembles fail to simulate the precipitation changes, underscoring a critical bottleneck for reliable future projections.

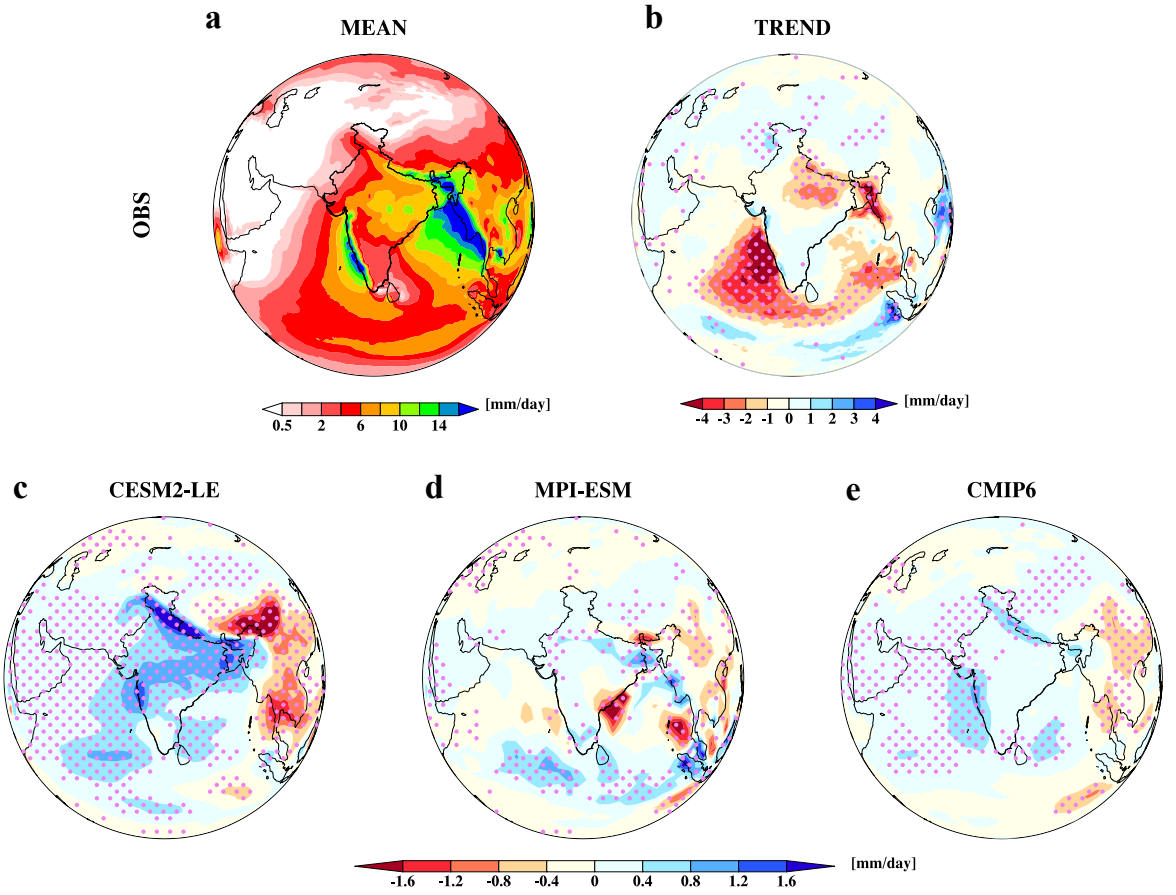


Figure 2.28 | Model fidelity in simulating the past changes in precipitation (mm day^{-1}). a Climatology and **b** trends of the precipitation data from India Meteorological Department (IMD) during the Indian Summer Monsoon months (June-September) over 41 years (1980-2020). The stippling represents the regions, where the trends exceed 95% statistically significant level. c, d, e, Same as b, but for precipitation from ensemble mean of 50-membered CESM2-LE, 100 membered MPI-ESM GE, multimodel mean of 40 models of CMIP6 data.

2.7.3 Model Uncertainty as a Challenge to Precipitation Simulation

Although observed precipitation patterns display clear links to circulation changes, global climate models reproduce these features only partially. Because precipitation in models is largely parameterized, its response to external forcing is more uncertain than that of explicitly resolved fields such as wind or pressure.

The limited agreement between observed and simulated precipitation patterns underscores persistent model uncertainties rooted in the representation of sub-grid scale processes. Current CMIP models depend heavily on parameterizations to approximate convection, cloud microphysics, and aerosol–radiation interactions—processes that are not explicitly resolved and are collectively referred to as the "missing physics" in climate models (Arakawa 2004; Slingo et al. 2022). These simplifications, though necessary, often lead to compensating errors, allowing models to reproduce certain climatological features for the wrong physical reasons and thereby undermining confidence in regional projections.

While the overall simulation of winds and pressure fields has improved across CMIP generations, progress in simulating tropical and monsoon precipitation remains uneven (Fiedler et al. 2020). Models tend to perform better in the extratropics, where precipitation arises from well-resolved synoptic systems, but struggle in convectively dominated regions like South Asia. The challenges intensify in areas with complex topography, strong land–sea contrasts, and high aerosol loading, where multiple processes interact nonlinearly.

Another limitation arises from the availability and distribution of high-quality observational data used for model tuning and validation. Regions with robust observational networks, mainly in the Global North, benefit from better-constrained models, while data-sparse regions such as South Asia continue to exhibit larger biases (Sun et al. 2018). Despite the rapid expansion of satellite observations, the assimilation of such data has not yet resolved these structural limitations.

These factors explain why models, despite capturing the large-scale weakening of circulation, fail to reproduce the spatial reorganization of precipitation seen in observations. Addressing this challenge will require a shift toward kilometer-scale modelling frameworks or short term strategies like regional model customizations

(discussed in detail in chapter 4 and 5) that bridge the gap between local convection and global dynamics, improving the physical realism of precipitation processes.

2.8 Summary, Limitations, and Directions for Future Research

This chapter has presented a comprehensive assessment of historical changes in monsoon winds and precipitation over South Asia, establishing a consistent dynamical and thermodynamic framework that links observed circulation weakening to externally forced drivers. The results show a robust and statistically significant weakening of the continental STWs since the mid-twentieth century, with trends extending coherently through the lower and mid-troposphere. This weakening is dynamically tied to a reduction in the zonal pressure gradient, driven by aerosol- and land-use–induced cooling and rising surface pressure over the Indian subcontinent, combined with greenhouse-gas–driven warming and pressure declines over the Arabian Peninsula. The cross-equatorial southwesterlies, by contrast, remain largely unchanged, indicating that the weakening is confined to the continental branch of the monsoon circulation.

These circulation adjustments have led to a spatial redistribution of precipitation rather than a uniform decline. The IGP and eastern India show persistent drying since the mid-twentieth century, while northwestern and parts of peninsular India exhibit increased precipitation in recent decades. This reorganization reflects reduced convergence and ascent over the core monsoon zone and enhanced moisture inflow and convection over the northwest. Thermodynamic diagnostics indicate that weakening continental winds reduce dry-air intrusion, increase lower-tropospheric humidity, and enhance convective potential energy, promoting more localized convective events. Together, these results indicate an

externally forced transformation of the South Asian monsoon system, with aerosols, land-use change, and greenhouse-gas warming jointly altering regional circulation and hydroclimate.

Despite capturing the large-scale weakening of winds, current climate models fail to reproduce the observed spatial heterogeneity of precipitation. Most ensembles simulate widespread wetting across South Asia, in contrast to the observed dipole of drying and wetting. This deficiency arises from the reliance on parameterized convection, simplified aerosol–cloud feedbacks, and insufficient resolution to represent the complex orographic and land–sea contrasts of the region. Furthermore, internal variability and the interaction between natural oscillations such as ENSO, the PDO, and the IOD contribute to discrepancies between observations and simulated trends.

While the circulation response is well constrained, uncertainties in the hydrological response remain a major challenge. Progress will depend on developing high-resolution, convection-permitting models with unified physics capable of resolving cloud and aerosol processes and their coupling with surface fluxes. Improved observational coverage across data-sparse regions of South Asia, along with better integration of satellite and in situ datasets, is essential for constraining these models. Future work should also examine how the weakening of continental circulation influences regional extremes—particularly the co-occurrence of droughts and intense short-duration precipitation—to refine understanding of the evolving risk landscape under continued anthropogenic forcing.

In summary, the weakening of the STWs emerges as a robust indicator of forced dynamical change in the South Asian monsoon system. However, the persistent model uncertainty in simulating precipitation underscores the need for a paradigm shift in representing multi-scale processes that govern regional hydroclimate, providing the foundation for the projection and model uncertainty

analyses discussed in the following chapter. This contrast between robust circulation changes and uncertain precipitation responses provides a central framework for interpreting past and future monsoon changes.

Together, the observational analyses and the single-forcing attribution experiments indicate that aerosol-induced surface cooling and land-use change were the dominant drivers of the historical weakening of STWs, whereas greenhouse-gas forcing produced the opposite dynamical response. These findings raise a key forward-looking question: as aerosols decline and land-use evolves, will these historical mechanisms continue to shape the monsoon circulation, or will the balance of forcings shift? Chapter 3 addresses this question by applying the same single-forcing framework to future SSP scenarios, enabling a direct comparison between the historical forcing regime diagnosed here and the projected regime of the mid-twenty-first century. It also assesses model simulations of future precipitation changes using both single-model large-ensemble frameworks and multimodel frameworks such as CMIP.

Chapter 3: Changes in Winds and Precipitation over South Asia: Future Projections

Chapter 3

Changes in Winds and Precipitation over South Asia: Future Projections

3.1 Introduction

Reliable climate projections are essential for anticipating future hydroclimatic risks and for planning adaptation in energy, water, and agriculture. The credibility of such projections depends not only on the magnitude of anthropogenic forcing but also on how well models represent regional feedbacks that modulate the large-scale response. In South Asia, where the monsoon governs both precipitation and surface winds, small errors in circulation translate into large differences in societal outcomes. Developing a physically consistent picture of how these systems will evolve under future forcing therefore remains a central challenge in climate research.

In our previous chapter, the analysis demonstrated substantial historical changes in South Asian circulation and precipitation, accompanied by considerable model limitations in reproducing observed spatial changes, particularly for precipitation. Chapter 2 also showed that aerosol forcing and land-surface cooling played a central role in shaping the late-twentieth-century weakening of STWs. This raises an important question for future climate: as aerosol emissions decline and land-surface conditions evolve, will the balance of forcings that governed historical

changes continue to influence the monsoon circulation, or will other drivers—particularly greenhouse-gas forcing—become more prominent? Building on that foundation, the focus of this chapter shifts to the future—to understanding how evolving anthropogenic forcings will shape South Asia's climate in the twenty-first century. While models differ in their ability to represent key processes, their demonstrated skill in simulating circulation and wind changes lends confidence to the assessment of future dynamical responses. Precipitation, in contrast, remains considerably more uncertain because it depends on parameterized sub-grid processes that vary widely across models.

Uncertainty in projections arises from three principal sources—scenario dependence, internal variability, and model structural differences (Hawkins and Sutton 2009; Lehner et al. 2020; Maher et al. 2021)—though their relative importance varies across regions and climate variables (Wang et al. 2021a). Over monsoon regions, precipitation poses a particular challenge, shaped by both large-scale circulation and local feedbacks that amplify model spread (Zhou et al. 2020). The South Asian climate stands out in this regard: the seasonal rains underpin agriculture, forestry, water resources, and livelihoods for hundreds of millions (Mishra et al. 2023). Yet, despite major advances, precipitation projections over South Asia remain characterized by large uncertainties and inter-model contradictions across generations of climate models. Reliable projections are thus essential for adaptation and mitigation planning.

Model projections of the monsoon circulation broadly suggest a weakening of the large-scale overturning circulation under greenhouse gas forcing, linked to a more stable atmosphere and reduced meridional temperature gradients (Luo et al. 2024). Multiple studies have reported a large-scale weakening of circulation (Ma and Yu 2014; Tanaka et al. 2004; Ueda et al. 2006), though contrasting evidence also exists for regional strengthening linked with enhanced rainfall (Hu et al. 2000). However,

moisture-budget analyses indicate a thermodynamic intensification of the monsoon through increased atmospheric moisture (Endo and Kitoh 2014), leading to the apparent paradox of rising precipitation despite weakened circulation (Li et al. 2017; Wang et al. 2021a). The South Asian monsoon is not a single coherent mode but a coupled system comprising distinct dynamical branches; its components may evolve differently under warming (Ma and Yu 2014). Lower-level westerlies are projected to strengthen owing to increased land–sea thermal contrast (Chen and Zhou 2015; Li et al. 2017), whereas upper-level winds weaken in response to diminished meridional gradients and increased atmospheric stability (Sooraj et al. 2015; Sun et al. 2010).

Remote forcings further modulate these circulation changes. Indian Ocean warming, through the meridional temperature-gradient mechanism, can induce atmospheric stability and weaken the circulation, while western-Pacific warming drives anomalies via a Gill-type response (Chen and Zhou 2015; Li et al. 2017). Tibetan Plateau latent-heating anomalies have been linked to an anomalous anticyclone over the Indian Ocean and weaker low-level westerlies (Luo et al. 2024). Some studies suggest a northward shift of the monsoon circulation driven by enhanced land–sea contrast (Chen et al. 2024; Sandeep and Ajayamohan 2015), although consensus remains limited. Recent energetic perspectives also highlight extratropical drivers—such as Eurasian cloud feedbacks and Southern Ocean heat uptake—as additional contributors to weakening over South Asia (Chen et al. 2024).

Regional anthropogenic forcings add further complexity. Warming over western and central Asia under anthropogenic influence has been identified as a driver of past circulation weakening, while cooling over the Indian subcontinent, largely due to aerosols and land-use change, has reduced the regional temperature gradient (Upadhyaya et al. 2024). The distinction between the southwesterly and northwesterly branches of the monsoon, often treated collectively, has recently been

emphasized (Singh et al. 2022; Upadhyaya et al. 2024). Regional forcings such as aerosol emissions, land-use change, and irrigation—and their interactions—are thus central to understanding future wind behaviour (Bollasina et al. 2011; Huang et al. 2020b, 2020a; Monerie et al. 2022; Singh et al. 2018; Upadhyaya et al. 2024; Wang et al. 2020).

While multi-model frameworks such as CMIP provide valuable intercomparison, their historical biases and limited skill in simulating regional circulation changes (Li et al. 2017) reduce confidence in projections. Model uncertainty stems from differences in parameterizations, aerosol–radiation interactions, and land-surface processes, while internal variability remains influential on near-term timescales (Huang et al. 2020a). Large ensembles (Maher et al. 2021) and single-forcing experiments, as applied in our previous chapter, help to separate forced responses from variability and clarify attribution, although structural differences among models continue to be a major limitation.

Changes in lower-tropospheric winds have implications that extend beyond circulation and precipitation. Near-surface winds form a vital renewable resource, and their evolution will directly affect the potential for wind-energy generation in South Asia, a region undergoing rapid expansion of its renewable-energy infrastructure (Jacobson et al. 2018; Ministry of New and Renewable Energy, Government of India 2022; World Bank 2021). Observations indicate widespread weakening of surface winds in the Northern Hemisphere mid-latitudes (Bichet et al. 2012; Karnauskas et al. 2018; Miao et al. 2020; Roderick et al. 2007; Tian et al. 2019; Torralba et al. 2017; Vautard et al. 2010; Wu et al. 2018; Zeng et al. 2019) and concurrent increases across parts of the tropics (Karnauskas et al. 2018; Shen et al. 2022). Although many studies attribute these changes to greenhouse-gas-driven temperature-gradient adjustments (Karnauskas et al. 2018; Shen et al. 2022), growing evidence points to the dominant role of regional forcings such as aerosols and land-

use change (Upadhyaya et al. 2024). These forcings are especially relevant for South Asia, where evolving air-quality and land-management policies will substantially alter the forcing trajectories in coming decades (Samset et al. 2019; Sherman et al. 2021). Yet the extent to which these changes in near-surface winds will shape future wind-energy potential remains uncertain, as socio-economic factors—land availability, population density, and urban expansion—impose additional limits on turbine deployment. Internal climate fluctuations and large-scale ocean–atmosphere interactions further modulate these changes (Gao et al. 2018; Shen et al. 2022; Zeng et al. 2019). Understanding both external forcings and the practical socio-economic constraints is therefore essential for credible projections of wind and associated energy resources.

Precipitation projections pose even greater challenges. As noted earlier, models capture circulation fields more faithfully than precipitation because the latter depends on parameterized sub-grid processes and feedbacks that differ across models. While global mean precipitation is expected to increase by about 2–3% $°C^{-1}$ of warming (Held and Soden 2006), regional outcomes depend strongly on circulation changes, which remain uncertain. Models generally concur that wet regions tend to get wetter (Chadwick et al. 2013), yet they diverge considerably in both magnitude and spatial pattern of change. Thermodynamic processes underpin the mean response, whereas dynamic feedbacks generate large inter-model spread (Elbaum et al. 2022).

Successive model generations—CMIP3, CMIP5, and CMIP6—have shown gradual refinement but persistent uncertainty. Early CMIP3 studies indicated increasing South Asian monsoon precipitation under greenhouse forcing (Fan et al. 2012; Kripalani et al. 2007; Meehl and Arblaster 2003; Sperber et al. 2013); CMIP5 confirmed modest intensification but with large spread (Kitoh et al. 2013; Lee and Wang 2014; Mei et al. 2015; Menon et al. 2013; Sharmila et al. 2015). CMIP6 continues

to project increases in multi-model mean precipitation (Salunke et al. 2023), yet the signal-to-noise ratio remains low across South Asia (Almazroui et al. 2020; Chen et al. 2024; Huang et al. 2020b; Rajesh and Goswami 2022). Sub-regional responses even differ in sign among models (Chen et al. 2024). Uncertainty originates from biases in circulation (Ma and Yu 2014; Monerie et al. 2022), cloud–radiation feedback (Li et al. 2017), SST patterns (Chen and Zhou 2015; Wang et al. 2021a), land–sea thermal contrast (Chen et al. 2024; Wang et al. 2020), and remote teleconnections (Huang et al. 2020a, 2020b; Shamal and Sanjay 2021). Historical biases (Fiedler et al. 2020; Li et al. 2017; Rajesh and Goswami 2022), evolving forcings (Monerie et al. 2022), internal variability (Huang et al. 2020a), and scenario uncertainty (Zhou et al. 2020) further compound this spread. Indeed, it is showed that by late century, up to 90% of global monsoon precipitation-projection spread arises from model uncertainty alone (Zhou et al. 2020).

Recent advances, particularly large ensembles (Deser et al. 2020), have improved the separation of internal variability from forced responses and allowed more robust evaluation of model skill (Simpson et al. 2025). Yet divergent precipitation responses across ensembles confirm that model uncertainty remains the dominant limitation. Accordingly, this chapter employs the latest large-ensemble and multi-model datasets to investigate projected changes in lower-tropospheric winds and precipitation over South Asia. Where models demonstrate credible skill—particularly for circulation and wind fields—the analysis extends to attribution and potential implications for wind-energy resources. For precipitation, where uncertainty remains high, the focus lies in diagnosing the physical and structural origins of projection spread, which are examined in greater depth in the next chapter. This chapter also reinforces the central theme of the analysis: the contrast between the more consistent and credible simulation of winds and the greater uncertainty in precipitation due to inherent limitations in climate models.

3.2 Data, Models, and Analytical Methods

This chapter analyses projected twenty-first-century changes in winds and precipitation over South Asia using coordinated climate-model ensembles that separate externally forced responses from internal variability. The analysis concentrates on the near term (2020–2050), a period that coincides with the planning horizon for renewable-energy infrastructure and with timescales over which mitigation and adaptation policies are most relevant. All diagnostics are restricted to the Indian summer monsoon months (June–September), when the large-scale circulation exerts its dominant influence on surface winds and regional hydroclimate.

The analysis primarily utilizes simulations from the CESM2-LE (Rodgers et al. 2021), extending from 1850 to 2100 under historical and SSP3–7.0 forcings. From the total of 100 members, fifty are used here to evaluate ensemble-mean climatologies and trends in NSW, SLP, and TS. The SSP3–7.0 pathway is selected because it represents a world of strong regional disparities, continued population growth, and limited mitigation—conditions that remain plausible for South Asia and thus provide a realistic assessment of near-term risk. This makes SSP3–7.0 the principal focus of subsequent analyses, while other scenarios serve as comparative references. Complementary ensembles under SSP2–4.5, SSP5–8.5, and the RCP8.5 scenario from CESM1 are analysed to quantify scenario and model uncertainty.

To assess how future wind changes arise from distinct external drivers, the analysis draws on SF-LE from CESM2 (Simpson et al. 2023). These experiments follow the same design described earlier but are extended here to isolate projected twenty-first-century responses under evolving forcings. Each experiment allows one forcing to vary while others remain fixed at pre-industrial levels, thus capturing its independent effect on the near-surface circulation. The ensemble includes

anthropogenic aerosols, biomass-burning aerosols, greenhouse gases, and a composite "everything else" forcing that aggregates natural and land-surface influences. Among these, land-use and land-cover change emerges as the most regionally consequential component, showing a sustained increase through the century and exerting strong control on surface fluxes and boundary-layer momentum exchange. CESM2's inclusion of dynamic irrigation processes enables a realistic representation of these effects, making it particularly suited for examining wind and surface-climate interactions over South Asia (Al-Yaari et al. 2022; Danabasoglu et al. 2020). Further details of ensemble design and forcing implementation are provided in Simpson et al. (2023). Complementary large-ensemble simulations from CESM2 under SSP2–4.5, SSP5–8.5, and RCP8.5 (15, 15, and 16 members, respectively) are also analysed to examine scenario uncertainty, while CESM1 and CESM2 ensembles under identical forcing permit evaluation of structural differences in projected wind responses

To place the CESM results in a wider context, simulations from the CMIP6 archive (Eyring et al. 2016) are also examined. Thirty-four models are used for SSP3–7.0 and thirty-eight for SSP5–8.5, each regridded to a common 1° × 1° grid. Trends are computed for each model, and the multi-model mean and standard deviation provide measures of the forced signal and structural spread. The individual models and resolutions are listed in Table 3.1.

The linear trends have been calculated using the Theil-Sen estimator, and the statistical significance test has been carried out using the Mann-Kendall test (https://www.ncl.ucar.edu/Document/Functions/Built-in/trend_manken.shtml).

Sr. No.	Model Name	Horizontal Resolution (lon x lat) in degrees	Sr. No.	Model Name	Horizontal Resolution (lon x lat) in degrees
1	ACCESS-CM2	1.87 x 1.25	23	GISS-E2-1-G	1.25 x 1.0
2	ACCESS-ESM1-5	1.87 x 1.25	24	GISS-E2-1-H	2.5 x 2
3	AWI-CM-1-1-MR	0.9375 x 0.935	25	GISS-E2-2-G	2.5 x 2
4	BCC-CSM2-MR	1.87 x 1.25	26	HadGEM3-GC31-LL	1.875 x 1.25
5	CAMS-CSM1-0	1.1 x 1.1	27	HadGEM3-GC31-MM	0.833 x 0.556
6	CanESM5	2.81 x 2.79	28	IITM-ESM	1.875 x 1.905
7	CanESM5-1	2.8 x 2.8	29	INM-CM4-8	2.0 x 1.5
8	CanESM5-CanOE	2.8 x 2.8	30	INM-CM5-0	2.0 x 1.5
9	CAS-ESM2-0	1.4 x 1.4	31	IPSL-CM5A2-INCA	3.75 x 1.875
10	CMCC-CM2-SR5	1.25 x 0.94	32	IPSL-CM6A-LR	2.5 x 1.267
11	CMCC-ESM2	1.25 x 0.94	33	KACE-1-0-G	1.875 x 1.25
12	CNRM-CM6-1	1.41 x 1.41	34	KIOST-ESM	2.5 x 2
13	CNRM-CM6-1-HR	0.5 x 0.5	35	MCM-UA-1-0	3.75 x 2.5
14	CNRM-ESM2-1	1.41 x 1.41	36	MIROC-ES2L	2.8 x 2.8
15	EC-Earth3	0.7 x 0.7	37	MIROC6	1.4 x 1.4
16	EC-Earth3-AerChem	0.7 x 0.7	38	MPI-ESM-1-2-HAM	1.87 x 1.87
17	EC-Earth3-CC	0.7 x 0.7	39	MPI-ESM1-2-HR	0.9 x 0.9
18	EC-Earth3-Veg	0.7 x 0.7	40	MPI-ESM1-2-LR	1.87 x 1.87
19	EC-Earth3-Veg-LR	1.125 x 1.125	41	MRI-ESM2-0	1.1 x 1.1
20	FGOALS-f3-L	1.25 x 1.0	42	NESM3	1.875 × 1.875
21	GFDL-CM4	1 x 1	43	UKESM1-0-LL	1.87 x 1.25
22	GFDL-ESM4	1.25 x 1.0			

Table 3.1 | Details of CMIP6 models used in the analysis. Models are color-coded based on the availability of near-surface wind variables in SSP scenarios. Maroon indicates models that provide variables for both SSP3-7.0 and SSP5-8.5 scenarios. Orange represents models that include these variables only for the SSP3-7.0 simulation, while dark green denotes models that provide them only for the SSP5-8.5 simulation.

3.2.1 Wind Power Calculation

The harnessed wind power by the wind turbines depends both on the wind resources availability at the hub-height and density of air (ρ) as well as technical parameters such as the hub height (h) and rotor diameter (d) of the turbine. To calculate the wind power, the wind speed are to be considered at the hub height (W_h), which can be obtained by extrapolating the near-surface winds to the hub height using a power law (Zeng et al. 2019).

$$W_h^* = W_{h0}\left(\frac{h}{h0}\right)^{\frac{1}{7}}$$

where W_{h0} is the near-surface wind speed. Since the turbine power curves are defined for standard atmospheric conditions (dry air density of 1.255 kg m^{-3} at a temperature of 15 °C and pressure of 1 atm) (Lu et al. 2009), the extrapolated wind speeds were subsequently corrected for variations in air density at the hub height. The air density was estimated using the barometric altitude formula assuming constant temperature (Bechtle et al. 2019) .

$$W_h = W_h^*\left(\frac{\rho}{\rho_0}\right)$$

$$\rho = \rho_0 \exp(-\frac{h}{H\rho})$$

where $\rho_0 = 1.225$ kg m^{-3} is the density of dry air, h = 120 m is the hub height and $H\rho = 8550$ m is the scale height.

The resulting density-corrected wind speeds were then used to evaluate the turbine power output using the power curve in the regime between the cut-in and rated wind speeds.

The calculation of wind power is carried out using available industrial power curve of General Electricals (GE) 2.5 MW turbine (Reiner Lemoine Institut 2019) (Fig.

3.1). Considering the hub height to be 120 m and rotor diameter to be 120 m for the turbine, the wind power is calculated using the interpolated wind speed (W_h) as

$$WPP(W_h)^* = \begin{cases} 0\ \text{W}, & W_h < 3.0\ m\ \text{sec}^{-1} \\ 440.7\ \text{W}_\text{h}^5 - 16780\ {W_h}^4 + 234600\ {W_h}^3 - 1476000\ {W_h}^2 + 4422000\ W_h - 5057000, & 3.0\ m\ \text{sec}^{-1} \le W_h < 12.0\ m\ \text{sec}^{-1} \\ 2530000\ \text{W}, & 12.0 \le\ W_h \le 25.0\ m\ \text{sec}^{-1} \\ 0\ \text{W}, & W_h > 25.0\ m\ \text{sec}^{-1} \end{cases}$$

The power calculation is carried out for four regimes of wind speed: below cut-in (< 3.0 m sec^{-1}), ramp-up (3.0 to 12.0 m sec^{-1}), rated power (12.0 to 25.0 m sec^{-1}) and above cut-out speed (> 25.0 m sec^{-1}); details are provided in the industry table. The polynomial equation that has been used for the ramp-up stage is obtained by fitting 5th order polynomial to the wind power curve between the below cut-in and rated power regime.

The wind power calculated from the wind power curve represents the power generated by a single wind turbine per grid cell. However, in practice, multiple wind turbines can be installed within a single grid cell, typically with a spacing of approximately nine rotor diameters in each direction (equivalent to ~1.14 km^2 per turbine). Therefore, to estimate the total wind power generation per grid cell, the calculated wind power, $WPP(\text{W}_\text{h})^*$, must be multiplied by the number of turbines that can fit within one grid cell. This adjustment is made to calculate the final wind power per grid using the following formula:

$$WPP(\text{W}_\text{h}) = P(\text{W}_\text{h})^* \times \frac{\text{Aij}}{1.14}$$

Where Aij is the area of the grid in km^2.

The calculated wind power represents the instantaneous power available over the region during the JJAS season. To estimate the corresponding energy over this period, the wind energy is obtained by integrating the wind power over time. Assuming that the mean wind power is representative of the entire JJAS period, the wind energy potential (WEP) is calculated as:

$$\mathrm{WEP} = \mathrm{WPP} \times \mathrm{T}$$

where T = 2928 hours corresponds to the total duration of the JJAS season. Consequently, wind energy is expressed in units of MWh.

Furthermore, the wind power potential regions are identified based on additional filtering. The wind power calculated earlier is used to compute the capacity factor (Gao et al. 2018), using the formula:

$$CF = \frac{P_{real}}{P_{rated}}$$

Where P_{real} is the estimated wind power, and P_{rated} is the rated maximum power output of the wind turbine. In our study, P_{rated} is set at 2.5 MW, corresponding to the GE 2.5 MW turbine. Initially, regions with a capacity factor below 0.15 are filtered out. Subsequently, physical constraints are applied to obtain a practical projection. Specifically, three physical constraints are considered: regions with elevations exceeding 3000 meters, slopes greater than 20%, and protected areas that are assumed to experience minimal changes in the future.

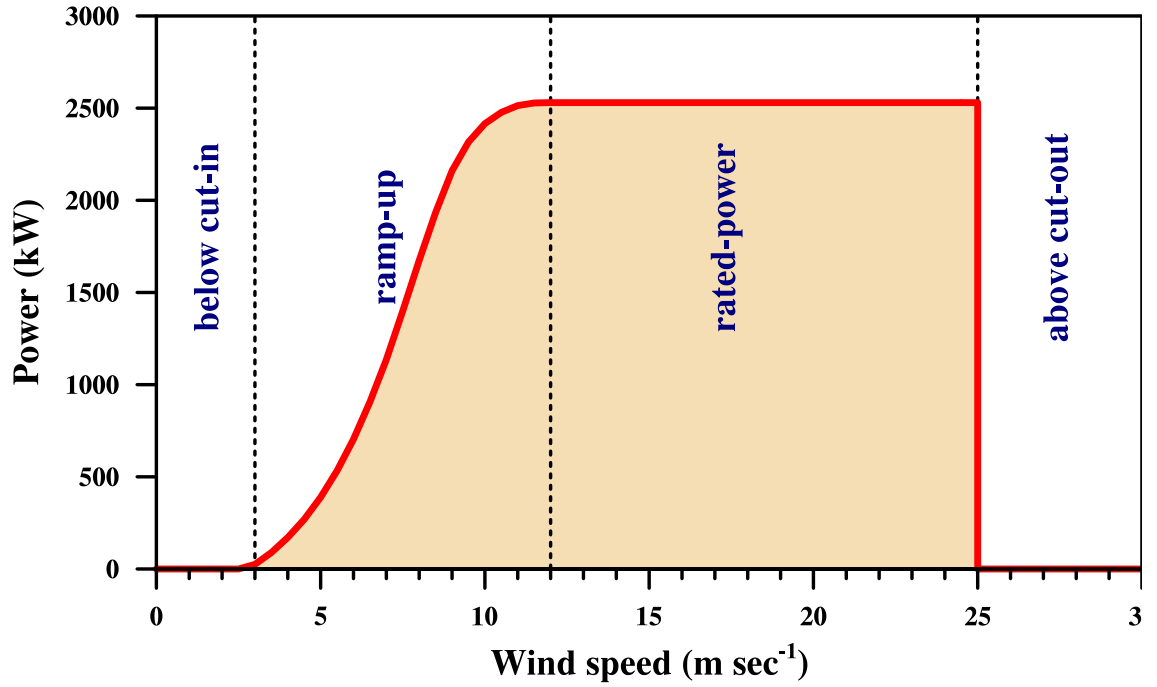


Figure 3.1 | Power curve for GE 2.5 MW turbine. The power curve for GE 2.5 MW turbine using the industry table. The power curve shows the wind power at a hub height of 120 m for different regimes of wind speed – below cut-in, ramp-up, rated power, and above cut-out stages.

3.3 Changes in Monsoon Winds

We begin by examining projected changes in lower-tropospheric winds (850 hPa) over the period 2020–2050 using the ensemble mean of 50 members from the CESM2-LE simulation (Fig. 3.2). The simulation follows the smoothed CMIP6 biomass burning protocol under the SSP3-7.0 scenario (Rodgers et al. 2021). The projections reveal a distinct land–ocean contrast. Over land, wind speeds are projected to significantly increase across the 20°–30°N belt encompassing the monsoon trough region, with the largest enhancement (~1 m sec^{-1}) over the eastern IGP (Fig. 3.2b). This pattern contrasts with the observed historical weakening in the same region (Upadhyaya et al. 2024) suggesting a strengthening of the STWs as the driver of the projected increase. In contrast, wind speeds over the surrounding

oceans are projected to decline, with the largest reduction near the southern tip of the Indian subcontinent. These changes are statistically significant at the 99% confidence level and exceed the range of internal variability, estimated as two standard errors. Given the demonstrated fidelity of CESM2-LE in reproducing observed historical wind changes, the projected changes likely reflect anthropogenically forced responses. In the context of the large-scale monsoon circulation, these changes imply a strengthening of the continental low-level flow along the monsoon trough, with potential implications for the positioning and intensity of precipitation and synoptic systems such as monsoon depressions originating over the Bay of Bengal.

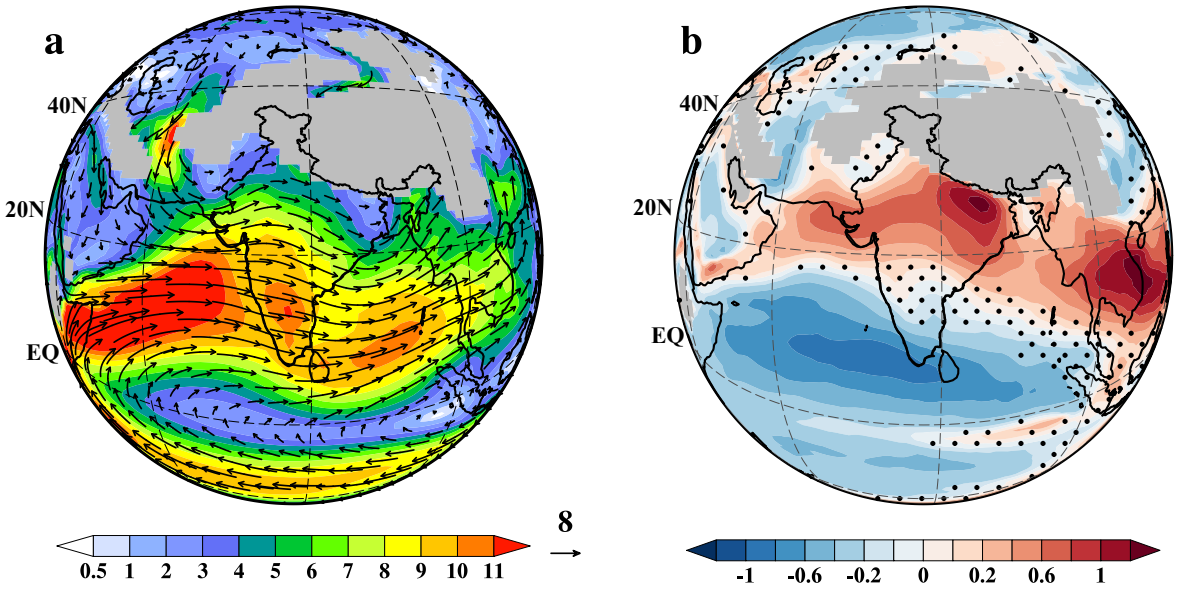


Figure 3.2 | Climatology and trends of monsoon winds at 850 hPa. a Climatology (m sec^{-1}) and **b** trends (m sec^{-1} per 31 years) of wind speed during the Indian Summer Monsoon (June–September) over 31 years (2020–2050) from CESM2-LE under SSP3-7.0. The shaded background in **a** represents the ensemble mean wind speed of 50 ensemble members. The shaded background in **b** shows the ensemble-mean wind speed trend, with stippling indicating regions where the trend do not exceed the 95% statistical significance level.

The 850 hPa winds represent the large-scale monsoon system at low-levels and are shaped primarily by broad thermodynamic and energetic constraints. These winds are closely linked to the lower branch of the monsoon circulation, namely the subtropical westerlies and the cross-equatorial low-level jet and associated moisture transport into the subcontinent. In contrast, winds near the surface respond more sensitively to surface roughness, land–sea thermal gradients, and boundary-layer mixing, all of which introduce strong regional variability that may not be evident aloft. Because NSWs were shown in the previous chapter to have undergone substantial historical changes with direct implications for wind-energy potential, it is important to view projected circulation changes in relation to how they influence the winds that matter most for regional planning. This continuity with the earlier analysis ensures that the projected large-scale signals are interpreted at the level where they carry the greatest socio-economic relevance. NSWs therefore provide the key link between projected circulation changes and their practical implications for energy planning and policy. In the following sections, we shift our focus to projections of wind-energy resources using the LE simulations and examine the drivers that shape their regional expression under future forcing scenarios.

3.4 Projected Changes in Near-Surface Winds

The projected forced trends of NSWs from the ensemble mean reveal a spatially heterogeneous response, with prominent strengthening over the Indian landmass, the Bay of Bengal, and the southern Arabian Sea (Fig. 3.3b). A band of enhanced wind speed extends from the coastal Arabian Peninsula across the northern Arabian Sea and NWI into the northern Bay of Bengal (BoB), accompanied by significant increases over the peninsular Indian region. Notably, this strengthening over peninsular India is absent in the 850 hPa winds, underscoring the stronger influence

of boundary-layer processes and surface forcings at near-surface levels. Local-scale topographic effects and land–sea thermal contrasts may strongly contribute to these non-uniform spatial patterns, unlike the smoother, large-scale response seen aloft. Conversely, a pronounced weakening is projected over the southern Arabian Sea and the equatorial IO. Collectively, these heterogeneous changes suggest substantial regional variations in the future wind energy potential across South Asia. Interestingly, the projected strengthening over land contrasts with the historical weakening observed over much of the same region, which has been primarily attributed to the cooling effects of anthropogenic aerosols and LULC changes (Chapter 2) (Upadhyaya et al. 2024). Looking ahead, these same forcings are expected to evolve in ways that differ markedly from their historical trajectories, essential for interpreting the projected strengthening of NSWs.

The area-averaged wind speed over the wind energy potential regions (defined based on Capacity Factor; see methods) across India shows a consistent increase, with ensemble-mean trends of 0.094 ± 0.030, 0.118 ± 0.040, and 0.259 ± 0.091 m s^{-1} for the SSP2-4.5, SSP3-7.0, and SSP5-8.5 scenarios, respectively, over the three decades. The uncertainty in the trends, estimated as twice the standard error ($2\sigma/\sqrt{N}$), is substantially smaller than the ensemble-mean trend in all scenarios (Fig. 3.3c), indicating that the projected increase is statistically significant across scenarios. Recognizing ensemble mean trend may not capture the whole distribution in the realizations, which is where the wind energy practitioners may be interested, the individual ensemble member trends were also examined. The median trends similarly show a consistent increase across scenarios, with values of 0.078, 0.096, and 0.266 m s^{-1} for SSP2-4.5, SSP3-7.0, and SSP5-8.5, respectively. The corresponding 5^{th}–95^{th} percentile ranges (0.035 to 0.215, −0.087 to 0.374, and 0.022 to 0.55 m s^{-1}) provide the range of plausible trends, with more than two-third of the ensemble members consistently showing increasing trends across the scenarios.

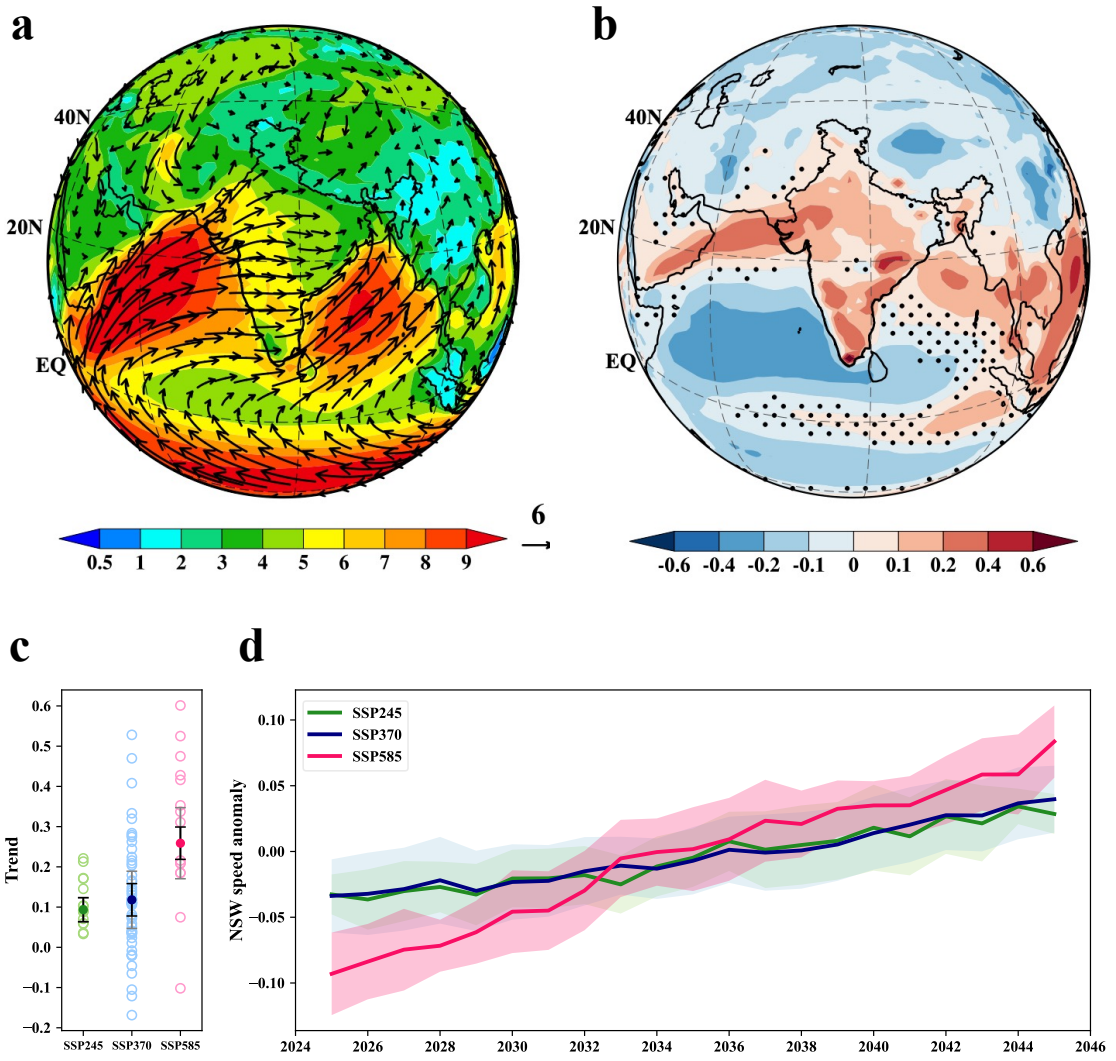


Figure 3.3 | Climatology and change in near-surface winds in CESM2-LE simulations in the coming decades. a Climatology (m sec^{-1}) and **b** trends (m sec^{-1} per 31 years) of NSW speed during the Indian Summer Monsoon (June–September) over 31 years (2020–2050) from CESM2-LE under SSP3-7.0. The shaded background in **a** represents the ensemble mean wind speed of 50 ensemble members, while the vectors depict winds at the lowest model level (992 hybrid level). The shaded background in **b** shows the ensemble-mean wind speed trend, with stippling indicating regions where the trend does not show the 95% statistical significance level. **c** Area averaged wind speed trends over India from individual ensemble members and their ensemble mean for the three scenarios with error bar representing the internal variability calculated as two standard error (i.e. $\boldsymbol{2\sigma/\sqrt{N}}$), where $\boldsymbol{\sigma}$ is the standard deviation of the trends from individual members and N is the number of ensemble members. The grey error bars denote half of the standard deviation of the ensemble trends for the respective scenario. **d** Time series of NSW speed anomaly w.r.t long term mean (2020-2050) under three scenarios SSP2-4.5, SSP3-7.0, and SSP5-8.5. The shading indicates the spread across the ensemble members.

Temporal evolution (Fig. 3.3d) shows steady strengthening under SSP2–4.5 and SSP5–8.5, while SSP3–7.0 exhibits a mild mid-2030s decline followed by recovery. These scenario-specific differences in projected wind-speed changes are likely because of the underlying socio-economic and policy assumptions embedded in each pathway, particularly in regard to LULC and aerosol emission. These findings call for an investigation into the relative influence of regional versus global forcings on South Asia's wind trends under SSP3-7.0, and the implications of emerging scenario uncertainties for sustainable energy development of the region (discussed in detail later).

Although the strongest enhancements in NSW speed occur during the summer monsoon, wind strengthening extends into other seasons as well, indicating a broader intensification of near-surface circulation over South Asia. The summer period nevertheless remains most critical: westerly winds during June–September deliver the highest onshore generation potential and simultaneously regulate moisture transport and convergence that underpin the monsoon hydrological cycle (Gao et al. 2018). For this reason, the attribution and diagnostic analyses that follow focus on the JJAS season, when physical coupling between circulation, energy generation, and precipitation is strongest.

3.5 Attribution – Insights from SF simulations

While GHG concentrations are projected to continue rising through mid-century, the forcings expected to evolve most rapidly are aerosols and LULC changes. Aerosol emissions are anticipated to decline under strengthened air-quality regulations, diminishing their surface-cooling influence and altering regional pressure gradients (Samset et al. 2019; Xiang et al. 2023). In contrast, continuing urbanization, agricultural expansion, and irrigation intensification across South

Asia are projected to amplify land–atmosphere feedbacks and modify surface roughness and energy exchange (Chou et al. 2018; Mehta et al. 2024; Popp et al. 2017). Together, these evolving forcings are likely to reshape the dynamical balance that controls near-surface winds.

To disentangle these contributions, the CESM2 SF-LE is analysed under the SSP3–7.0 scenario (Fig. 3.4). Each experiment allows a single forcing—anthropogenic aerosols (AER), greenhouse gases (GHGs), biomass-burning aerosols (BMB), or land-use and land-cover change—to evolve independently while all others remain fixed at pre-industrial levels (Simpson et al., 2023). This experimental design isolates the climatic response to each forcing agent and provides a clear basis for attribution. It has been applied earlier in Chapter 2 to evaluate the drivers of historical wind changes over South Asia. Trend analysis indicates that GHGs are the dominant contributors to the projected NSW intensification in terms of spatial extent, followed by LULC changes, with 76% and 62% of the grids in the wind energy potential regions region showing an increase, respectively (Fig. 3.4a and b). However, LULC-induced changes are locally stronger and emerge as the primary driver over Peninsular India, whereas GHG forcing shows a broader spatial extent in changes across the domain (Fig. 3.4b). In contrast, anthropogenic and BMB aerosols play a negligible role in future wind changes (Fig. 3.4c, d).

Declining emissions under stricter air-quality measures reduce the cooling and stabilizing effects that once suppressed the monsoon circulation. The complementary "all-but-one" experiment, in which anthropogenic aerosols are fixed at pre-industrial levels (xAER), produces a response nearly identical to the fully forced ensemble (Fig. 3.5a and 3.3b), reaffirming that GHGs and LULC are the primary drivers of the mid-century wind increase. The aerosol-only experiment (Fig. 3.5b) exhibits a flat trend after 2020, consistent with emissions stabilization.

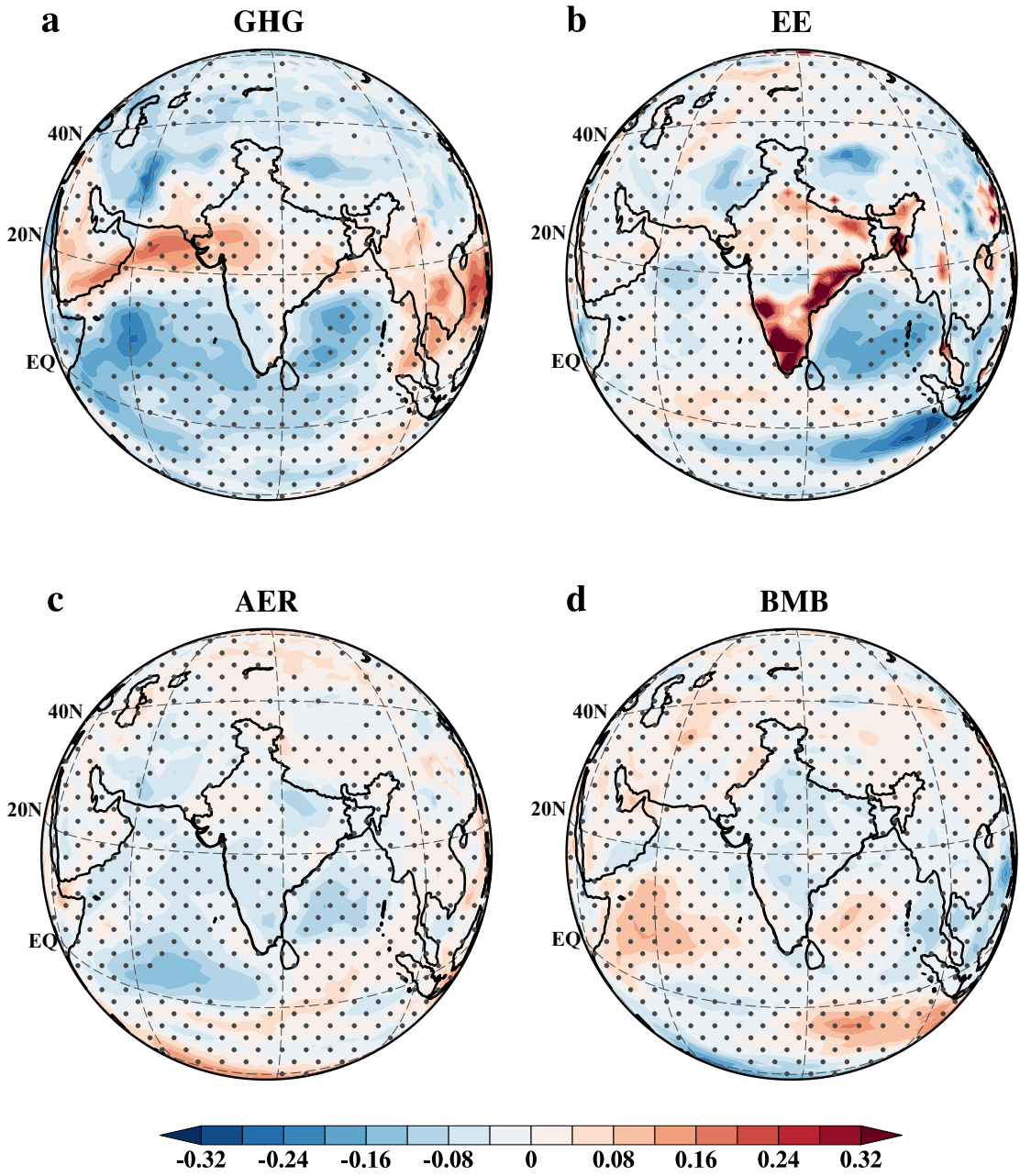


Figure 3.4 | Trends of near-surface wind speed in Single Forcing Large Ensemble (SF-LE) simulations of CESM2 (ms^{-1} per 31 years). Trends of near-surface wind speed during the Indian Summer Monsoon (June–September) over 31 years (2020–2050) from CESM2 SF-LE for four individual forcings: **a** anthropogenic aerosols (AER), **b** everything else (EE), **c** greenhouse gases (GHG), and **d** biomass burning aerosols (BMB) (see Methods). Trends are calculated using the ensemble mean of 20 members for AER (**a**) and 15 members for the other forcings. Stippling indicates regions where the trend does not exceed the 95% statistical significance level.

These results differ sharply from those for the twentieth century, when reduced solar radiation from aerosols weakened the thermal gradient and suppressed lower-tropospheric winds (Upadhyaya et al. 2024). The relatively small role of aerosol forcing in mid-century projections contrasts with the historical period: SF-LE historical experiments (Chapter 2; Fig. 2.14) show aerosol-only forcing produced positive continental SLP anomalies and weakened 850 hPa westerlies during 1980–2020.

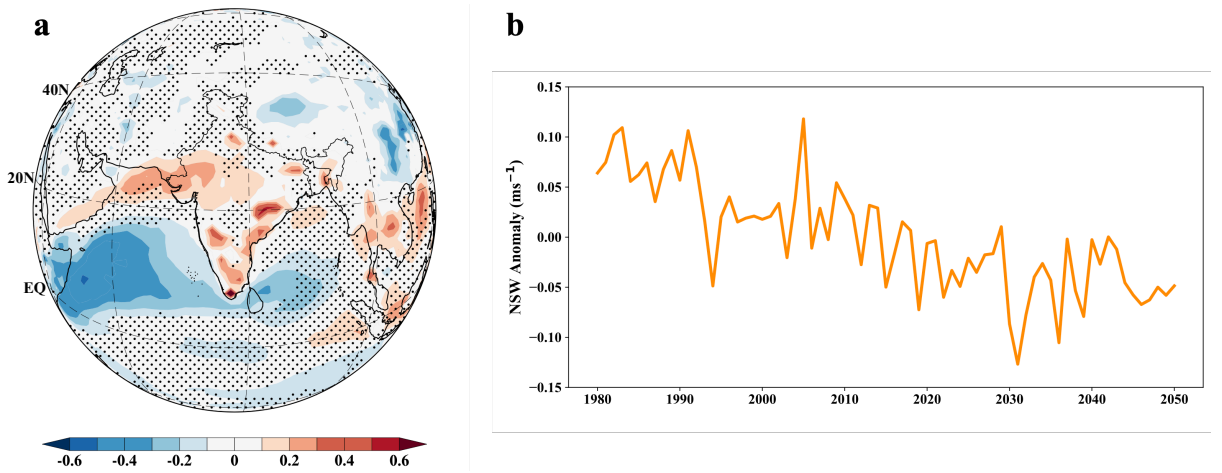


Figure 3.5 | Comparative role of anthropogenic aerosol emission. a Trends of near-surface wind speed (ms^{-1}) during the Indian Summer Monsoon (June–September) over 31 years (2020–2050) for xAER forcing in CESM2 SF-LE simulations, where all forcings –GHG, EE, and BMB are evolving, while AER emission held constant at PI levels (see Methods). Trends are calculated using the ensemble mean wind speed from the available 10 ensemble members. Stippling indicates regions where the trend does not exceed the 95% statistical significance level. **b** Time series (1980-2050) of ensemble mean wind speed anomaly w.r.t climatological mean for AER forcing simulations, where only anthropogenic aerosols are evolving under SSP3-7.0 scenario.

Under SSP3–7.0, projected aerosol declines mean that aerosols no longer exert the same suppressing influence, allowing GHG and LULC effects to dominate near-term wind trends. The emerging pattern thus marks a transition in the forcing regime governing South-Asian circulation—from aerosol-driven weakening in the recent past to GHG- and land-use-dominated strengthening that defines the future climate trajectory.

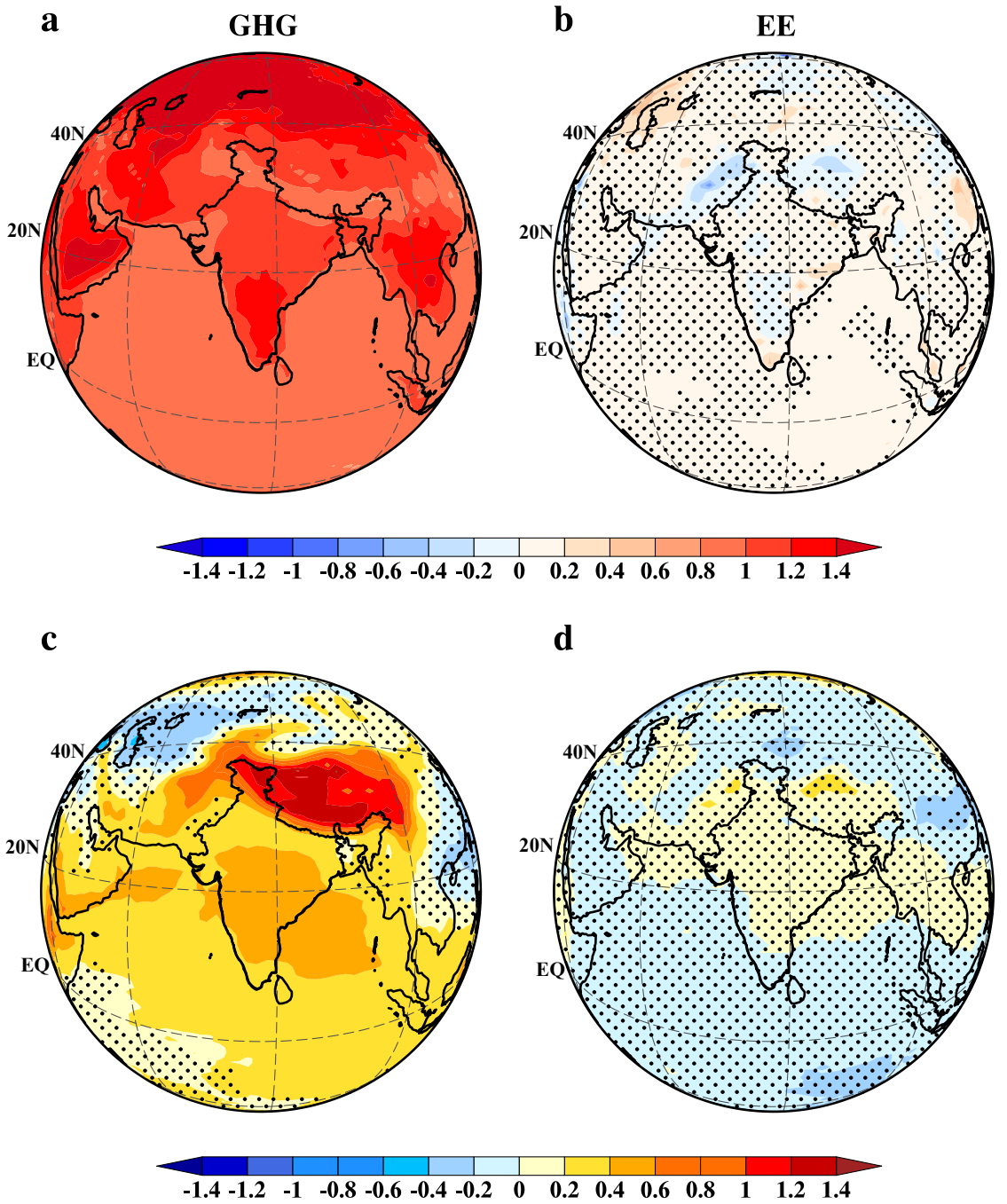


Figure 3.6 | Trends of TS and SLP in SF-LE simulations of CESM2. Trends of TS (°C per 31 years) during the Indian Summer Monsoon (June-September) over 31 years (2020-2050) from CESM2 SF-LE for two individual forcings: **a** GHG and **b** EE (see Methods). **c, d** Same as **a, b** but for SLP (hPa per 31 years). Trends are calculated using the ensemble mean of 15 members.

3.6 Thermodynamic and Pressure Responses

The near-surface wind changes described above are consistent with projected adjustments in temperature and pressure fields. Ensemble-mean trends in surface temperature and mean-sea-level pressure for 2020–2050 (Figs. 3.6–3.7) reveal coupled thermodynamic–dynamic responses characteristic of an increasingly greenhouse-gas-forced climate. Pressure rises sharply over the Himalayan–Tibetan Highland and more modestly over Peninsular India and the Bay of Bengal, leaving a relative low-pressure zone across northern India that aligns with the strengthened westerly anomalies. The pattern produced by the greenhouse-gas-only ensemble closely resembles that of the all-forcing case, confirming that greenhouse gases dominate the large-scale SLP changes. Within the large-scale monsoon framework, this configuration reflects a reorganization of the continental pressure gradient that governs the strength and positioning of the monsoon trough.

The projected circulation changes are not directly tied to thermodynamic adjustments in land–ocean temperature gradients, as discussed in Chapter 2. Surface temperatures increase over much of India, with maxima over the eastern and central regions (Figs. 3.6a and 3.7a). However, the spatial correspondence between warming and pressure change is not straightforward, indicating that surface temperature alone cannot explain the projected pressure patterns. This mismatch shows that surface temperature alone cannot account for the projected pressure patterns, suggesting that the response is shaped by a combination of land–sea thermal contrast, circulation-induced advection, and temperature gradients aloft. Because mean sea-level pressure reflects the integrated effect of the entire atmospheric column, understanding these changes requires examining the vertical distribution of temperature. The climatology of 850 hPa temperature and its zonal gradient (Fig. 3.8) exhibits the familiar west-to-east asymmetry that sustains the low-level

monsoon westerlies. Projected trends indicate a weakening of the continental temperature gradient relative to adjacent oceans. This adjustment constrains further intensification of the monsoon flow. Such thermodynamic adjustments are also likely to influence the strength of the lower branch of the monsoon circulation and associated moisture transport into the subcontinent.

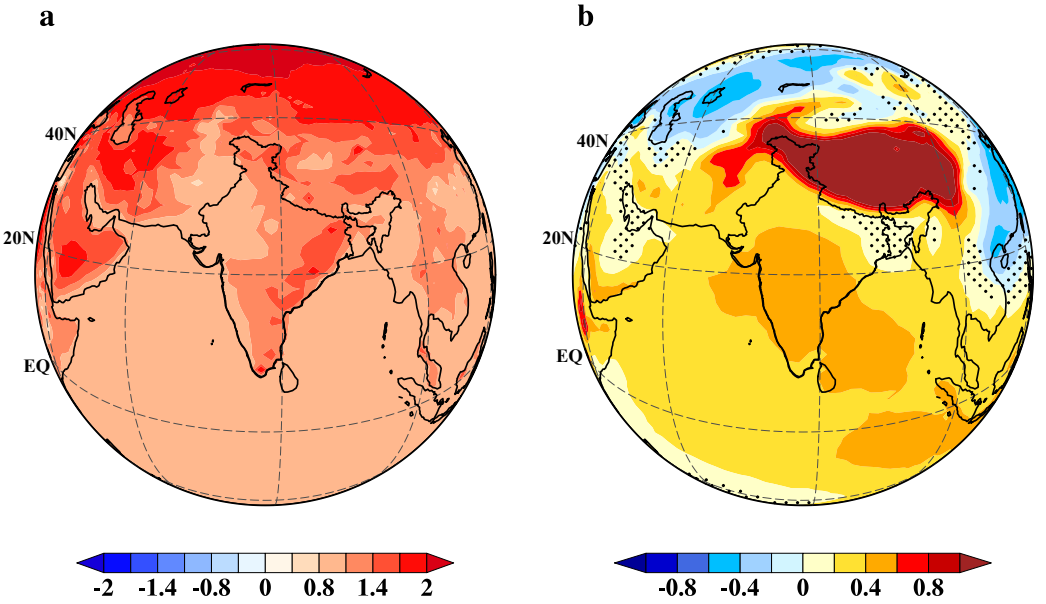


Figure 3.7 | Trends of TS (°C per 31 years) and SLP (hPa per 31 years) in CESM2-LE simulations. **a** Trends of TS during the Indian Summer Monsoon (June–September) over 31 years (2020–2050) from CESM2-LE simulations. The shaded background represents the trend in the ensemble mean of 50 members. **b** Same as **a** but for SLP. Stippling indicates regions where the trend does not exceed the 95% statistical significance level based on the Mann-Kendall test.

Vertical profiles of zonal temperature anomalies (Fig. 3.9) further elucidate the thermodynamic structure underlying the projected pressure changes. The analysis reveals a pronounced land–sea contrast, with strong upper-tropospheric warming over the Arabian Sea and relative cooling over Peninsular India and the Bay of Bengal (Figs. 3.9b–c). This pattern reflects spatial variations in convective heating—enhanced latent heat release over oceanic regions and comparatively weaker convection over land—associated with the highly convective monsoon

system. These thermal changes in atmosphere is primarily driven by greenhouse-gas forcing, as evident from the vertical profiles in the single-forcing simulations (Fig. 3.9c).

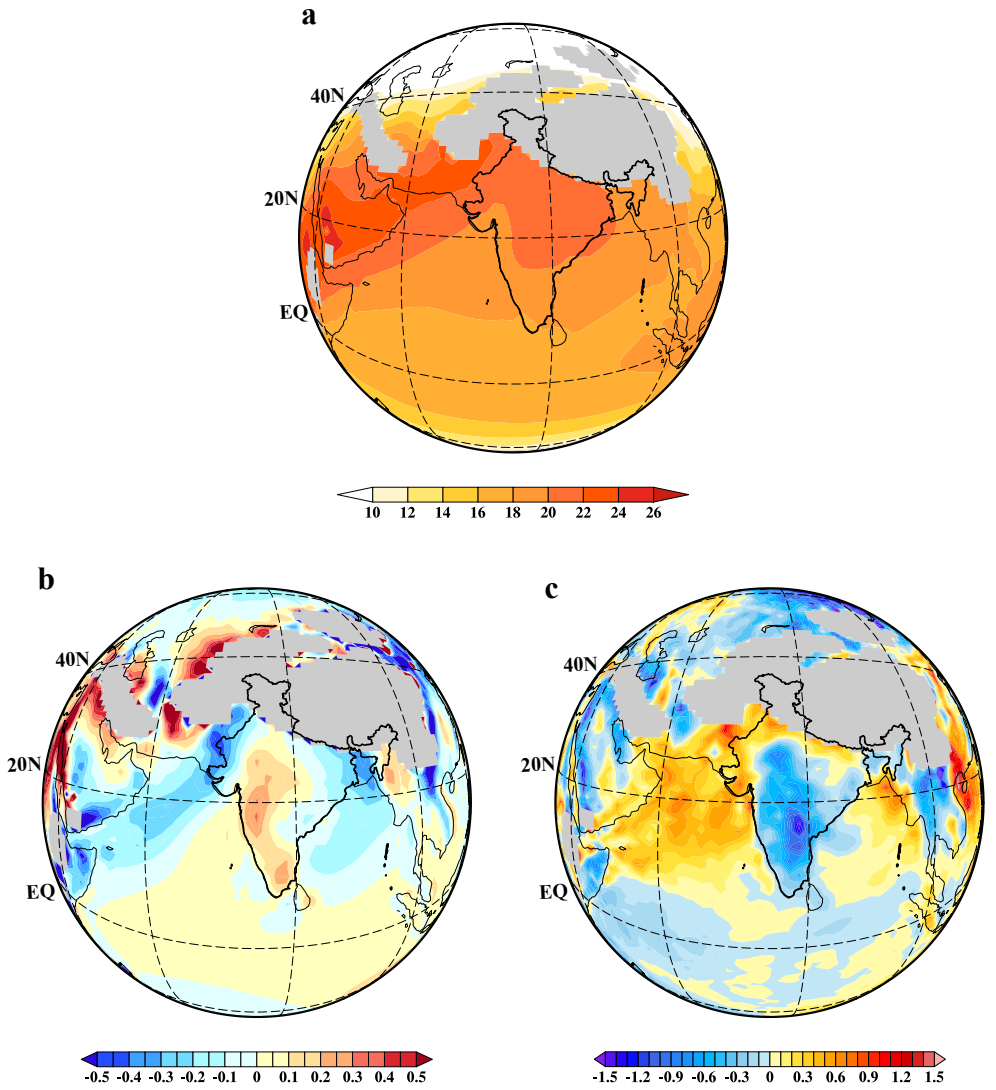


Figure 3.8 | Climatology of mean temperature (°C) and its zonal gradient (°C per degree longitude) at 850 hPa, and the trend in zonal temperature gradient (°C per degree longitude per 31 years). a Climatology of mean temperature at 850 hPa during the Indian Summer Monsoon (June–September) for the period 2020–2050 from CESM2-LE. **b** Climatology of the zonal gradient of temperature at 850 hPa for the same period. Upscaled by 10^5 **c** Trend in the zonal gradient of temperature at 850 hPa for the same period. Stippling in **c** indicates regions where the trend does not exceed the 95% significance level.

The associated temperature gradients induce large-scale adjustments in vertical motion, captured by the trend in pressure velocity (Fig. 3.10b). Regions of relative cooling correspond to enhanced subsidence over Peninsular India and the adjacent BoB, reinforcing the secondary surface-pressure maxima identified earlier, while persistent warming aloft over the Arabian Sea supports ascending motion and lower surface pressure. These opposing vertical motions reflect adjustments in the regional overturning circulation, analogous to shifts in the Hadley-type meridional circulation and Walker-type zonal circulation over the Indian region. Together, these features describe a GHG-dominated reorganization of regional thermodynamics in which the strongest warming occurs aloft over oceanic regions, while near-surface differential heating between land and sea diminishes, shaping the pressure distribution that governs projected near-surface wind changes across South Asia.

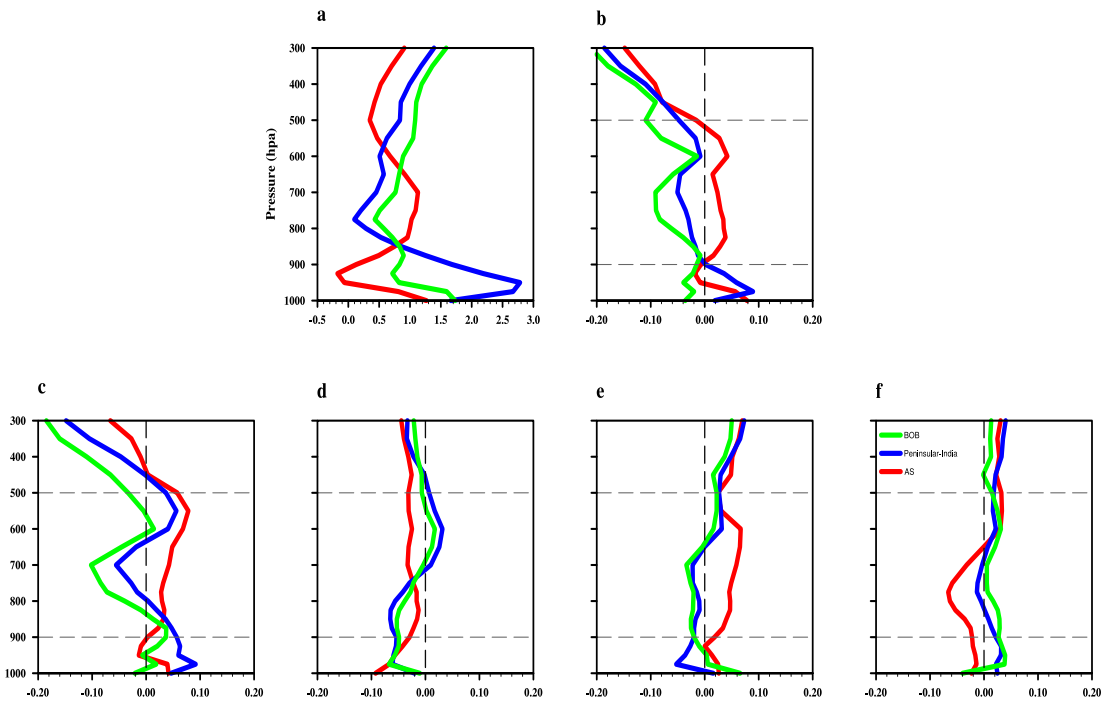


Figure 3.9 | Zonal temperature anomaly and its trend. Vertical profile of **a** climatology (°C), **b** trends (°C per 31 years) of the area averaged zonal temperature anomaly over the Bay of Bengal (green), Peninsular India (blue), and the Arabian Sea (red) from the all-forcing CESM2-LE simulations during Indian Summer Monsoon (June-September). The bottom row shows trends from single-forcing simulations: **c** GHG, **d** AER, **e** BMB aerosol, and **f** EE simulation.

Single-forcing experiments for aerosols and biomass-burning emissions (Fig. 3.11) produce negligible changes in temperature and SLP, demonstrating that their future influence on South-Asian circulation will be minor compared with that of greenhouse gases and land-use change. These results collectively suggest that cleaner atmospheric conditions and sustained greenhouse warming will reshape the regional thermal gradients that anchor the monsoon circulation, leading to the observed pattern of near-surface wind strengthening over land and moderation over oceanic regions.

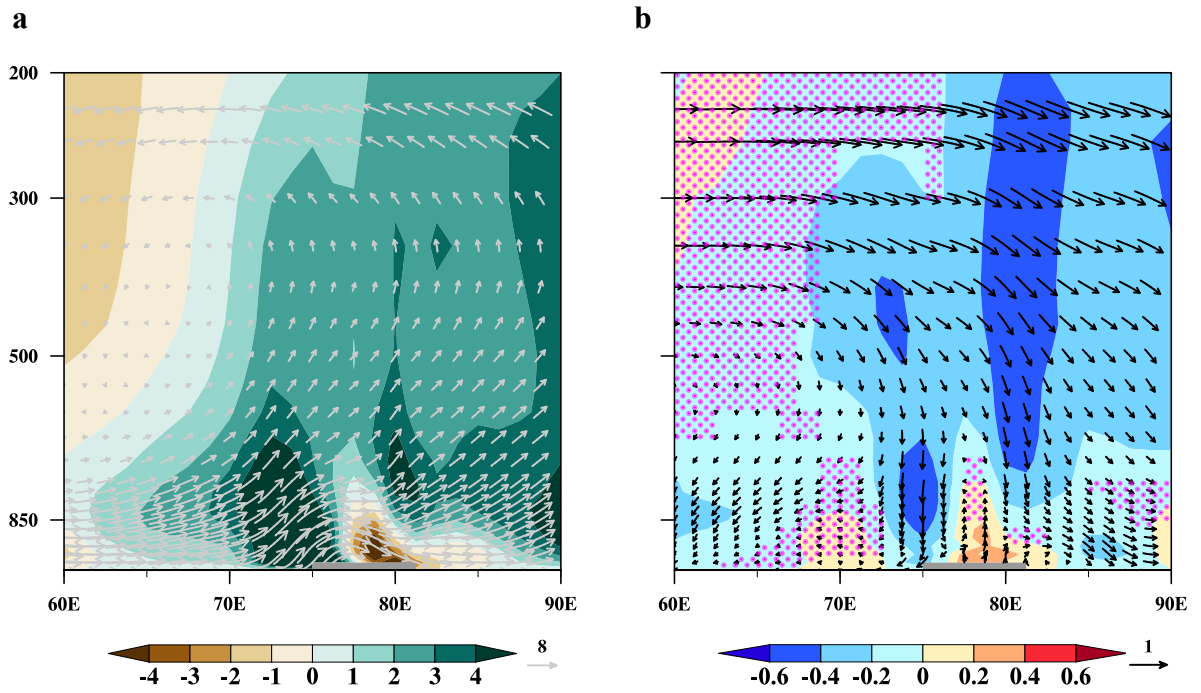


Figure 3.10 | Seasonal mean zonal circulation and trend in the pressure-latitude plane averaged over the region between 8°N and 25°N. a Climatology of zonal mean circulation for the Indian Summer Monsoon (June–September) during the period 2020–2050 from CESM2-LE. **b** Trend in zonal mean circulation for the same period. In **a** shading represents the mean pressure velocity (Pa s^{-1}) (ω*100), with positive values indicating upward motion; vectors depict the resultant of zonal winds and pressure velocity. In **b**, shading represents the trend in pressure velocity, with the same sign convention as in **a**; vectors show the trends in resultant of zonal winds and pressure velocity.

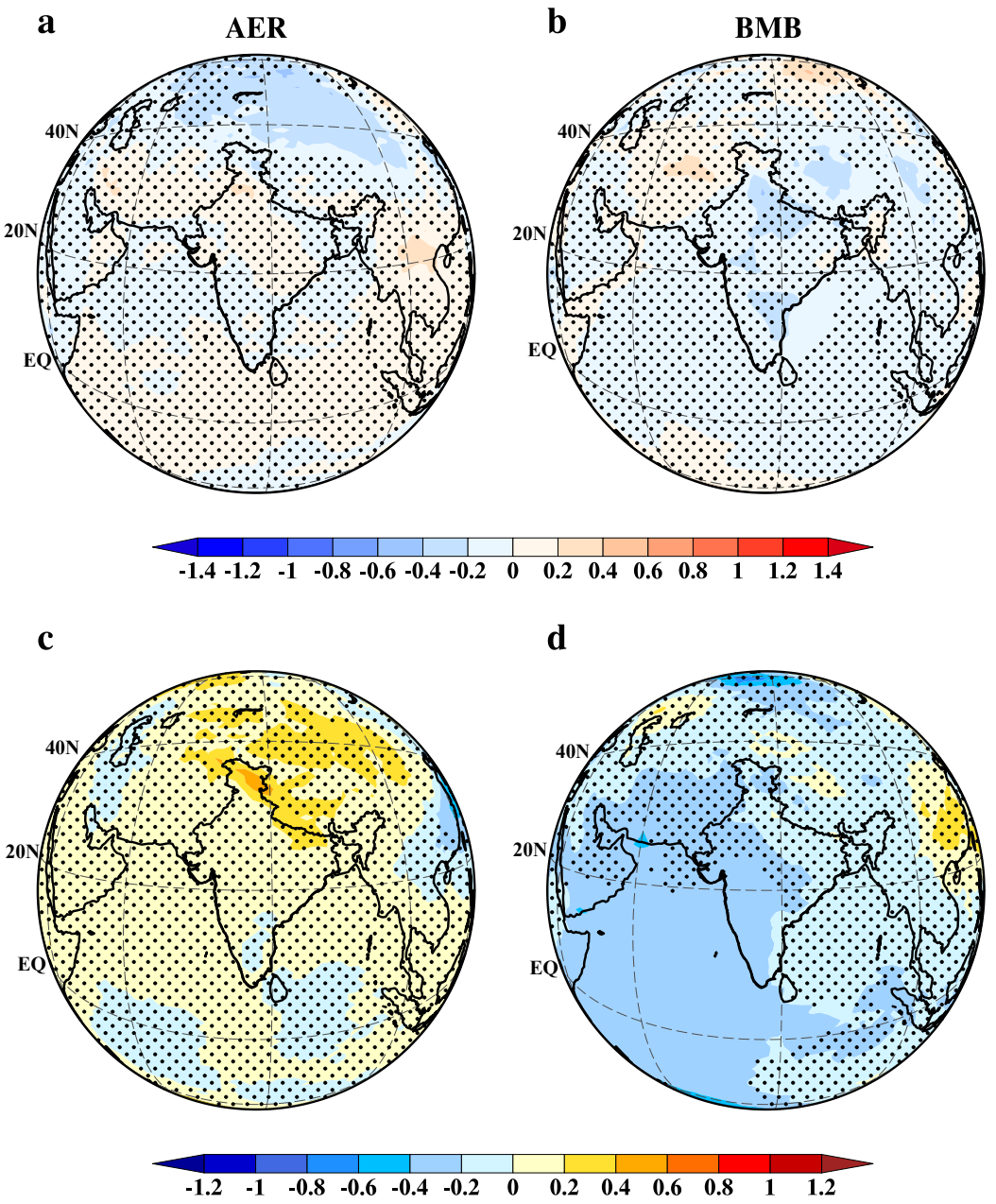


Figure 3.11 | Trends of TS and SLP in Single Forcing Large Ensemble (SF-LE) simulations of CESM2. a Trends of TS (°C per 31 years) during the Indian Summer Monsoon (June-September) for 31 years (2020-2050) from CESM2 SF-LE for AER. **b** Same as **a** but for BMB aerosols. **c, d** Same as **a, b** but for SLP (hPa per 31 years). Trends are calculated for the ensemble mean of 20 ensemble members for AER and 15 ensemble members for BMB. The stippling represents regions where the trends do not exceed the 95% significance level.

3.7 Land-Use and Irrigation Controls

Projected changes in land cover and surface fluxes exert an additional influence on near-surface winds through their control of surface roughness, albedo, and evaporation. Under the SSP3–7.0 pathway, widespread cropland expansion and irrigation intensification are projected to alter the surface energy balance across much of South Asia. Ensemble projections indicate a substantial increase in cropland fraction, most pronounced over Peninsular India, accompanied by corresponding reductions in tree and shrub cover (Figs. 3.12a–f). These transitions are consistent with the "rocky road" storyline of SSP3–7.0, characterized by weak land-use regulation, rapid population growth, and declining agricultural yields that drive large-scale conversion of natural vegetation to farmland (Popp et al. 2017). Much of this expansion is associated with agricultural intensification, particularly the increased adoption of irrigation, which modifies both the partitioning of surface fluxes and the aerodynamic roughness of the land surface.

The influence of these land-use transitions on wind speed operates through multiple interconnected pathways. Expanded irrigation enhances soil moisture and latent heat flux while suppressing sensible heating, thereby cooling the local surface and increasing boundary-layer humidity (Fig. 3.13d). This local thermodynamic adjustment can alter TS gradients and, in turn, modulate surface pressure fields. Over Peninsular India, where irrigation is projected to expand most rapidly, these changes are consistent with the secondary SLP maximum identified earlier (Figs. 3.6–3.7), suggesting a link between land-surface moistening and pressure redistribution under greenhouse-driven circulation changes. In parallel, deforestation and cropland expansion modify surface roughness, altering the vertical momentum transfer that regulates near-surface wind speed (Singh et al. 2018). The combination of these effects—enhanced latent heat flux in irrigated

regions and increased drag over converted landscapes—contributes to regional heterogeneity in projected wind trends. Overall, the results suggest the importance of LULC as a dynamically active forcing that not only modulates local thermodynamics but also interacts with large-scale monsoon circulation to shape the spatial pattern and uncertainty of future near-surface winds.

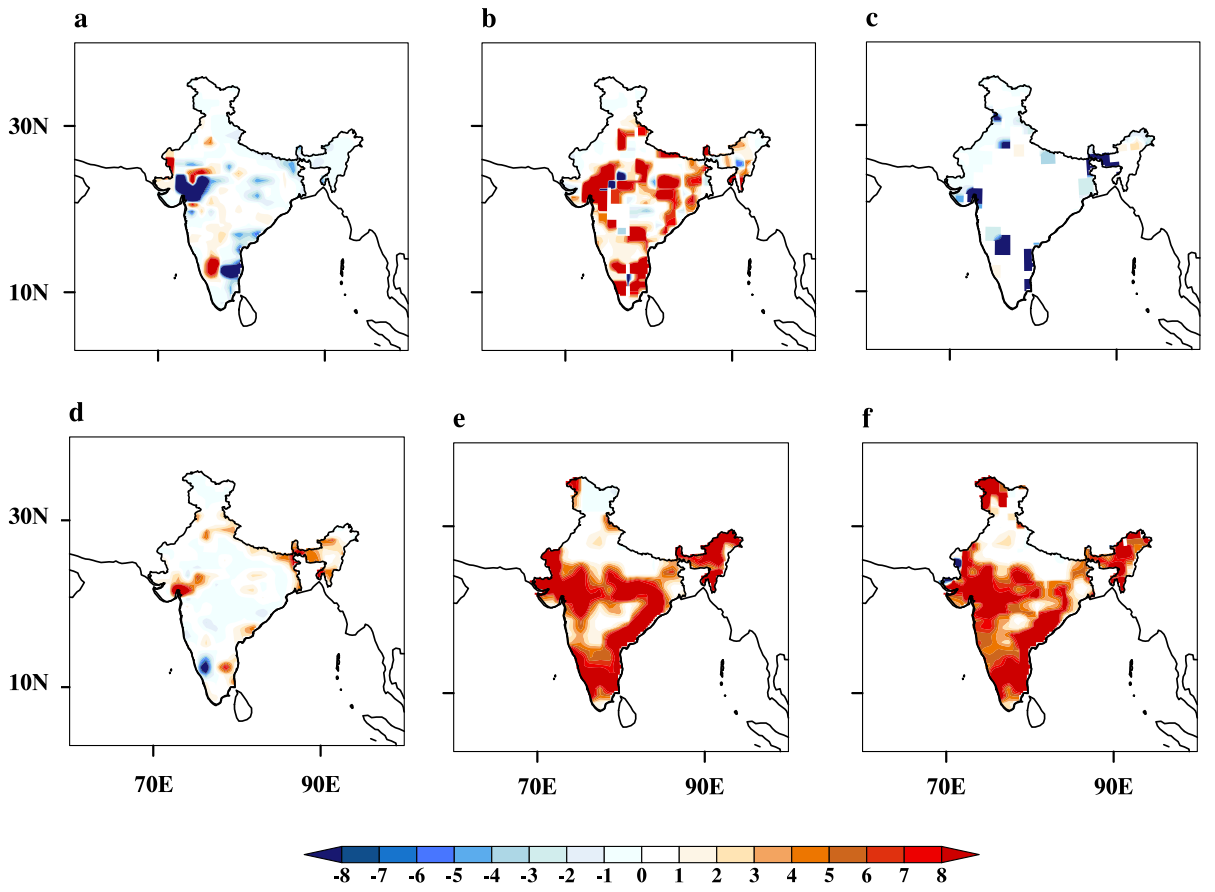


Figure 3.12 | Percentage changes in land cover types in the future under scenario SSP3-7.0. The changes depict differences in the fractional coverage of each land cover type between the early (2021–2030) and late (2041–2050) periods for: **a** tree cover, **b** shrub cover, **c** bare land, **d** grassland, **e** crop cover, and **f** irrigated crop cover.

Similar analyses of major land cover components across other SSP scenarios also reveal distinct regional changes in land cover patterns compared to SSP3-7.0, potentially inducing regional differences in wind speed. For instance, the SSP2-4.5

scenario, representing moderate sustainable development, projects a modest mid-century increase in wind speed, which intensifies under higher-emission scenarios (Fig. 3.14).

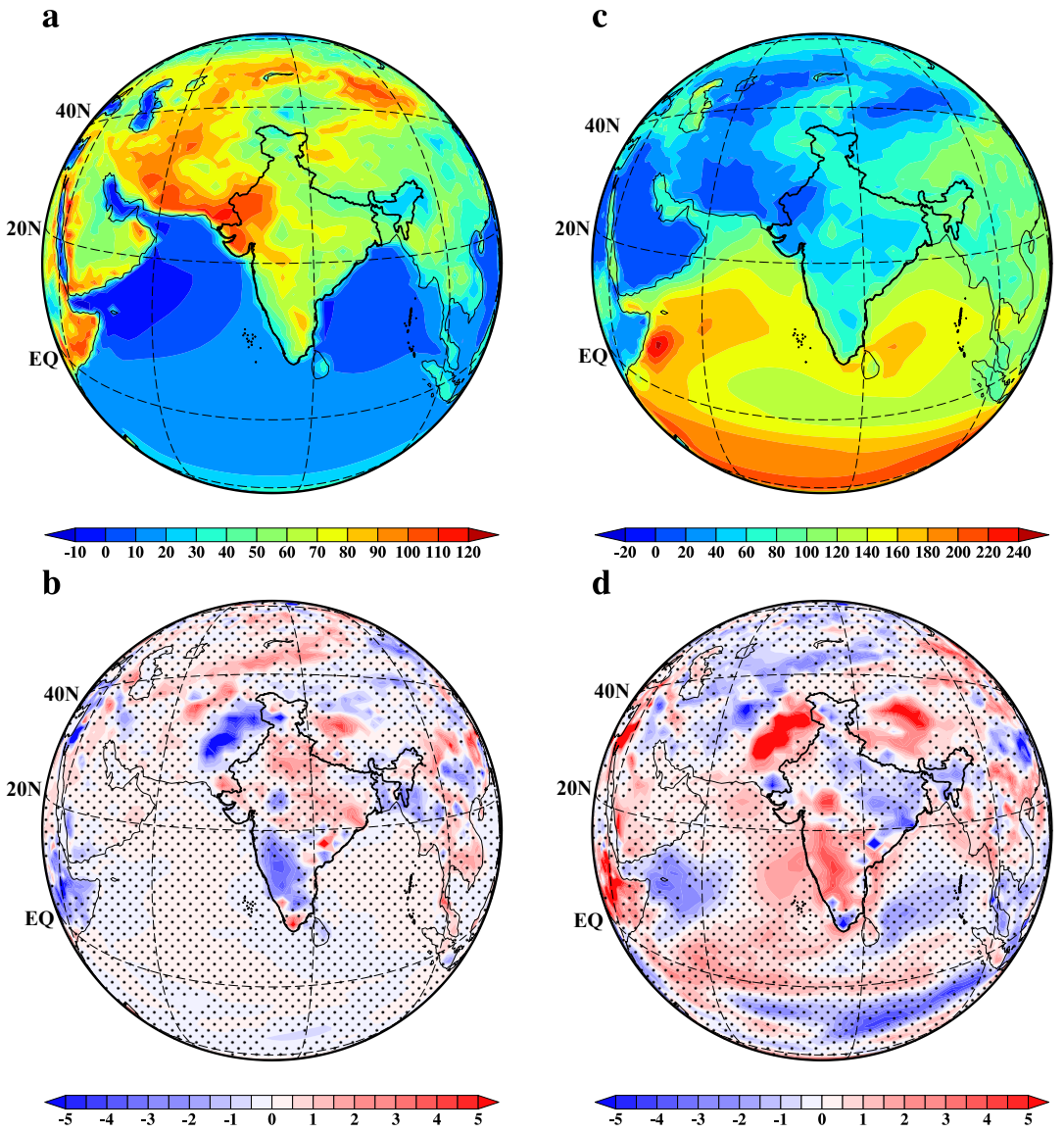


Figure 3.13 | Climatology and trend of surface energy fluxes. **a** Climatology in sensible heat flux (Wm^{-2}) during the Indian Summer Monsoon (June–September) for the period 2020–2050. **b** Trend in sensible heat flux (Wm^{-2} per 31 years) for the same period as of **a.** **c** Same as **a** but for latent heat flux. **d** Same as **b** but for latent heat flux.

3.8 Scenario and Model Dependence of Wind Projections

Although the overall signal of near-surface wind strengthening is consistent across scenarios, its magnitude and spatial expression vary with both the forcing pathway and the model framework. The CESM2-LE ensembles for SSP2–4.5, SSP3–7.0, and SSP5–8.5 (Fig. 3.14) all indicate positive trends across most of India, but with differing amplitudes. The moderate-forcing SSP2–4.5 shows the weakest increase, SSP3–7.0 exhibits a spatially heterogeneous response, and SSP5–8.5 produces the strongest enhancement. The coherence of the signal—most evident along the western coast and the Arabian Sea—suggests a thermodynamic control that scales with greenhouse forcing. However, notable regional differences, particularly over Peninsular India, point to the influence of evolving land-use patterns and surface feedbacks.

These contrasts stem from the distinct socio-economic narratives embedded in the SSPs. Scenarios such as SSP2–4.5 and SSP5–8.5 assume globally coordinated mitigation policies and technological progress, producing comparatively uniform regional forcings. In contrast, SSP3–7.0 is characterized by weak international cooperation and regionally divergent policies (Popp et al. 2017), resulting in stronger spatial heterogeneity in emissions, land-use change, and adaptation measures. Such disparities amplify local feedbacks and produce sharper gradients in regional climate responses, including wind-speed trends. In this context, the modest or insignificant change in winds over Peninsular India under RCP8.5 (Fig. 3.14d) reflects the combined effects of LULC forcing and localized circulation adjustments rather than the large-scale thermodynamic signal alone.

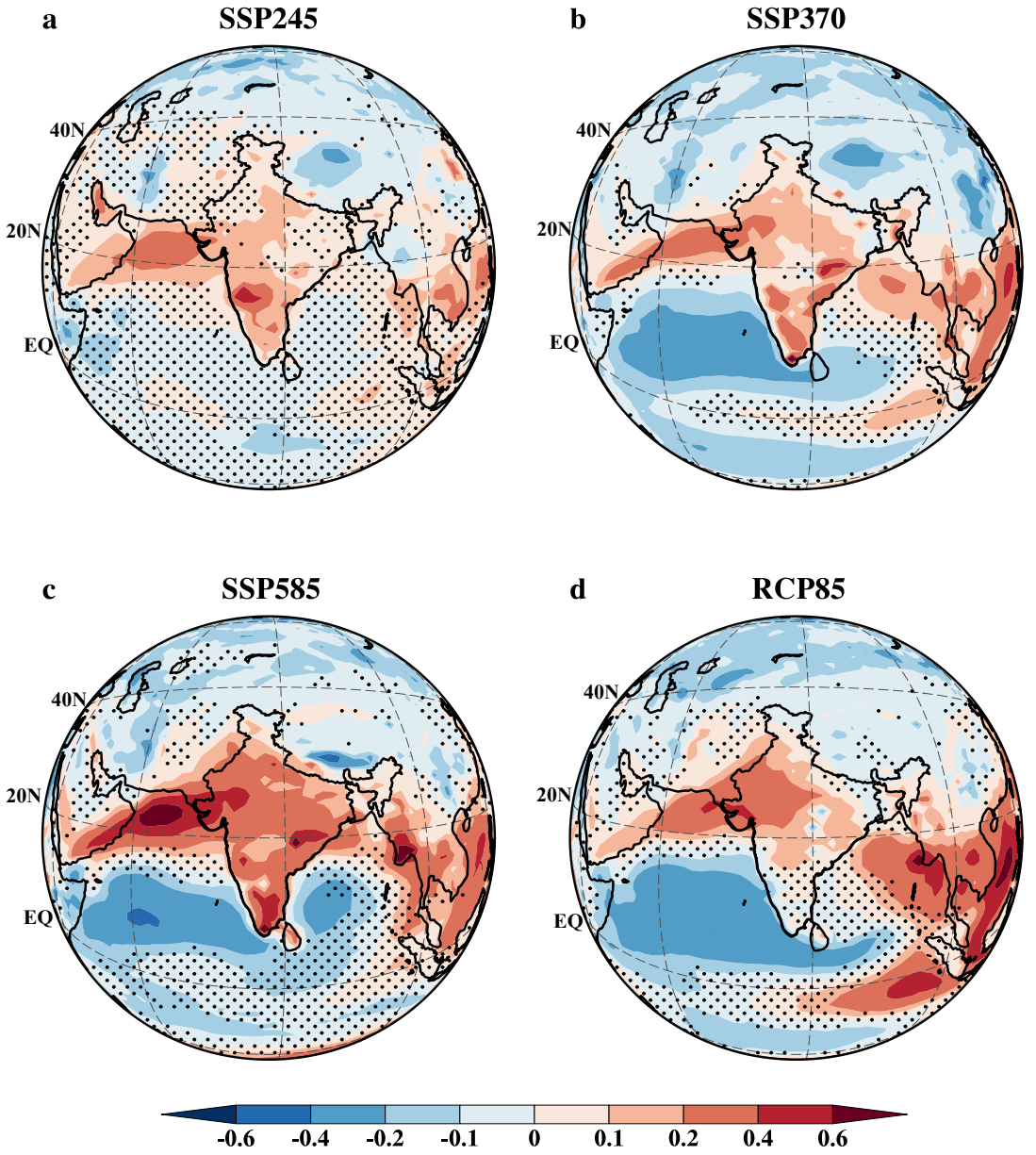


Figure 3.14 | Trends of near-surface wind speed (ms^{-1} per 31 years) in CESM2-LE simulations. Trends in ensemble-mean near-surface wind speed during the Indian Summer Monsoon (June–September) for the period 2020–2050 from CESM2-LE under different scenarios: **a** SSP2-4.5, **b** SSP3-7.0, **c** SSP5-8.5, and **d** RCP8.5. Trends are calculated using 15, 50, 15, and 16 ensemble members, respectively. The stippling represents regions where the trends do not exceed the 95% statistical significance level.

Uncertainty also arises from structural differences between models. A comparison of CESM1 and CESM2 large ensembles under identical RCP8.5 forcing (Fig. 3.15) reveals systematic discrepancies: CESM1 projects an increase along the western coastal belt, whereas CESM2 confines the maximum to the northwestern interior. These differences originate from updates to boundary-layer, cloud, and land-surface parameterizations in CESM2 that improve process realism but alter the sensitivity of surface winds to external forcing. Such structural dependencies, magnified in multi-model ensembles like CMIP6, highlight that while the direction of change is robust, regional details remain contingent on model formulation and representation of key processes such as land–atmosphere coupling and aerosol–cloud interactions

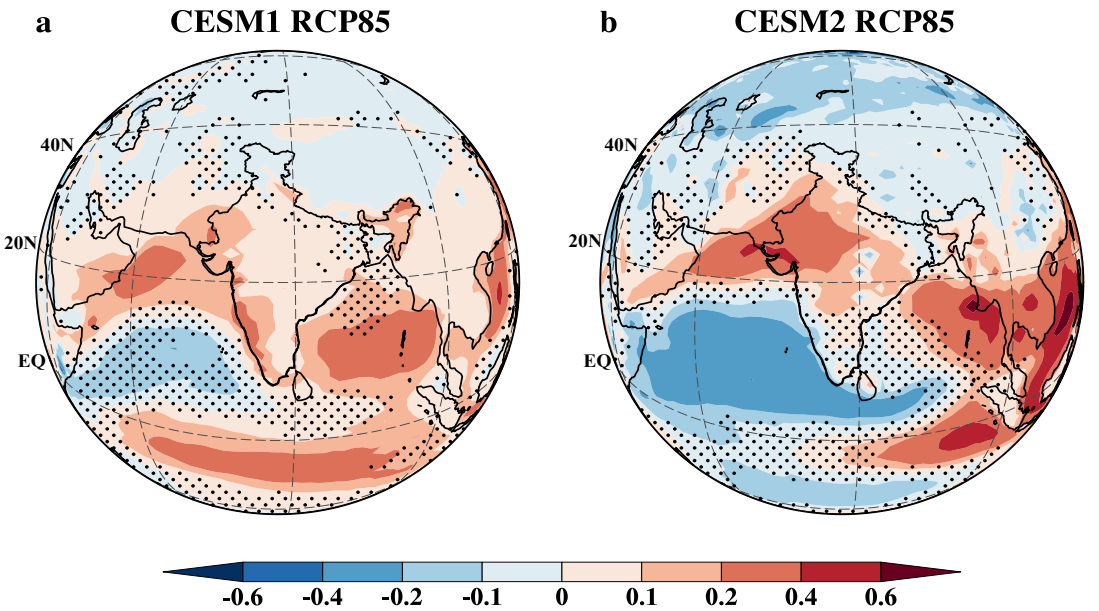


Figure 3.15 | Trends of near-surface wind speed (ms^{-1} per 31 years) in CESM large ensembles. Trends in ensemble-mean near-surface wind speed during the Indian Summer Monsoon (June–September) for the period 2020–2050 from **a** CESM1-LE and **b** CESM2-LE under the RCP8.5 scenario. Trends are calculated using 35 and 16 ensemble members, respectively. The stippling represents regions where the trends do not exceed the 95% statistical significance level.

When the analysis is extended to the CMIP6 multi-model ensemble, the diversity of projected wind responses becomes even more evident (Fig. 3.16). The multi-model mean under SSP3–7.0 reproduces the broad pattern seen in CESM2 but with weaker amplitude and greater regional variability. Several models disagree not only in magnitude but also in the sign of the projected trends, as indicated by the hatching denoting sign disagreement. Much of this spread stems from differences in how models represent irrigation. Only a few, including CESM2, GISS-E2-1-G, and NorESM2-LM, incorporate irrigation as a dynamic process (Al-Yaari et al. 2022). CESM2's time-varying irrigation modifies surface energy fluxes and boundary-layer humidity, improving realism over agricultural regions, whereas most CMIP6 models omit this forcing altogether. The absence of irrigation introduces bias in the simulated near-surface climate and amplifies uncertainty in projected winds. The standard error of the CMIP6 multi-model mean is roughly 1.5 times greater than that of CESM2-LE, with area-averaged wind-speed trends of 0.0513 ± 0.023 m sec^{-1} for CMIP6 compared to 0.1029 ± 0.0149 m sec^{-1} for CESM2-LE. The higher spread across CMIP6 models reflects both structural diversity and missing regional processes. Scenario-specific differences persist as well: inter-model variability is greater under SSP3–7.0 than under SSP5–8.5 (Figs. 3.16a–d), consistent with the stronger influence of socioeconomic and land-use forcing in the former.

Because cropland expansion in SSP3–7.0 is tightly linked to irrigation intensification, its role as a regional forcing becomes critical. Yet irrigation remains crudely represented in most global models, with simplified treatment of timing, intensity, and feedbacks on the surface energy balance (Al-Yaari et al. 2022; McDermid et al. 2023). Over South Asia, where extensive irrigation alters soil moisture and evapotranspiration (Lee et al. 2011), this omission contributes significantly to uncertainty in near-surface wind projections, underscoring the need for high-resolution, regionally calibrated modeling approaches. These insights into

model and scenario dependence provide the foundation for evaluating the practical implications for wind-energy potential.

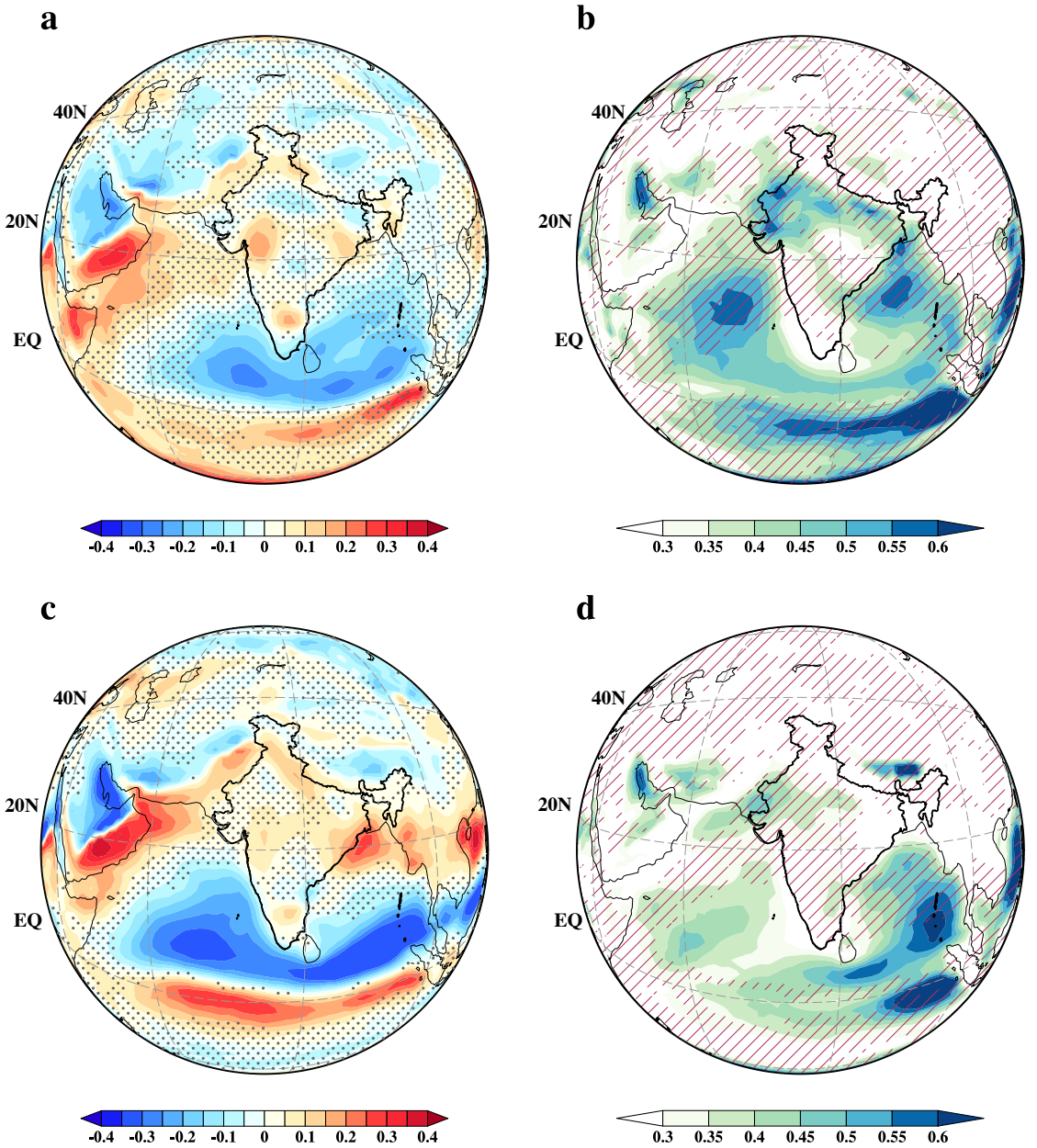


Figure 3.16 | Trend (ms^{-1} per 31 years) and standard deviation of near-surface winds in CMIP6 multi-model simulations for the future. a Trend in NSW from 34 CMIP6 models for the period 2020–2050 under scenario SSP3-7.0. Stippling indicates regions where the trend does not exceed the 95% statistical significance level. **b** Standard deviation of trends across the 34 models, with hatching representing regions where less than 66% of the models agree on the sign of change. **c** Same as **a**, but for the multi-model mean of 38 CMIP6 models under scenario SSP5-8.5. **d** Same as **b**, but for 38 CMIP6 models under scenario SSP5-8.5.

3.9 Future WEP and Socio-Economic Constraints

South Asian countries have invested heavily in wind power over recent decades, led by India, whose installed capacity of about 45 GW is expected to increase substantially in the coming years (Ministry of New and Renewable Energy, Government of India 2022). Pakistan and Bangladesh remain at earlier stages of deployment, yet their investment trajectories are accelerating in response to rising energy demand and the need for clean alternatives (Jacobson et al. 2018; World Bank 2021).

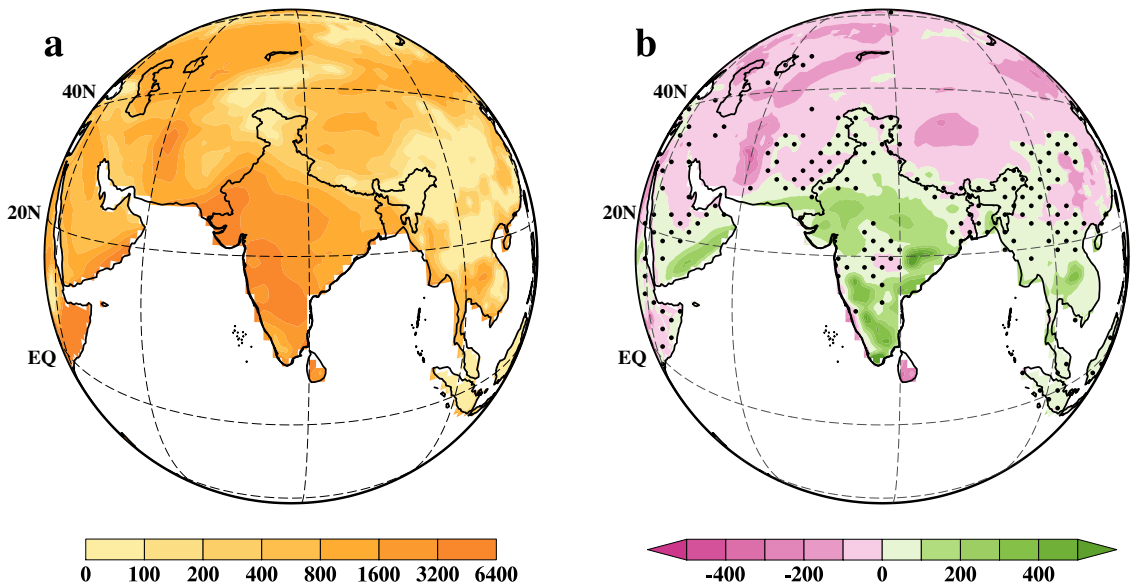


Figure 3.17 | Climatology (GWh/grid) and trends of wind energy potential (WEP) in CESM2-LE simulations in the coming decades (GWh/grid per 31 years). a Climatology and **b** trends of wind power during the Indian Summer Monsoon (June–September) over 31 years (2020–2050) from CESM2-LE. The shaded background in **a** represents the ensemble mean wind power of 50 ensemble members, while the shaded background in **b** shows the trend in the ensemble mean. The stippling in **b** indicates regions where trends do not exceed the 95% statistical significance level.

Given that wind energy density is proportional to the cube of wind speed ($P \propto V^3$), the strengthening of winds over the South Asian land translates into a

substantial enhancement in regions onshore wind energy potential. To quantify these changes, we use an industrial wind power curve of 2.5 MW GE turbine (see Methods) to analyze the spatiotemporal distribution of WEP (Fig. 3.17a). The mean WEP is significantly higher (more than 800 GWh per grid) over the western coastal states of India, southern parts of Pakistan, coastal Bangladesh regions and over Sri-Lanka than the north-eastern parts of India for evident reasons that the monsoon south-westerlies are stronger over these regions. These distributions however only reflects the wind energy density without any local spatial and geographic constraints as well as technical details in wind farm planning. The actual realizable potential may be very different due to such limitations, some of which are demonstrated in the following section.

The trends in this WEP suggest a significant increase in wind power generation, with an estimated rise of ~300 GWh over key WEP regions, consistent with the projected strengthening of winds (Fig. 3.17b). This increase in WEP is however only the climate-driven component, prior to accounting for many physical and dynamical constraints including land-use, urbanization, and demand that govern realizable deployment. Notably, a significant increase in WEP is evident along India's eastern coast. However, wind energy investments in India are currently concentrated (~70%) in the western and southern states of Gujarat, Rajasthan, Maharashtra, and Tamil Nadu, where westerly monsoon winds during summer provide high WEP (Gao et al. 2018). The projected expansion of WEP into eastern India highlights a crucial opportunity for diversifying the country's wind energy investments and informs future policy directions for sustainable energy development.

However, the realizable potential is strongly constrained by socio-economic and land-use factors. Accounting for terrain, land availability, and population density substantially reduces the feasible deployment area, in some cases lowering

the effective WEP by nearly an order of magnitude despite favourable wind conditions. In addition, rising electricity demand and urban expansion further limit the fraction of demand that can be met through wind power alone. These results highlight that while the physical potential for wind energy increases under future climate forcing, its practical deployment remains tightly coupled to non-climatic constraints, underscoring the need to interpret projected gains within a broader socio-economic and planning context.

These considerations highlight that while SSP-based projections capture the climatic drivers of wind changes, the role of socio-economic factors in shaping the deployment of wind energy remains critical. Land-use constraints, urban expansion, and evolving energy demand can significantly influence how much of the projected wind resource is practically utilized. This underscores the importance of integrating climate projections with planning and policy frameworks that account for land-use dynamics and energy demand. Such integration is essential for developing a resilient and balanced renewable energy portfolio capable of adapting to future climatic and socio-economic changes.

3.10 Projected Changes in Precipitation

Simulating monsoon precipitation remains a major challenge, as models struggle to translate dynamically consistent circulation changes into realistic regional rainfall patterns. As shown in Chapter 2, ensemble means capture large-scale circulation changes but fail to reproduce the observed spatial redistribution of precipitation. In this section, the focus is therefore on characterizing projected precipitation changes and their spread across ensembles, while the underlying sources of uncertainty are examined in Chapter 4.

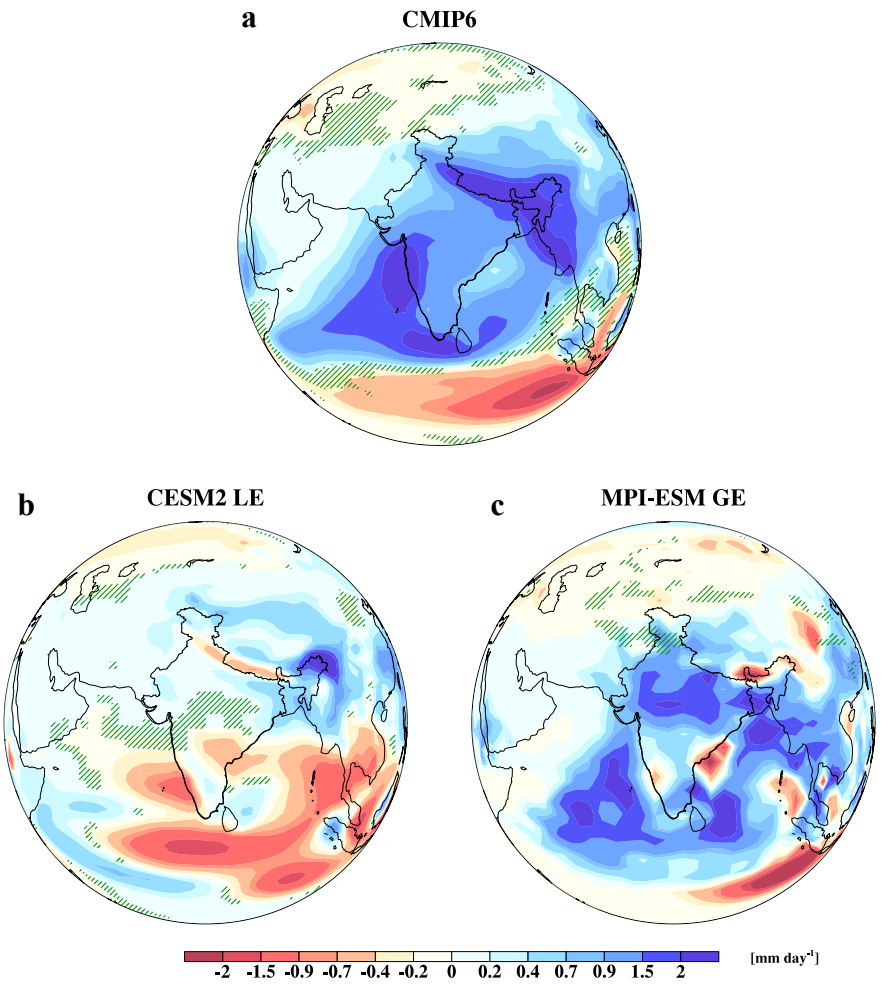


Figure 3.18 | Projected changes in precipitation at the end of the 21st century (2065–2099) relative to the historical period (1980–2014) from different climate model ensembles. a Multi-model mean (MMM) of CMIP6 models. **b** Ensemble mean (EM) of the 50-member CESM2 Large Ensemble (CESM2-LE). **c** Ensemble mean (EM) of the 100-member MPI-ESM Grand Ensemble (MPI-ESM-GE). Stippling denotes regions where less than two-thirds of ensemble members agree on the sign of change.

Figure 3.18 presents projected changes in precipitation at the end of the twenty-first century (2065–2099) relative to the historical baseline (1980–2014) from three model ensembles: the CMIP6 multi-model mean (MMM), the CESM2 Large Ensemble (LE), and the MPI-ESM Grand Ensemble (GE). The CMIP6 MMM (40 models; see section 4.2.2 of chapter 4) and MPI-ESM GE both indicate widespread increases in precipitation across the South Asian monsoon domain, consistent with

a robust forced response to greenhouse warming. In contrast, CESM2-LE exhibits a more heterogeneous pattern, featuring reductions over the northern Indian Ocean and the Himalayan foothills. Moreover, while most CMIP6 and MPI-ESM members agree on the sign of change, less than two-thirds of CESM2-LE members concur in key regions such as central India and the Arabian Sea, highlighting a weaker consensus within the ensemble. The close alignment of MPI-ESM GE with the CMIP6 MMM suggests that its ensemble mean captures the broader multi-model signal, whereas CESM2's response remains more model-specific.

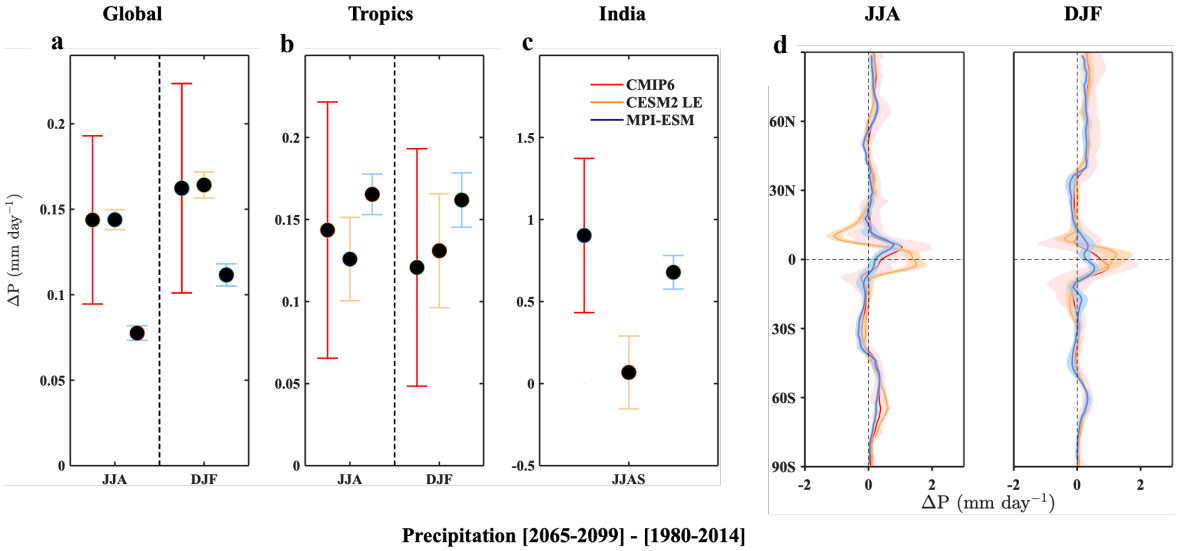


Figure 3.19 | Area-averaged precipitation projections at multiple spatial scales for the late 21st century (2065–2099) relative to the historical baseline (1980–2014). Projected changes are shown for **a** global mean precipitation, **b** tropical mean precipitation, **c** Indian regional mean precipitation, and **d** zonal mean precipitation. Filled circles denote ensemble means: CMIP6 multi-model mean (MMM), CESM2 Large Ensemble (CESM2-LE), and MPI-ESM Grand Ensemble (MPI-ESM-GE). Error bars represent inter-model spread for CMIP6, and inter-ensemble spread for the two large ensembles. For panel **d**, the spread corresponds to the inter-model spread (CMIP6) and inter-ensemble spread (CESM2-LE and MPI-ESM-GE) at each latitude band.

Area-averaged projections (Fig. 3.19) further illustrate these differences across spatial scales. At the global scale, precipitation increases consistently across ensembles, indicating a strong forced signal. Uncertainty increases toward the

tropics, where convective processes dominate, and peaks over South Asia. Over India, the inter-model spread is comparable to the mean change, indicating a weak signal-to-noise ratio. Differences between CESM2-LE and MPI-ESM GE, despite their limited internal variability, point to model-related uncertainty as the primary source of spread. This uncertainty arises from both structural differences across models and parameter choices within individual models, although their relative contributions cannot be separated at this stage.

In the broader monsoon context, this spread reflects uncertainties in how large-scale circulation changes translate into regional precipitation responses. A more detailed quantification of these processes, particularly the role of large-scale overturning circulations and their interaction with convection, is explored further in Chapter 4.

3.11 Summary, Limitations, and Directions for Future Research

This chapter examined projected twenty-first-century changes in near-surface winds and precipitation over South Asia using coordinated climate-model ensembles designed to separate externally forced signals from internal variability. The analysis employed CESM2-LE and CESM2 Single-Forcing simulations, complemented by the MPI-ESM Grand Ensemble and CMIP6 multi-model experiments, to assess how greenhouse gases, aerosols, and land-use change shape regional circulation responses. Building on the historical assessment in Chapter 2—which showed that ensemble means reproduced the large-scale circulation weakening but failed to capture the observed spatial reorganization of precipitation—the present analysis evaluated how these biases evolve under future forcing scenarios.

Across all ensembles, the projections reveal a consistent though spatially heterogeneous strengthening of near-surface winds through mid-century. Increases are concentrated over western India and the adjoining Arabian Sea, while central and eastern India exhibit smaller or neutral trends. This spatial pattern signals a transition from the aerosol-driven weakening of the historical period to a GHG- and land-use-dominated regime. GHG forcing enhances land–sea thermal contrast and reinforces lower-tropospheric westerlies, whereas land-use and irrigation changes modulate these trends regionally by altering surface fluxes and roughness. Thermodynamic adjustments further shape this response: upper-tropospheric warming over the oceans and subsidence over Peninsular India generate secondary surface-pressure maxima that regulate near-surface flow. Scenario comparisons show broadly consistent direction of change, but the amplitude and coherence vary with the forcing trajectory, being strongest under SSP5-8.5 and weakest under SSP2-4.5. Structural differences between models, particularly in boundary-layer and land-surface parameterizations, introduce additional spread in the regional signal.

Projected precipitation responses mirror these dynamical contrasts. While the global mean shows a robust increase across ensembles, uncertainty grows toward the tropics and peaks over South Asia, where convective and land-atmosphere processes dominate. The CMIP6 and MPI-ESM ensembles suggest a large-scale intensification of monsoon precipitation, whereas CESM2-LE exhibits more heterogeneous behaviour, including regional decreases over the northern Indian Ocean and Himalayan foothills. These inconsistencies underscore that, despite improved representation of circulation, translating those changes into realistic precipitation outcomes remains a major modeling challenge. A more detailed quantification of how changes in large-scale overturning circulations, including continental jets, low-pressure systems, Hadley- and Walker-type adjustments, influence regional precipitation variability and its projected evolution remains an

important direction for future work, particularly using coordinated CMIP6-based analyses and SMILEs. Developing physically based emergent constraints that explicitly link convection–circulation pathways offers a promising direction for reducing uncertainty in regional precipitation projections (Ferguglia et al. 2023).

Several limitations temper the interpretation of these results. First, the coarse resolution of global models restricts their ability to resolve mesoscale convection, orography, and coastal circulations critical to South Asia's hydroclimate. Similarly, coarse model resolution limits the use of wind energy projections for local planning, particularly in complex terrain and transboundary regions. Second, structural uncertainty arising from differences in physical parameterizations—especially for convection, boundary-layer mixing, and land-surface coupling—remains substantial. Third, the representation of irrigation and land-management processes, though improved in CESM2, remains simplified and does not fully capture spatial or temporal variability in human water use. Fourth, the analysis focuses on near-term projections; potential feedbacks emerging later in the century, such as soil-moisture–temperature coupling and aerosol–GHG co-evolution, are not explicitly evaluated. Finally, the wind-energy assessment is physical rather than techno-economic and therefore does not incorporate infrastructure or policy constraints that could affect realized capacity.

Future research should address these limitations through higher-resolution and targeted modeling. Convection-permitting and regionally calibrated simulations are needed to better capture orographic and coastal precipitation systems and sub-seasonal variability. Perturbed-physics and single-process experiments could help quantify parameter sensitivities in convection and land-surface coupling—key sources of inter-model spread. Improved representation of irrigation, groundwater extraction, and land-management practices is essential to constrain land-use-related uncertainties. Coordinated comparisons among large

ensembles from different modeling centers would further distinguish robust forced signals from model-specific responses. Finally, coupling regional climate projections with hydrological and water-resource models will enhance the utility of precipitation projections for climate-adaptation planning in South Asia.

In summary, while the projected circulation and near-surface wind responses reveal a transition toward greenhouse-gas- and land-use-dominated forcing, large uncertainties persist in how these dynamical changes translate into precipitation outcomes. This highlights persistent challenges in representing the multi-scale processes that control regional precipitation. The contrast in the credibility of historical changes in winds and precipitation extends to their future projections, reinforcing the central argument of this thesis. These uncertainties arise from both structural differences across models and parameter choices within individual models, although their relative contributions remain difficult to quantify at this stage. The next chapter focuses specifically on diagnosing the physical and structural origins of model uncertainty in precipitation simulations, providing a systematic framework for interpreting and improving their reliability.

Chapter 4: Modeling Limitations: Diagnosing the Uncertainty in Precipitation Changes

Chapter 4

Modeling Limitations: Diagnosing the Uncertainty in Precipitation Changes

4.1 Introduction

Despite major advances in climate modeling and experimental design over the recent decades, substantial disagreement continues to characterize precipitation projections, especially across the tropics where convection governs much of the climate's sensitivity to warming. Understanding the sources of this uncertainty is essential for improving the reliability of regional projections and for translating climate information into actionable guidance.

While the previous chapter established that circulation and wind responses are relatively robust, it also revealed that precipitation projections remain highly inconsistent across models in South Asia. Even when forced responses can be separated from internal variability using LEs, models continue to disagree on both the sign and spatial pattern of precipitation change. The wide inter-model spread in simulated precipitation trends—exceeding internal variability—clearly suggests that the uncertainty arises less from stochastic variability and more from how models translate impacts of external forcings into diverse climate responses. Understanding this behavior requires systematical investigation of how models respond to controlled perturbations in external forcing and whether those responses

are consistent across regions and modeling choices. Uncertainties in parameterizations, radiative forcing, and emission scenarios can obscure causal relationships or introduce circular reasoning (Curry and Webster 2011; Hegerl and Zwiers 2011). These challenges are particularly acute for tropical precipitation, where simulated responses to warming differ markedly among models (Allen and Ingram 2002; Liu et al. 2013), undermining confidence in regional risk assessments and the credibility of adaptation strategies derived from them.

One of the most direct approaches to probing these uncertainties is to examine how the precipitation responds to prescribed SST anomalies—an experimental design that isolates the effects of oceanic forcing on precipitation. Beyond scientific quest, understanding how warming in specific ocean basins influences precipitation over land has far-reaching implications for prediction, process understanding, and adaptation. SST anomalies evolve on seasonal to interannual timescales and can modulate large-scale circulation and precipitation across continents, offering a major source of predictability. Canonical examples include the ENSO, the IOD, and Atlantic SST variability, which strongly influence the hydroclimates of South Asia, East and West Africa, and the Amazon (Cai et al. 2019; Lau and Nath 2000; Li et al. 2016a; Ueda et al. 2015). These ocean–atmosphere linkages—collectively known as climate teleconnections—form the backbone of seasonal forecasting and are routinely used to interpret observed variability and to project changes under global warming. Yet, despite their importance, quantifying their influence remains deeply uncertain, particularly when inferred from models whose responses depend on uncertain process representations.

Within climate models, significant challenges persist not only in accurately diagnosing these teleconnections, but also in attributing observed changes, predicting future responses, and conducting fundamental process studies, as the influence of SST anomalies on precipitation is strongly shaped by specific structural

and parametric choices. This dependency of precipitation response is shown in this paper. We illustrate how the simulated precipitation response to identical SST forcing can vary widely, contingent upon a model's representation of convection, cloud processes, and other sub-grid scale phenomena. This entails a critical implication: what appears to be a robust teleconnection may, in some cases, be a byproduct of subjective model design rather than an objective reflection of physical reality.

This uncertainty originates in how models represent the small-scale physical processes that control convection. Within climate models, precipitation is not explicitly resolved but parameterized through empirical relationships that depend on adjustable quantities known as model parameters. These parameters govern sub-grid processes such as convection, cloud microphysics, and turbulent mixing—phenomena that occur on spatial scales too fine to be explicitly simulated (Mishra, 2009). Many parameters cannot be directly observed or constrained by available data and are therefore tuned to achieve realistic climatology (Gettelman et al. 2024; Mishra 2012). Different models employ different parameter values and formulations; even within a single model family, parameter choices vary across configurations to maintain energy balance. This diversity introduces both parameter and structural uncertainty, rendering the simulated precipitation response to a given SST perturbation highly model-dependent. The consequence is that what appears to be a robust SST–precipitation relationship in one model may be absent or even reversed in another. Thus, a teleconnection that seems physically well-founded could, in some cases, reflect model design choices rather than objective physical causality. This realization raises two critical questions: (i) how sensitive are precipitation responses to uncertainties in model parameters, and (ii) how region-specific are these sensitivities? While these questions have global relevance, their implications are particularly acute for South Asia, where precipitation projections

show persistent inter-model contradictions across successive generations of IPCC assessments.

To address this issue, the present chapter investigates model uncertainty in the precipitation response to SST forcing with a dual objective. First, it seeks to diagnose the extent to which parameter uncertainty contributes to the divergence of simulated precipitation responses. Second, it examines whether this sensitivity is confined to South Asia or represents a broader feature of the global tropics. By comparing results across regions, the analysis aims to identify the physical processes and parameter dependencies that most strongly govern precipitation uncertainty, thereby placing the South Asian problem within the larger context of global modeling challenges.

We focus our analysis on the tropics, with particular emphasis on South Asia, a region where SST variability in the Indian and Pacific Oceans exerts a dominant control on rainfall variability (Chung and Ramanathan 2006; Fasullo and Webster 2002; Ueda et al. 2015). Given the persistent inter-model spread and self-contradictory precipitation projections noted in the previous chapter, the South Asian monsoon provides an ideal test bed for diagnosing the influence of parameter uncertainty. Attribution and projection of South Asian precipitation are highly policy-relevant: small changes in seasonal rainfall translate into major impacts on agriculture, water availability, and disaster risk. At the same time, extending the analysis to other tropical regions allows us to evaluate whether the South Asian uncertainty represents a regional peculiarity or a manifestation of a broader, model-structural limitation that affects tropical precipitation simulation globally. Understanding the sources of model disagreement—both regional and global—is therefore essential not only for improving process understanding but also for enhancing the reliability of climate information that underpins adaptation and mitigation planning in South Asia and across the wider tropics.

4.2 Data, Models, and Analytical Methods

This chapter investigates how uncertainties in model formulation and parameter specification influence the simulated precipitation response to surface warming. The analysis combines large-ensemble perturbation experiments, targeted numerical tests, and multi-model comparisons to establish a consistent framework for diagnosing parameter-driven and structural components of uncertainty.

4.2.1 Perturbed Parameter Ensemble Simulations

To systematically investigate how parameter uncertainty affects attribution of precipitation responses to SST anomalies, we employ a Perturbed Parameter Ensemble (PPE) approach (Collins et al. 2011) . This method allows us to explore a wide range of plausible model configurations by varying key parameters related to convection, cloud processes, and mixing—thereby quantifying how sensitive the simulated SST-precipitation linkages are to parameter choices.

We analyzed data from the PPE simulations conducted using the CESM Community Atmosphere Model version 6 (CAM6) (Eidhammer et al. 2024). This ensemble consists of 263 atmosphere-only simulations in which 45 key atmospheric parameters—spanning convection, microphysics, turbulence, and aerosol processes—are simultaneously but independently perturbed. The perturbation ranges were defined based on expert judgment (Duffy et al. 2024), and Latin Hypercube Sampling (Mckay et al. 2000), was employed to efficiently explore the high-dimensional parameter space.

Each simulation is conducted under two experimental setups. The control configuration, referred to as Present Day (PD), uses prescribed monthly climatological SSTs and sea ice concentrations averaged over the period 1995–2010. In the perturbed configuration, referred to as SST4K, a uniform +4K SST anomaly is

added globally relative to the PD SSTs, with all other model settings held constant. The precipitation response is calculated as the difference between the SST4K and PD simulations. While the PPE encompasses a broad range of plausible parameter space, not all combinations of parameter values necessarily yield realistic precipitation simulations. To ensure our analyses reflect physically plausible climate states, we considered a subset of 211 from the total 263 PPE members, selecting those whose PD precipitation simulations showed better agreement with observation. A comprehensive description of the perturbed parameters and CAM6 model components is provided in Eidhammer et al. 2024.

In addition, through a set of ensemble experiments, we show that precipitation responses to identical SST anomalies vary widely across model configurations. To conduct targeted numerical experiments, we use the CESM Community Atmosphere Model version 5 (CAM5) with its default physical parameterizations. To diagnose the precipitation response to SST warming, a pair of numerical experiments is performed. In the control experiment, the model is forced with observed SSTs averaged over 1982–2001. In the warmed SST experiment, a tropical SST warming pattern is added to the control SSTs: +1°C at the equator, tapering linearly to 0°C at 30°N and 30°S. This idealized warming pattern creates a smooth and broad tropical SST increase, enhancing the signal-to-noise ratio and enabling clearer detection of precipitation responses.

To assess the sensitivity of precipitation responses to model parameters, we first conduct a baseline pair of simulations using the default parameter settings. We then repeat this pair ten additional times by perturbing five key cumulus convection parameters—tau, CAPE limit, Ke, c0_lnd, and c0_ocn—one at a time, with two perturbation values per parameter, chosen within their scientifically permissible ranges (Mckay et al. 2000) (see table 4.1). The tau represents the convective relaxation timescale that governs the intensity as well as the duration of convection, the CAPE

limit decides whether the environment is conducive to convection or not, the Ke governs the evaporation rate of raindrops, and the c0_land and c0_ocn determines the cloud condensate rate over land and ocean, respectively. This results in a total of 11 experiment pairs (1 default + 10 perturbed), enabling a targeted assessment of parameter-driven uncertainty in precipitation responses. To evaluate the influence of simulation length on the results, two of these experiment pairs are extended to 40 years: CASE 1, the default configuration, and CASE 2, where the tau parameter is perturbed. This allows us to examine the robustness of seasonal-scale conclusions over longer climatological timescales.

Each simulation is run for six months—from April 1 to September 30. This initialization period captures the critical April lead time, which has been shown to provide reliable seasonal monsoon forecasts. The first two months (April–May) are discarded as spin-up; analyses focus on the June–September South Asian summer monsoon (SASM) period.

Importantly, the parameter perturbations have minimal impact on the model's large-scale climate state. The top-of-atmosphere (TOA) energy balance remains stable, with some cases even exhibiting improved energy closure. Across the parameter space: Global mean precipitation varies by approximately 1.72%, net solar flux at TOA by 0.86%, and net longwave flux at TOA by 0.21%. Crucially, the model's ability to simulate other key climate variables remains consistent—and in many cases, improves—across these experiments (Fig. 4.1). The model simulations for precipitation are validated against observation from Global Precipitation Climatology Project (GPCP) (Adler et al. 2003) and for TS, winds, and total cloud cover, reanalysis data from ECMWF Reanalysis v5 (ERA5) (Hersbach et al. 2020). This demonstrates that the targeted parameter perturbations do not compromise, and may in some cases enhance, the overall integrity of the simulated climate system.

Model version	Configuration details	Length of simulation
CASE 1	Default configuration: c0_lnd = 0.0035m^{-1}, c0_ocn = 0.0035m^{-1}, CAPE limit = 70$m^{-2}s^{-2}$, K_e = 1.0E-06(kg $m^{-2}s^{-1})^{-1/2}s^{-1}$, and tau = 3600s	40–Years
CASE 2	tau = 7200s	40–Years
CASE 3	tau = 3600s	6–Months
CASE 4	tau = 7200s	6–Months
CASE 5	CAPE limit = 300$m^{-2}s^{-2}$	6–Months
CASE 6	CAPE limit = 500$m^{-2}s^{-2}$	6–Months
CASE 7	K_e = 0.5E-06(kg $m^{-2}s^{-1})^{-1/2}s^{-1}$	6–Months
CASE 8	K_e = 1.5E-06(kg $m^{-2}s^{-1})^{-1/2}s^{-1}$	6–Months
CASE 9	c0_lnd = 0.0059m^{-1}	6–Months
CASE 10	c0_lnd = 0.001m^{-1}	6–Months
CASE 11	c0_ocn = 0.045m^{-1}	6–Months
CASE 12	c0_ocn = 0.001m^{-1}	6–Months
CASE 13	tau = 2400s	6–Months
CASE 14	tau = 4800s	6–Months

Table 4.1 | Description of targeted experiments. This table details the experimental setup. Simulations include a control (CTRL) run, forced with observed climatological SSTs averaged over 1982–2001, and a warmed SST experiment, which adds a tropical warming pattern (+1°C at the equator, tapering to 0°C at 30°N/S). Beyond the baseline default simulations, ten additional experiment pairs were conducted by perturbing five key cumulus convection parameters (c0_lnd, c0_ocn, CAPE limit, Ke, tau) with two scientifically permissible values each. Two specific pairs, CASE 1 (default configuration) and CASE 2 (perturbed tau), were extended to 40 years.

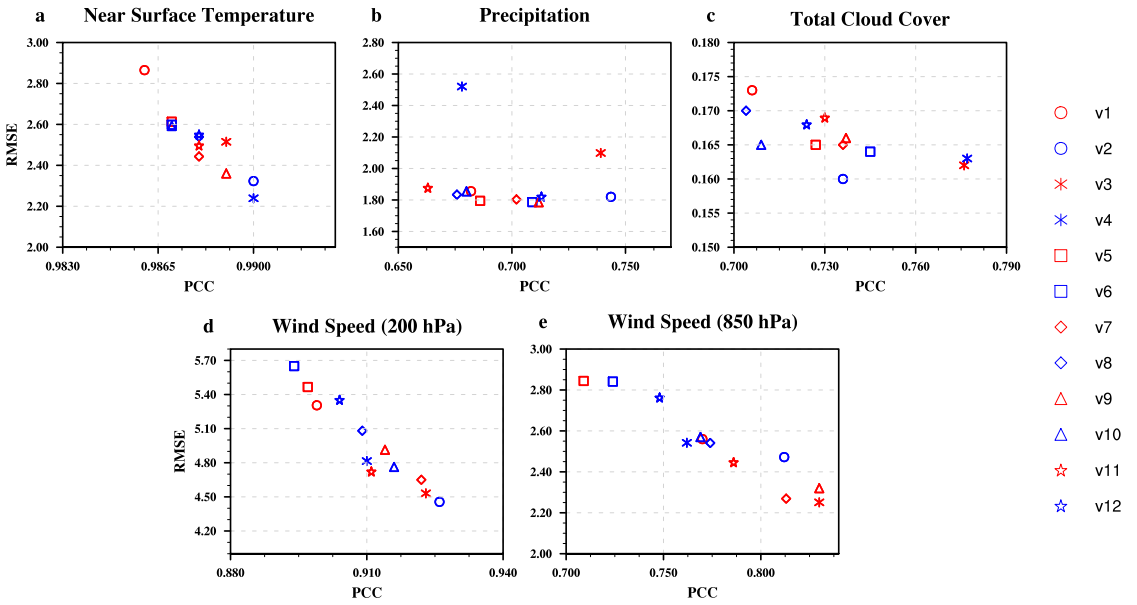


Figure 4.1 | Performance evaluation of different cases of model simulation using CESM CAM5. a-e, Performance shown as the scatter plot of PCC vs. RMSE for the simulated variables — **a** Near Surface Temperature, **b** Precipitation, **c** Total Cloud Cover, **d** Wind Speed at 200 hPa, and **e** Wind Speed at 850 hPa during June to August over the globe for the twelve different cases of model simulation (see Table 4.1 for simulation details).

4.2.2 CMIP6 and AMIP Experiments

To compare precipitation response uncertainty from PPE with that from multi-model ensembles (MME), we analyzed simulations from both CMIP6-AMIP and CMIP6 coupled models. The AMIP analysis focused on precipitation changes between control runs (amip-hist; 1979–2014, forced with observed SSTs and sea ice) and warm SST experiments (amip-p4K), which impose a uniform +4 K warming atop observed SSTs. Data from nine AMIP models (r1i1p1f1 ensemble) were used where available. To assess the role of parameter uncertainty in broader structural uncertainty, we compared precipitation changes from PPEs and AMIPs to 40 CMIP6 coupled models under SSP5-8.5 (2065–2099 vs. 1980–2014) for both summer and winter seasons (see Table 4.2). Detailed CMIP6 protocols are available in Eyring et al. 2016.

Sl. No.	CMIP6 Models	Resolution (lat x lon) (°)
1	ACCESS-CM2	1.25 x 1.875
2	ACCESS-ESM1-5	1.24 x 1.875
3	AWI-CM1-1-MR	0.937 x 0.937
4	BCC-CSM2-MR	1.125 x 1.125
5	CAMS-CSM1-0	1.125 x 1.125
6	CanESM5	2.812 x 2.812
7	CAS-ESM2-0	1.406 x 1.406
8	CESM2	0.937 x 1.25
9	CESM2-WACCM	0.937 x 1.25
10	CMCC-CM2-SR5	0.937 x 1.25
11	CMCC-ESM2	0.937 x 1.25
12	CNRM-CM6-1	1.406 x 1.406
13	CNRM-ESM6-1-HR	0.5 x 0.5
14	CNRM-ESM2-1	1.406 x 1.406
15	E3SM-1-1	1 x 1
16	EC-Earth3	0.703 x 0.703
17	EC-Earth3-Veg	0.703 x 0.703
18	FGOALS-f3-L	1 x 1.25
19	FGOALS-g3	2.25 x 2
20	FIO-ESM-2-0	0.937 x 1.25
21	GFDL-CM4	1 x 1.25
22	GFDL-ESM4	1 x 1.25
23	GISS-E2-1-G	2 x 2.5
24	HadGEM3-GC31-LL	1.25 x 1.875
25	IITM-ESM	1.914 x 1.875
26	INM-CM4-8	1.5 x 2
27	INM-CM5-0	1.5 x 2
28	IPSL-CM6A-LR	1.258 x 2.5
29	KACE-1-0-G	1.25 x 1.875
30	MCM-UA-1-0	2.25 x 3.75
31	MIROC-ES2L	2.812 x 2.812
32	MIROC6	1.406 x 1.406
33	MPI-ESM1-2-HR	0.937 x 0.937
34	MPI-ESM1-2-LR	1.875 x 1.875
35	MRI-ESM2-0	1.125 x 1.125
36	NESM3	1.875 x 1.875
37	NorESM2-LM	1.875 x 2.5
38	NorESM2-MM	0.937 x 1.25
39	TaiESM1	0.937 x 1.25
40	UKESM1-0-LL	1.25 x 1.875

Table 4.2 | Details of CMIP6 Models used in this chapter. 40 CMIP6 couple models used in this study, where the AMIP simulations from 9 climate models used in the study are highlighted with blue color.

4.2.3 Selection of Wet and Dry Regions

"Wet" and "dry" zones were defined based on positive and negative precipitation anomalies in response to SST warming, derived from CAM6 and CAM5 default simulations. Using these anomalies, spatial masks were applied to isolate and area-average wet and dry regions within each ensemble/model. For AMIP and CMIP6 MMEs, the CESM2 model served as the reference for region masking to ensure cross-model consistency. Disagreement in spatial patterns was assessed by identifying grid points where more than one-third of models differed in the sign of change. Uncertainty was quantified as ±2σ across ensemble members or models.

The observation and reanalysis data used in this chapter are publicly available. The global monthly observed precipitation data of GPCP can be downloaded from https://www.ncei.noaa.gov/data/global-precipitation-climatology-project-gpcp-monthly/access/ and the monthly data of ERA5 reanalysis for rest of the variables are available at https://www.ecmwf.int/en/forecasts/dataset/ecmwf-reanalysis-v5. The perturbed parameter ensemble (PPE) datasets can be downloaded from https://www.earthsystemgrid.org/dataset/ucar.cgd.cesm2.cam6.ppe.html. The model simulated monthly precipitation datasets for both historical and future period, and AMIP experiments of CMIP6 group of models can be obtained from https://esgf-node.ipsl.upmc.fr/search/cmip6-ipsl/. The model codes of CESM1.2-CAM5.3 are publicly available at http://www.cesm.ucar.edu/models/cesm1.2.

4.3 Precipitation Response to SST Warming in PPE Simulations

The analysis begins with the PPE to establish how variations in model physics influence the simulated precipitation response to surface warming. Because this

ensemble systematically samples a broad range of physical configurations within a single model framework, it provides a clear view of the parameter-driven diversity in precipitation behavior under identical external forcing. The results from the PPE form the foundation for subsequent sections, which explore the underlying mechanisms and regional expressions of this uncertainty.

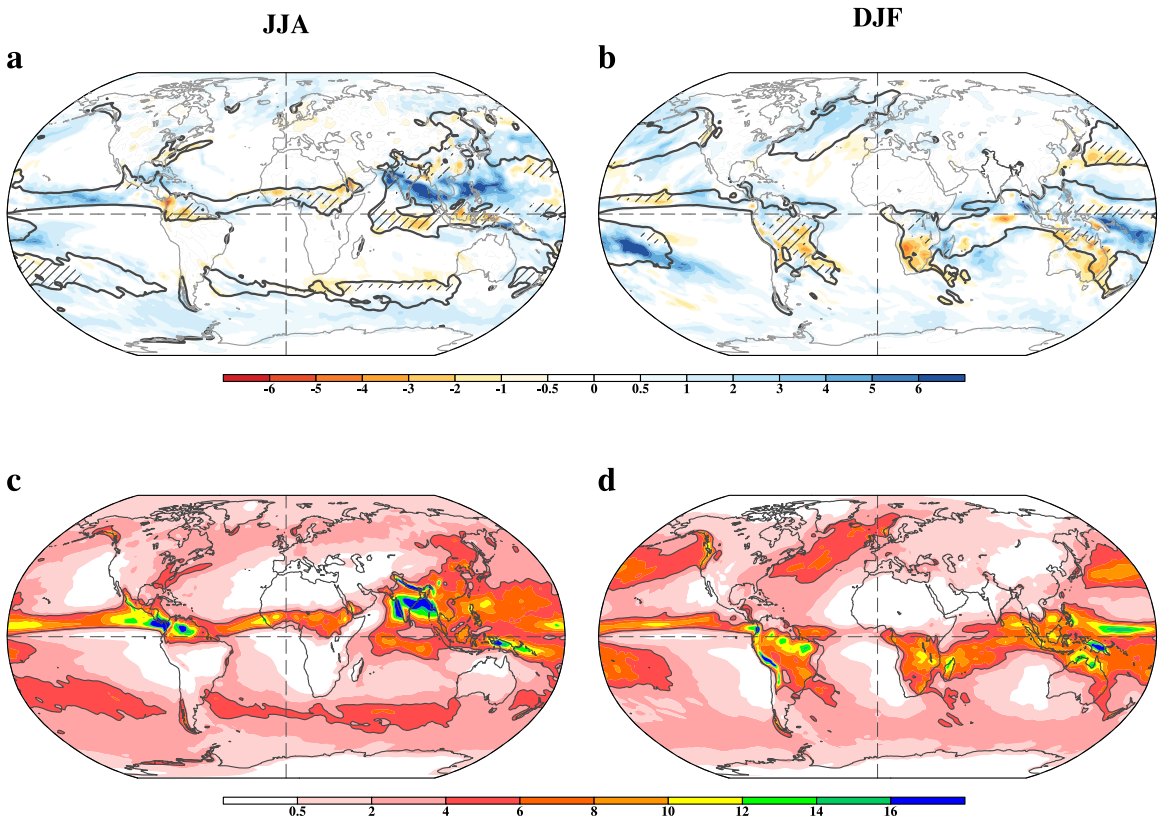


Figure 4.2 | Effect of warming sea surface temperatures on precipitation patterns in the PPE simulations. **a, b** Change in precipitation (warmed SST minus present day; units mm day^{-1}) during **a** boreal summer and **b** winter from the default model setup. Hatched areas indicate where more than one-third of the ensemble members disagree. Only regions with high average precipitation (over 4 mm day^{-1}, outlined in gray) are considered for model disagreement. **c, d** Mean precipitation for boreal **c** winter and **d** summer in present day simulation.

To examine the large-scale structure of precipitation change and its consistency across ensemble members, Figure 4.2 presents the spatial pattern of

precipitation response to uniform SST warming. The ensemble mean indicates an overall intensification of precipitation in convectively active regions, particularly across the Indo-Pacific warm pool and the South Pacific Convergence Zone, consistent with large-scale moisture availability. However, the spatial pattern is highly heterogeneous. Significant drying appears across continental regions and along the margins of primary convection zones—including parts of Africa, South America, and the Maritime Continent—revealing that the regional signal deviates substantially from the canonical "wet-get-wetter" behavior. In contrast, widespread drying is evident across many parts of the tropics, including regions of Africa, South America, Amazonia, and the Maritime Continent, as well as over parts of the equatorial Indian Ocean and western Pacific. These areas are mostly over land and/or located along the margins of primary convective zones or within secondary convective zones, such as the IO branch of the ITCZ.

The default model configuration shows substantial precipitation changes (Fig. 4.2a and b), which might initially be interpreted as the effect of SST warming. However, this inference may be misleading. It is based on a single fixed choice of model parameters and does not reflect the deeper uncertainty arising from parameter uncertainty. When these parameters are systematically varied across the PPE, the precipitation responses exhibit a substantial spread (Fig. 4.3), with many regions showing a reversal in the sign of change. For example, areas identified as drying in the default configuration show wetting in a sizable fraction of ensemble members, and vice versa. In many regions, more than one-third of the ensemble members disagree on whether conditions become wetter or drier, as indicated by hatching in Fig. 4.2, suggesting the profound uncertainty introduced by parameter variations. Notably, many of these regions correspond to the drying areas mentioned earlier, with the land areas especially vulnerable to climate change.

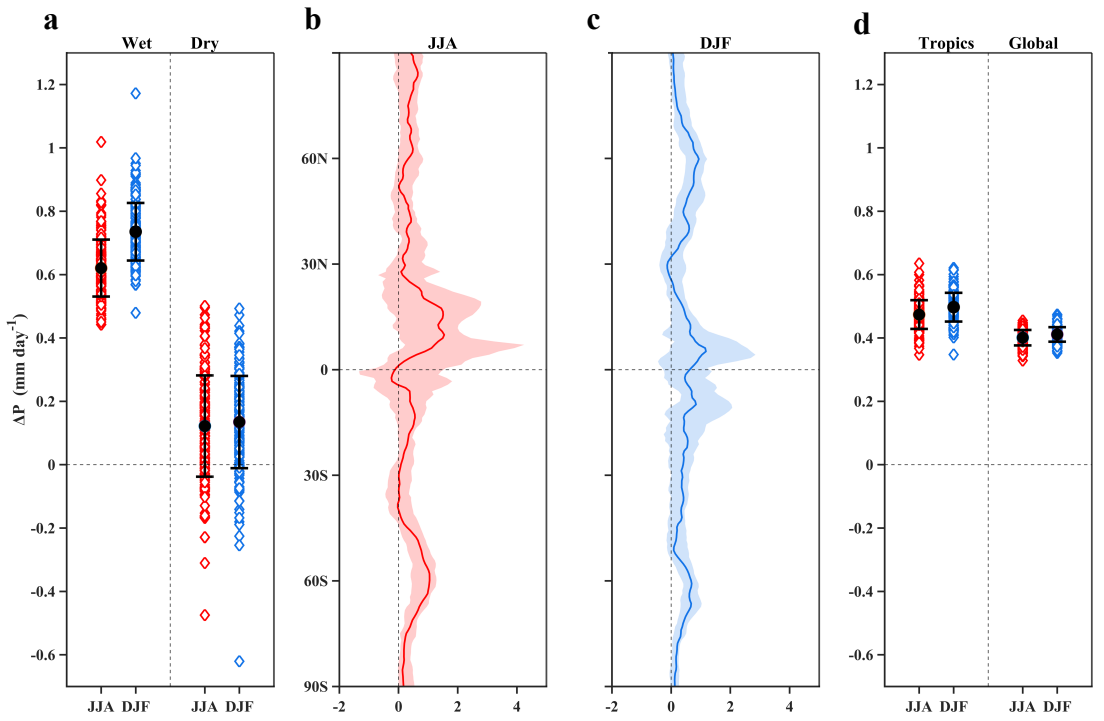


Figure 4.3 | Effect of warming sea surface temperatures on average and zonal precipitation in the PPE simulations. Panels **a–d** show the change in precipitation (warmed SST minus present day) for: **a** tropical wet and dry regions, **b** zonal average precipitation during boreal summer, and **c** zonal average precipitation during boreal winter, and **d** for tropical (30°S–30°N) and global averages. Filled circles show the average of all ensemble runs, while open diamonds show individual runs. Wet and dry regions are identified from the default model run. Error bars in **a** and **d** show variability across the ensemble. In **b** and **c**, the solid line shows the average zonal change, and the shaded area shows the range across ensemble members.

This uncertainty is highlighted in Figure 4.3a, which shows a wide, multi-fold spread in precipitation changes across ensemble members, particularly in regions prone to drying, where a sizable fraction of members exhibit opposing signs, indicating an increase in precipitation in response to SST warming. Zonal mean precipitation responses also reveal significant variability, including sign reversals in the deep tropics during boreal summer (Fig. 4.3b and c). In several sensitive regions, this spread exceeds 80% of the local seasonal mean precipitation (Fig. 4.4a, b). These results demonstrate that parameter uncertainty alone can obscure or even reverse the sign of regional precipitation change. Consequently, efforts to attribute observed

or projected regional precipitation trends to SST warming are fundamentally uncertain unless these structural uncertainties are better constrained.

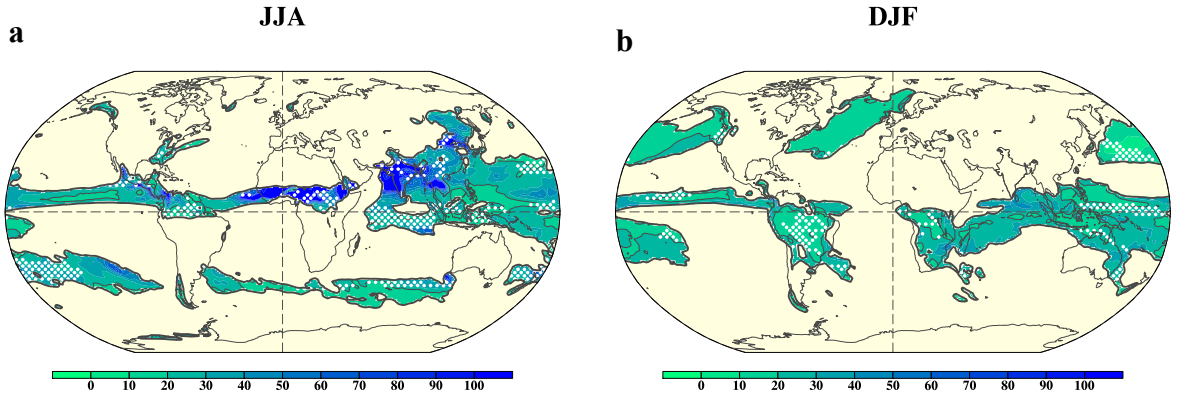


Figure 4.4 | Variability in effect of warming sea surface temperatures (SSTs) on precipitation response in the PPE simulations. Spread (standard deviation) in precipitation changes (warmed SST minus present day) across ensemble members during boreal **a** summer and **b** winter. Stippling shows areas where more than one-third of the ensemble members disagree on the direction of change. Only regions with high average precipitation (over 4 mm day^{-1}, outlined in gray contour) are considered.

In contrast to the ambiguity at regional scales, precipitation responses averaged over larger areas exhibit strong agreement across ensemble members. As shown in Fig. 4.3d, the spread narrows considerably for both tropical (30°S–30°N) and global mean precipitation, with no sign reversals—wet regions remain wet and dry regions remain dry in response to SST warming across the full parameter space. This scale-dependent behavior reflects fundamental physical constraints: while energy and moisture budgets impose very tight controls at the global scale, these constraints become progressively relaxed at smaller scales and are far less restrictive at regional scales. Thus, although large-scale precipitation responses to SST warming can be consistently attributed, regional attribution remains critically contingent on narrowing uncertainty in model parameterizations. This underscores that model consistency at the planetary scale does not guarantee accuracy at the regional scale; rather, it merely serves as a prerequisite.

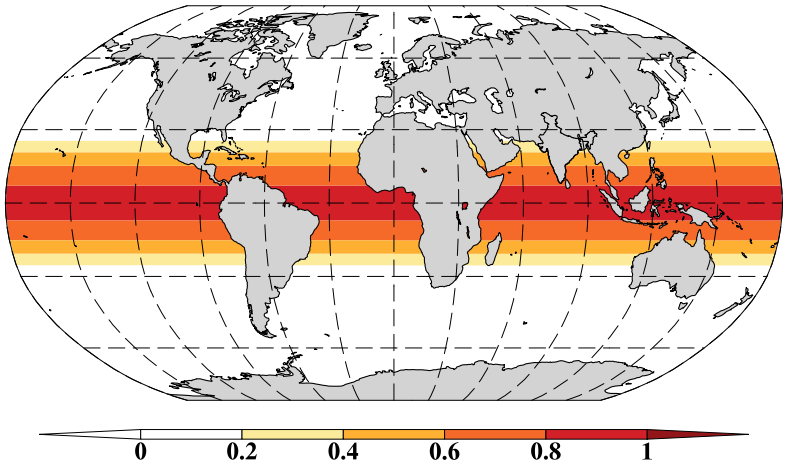


Figure 4.5 | Modified tropical SSTs. SST changes ranging from 0 to 1°C are added to the prescribed SSTs across the tropical belt (30°N to 30°S), following a Gaussian distribution used in the modified SST experiments.

4.4 Precipitation Response to SST in Targeted Parameter Experiments

The global PPE analysis showed that precipitation responses to SST warming are highly sensitive to model parameterization, with the greatest uncertainty concentrated across the tropical belt where convection and moisture convergence dominate the hydrological adjustment to surface forcing. This pattern aligns with the findings of the previous chapters, which identified South Asia as a region of large inter-model divergence in precipitation despite comparatively robust circulation responses. To investigate the origin of this spread, the analysis now shifts from the global PPE framework to a series of targeted experiments that test how parameter uncertainty influences precipitation sensitivity under a controlled tropical SST warming scenario. South Asia, located within the core of the tropical convection zone and characterized by strong land–ocean thermal contrasts, provides

an appropriate focus for assessing how variations in convective and surface-exchange parameters shape regional precipitation responses within the broader tropical context.

In the targeted set of experiments, we analyze monsoon precipitation changes across 14 simulations, each configured with different values for one of five key convective parameters—τ (tau), CAPE limit, Ke, c0_lnd, and c0_ocn—systematically varied within their allowable ranges (see section 4.2; Table 4.1). These experiments avoid regions of the parameter space known to produce extreme precipitation sensitivity, thereby excluding "dangerous zones" (Bernstein and Neelin 2016). Unlike the uniform SST warming applied in the PPE simulations, here we impose SST anomalies only over the tropical belt (30°S–30°N), consistent with many prior attribution studies, while ensuring an adequate signal-to-noise ratio. The imposed SST anomaly follows a Gaussian distribution with maxima near the equator (Figure 4.5).

Figure 4.6 illustrates the June–September SASM precipitation response for two extended multidecadal experiment pairs—CASE 1 and CASE 2—as well as for the broader ensemble of short simulations. In the default configuration (CASE 1), SST warming causes significant drying over key monsoon regions, including the Western Ghats and eastern India (Fig. 4.6a), with reductions of up to 5 mm day^{-1} (~30% of the climatological mean). In contrast, CASE 2—differing from CASE 1 by a single parameter change—shows no such substantial change in precipitation (Fig. 4.6b). Spatial disagreement across all parameter is shown in Figure 4.7, where hatched areas denote regions where more than one-third of simulations differ in sign. The spatial patterns of precipitation change vary substantially, underscoring the strong parameter sensitivity of the monsoon response.

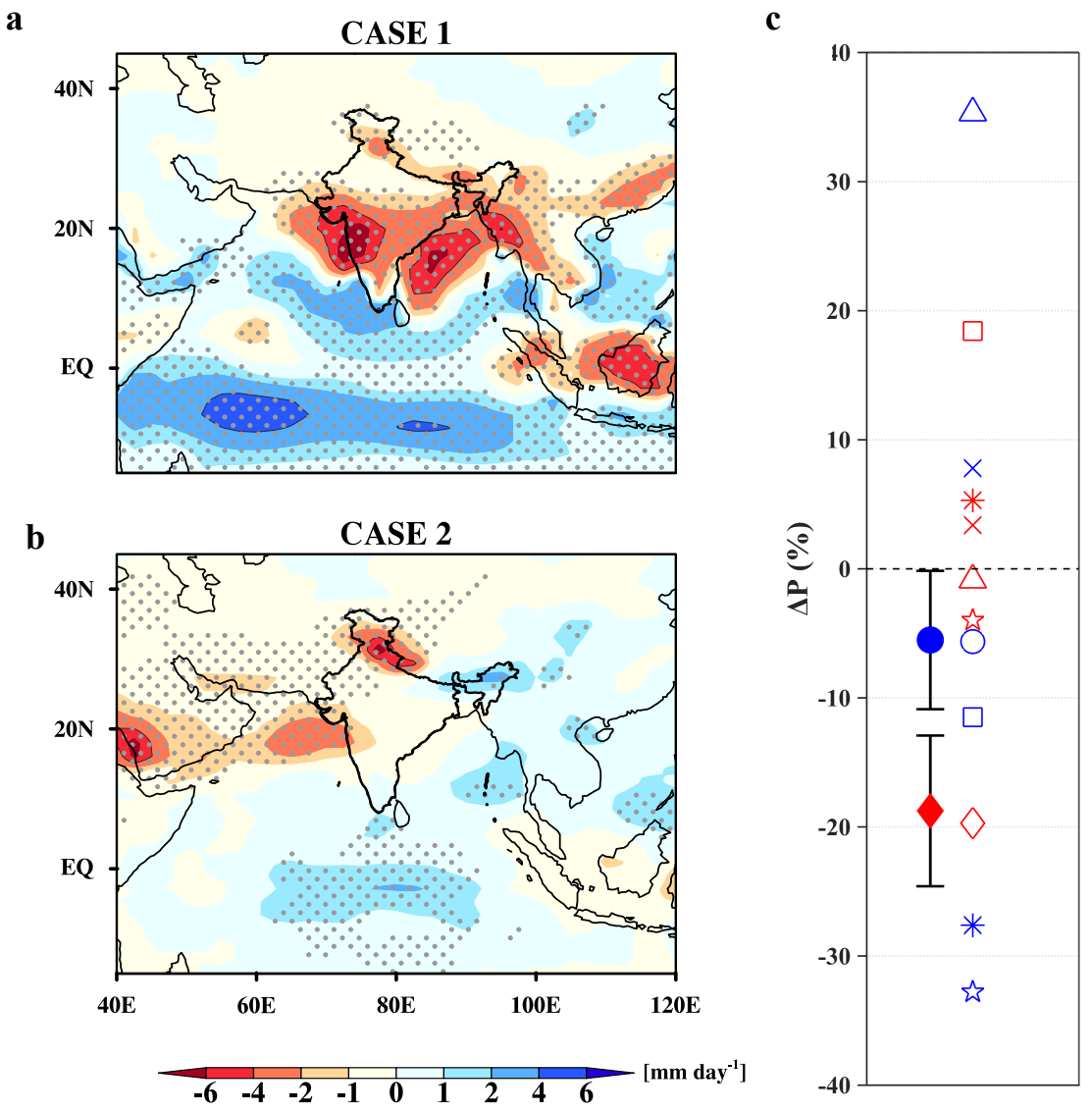


Figure 4.6 | Effect of warming sea surface temperatures on precipitation patterns in the targeted parameter experiment. (a, b) Changes in precipitation (warmed SST minus control) during JJAS over South Asia and nearby regions due to tropical SST warming (30°S–30°N) from two multi-model simulations: CASE 1 (a) and CASE 2 (b). Stippled areas are statistically significant at the 99% significance level (Student's t-test). (c) Area-averaged Percentage change in precipitation over India relative to the control mean precipitation from the experiments differing in parameters (see Table 4.1). Filled circle and diamond indicate the multi-decadal simulations. Error bars (±σ) represent internal variability.

Importantly, simulations run over a single season (e.g., CASE 3 and CASE 4) exhibit nearly identical precipitation responses to their multidecadal counterparts

(CASE 1 and CASE 2), indicating that parameter-driven uncertainty can be captured even in shorter simulations (Fig. 4.8). Area-averaged precipitation changes over India span a ±35% range relative to the control climate mean across the short simulations (Fig. 4.6c), with half the ensemble members projecting drying and the other half indicating wetter conditions in response to the same SST perturbation. These inter-case (CASE 1 vs. CASE2) differences exceed or match the magnitude of internal variability (estimated as ±1σ from multidecadal runs), highlighting that parameter sensitivity can dominate the precipitation response.

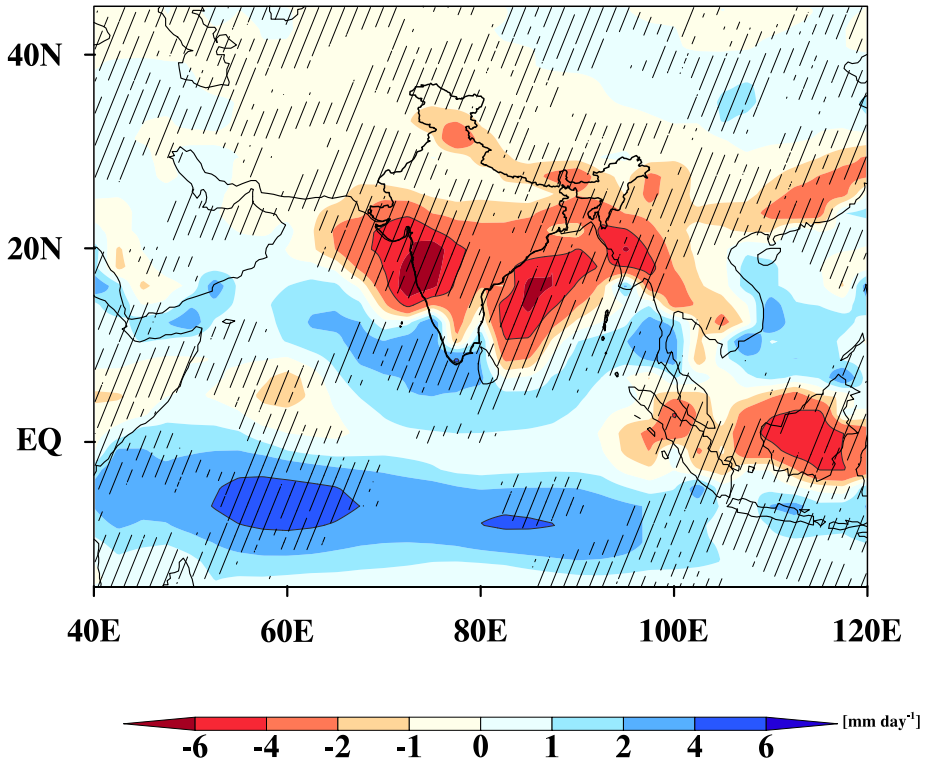


Figure 4.7 | Uncertainty in the effect of warming SSTs on precipitation patterns in the targeted parameter experiment. Changes in precipitation (warmed SST minus present day) during JJAS over South Asia and nearby regions due to tropical SST warming (30°S–30°N) from the default CESM CAM5 (CASE 1). Hatched areas indicate where more than one-third of the cases disagree on the direction of precipitation change (see Table 4.1 for details).

Similar levels of disagreement are observed in other parts of the extended South Asian domain, including the northern Indian Ocean, East Asia, and the Maritime Continent. These findings reveal that regional precipitation responses to SST warming, especially in vulnerable monsoon regions, are not robust across equally plausible model configurations.

4.5 Role of Internal Variability

The preceding analysis demonstrated that parameter uncertainty exerts a strong influence on regional precipitation responses to SST warming, particularly across South Asia and adjacent tropical zones. To evaluate whether these sensitivities are confined to regional scales or extend to the global hydrological response, we now examine the precipitation patterns from the two multidecadal targeted simulations (CASE 1 and CASE 2) in a global context (Figure 4.9). This step provides a direct link between the regional diagnostics of the targeted experiments and the broader ensemble behavior captured by the PPE, allowing us to test the consistency of parameter-driven uncertainty across spatial scales.

In doing so, it is also important to account for the role of internal variability, which arises from the intrinsic, chaotic fluctuations of the climate system even under identical external forcing. Unlike parameter uncertainty, which reflects differences in model formulation, internal variability represents the natural spread due to processes such as large-scale circulation variability and ocean–atmosphere interactions. By comparing the magnitude and spatial structure of precipitation differences between CASE 1 and CASE 2 against this background variability, we can assess whether the simulated changes exceed the range expected from internal variability alone, thereby isolating the contribution of parameter perturbations to global precipitation responses.

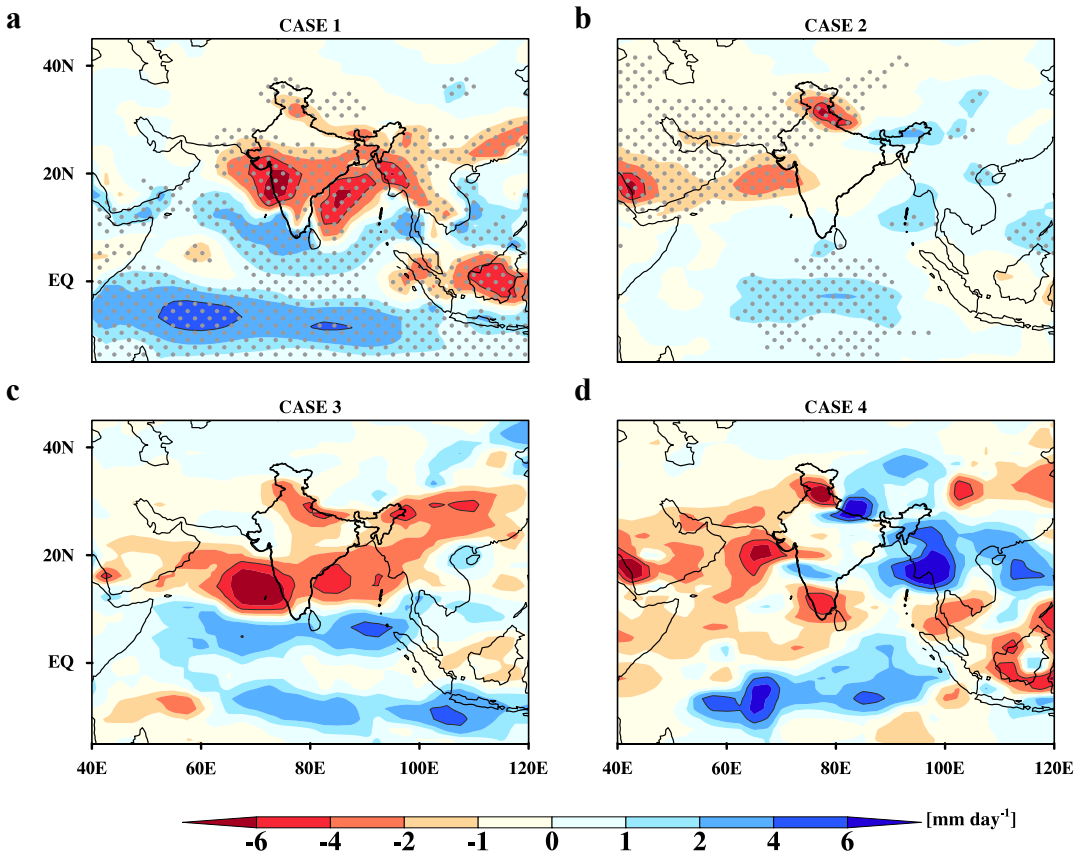


Figure 4.8 | Comparison of the impact of warming SSTs on JJAS precipitation in multidecadal and seasonal experiments. a–b Changes in precipitation (warmed SST minus present day) for CASE 1 and CASE 2 multidecadal runs. **c–d** Same as **a–b** for CASE 3 and CASE 4 seasonal runs. Stippling in **a–b** indicates changes significant at the 99% level.

We examine global precipitation responses from the two multidecadal simulations (Fig. 4.9). At first glance, the global response to SST warming appears robust in both experiments, as the precipitation anomalies are statistically significant over large areas. However, this apparent robustness is deceptive. When the spatial structure of change is compared between CASE 1 and CASE 2, substantial disagreement emerges in the sign of the response across many regions. During both boreal summer and winter, most of the areas showing negative anomalies—particularly in the tropical and subtropical belts—also exhibit the strongest parameter sensitivity, while the wet regions show comparatively stable, positive

responses. This pattern closely mirrors the results from the PPE despite differences in experimental design, indicating that the imprint of parameter uncertainty on precipitation extends beyond regional domains and persists even under globally coherent SST forcing. The persistence of these differences under distinct boundary conditions—tropical-only versus globally uniform SST anomalies—further confirms that such sensitivities are intrinsic to the model physics rather than an artifact of experimental configuration.

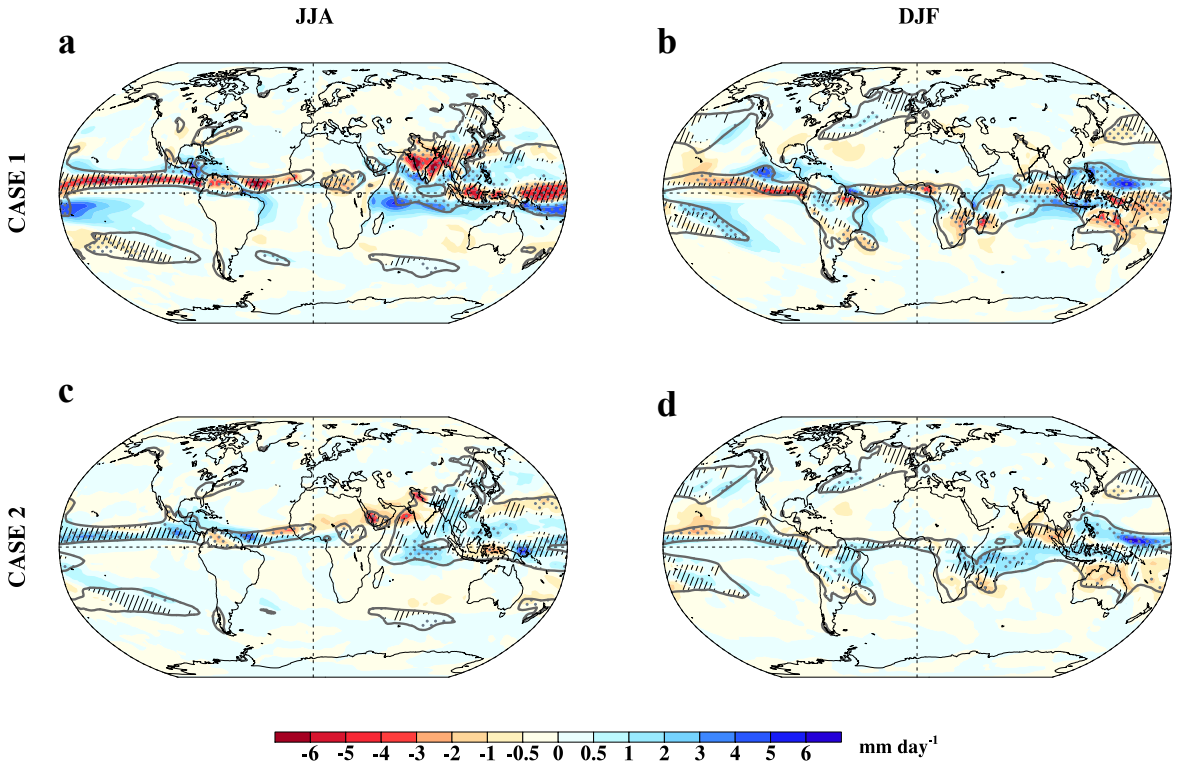


Figure 4.9 | Effect of warming SSTs on precipitation patterns across the global in the targeted parameter experiment. a, b Changes in precipitation (warmed SST minus present day) for boreal **a** summer (June-July-August) and **b** winter (December-January-February) due to changes in SST in the default multidecadal case (CASE 1). **c, d** Same as **a, b**, except for CASE 2. Stippling shows areas where changes are significant at the 99% significance level. Hatched areas indicate where there are disagreements on the sign of change in precipitation between the two cases, only regions with high average precipitation (over 4 mm day^{-1}, outlined in gray) are considered for disagreement.

We also evaluate the role of internal variability relative to parameter sensitivity using the same multidecadal simulations. For India, precipitation responses differ substantially between CASE 1 and CASE 2, with their difference exceeding the envelope of internal variability (Fig. 4.10a). A similar pattern emerges in tropical dry zones (Fig. 4.10b), while wet regions show more robust and consistent changes. Zonal mean responses reveal the greatest divergence in the deep tropics, with opposing signs and amplitudes differing by ~1.5 mm day^{-1} (Fig. 4.10c, d). At higher latitudes, by contrast, internal variability tends to match or exceed inter-model differences.

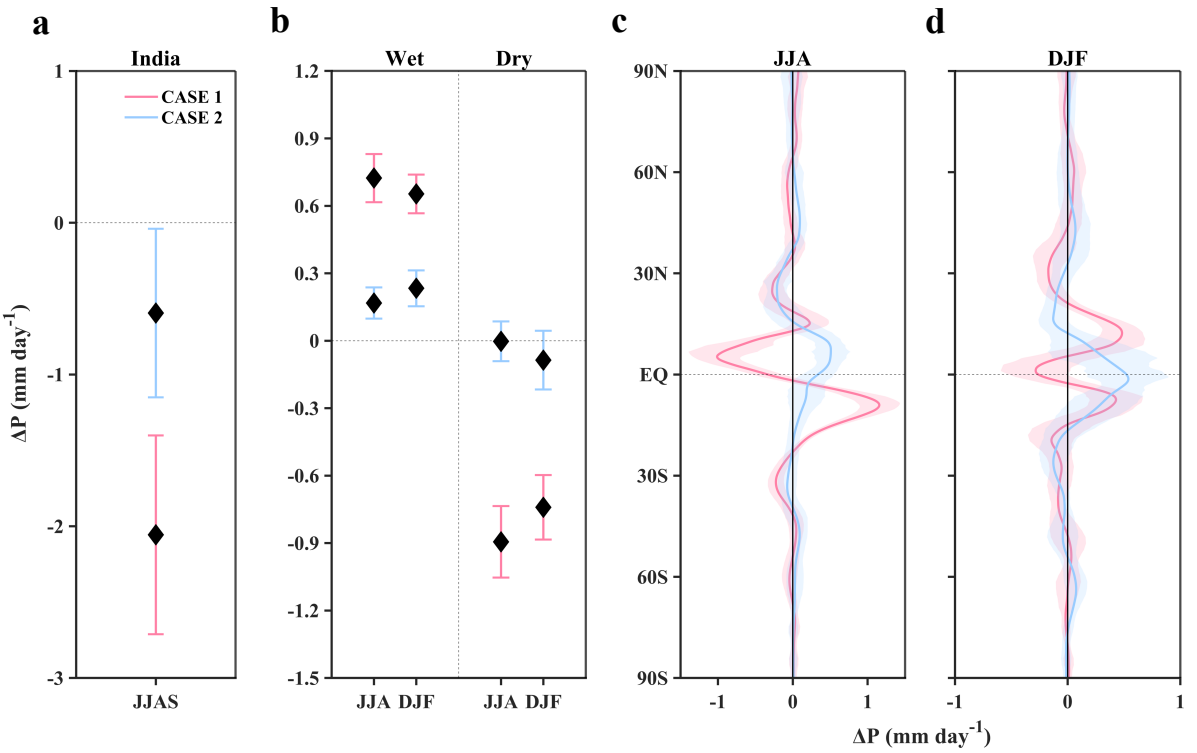


Figure 4.10 | Effect of warming SSTs on average and zonal precipitation in the targeted parameter experiment. a, b Changes in precipitation (warmed SST minus present day) over **a** India, **b** wet and dry regions of tropics from the two multidecadal cases of simulation (CASE 1 and CASE 2) during boreal summer and winter. **c,d,** The zonal mean precipitation changes from the two cases. The error bar ($\pm\sigma/2$) in **a,b** represents the range of internal variability. The latitudinal mean changes in precipitation is shown as the solid line in **c,d** and the spread represents the range of internal variability at each latitude.

These results reaffirm the conclusions from the PPE analyses: regional precipitation changes, especially drying responses in the tropics, remain highly uncertain due to their dependence on poorly constrained model parameters. This uncertainty often surpasses internal variability and can rival the magnitude of the forced signal itself.

4.6 Drivers of Regional Precipitation Uncertainty

The results so far indicate that parameter uncertainty exerts a strong influence on regional precipitation responses to warming, particularly across regions that exhibit drying. Yet the physical origin of this sensitivity remains uncertain. It is not clear how variations in parameterization schemes alter the convective response to SST forcing, or whether feedbacks within the convection–circulation system contribute to amplifying these differences. To investigate this question, we examine how changes in model parameters affect the vertical distribution of heating and circulation, which together govern the atmospheric energy balance and shape the simulated precipitation response.

Perturbations to model parameters lead to substantial differences in mid-tropospheric heating near 500 hPa, even under identical SST forcing (Figure 4.11). This level captures the core of convective heating, where latent energy release from condensation dominates the vertical energy redistribution in the tropical atmosphere. Differences here therefore serve as a direct indicator of how parameter settings alter the intensity and vertical extent of convection.

Across the ensemble, the magnitude and sign of these anomalies vary widely. In the Northern Hemisphere tropics, heating differences range from about –0.2 to 0.2 K day^{-1}, or roughly 16% of the control climatology. Over the Indian region during boreal summer, the spread is far larger, from –2 to 1.5 K day^{-1}—nearly 65% of the

control mean—reflecting the strong sensitivity of convective intensity to parameter perturbations in this region. Comparable variability is found in other drying-prone parts of the tropics, while the deep convective cores, such as over the central Pacific and western equatorial Indian Ocean, display more coherent positive heating anomalies and smaller spread.

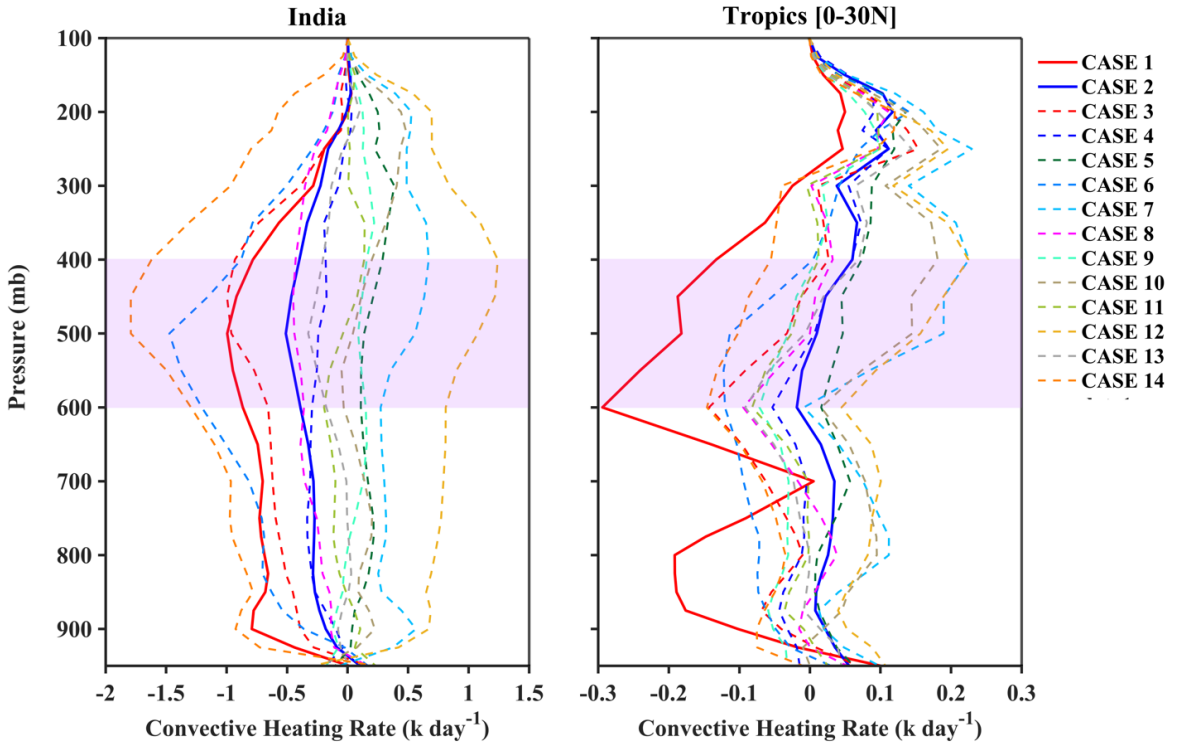


Figure 4.11 | Effect of warming SSTs on convective heating in the targeted parameter experiment. Changes in convective heating (warmed SST minus present day) over India and NH tropics (0-30°N) during boreal summer due to changes in SST in different cases of model simulation (see Table 4.1 for simulation details).

Although the tropical free troposphere is often assumed to be horizontally uniform in temperature, our results show that parameter-driven variability in convective heating can produce substantial local departures. These local temperature anomalies feed back onto circulation patterns, reinforcing or suppressing vertical motion and precipitation depending on their location. As

tropical precipitation is often more sensitive to low-level moisture convergence and large-scale pressure gradients than to local SST maxima, buoyancy-driven ascent remains tightly linked to the spatial structure of latent heating (Lindzen and Nigam 1987). Where this heating aligns with ascending branches of major circulations, such as the Hadley or Walker cells or monsoon systems, it reinforces updrafts and yields more coherent precipitation signals. In contrast, at the margins of these convective zones and/or nearby secondary convective zones, where many drying signals emerge, precipitation becomes more susceptible to perturbations introduced by parameter variability. Although latent heating occurs in both wet and drying regions, its dynamical anchoring differs: in convective core regions, precipitation is sustained by strong large-scale ascent and positive feedbacks, making it relatively insensitive to modest changes in parameter settings. In contrast, in drying zones, where vertical motion is more weakly forced and closer to convective thresholds, even small perturbations to parameterized heating can shift the balance between ascent and descent, flipping the sign of the precipitation response. As a result, parameter uncertainty plays a disproportionate role in shaping precipitation changes in these regions.

These results underscore that latent heating serves as a critical pathway through which model parameters influence regional precipitation. While not all parameters in the PPE directly affect convection, many exert indirect control by influencing cloud processes, microphysics, or turbulence, all of which ultimately impact the structure of convective heating. Thus, parameter sensitivity, via its influence on latent heating, emerges as a key source of uncertainty in regional precipitation response, especially in the tropical drying zones identified earlier. Importantly, this sensitivity is much less pronounced in extratropical regions, where precipitation is governed more by synoptic-scale dynamics than by convective feedbacks.

4.7 Limits to Confidence in Future Precipitation Projections

The spread in precipitation responses diagnosed here offers a physical explanation for the uncertainty that persists across coupled climate models. While large-scale circulation responses remain relatively robust, projected precipitation continues to vary widely, particularly over South Asia. The perturbed-parameter experiments show that a comparable range of variability can arise within a single model when convective and cloud-process parameters are modified, suggesting that much of the inter-model spread in CMIP projections may originate from parameterization differences rather than distinct large-scale dynamics.

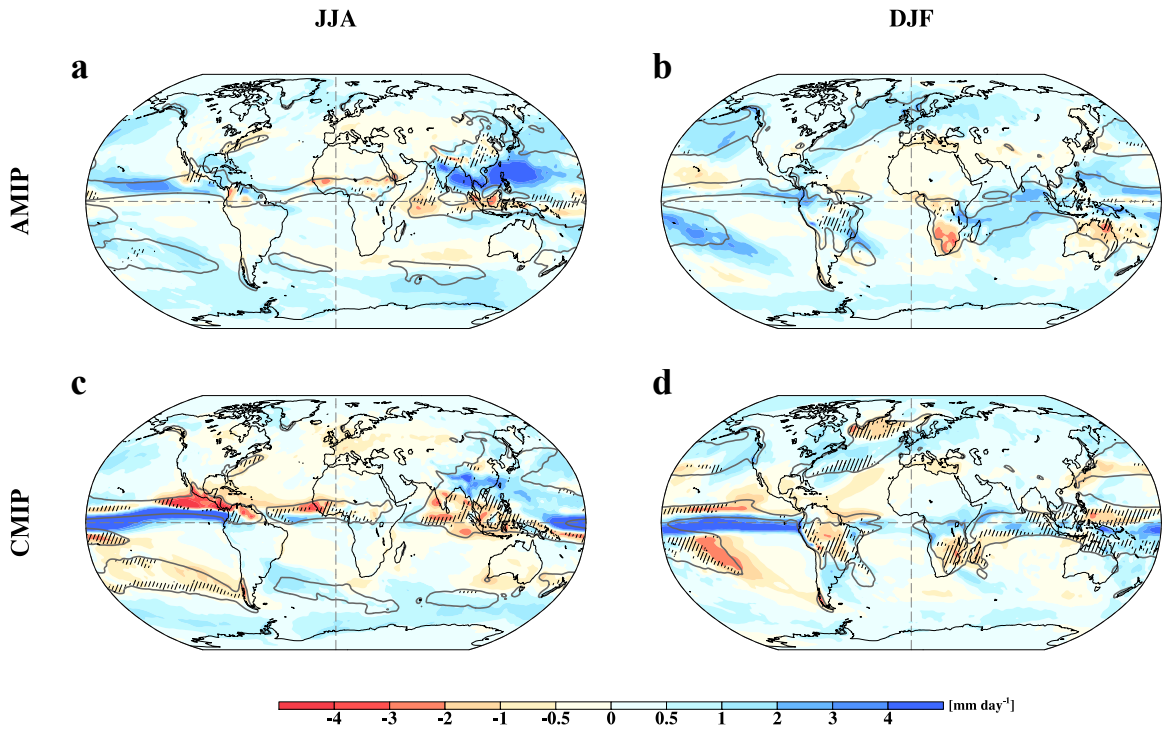


Figure 4.12 | Uncertainty in precipitation response from AMIP and future projections from CMIP6. a, b Change in precipitation (warmed SST minus historical) from NCAR CESM2-AMIP simulations during boreal summer **a** and winter **b** due to an imposed uniform 4K SST increase. **c, d** Projected precipitation changes by the end of the 21st century (2065–2099) compared to historical (1980–2014) from NCAR CESM2 coupled model for boreal summer **c** and winter **d**. Hatched areas indicate where more than one-third of the models disagree on the direction of change. Only regions with high average precipitation (over 4 mm day^{-1}, outlined in gray) are considered for model disagreement.

Uncertainty in precipitation projections remains a major constraint on regional climate assessment, especially for regions such as South Asia where hydrological changes directly affect societal risk (Mishra et al. 2023). Comparisons between single-model perturbed-physics ensembles (SMEs) and multi-model ensembles (MMEs), including CMIP, indicate that SMEs can reproduce a similar spread for key variables such as precipitation, providing an effective framework for identifying and constraining physical sources of projection uncertainty (Collins et al. 2011). This comparison also provides insight into the relative roles of parametric uncertainty, arising from parameter choices within a model, and structural uncertainty, arising from differences across models, in shaping precipitation projections.

To evaluate this connection, precipitation responses from the CESM perturbed-physics ensemble are compared with those from CMIP6 atmosphere-only (AMIP) and coupled simulations. The AMIP experiments isolate atmospheric behavior under prescribed SSTs, whereas the coupled integrations include interactive ocean feedbacks. Together, they enable assessment of whether parameter-driven uncertainty within a single model parallels the diversity observed across structurally distinct modeling systems. We first compare precipitation responses from the PPE with those from CMIP6 AMIP simulations, both of which represent atmospheric-only model experiments (Fig. 4.2c, d vs. Fig. 4.12a, b). In both ensembles, regions at the margins of deep convection, particularly tropical dry zones and adjacent areas, exhibit the greatest uncertainty, as indicated by the hatched regions. In contrast, core convective regions show robust and consistent responses across ensemble members.

We further examine end-of-century precipitation changes (2065–2099 relative to 1980–2014) from 40 CMIP6 models under a high-emissions scenario (SSP5-8.5; Fig. 4.12c, d). These projections similarly reveal large inter-model spread over the same

sensitive tropical regions identified in both the PPE and AMIP simulations. Across spatial scales, the ensemble spread is consistently greater in dry regions (Fig. 4.13), reinforcing our earlier findings that parameter-induced uncertainty dominates in areas where convective responses are poorly constrained.

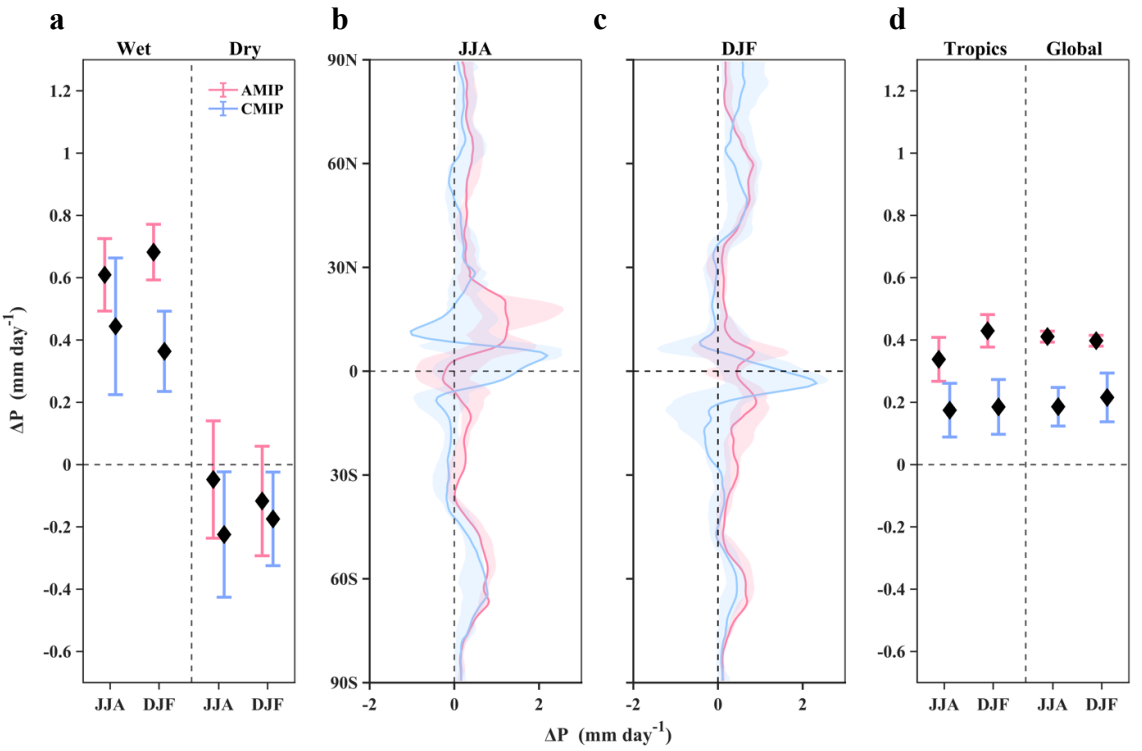


Figure 4.13 | Effect of SSTs warming on precipitation in the AMIP and end of the century projections from CMIP6 simulations. a-d The changes in area-averaged precipitation (warmed SST minus historical) in AMIP due to uniform SST warming by 4K and projected changes by the end of the 21st century (2065–2099) compared to historical (1980–2014) in CMIP6 for: **a** tropical wet and dry regions, **b** zonal average precipitation during boreal summer, and **c** zonal average precipitation during boreal winter, and **d** for tropical (30°S–30°N) and global averages. The error bar (±σ) **a** and **d** represents the inter-model differences in the precipitation changes. The solid line and the spread in (b, c) represents the latitudinal mean change in multimodel precipitation for the AMIP (pink)/CMIP (blue) and the range of inter-model differences at each latitude, respectively.

These results indicate that a substantial fraction of the inter-model spread in CMIP precipitation projections can be attributed to parametric uncertainty within models, while structural differences may further modulate and amplify this spread. They

also reinforce that parameter uncertainty is a major contributor to the spread in precipitation projections across the tropical drying regions identified earlier. This underscores the critical need to reduce such uncertainties, in order to improve the reliability of regional climate projections. Ultimately, enhancing confidence in future precipitation projections depends on a deeper understanding and tighter constraints of the physical parameterizations that control convective and related processes within climate models.

4.8 Summary, Limitations, and Directions for Future Research

Building on the earlier chapters, which showed that large-scale circulation and wind responses to external forcing are relatively robust but that precipitation projections remain highly inconsistent, this chapter set out to identify the origins of that uncertainty. The analysis demonstrates that regional precipitation responses to surface warming, particularly within the tropics, are acutely sensitive to model parameterization. The largest discrepancies arise in the so-called "dry zones" at the margins of deep convection, where small perturbations in convective or surface-exchange parameters can substantially alter both the magnitude and the sign of simulated change. While large-scale precipitation patterns are constrained by energetic and thermodynamic balances, regional outcomes depend critically on how convection, cloud feedbacks, and circulation adjustments are represented through parameter choices.

These findings underscore a structural vulnerability in climate modeling: while efforts to improve spatial resolution and emissions scenarios have advanced, uncertainties in physical parameterizations—particularly those governing convection and associated feedbacks—remain poorly constrained. The sensitivity of

regional precipitation to small parameter perturbations under identical boundary conditions demonstrates that model spread arises from both structural differences across models and parameter choices within them. The fact that a substantial fraction of this spread can be reproduced within a single model highlights parametric uncertainty as a major contributor to inter-model differences, underscoring the limitations of relying solely on multi-model ensembles to assess projection confidence and reinforcing the need to explicitly separate and constrain these sources of uncertainty. This helps explain the persistent inconsistencies, and at times apparent contradictions, in precipitation projections across successive IPCC assessments, particularly for regions in the Global South (Mishra et al. 2023).

This sensitivity presents a significant challenge not only for reliable future projections but also for the detection and attribution of observed precipitation changes, particularly in vulnerable tropical regions located at the margins of deep convection, where drying trends are projected but remain highly uncertain (Mishra et al. 2023). These include areas in South Asia, the Maritime Continent, Africa, and South America, where even modest precipitation shifts can have outsized societal and ecological consequences. Caution is therefore warranted when interpreting model-based regional precipitation changes, and attribution frameworks must explicitly consider parameter uncertainties.

Importantly, the findings also offer a degree of optimism: despite substantial regional uncertainties, precipitation responses averaged over tropical and global scales remain robust across ensemble members and model versions. This suggests that while regional-scale projections require better constraints, large-scale hydrological cycle changes are more consistently simulated and perhaps better constrained by physical principles (Held and Soden 2006). This suggests that physically based emergent constraints (Ferguglia et al. 2023), particularly those

linking large-scale circulation and convection, may offer a promising pathway to improve the reliability of regional precipitation projections.

Here, only the role of uniform SST warming on precipitation has been considered for evaluating the sensitivity of tropical precipitation, but the precipitation over tropical oceans are strongly modulated by the SST-pattern effect as well (Zhang et al. 2023). However, over land, precipitation has been reported to be more influenced by the uniform SST warming and direct CO2 forcings than the SST pattern effect (Bernstein and Neelin 2016; Zhang et al. 2023). Although we did not analyze the future SST pattern effect on the tropical precipitation, it is important to consider all these aspects to clearly decipher the mechanisms of future precipitation change (Chou et al. 2009) and hence to understand the role of parameter uncertainty under such added complexities. Moreover, in the present study the parameter uncertainty in SST's impact on precipitation has been explored in atmosphere-only (AMIP class) model simulations due to heavy computational requirement to carry out couple simulations with perturbed parameters (Dunbar et al. 2021; Rowell 2012). Generally, such atmosphere-only ensemble simulations are informative about the uncertainties in couple model under different parameter combinations (Rowell 2012), exploration of model uncertainties using couple model simulations are desirable with the advent of the higher computational powers and techniques (Keil et al. 2021; Mishra 2012). The sensitivity of tropical precipitation may be anticipated to increase due to further increase in uncertainties arising from coupled feedback (He et al. 2018; Rowell 2012; Xie et al. 2015) in a couple model framework. Furthermore, with the recent availability of large LE simulations from multiple models (Deser et al. 2020; Lehner et al. 2020; Maher et al. 2021), the relative role of internal variability and the parameter uncertainty at regional scale should be investigated to understand the total uncertainty in precipitation simulation.

Given that the present-day modeling architecture extensively rely on parameterizations, involvement of numerous tunable parameters with different degree of approximations in tunning them while modeling the tropical precipitation is a challenge that cannot be done away with immediately. To address these challenges, we advocate integrating emerging artificial intelligence and machine learning techniques to more systematically tune and constrain parameterizations in climate models, especially in regions with poor model fidelity (Schneider et al. 2024). Additionally, advancing kilometer-scale convection-permitting modeling can reduce reliance on parameterized convection and thereby minimize parameter-induced uncertainties, offering a promising path forward for improving the fidelity and credibility of tropical precipitation projections (Palmer 2011). However, implementing this approach is currently a challenge considering the enormous resources it demands.

The uncertainty arising from loosely constrained model parameters remains a critical yet often underappreciated limitation on confidence in regional precipitation attribution and projection under climate warming. Reducing this uncertainty is essential for producing credible and actionable climate information, particularly for tropical regions where societal vulnerability is high and precipitation change exerts a disproportionate influence on risk. Advancing this objective will require tighter physical constraints on model parameterizations, improved representation of convective processes, and a systematic integration of ensemble-based diagnostics across modeling frameworks. These steps are vital for strengthening the reliability of regional climate projections and for translating scientific understanding into more effective adaptation and resilience strategies.

Chapter 5: Summary and Future Scope

Chapter 5

Summary and Future Scope

5.1 Overview

The regional climate of South Asia represents one of the most intricate expressions of atmosphere–land–ocean coupling anywhere on Earth. It governs vital hydroclimatic processes that sustain water resources, ecosystems, and livelihoods for more than a billion people. At the same time, it is a region where multiple anthropogenic forcings—GHG, aerosol emissions, and LULC changes—intersect to produce complex and sometimes competing influences on winds, precipitation, and temperature. Understanding how these forcings collectively shape the regional circulation and hydrological cycle is crucial for climate informed planning. Yet despite major advances in modeling and observation, large uncertainties persist in simulating historical trends and projecting future changes, particularly in reconciling model responses with observed changes.

This thesis was conceived to address the persistent challenge of understanding how external forcings have reshaped, and are likely to continue reshaping, winds and precipitation over South Asia, and to evaluate the extent to which current models can credibly represent these changes. Winds emerge from the

model's resolved dynamics, where the momentum equations are explicitly solved, and therefore provide smoother and physically consistent information about large-scale adjustments with comparatively high confidence. Precipitation, by contrast, is implicitly simulated through parameterization of sub-grid scale processes such as convection, cloud microphysics, and land–atmosphere interactions. Because it depends on how these processes are represented, it is more sporadic, more sensitive to model formulation (Mishra, 2009). Parametrization remains a major source of systematic error, with regional biases over South Asia reaching up to 100% in current generation climate models (Jain et al. 2019, Anand et al. 2018). By integrating observational evidence with coordinated modelling frameworks—including large ensembles, single-forcing experiments, and perturbed-parameter simulations—the thesis develops a coherent physical interpretation of externally forced change and the uncertainties that accompany it. Through this combination of empirical grounding and controlled experimentation, the work clarifies the drivers of historical wind changes, assesses how evolving forcings are likely to influence future climate, and explains why precipitation remains the aspect of the regional climate system for which model divergence is greatest, even when dynamical responses are comparatively robust.

The importance of this investigation extends well beyond regional analysis. The patterns identified over South Asia exemplify broader questions confronting climate science: how local and remote forcings interact to shape regional outcomes, how uncertainty propagates from process representation to projection, and how physically interpretable signals can be distinguished from statistical noise. By focusing on winds and precipitation as coupled indicators of the energy–water cycle, the thesis advances understanding of the pathways through which anthropogenic influence is expressed in regional climates.

The thesis integrates multiple lines of evidence to establish a coherent narrative linking external forcings, atmospheric adjustment, and hydrological change. In doing so, it contributes not only to regional climate diagnosis but also to the wider effort to build reliable, informed projections of climate change. The results underscore that credible regional projections arise not only from increasing model complexity alone, but from improving physical understanding and clarifying uncertainty—goals that remain at the heart of both scientific inquiry and societal adaptation.

5.2 Synthesis of Key Findings

The evidence presented throughout this thesis shows that South Asia's winds have undergone externally forced changes in the past and are likely to continue changing in the coming decades, with these changes being more reliably attributed despite uncertainties from scenarios and socio-economic factors. In contrast, precipitation changes cannot be identified, attributed, or projected with similar confidence because they depend heavily on parameterized processes and are therefore strongly limited by the way current climate models represent convection and related physics.

The most coherent feature emerging across multiple reanalyses is a persistent weakening of the lower-tropospheric westerlies over the continental region since the late twentieth century. This weakening extends vertically through the mid-troposphere and is strongest between 20° and 30° N, arising due to weakening of STWs that originates in west Asia. The weakening of continental winds occurs independently of changes in the oceanic and cross-equatorial branches. The Somali Jet shows only local strengthening but with no discernible shift in its location, while the STWs weaken due to regional thermodynamic and radiative imbalances. The LE model analyses reproduce the large-scale weakening of winds and associated

pressure and temperature patterns, lending confidence that the observed circulation trend is an externally forced signal. Attribution with single-forcing ensembles revealed that surface cooling and increased atmospheric stability over northern India, induced by aerosol dimming and widespread irrigation, have reduced the pressure contrast with the adjacent Arabian Peninsula, where GHG-driven warming has deepened the pressure low. The resulting flattening of the zonal pressure gradient explains the observed westward deflection and slowdown of the STWs.

Precipitation changes exhibit a spatially heterogeneous pattern consistent with these circulation adjustments. Observations reveal a century-long decline in precipitation over the IGP and east-central India, contrasted by increasing precipitation in north-western and peninsular regions during recent decades. The weakening of STWs contributed to this redistribution of monsoon precipitation, with drying in the core monsoon zone and enhanced precipitation over climatologically semi-arid northwestern regions. However, the models fail to replicate the observed spatial heterogeneity of precipitation changes. The discrepancy arises primarily from the parameterized treatment of convection, microphysics, and aerosol–cloud interactions. Thus, while the circulation response to anthropogenic forcing appears robust and physically interpretable, the hydrological response remains uncertain and model-dependent bearing critical implications for attribution and projection.

Future projections indicate a shift in the forcing regime that not only impacts the winds alone, but also affects South Asia's future wind-energy potential. As aerosol emissions in the region decline, their earlier cooling effect weakens and no longer masks the GHG-driven warming. Consequently, GHGs and LULC changes emerge as the main drivers of circulation, strengthening near-surface winds across large parts of South Asia through changes in pressure gradients and surface fluxes associated with expanding irrigated croplands. This strengthening increases the

physical wind-energy potential in regions that are already rich in wind resources and extends it to new potential areas. However, the realizable wind-energy potential remains tightly constrained by uncertainties linked to the crude representation of irrigation in current models and by urbanization, competing land use, and rising electricity demand. These factors together underscore that the future contribution of wind energy will depend not only on the physical climate response but also on how land and energy systems evolve.

For precipitation, global-scale increases of ~2–3% per °C of warming emerged consistently, but South Asia's regional projections remained highly uncertain. While CMIP6 suggested modest increases in SASM precipitation, single-model ensembles diverged: CESM2-LE produced muted or even negative trends in some areas, while MPI-ESM-GE indicated more spatially consistent increases. The inter-model spread in precipitation projections was nearly as large as the mean change, reflecting the dominance of structural model uncertainty over internal variability.

Diagnosing the sources of uncertainty further clarified why precipitation projections substantially differ across models and remain difficult to constrain. Comparative analyses across perturbed-parameter, atmosphere-only, and coupled modeling frameworks show that much of the inter-model spread in tropical and South Asian precipitation originates from parameterization choices, particularly those governing convection, cloud processes, and land–atmosphere exchanges. The spatial coherence and magnitude of this spread indicate that even small variations in parameter values can substantially alter regional outcomes, including the sign of change in areas near the margins of deep convection and areas of secondary convection. This parameter-driven uncertainty is distinct from internal variability and reflects a structural limitation of current climate models: while energetic and thermodynamic constraints yield coherent large-scale responses, regional hydrological outcomes remain highly sensitive to model parametrization choices.

The implications extend beyond South Asia. Similar sensitivities are evident across other tropical regions—including the Maritime Continent, Africa, and South America—where drying response to warming are simulated but remain uncertain due to the same limitations in convective representation. These findings explain the limited consensus in precipitation projections across successive model generations (Mishra et al. 2023).

Overall, the findings emphasize a key contrast: winds show relatively more robust responses, with consistent physical drivers that can be attributed and projected, whereas precipitation projections remain fragile, plagued by parameterization uncertainties and divergent model physics.

5.3 Scientific Contributions and Methodological Advances

The thesis establishes several advances that extend beyond the chapter-wise results and together contribute to understanding how regional climate change over South Asia is interpreted and assessed. It introduces a broader perspective on circulation by demonstrating that continental wind changes cannot be explained solely through the conventional meridional gradient framework. The analyses underscore the role of east–west thermal contrasts as an additional axis of control on winds, providing a more complete basis for understanding externally forced circulation change. Methodologically, the work represents the first systematic application of large-ensemble and single-forcing large-ensemble experiments for South Asia—an emerging class of simulations that only recently became feasible owing to advances in computational resources (Simpson et al. 2025). Earlier studies were typically limited to a handful of ensemble members, but the use of large ensembles here enables robust separation of externally forced responses from internal variability and quantification of individual forcing influences with greater confidence.

The results also challenge the widely accepted notion of a northward shift in the low-level jet that is often invoked to explain recent monsoon precipitation changes. The analyses reveal no robust evidence of such a displacement and, when extended over longer periods, suggest a weak southward tendency. This calls for caution in attributing precipitation changes solely to jet migration, as the weakening of the STWs emerges as an additional and traceable influence on regional hydroclimate.

In parallel, PPE experiments show that uncertainties in model physics, arising from the parameterization of sub-grid-scale processes, account for much of the spread in simulated precipitation changes over South Asia and, more broadly, across many vulnerable regions of the Global South. These results have two major implications. First, they call for caution in interpreting attribution studies that rely on small-ensemble SST perturbation experiments, as many such model-derived hypotheses provided over the years may conflate the apparent effects of external forcing with differences in parameterization schemes. Second, they provide a physical explanation for the persistent inconsistency of precipitation projections across successive generations of climate models (Mishra et al. 2023). Together, these insights are critical for advancing model development and for generating actionable climate information for regions where the risks associated with precipitation uncertainty are greatest.

Finally, by linking regional forcings such as aerosols, irrigation, and land-use change to variations in wind resources and renewable-energy potential, the thesis establishes that policies aimed at aerosol mitigation and land management across South Asia will have direct consequences for the region's sustainable energy trajectory. This finding is particularly novel in demonstrating that, alongside the well-recognized influence of GHGs, regional forcings play an equally critical role in

shaping realizable wind energy potential and therefore must be explicitly considered in both climate and development planning.

Together, these advances refine the physical understanding of South Asia's circulation, improve the methodological foundation for attribution, and highlight the intersection of scientific and societal priorities in regional climate research.

5.4 Limitations of the Thesis

Although this thesis integrates multiple modelling frameworks and observational analyses to provide a coherent assessment of changes in South Asian winds and precipitation, its scope remains bounded by several methodological and conceptual constraints. These limitations do not undermine the integrity of the findings but delineate the extent to which the conclusions can be generalized or extended beyond the specific tools and methodologies employed here.

A primary limitation arises from the continued inadequacy of current global models to represent regional precipitation with sufficient spatial fidelity. This constraint inherently restricted the thesis from undertaking a fully attribution-based analysis of precipitation similar to that achieved for winds. The assessment therefore concentrated on diagnosing the origins of model disagreement rather than assessing the externally forced change. Until models can reliably reproduce observed regional changes, the potential for deterministic attribution of precipitation trends remains limited despite advent of LE simulations. This challenge, while common across contemporary climate research, forms the most fundamental boundary on what the present work could accomplish.

A second limitation concerns the representation of land-surface processes, particularly irrigation and land-use change, which were shown to exert a strong influence on regional climate response. Within the employed modelling framework,

these processes are formulated through simplified parameterizations that prescribe surface flux adjustments without resolving their temporal or hydrological dynamics. Consequently, while the thesis established the importance of land-surface forcing, it could not quantify its magnitude or distinguish the direct effect of irrigation from that of other anthropogenic drivers. The incomplete realism of these schemes remains a source of interpretive uncertainty that can only be resolved through models capable of explicit human-land feedback representation.

The extension of climatic findings to wind-energy potential was similarly bounded by disciplinary scope. The assessment was restricted to physical feasibility, without integrating economic, infrastructural, or policy constraints that shape real-world deployment. This framing ensured analytical focus on the climatic drivers themselves, but it limits the direct applicability of the results to energy-system planning. Linking the physical projections with techno-economic evaluations would require a separate, integrated modelling framework beyond the objectives of the present study.

Another limitation stems from the reliance on atmosphere-only experiments in both the attribution and uncertainty analyses. By prescribing sea-surface temperatures, these configurations precluded the two-way feedbacks through which oceanic adjustments influence climate response. The absence of interactive coupling constrained the ability to assess how ocean-atmosphere coupling and evolving temperature gradients might modify regional responses. This omission, dictated by computational feasibility and the experimental design of available large ensembles, nonetheless represents a critical gap between diagnostic evaluation and fully coupled attribution.

The idealized experimental design of the PPE adds an additional boundary. The use of a globally uniform sea-surface-temperature perturbation was necessary to isolate thermodynamic sensitivities and parameter effects, yet it inevitably

excluded the spatially heterogeneous warming patterns that dominate real-world forcing. The resulting diagnostics therefore represent conceptual tendencies rather than realistic projections. This simplification, while deliberate, defines the limits of the inferences that can be drawn about the sensitivity of regional precipitation to future warming.

Finally, the diagnosis of parameter uncertainty was confined to a single-model family. The CESM based PPE provided an extensive exploration of internal parameter space but did not encompass structural differences across independent modelling systems. As such, the thesis could not disentangle how much of the total uncertainty arises from parameter choices versus fundamental model design. This limitation reflects both data availability and computational cost, but it also underscores the need for coordinated multi-model ensembles that can translate single-model insights into generalizable understanding.

These limitations define the methodological and conceptual boundaries within which the conclusions of this thesis should be interpreted. They point to the aspects of the regional climate system that remain incompletely represented: the precision of precipitation simulation, the realism of land-surface feedbacks, the role of coupled ocean processes, and the diversity of model structures. Recognizing these constraints clarifies both the strengths and the scope of the present work. The following section outlines how these limitations can direct future research and for extending the integrative approach established here.

5.5 Future Scope

The limitations outlined above define the boundaries of this thesis while also pointing toward the directions in which future research should advance. They highlight methodological and conceptual areas that must be strengthened to refine

understanding of regional climate processes over South Asia and to enhance the reliability of their projection and support more robust adaptation and mitigation strategies.

An immediate and highly feasible step is the coordinated use of multi-model large ensembles i.e. SMILEs. These ensembles, now available for several global models with tens to hundreds of members, offer a robust way to jointly evaluate internal variability, model diversity, and non-linear responses to external forcing (Simpson et al. 2025). They can be readily applied to South Asia with existing computational resources, and they provide a much clearer basis for separating forced signals from internal noise. Beyond precipitation, SMILEs are especially valuable for diagnosing biases and non-linear differences in simulated wind changes, which often remain obscured in conventional multi-model means. Expanding their use can therefore improve model reliability and enhance confidence in estimating forced circulation and hydrological signals in the near term.

Strengthening regional customization initiatives represents another practical avenue that can be implemented without requiring major computational investment (Mishra et al. 2023, Bhuyan et al. 2026). Countries in the Global South can immediately improve the usability of climate information by tailoring global models to local conditions, as illustrated by India's South Asia Regional Climate Information (SARCI) framework (Mishra et al. 2023). Outputs from such frameworks can be downscaled and bias-corrected through observationally guided post-processing tools to produce high-resolution inputs for sectoral assessments. Because this approach operates on existing modelling infrastructure, it can be rapidly expanded across the region. Alongside these developments, emerging applications of machine learning and AI-assisted parameter optimization offer additional short-term opportunities to refine uncertain parameterizations. Integrating machine learning with data assimilation and high-resolution observations can help narrow

uncertainties in sub-grid-scale processes and develop efficient emulators of convection and cloud dynamics, particularly when designed with regional modelling centres in the Global South.

An important direction for reducing uncertainty in regional precipitation projections lies in the development of physically based emergent constraints—statistical relationships that link observable aspects of the current climate to future model responses. Existing emergent constraints for precipitation have often lacked robustness across model generations, in part due to the absence of a clear physical foundation linking large-scale circulation and convective processes (Ferguglia et al. 2023; Simpson et al. 2021). The comparatively robust and consistently simulated large-scale circulation responses, contrasted with the strong sensitivity of regional precipitation to convective heating, point to a physically grounded pathway for constraining precipitation. In particular, the dynamical control of precipitation—mediated through interactions between convection and large-scale circulation—offers a key mechanism for constraining projections (Dagan and Stier 2020; Yang et al. 2022). Anchoring these pathways to observations remains challenging, as key variables such as convective heating are not directly observable; however, physically based proxies, such as circulation-derived constraints using wind observations and thermal wind relationships, provide a viable alternative (Allen and Sherwood 2008). By explicitly linking convection–circulation pathways within the broader monsoon-scale circulation framework, such emergent constraints provide a promising pathway for improving the reliability of regional precipitation projections.

A further priority, which sits at an intermediate time horizon, is to improve the representation of regionally dominant forcings such as aerosols, land-use change, and irrigation. Aerosol–radiation and aerosol–cloud interactions remain major contributors to uncertainty in projected climate responses, and rapidly changing emission trajectories under air-quality policies further complicate these projections

(Curry and Webster 2011; Hegerl and Zwiers 2011). Likewise, irrigation, vegetation change, and urban expansion are represented in climate models through simplified parameterizations that cannot capture the full extent of land–atmosphere feedbacks. Strengthening the physical representation of these forcings and coupling them with observation-based datasets of irrigation extent and evapotranspiration, would yield more context-specific and policy-relevant projections for South Asia. At the same time, advancing the experimental design of uncertainty analysis by moving beyond atmosphere-only configurations toward fully coupled ocean–atmosphere experiments would allow a more complete assessment of how sea-surface temperature gradients and ocean heat uptake shape circulation and precipitation. Moving from idealized, uniform surface-warming perturbations to spatially explicit, pattern-based forcing derived from coordinated projections would further improve the realism of modelled responses. Advancing from single-model PPEs to coordinated multi-model perturbation frameworks would further enable the separation of parametric and structural components of uncertainty (Bernstein and Neelin 2016; Gettelman et al. 2024).

In the longer term, substantial gains will depend on addressing the poor fidelity of models in simulating precipitation responses. Parameterized physics remains the dominant source of this uncertainty, since sub-grid processes such as convection and mesoscale circulations are only statistically represented. Kilometre-scale, or convection-permitting, modelling offers a major advance by explicitly resolving these processes and reducing dependence on empirical parameterizations, thereby improving the representation of precipitation and surface fluxes (Kendon et al. 2021; Slingo et al. 2022). Although already used for regional projections in some regions, such systems require considerable computational resources, making them a long-term goal for South Asia. Their eventual development would transform both regional climate diagnosis and sectoral applications.

Expanding the translation of climatic projections into societal applications also falls within this longer-term trajectory. The wind-energy assessment in this thesis demonstrated the feasibility of coupling climate information with renewable-resource evaluation but was limited to physical and some socio-economic constraints. Future studies should incorporate techno-economic and infrastructural considerations, combining climate signals with grid integration, storage, and cost-optimization models. High-resolution modelling will be particularly valuable for such applications, especially in regions with complex orography, where kilometre-scale simulations can provide finer detail for siting and operational planning. Parallel efforts could assess how projected wind and precipitation changes together shape agricultural productivity, water demand, and energy security, enabling integrated evaluations of regional resource resilience.

5.6 Concluding Remarks

This thesis demonstrate that the regional climate of South Asia is undergoing discernible changes shaped by the interplay of multiple anthropogenic and natural drivers. Through an integrated use of observations, reanalyses, and coordinated modelling experiments, the work has clarified key mechanisms governing recent and projected changes in atmospheric circulation and precipitation. The analyses have clarified several dimensions of this evolution while also exposing the limits of present modelling systems and the opportunities for progress that accompany them.

Beyond the scientific outcomes, the broader contribution of this thesis lies in establishing a physically consistent basis for interpreting regional climate change in a densely populated and climatically sensitive region. The results confirm that even when global forcing mechanisms are well understood, their regional manifestations depend critically on the interaction of aerosols, land-use change, and oceanic

feedbacks operating across multiple scales. The weakening of continental winds, the redistribution of precipitation, and the associated implications for renewable-energy potential together emphasize that regional climate change is not a uniform amplification of global trends but a reorganization of energy and moisture within the Earth system.

The rapid developments in kilometre-scale modelling, coupled large ensembles, and machine-learning-assisted parameter optimization mark a decisive shift in how climate processes can be represented. Together, they promise a generation of models that are not only more accurate but also more adaptable to regional contexts. Yet technological advances alone are insufficient. Sustained regional initiatives, such as India's SARCI framework (Bhuyan et al. 2025), illustrate the growing recognition that credible climate information must emerge from within the regions most affected. Strengthening such efforts across the Global South will be essential to ensure that model development, evaluation, and application remain grounded in local realities.

Beyond the scientific frontiers, this work also underscores a deeper imperative—to integrate climate understanding with societal foresight. The capacity to project wind and precipitation changes gains meaning only when linked to questions of water security, agriculture, energy, and human wellbeing. The challenge now is to transform enhanced simulation skill into actionable knowledge that informs sustainable development and equitable adaptation.

This requires strengthening the interface between climate science and decision-making through co-production of knowledge with stakeholders, including policymakers, resource managers, and local communities. Translating model outputs into risk-relevant metrics—such as changes in extreme rainfall, drought frequency, or wind-energy potential—can support sector-specific planning. Equally important is communicating uncertainty transparently, enabling informed choices

under risk rather than deterministic expectations. By embedding climate insights within planning frameworks and early warning systems, this work contributes to bridging the gap between predictive capability and real-world resilience.

In conclusion, the thesis affirms that the pathway toward credible and actionable climate information for South Asia lies in coupling scientific rigor with regional relevance. Continued investment in high-resolution modelling, interdisciplinary collaboration, and open data exchange will be essential for narrowing the gap between knowledge and application. The insights developed through this work provide a foundation on which future studies can build to advance both the science of regional climate and its practical contribution to societal resilience.

Bibliography

Adler, R. F., Huffman, G. J., Chang, A., Ferraro, R., Xie, P.-P., Janowiak, J., Rudolf, B., Schneider, U., Curtis, S., Bolvin, D., Gruber, A., Susskind, J., Arkin, P., & Nelkin, E. (2003). The Version-2 Global Precipitation Climatology Project (GPCP) Monthly Precipitation Analysis (1979–Present). *Journal of Hydrometeorology*, *4*(6), 1147–1167. https://doi.org/10.1175/1525-7541(2003)004%253C1147:TVGPCP%253E2.0.CO;2

Allen, M. R., & Ingram, W. J. (2002). Constraints on future changes in climate and the hydrologic cycle. *Nature*, *419*(6903), 224–232. https://doi.org/10.1038/nature01092

Allen, R. J., & Sherwood, S. C. (2008). Warming maximum in the tropical upper troposphere deduced from thermal winds. *Nature Geoscience*, *1*(6), 399–403. https://doi.org/10.1038/ngeo208

Almazroui, M., Saeed, S., Saeed, F., Islam, M. N., & Ismail, M. (2020). Projections of Precipitation and Temperature over the South Asian Countries in CMIP6. *Earth Systems and Environment*, *4*(2), 297–320. https://doi.org/10.1007/s41748-020-00157-7

Al-Yaari, A., Ducharne, A., Thiery, W., Cheruy, F., & Lawrence, D. (2022). The Role of Irrigation Expansion on Historical Climate Change: Insights From CMIP6. *Earth's Future*, *10*(11), e2022EF002859. https://doi.org/10.1029/2022EF002859

Anand, A., Mishra, S. K., Sahany, S., Bhowmick, M., Rawat, J. S., & Dash, S. K. (2018). Indian Summer Monsoon Simulations: Usefulness of Increasing Horizontal Resolution, Manual Tuning, and Semi-Automatic Tuning in Reducing Present-Day Model Biases. *Scientific Reports*, *8*(1), 3522. https://doi.org/10.1038/s41598-018-21865-1

Andrews, T., Andrews, M. B., Bodas-Salcedo, A., Jones, G. S., Kuhlbrodt, T., Manners, J., Menary, M. B., Ridley, J., Ringer, M. A., Sellar, A. A., Senior, C. A., & Tang, Y. (2019). Forcings, Feedbacks, and Climate Sensitivity in HadGEM3-GC3.1 and UKESM1. *Journal of Advances in Modeling Earth Systems*, *11*(12), 4377–4394. https://doi.org/10.1029/2019MS001866

Arakawa, A. (2004). The Cumulus Parameterization Problem: Past, Present, and Future. *Journal of Climate*, *17*(13), 2493–2525. https://doi.org/10.1175/1520-0442(2004)017%253C2493:RATCPP%253E2.0.CO;2

Arshad, A., Mirchi, A., He, C., Shah, A. A., & AghaKouchak, A. (2025). Anthropogenic and climatic drivers of the 2022 mega-flood in Pakistan. *Npj Natural Hazards*, *2*(1), 57. https://doi.org/10.1038/s44304-025-00109-z

Bechtle, P., Schelbergen, M., Schmehl, R., Zillmann, U., & Watson, S. (2019). Airborne wind energy resource analysis. *Renewable Energy*, *141*, 1103–1116. https://doi.org/10.1016/j.renene.2019.03.118

Bernstein, D. N., & Neelin, J. D. (2016). Identifying sensitive ranges in global warming precipitation change dependence on convective parameters. *Geophysical Research Letters*, *43*(11), 5841–5850. https://doi.org/10.1002/2016GL069022

Bichet, A., Wild, M., Folini, D., & Schär, C. (2012). Causes for decadal variations of wind speed over land: Sensitivity studies with a global climate model. *Geophysical Research Letters*, *39*(11), 2012GL051685. https://doi.org/10.1029/2012GL051685

Bollasina, M. A., Ming, Y., & Ramaswamy, V. (2011). Anthropogenic Aerosols and the Weakening of the South Asian Summer Monsoon. *Science*, *334*(6055), 502–505. https://doi.org/10.1126/science.1204994

Boucher, O., Servonnat, J., Albright, A. L., Aumont, O., Balkanski, Y., Bastrikov, V., Bekki, S., Bonnet, R., Bony, S., Bopp, L., Braconnot, P., Brockmann, P., Cadule, P., Caubel, A., Cheruy, F., Codron, F., Cozic, A., Cugnet, D., D'Andrea, F., … Vuichard, N. (2020). Presentation and Evaluation of the IPSL-CM6A-LR Climate Model. *Journal of Advances in Modeling Earth Systems*, *12*(7), e2019MS002010. https://doi.org/10.1029/2019MS002010

Cai, W., Wu, L., Lengaigne, M., Li, T., McGregor, S., Kug, J.-S., Yu, J.-Y., Stuecker, M. F., Santoso, A., Li, X., Ham, Y.-G., Chikamoto, Y., Ng, B., McPhaden, M. J., Du, Y., Dommenget, D., Jia, F., Kajtar, J. B., Keenlyside, N., … Chang, P. (2019). Pantropical climate interactions. *Science*, *363*(6430), eaav4236. https://doi.org/10.1126/science.aav4236

Chadwick, R., Boutle, I., & Martin, G. (2013). Spatial Patterns of Precipitation Change in CMIP5: Why the Rich Do Not Get Richer in the Tropics. *Journal of Climate*, *26*(11), 3803–3822. https://doi.org/10.1175/JCLI-D-12-00543.1

Chen, X., & Zhou, T. (2015). Distinct effects of global mean warming and regional sea surface warming pattern on projected uncertainty in the South Asian summer monsoon. *Geophysical Research Letters*, *42*(21), 9433–9439. https://doi.org/10.1002/2015GL066384

Chen, Y.-J., Hwang, Y.-T., & Lu, J. (2024). Robust increase in South Asian monsoon rainfall under warming driven by extratropical clouds and ocean. *Npj Climate and Atmospheric Science*, *7*(1), 318. https://doi.org/10.1038/s41612-024-00843-7

Chou, C., Neelin, J. D., Chen, C.-A., & Tu, J.-Y. (2009). Evaluating the "Rich-Get-Richer" Mechanism in Tropical Precipitation Change under Global Warming. *Journal of Climate*, *22*(8), 1982–2005. https://doi.org/10.1175/2008JCLI2471.1

Chou, C., Ryu, D., Lo, M.-H., Wey, H.-W., & Malano, H. M. (2018). Irrigation-Induced Land–Atmosphere Feedbacks and Their Impacts on Indian Summer Monsoon. *Journal of Climate*, *31*(21), 8785–8801. https://doi.org/10.1175/JCLI-D-17-0762.1

Chung, C. E., & Ramanathan, V. (2006). Weakening of North Indian SST Gradients and the Monsoon Rainfall in India and the Sahel. *Journal of Climate*, *19*(10), 2036–2045. https://doi.org/10.1175/JCLI3820.1

Collins, M., Booth, B. B. B., Bhaskaran, B., Harris, G. R., Murphy, J. M., Sexton, D. M. H., & Webb, M. J. (2011). Climate model errors, feedbacks and forcings: A comparison of perturbed physics and multi-model ensembles. *Climate Dynamics*, *36*(9–10), 1737–1766. https://doi.org/10.1007/s00382-010-0808-0

Cook, B. I., Shukla, S. P., Puma, M. J., & Nazarenko, L. S. (2015). Irrigation as an historical climate forcing. *Climate Dynamics*, *44*(5–6), 1715–1730. https://doi.org/10.1007/s00382-014-2204-7

Curry, J. A., & Webster, P. J. (2011). Climate Science and the Uncertainty Monster. *Bulletin of the American Meteorological Society*, *92*(12), 1667–1682. https://doi.org/10.1175/2011BAMS3139.1

Dagan, G., & Stier, P. (2020). Constraint on precipitation response to climate change by combination of atmospheric energy and water budgets. *Npj Climate and Atmospheric Science*, *3*(1), 34. https://doi.org/10.1038/s41612-020-00137-8

Danabasoglu, G., Lamarque, J. -F., Bacmeister, J., Bailey, D. A., DuVivier, A. K., Edwards, J., Emmons, L. K., Fasullo, J., Garcia, R., Gettelman, A., Hannay, C., Holland, M. M., Large, W. G., Lauritzen, P. H., Lawrence, D. M., Lenaerts, J. T.

M., Lindsay, K., Lipscomb, W. H., Mills, M. J., … Strand, W. G. (2020). The Community Earth System Model Version 2 (CESM2). *Journal of Advances in Modeling Earth Systems*, *12*(2), e2019MS001916. https://doi.org/10.1029/2019MS001916

Deser, C., Lehner, F., Rodgers, K. B., Ault, T., Delworth, T. L., DiNezio, P. N., Fiore, A., Frankignoul, C., Fyfe, J. C., Horton, D. E., Kay, J. E., Knutti, R., Lovenduski, N. S., Marotzke, J., McKinnon, K. A., Minobe, S., Randerson, J., Screen, J. A., Simpson, I. R., & Ting, M. (2020). Insights from Earth system model initial-condition large ensembles and future prospects. *Nature Climate Change*, *10*(4), 277–286. https://doi.org/10.1038/s41558-020-0731-2

Díaz, L. B., Saurral, R. I., & Vera, C. S. (2021). Assessment of South America summer rainfall climatology and trends in a set of global climate models large ensembles. *International Journal of Climatology*, *41*(S1). https://doi.org/10.1002/joc.6643

Dong, B., Sutton, R. T., Shaffrey, L., & Harvey, B. (2022). Recent decadal weakening of the summer Eurasian westerly jet attributable to anthropogenic aerosol emissions. *Nature Communications*, *13*(1), 1148. https://doi.org/10.1038/s41467-022-28816-5

Duffy, M. L., Medeiros, B., Gettelman, A., & Eidhammer, T. (2024). Perturbing Parameters to Understand Cloud Contributions to Climate Change. *Journal of Climate*, *37*(1), 213–227. https://doi.org/10.1175/JCLI-D-23-0250.1

Dunbar, O. R. A., Garbuno-Inigo, A., Schneider, T., & Stuart, A. M. (2021). Calibration and Uncertainty Quantification of Convective Parameters in an Idealized GCM. *Journal of Advances in Modeling Earth Systems*, *13*(9), e2020MS002454. https://doi.org/10.1029/2020MS002454

Dunne, J. P., Horowitz, L. W., Adcroft, A. J., Ginoux, P., Held, I. M., John, J. G., Krasting, J. P., Malyshev, S., Naik, V., Paulot, F., Shevliakova, E., Stock, C. A., Zadeh, N., Balaji, V., Blanton, C., Dunne, K. A., Dupuis, C., Durachta, J., Dussin, R., … Zhao, M. (2020). The GFDL Earth System Model Version 4.1 (GFDL-ESM 4.1): Overall Coupled Model Description and Simulation Characteristics. *Journal of Advances in Modeling Earth Systems*, *12*(11), e2019MS002015. https://doi.org/10.1029/2019MS002015

Eidhammer, T., Gettelman, A., Thayer-Calder, K., Watson-Parris, D., Elsaesser, G., Morrison, H., Van Lier-Walqui, M., Song, C., & McCoy, D. (2024). An extensible perturbed parameter ensemble for the Community Atmosphere Model version

6. *Geoscientific Model Development*, *17*(21), 7835–7853. https://doi.org/10.5194/gmd-17-7835-2024

Elbaum, E., Garfinkel, C. I., Adam, O., Morin, E., Rostkier-Edelstein, D., & Dayan, U. (2022). Uncertainty in Projected Changes in Precipitation Minus Evaporation: Dominant Role of Dynamic Circulation Changes and Weak Role for Thermodynamic Changes. *Geophysical Research Letters*, *49*(12), e2022GL097725. https://doi.org/10.1029/2022GL097725

Endo, H., & Kitoh, A. (2014). Thermodynamic and dynamic effects on regional monsoon rainfall changes in a warmer climate. *Geophysical Research Letters*, *41*(5), 1704–1711. https://doi.org/10.1002/2013GL059158

Eyring, V., Bony, S., Meehl, G. A., Senior, C. A., Stevens, B., Stouffer, R. J., & Taylor, K. E. (2016). Overview of the Coupled Model Intercomparison Project Phase 6 (CMIP6) experimental design and organization. *Geoscientific Model Development*, *9*(5), 1937–1958. https://doi.org/10.5194/gmd-9-1937-2016

Fan, F., Mann, M. E., Lee, S., & Evans, J. L. (2012). Future Changes in the South Asian Summer Monsoon: An Analysis of the CMIP3 Multimodel Projections. *Journal of Climate*, *25*(11), 3909–3928. https://doi.org/10.1175/JCLI-D-11-00133.1

Fasullo, J., & Webster, P. J. (2002). Hydrological Signatures Relating the Asian Summer Monsoon and ENSO. *Journal of Climate*, *15*(21), 3082–3095. https://doi.org/10.1175/1520-0442(2002)015%253C3082:HSRTAS%253E2.0.CO;2

Ferguglia, O., Von Hardenberg, J., & Palazzi, E. (2023). Robustness of precipitation Emergent Constraints in CMIP6 models. *Climate Dynamics*, *61*(3–4), 1439–1450. https://doi.org/10.1007/s00382-022-06634-1

Fiedler, S., Crueger, T., D'Agostino, R., Peters, K., Becker, T., Leutwyler, D., Paccini, L., Burdanowitz, J., Buehler, S. A., Cortes, A. U., Dauhut, T., Dommenget, D., Fraedrich, K., Jungandreas, L., Maher, N., Naumann, A. K., Rugenstein, M., Sakradzija, M., Schmidt, H., … Stevens, B. (2020). Simulated Tropical Precipitation Assessed across Three Major Phases of the Coupled Model Intercomparison Project (CMIP). *Monthly Weather Review*, *148*(9), 3653–3680. https://doi.org/10.1175/MWR-D-19-0404.1

Frankcombe, L. M., England, M. H., Kajtar, J. B., Mann, M. E., & Steinman, B. A. (2018). On the Choice of Ensemble Mean for Estimating the Forced Signal in the Presence of Internal Variability. *Journal of Climate*, *31*(14), 5681–5693. https://doi.org/10.1175/JCLI-D-17-0662.1

Friedman, A. R., Hwang, Y.-T., Chiang, J. C. H., & Frierson, D. M. W. (2013). Interhemispheric Temperature Asymmetry over the Twentieth Century and in Future Projections. *Journal of Climate*, *26*(15), 5419–5433. https://doi.org/10.1175/JCLI-D-12-00525.1

Gao, M., Ding, Y., Song, S., Lu, X., Chen, X., & McElroy, M. B. (2018). Secular decrease of wind power potential in India associated with warming in the Indian Ocean. *Science Advances*, *4*(12), eaat5256. https://doi.org/10.1126/sciadv.aat5256

Gelaro, R., McCarty, W., Suárez, M. J., Todling, R., Molod, A., Takacs, L., Randles, C. A., Darmenov, A., Bosilovich, M. G., Reichle, R., Wargan, K., Coy, L., Cullather, R., Draper, C., Akella, S., Buchard, V., Conaty, A., Da Silva, A. M., Gu, W., … Zhao, B. (2017). The Modern-Era Retrospective Analysis for Research and Applications, Version 2 (MERRA-2). *Journal of Climate*, *30*(14), 5419–5454. https://doi.org/10.1175/JCLI-D-16-0758.1

Gettelman, A., Eidhammer, T., Duffy, M. L., McCoy, D. T., Song, C., & Watson-Parris, D. (2024). The Interaction Between Climate Forcing and Feedbacks. *Journal of Geophysical Research: Atmospheres*, *129*(18), e2024JD040857. https://doi.org/10.1029/2024JD040857

Gillett, N. P., Shiogama, H., Funke, B., Hegerl, G., Knutti, R., Matthes, K., Santer, B. D., Stone, D., & Tebaldi, C. (2016). The Detection and Attribution Model Intercomparison Project (DAMIP v1.0)contribution to CMIP6. *Geoscientific Model Development*, *9*(10), 3685–3697. https://doi.org/10.5194/gmd-9-3685-2016

Guilbert, M., Terray, P., & Mignot, J. (2023). Intermodel Spread of Historical Indian Monsoon Rainfall Change in CMIP6: The Role of the Tropical Pacific Mean State. *Journal of Climate*, *36*(12), 3937–3953. https://doi.org/10.1175/JCLI-D-22-0585.1

Guo, L., Turner, A. G., & Highwood, E. J. (2015). Impacts of 20th century aerosol emissions on the South Asian monsoon in the CMIP5 models. *Atmospheric Chemistry and Physics*, *15*(11), 6367–6378. https://doi.org/10.5194/acp-15-6367-2015

Harris, I. (2013). *CRU TS3.21: Climatic Research Unit (CRU) Time-Series (TS) Version 3.21 of High Resolution Gridded Data of Month-by-month Variation in Climate (Jan. 1901 - Dec. 2012)* (Version 3.21) [Dataset]. NERC British Atmospheric Data Centre. https://doi.org/10.5285/D0E1585D-3417-485F-87AE-4FCECF10A992

Hawkins, E., & Sutton, R. (2009). The Potential to Narrow Uncertainty in Regional Climate Predictions. *Bulletin of the American Meteorological Society*, *90*(8), 1095–1108. https://doi.org/10.1175/2009BAMS2607.1

He, J., Johnson, N. C., Vecchi, G. A., Kirtman, B., Wittenberg, A. T., & Sturm, S. (2018). Precipitation Sensitivity to Local Variations in Tropical Sea Surface Temperature. *Journal of Climate*, *31*(22), 9225–9238. https://doi.org/10.1175/JCLI-D-18-0262.1

Hegerl, G., & Zwiers, F. (2011). Use of models in detection and attribution of climate change. *WIREs Climate Change*, *2*(4), 570–591. https://doi.org/10.1002/wcc.121

Held, I. M., & Soden, B. J. (2006). Robust Responses of the Hydrological Cycle to Global Warming. *Journal of Climate*, *19*(21), 5686–5699. https://doi.org/10.1175/JCLI3990.1

Hersbach, H., Bell, B., Berrisford, P., Hirahara, S., Horányi, A., Muñoz-Sabater, J., Nicolas, J., Peubey, C., Radu, R., Schepers, D., Simmons, A., Soci, C., Abdalla, S., Abellan, X., Balsamo, G., Bechtold, P., Biavati, G., Bidlot, J., Bonavita, M., … Thépaut, J. (2020). The ERA5 global reanalysis. *Quarterly Journal of the Royal Meteorological Society*, *146*(730), 1999–2049. https://doi.org/10.1002/qj.3803

Hu, Z., Latif, M., Roeckner, E., & Bengtsson, L. (2000). Intensified Asian Summer Monsoon and its variability in a coupled model forced by increasing greenhouse gas concentrations. *Geophysical Research Letters*, *27*(17), 2681–2684. https://doi.org/10.1029/2000GL011550

Huang, X., Zhou, T., Dai, A., Li, H., Li, C., Chen, X., Lu, J., Von Storch, J.-S., & Wu, B. (2020a). South Asian summer monsoon projections constrained by the interdecadal Pacific oscillation. *Science Advances*, *6*(11), eaay6546. https://doi.org/10.1126/sciadv.aay6546

Huang, X., Zhou, T., Turner, A., Dai, A., Chen, X., Clark, R., Jiang, J., Man, W., Murphy, J., Rostron, J., Wu, B., Zhang, L., Zhang, W., & Zou, L. (2020b). The Recent Decline and Recovery of Indian Summer Monsoon Rainfall: Relative Roles of External Forcing and Internal Variability. *Journal of Climate*, *33*(12), 5035–5060. https://doi.org/10.1175/JCLI-D-19-0833.1

IPCC. (2021). *Climate Change 2021: The Physical Science Basis. Contribution of Working Group I to the Sixth Assessment Report of the Intergovernmental Panel on Climate Change* (V. Masson-Delmotte, P. Zhai, A. Pirani, S. L. Connors, C. Péan, S. Berger, N. Caud, Y. Chen, L. Goldfarb, M. I. Gomis, M. Huang, K. Leitzell, E. Lonnoy, J.

B. R. Matthews, T. K. Maycock, T. Waterfield, O. Yelekçi, R. Yu, & B. Zhou, Eds.). Cambridge University Press. https://doi.org/10.1017/9781009157896

Jacobson, M., Draxl, C., Jimenez, T., O'Neill, B., Capozzola, T., Lee, J. A., Vandenberghe, F., & Haupt, S. E. (2018). *Assessing the Wind Energy Potential in Bangladesh: Enabling Wind Energy Development with Data Products* (NREL/TP--5000-71077, 1476253; p. NREL/TP--5000-71077, 1476253). https://doi.org/10.2172/1476253

Jain, S., Salunke, P., Mishra, S. K., & Sahany, S. (2019). Performance of CMIP5 models in the simulation of Indian summer monsoon. *Theoretical and Applied Climatology*, *137*(1–2), 1429–1447. https://doi.org/10.1007/s00704-018-2674-3

Jin, Q., & Wang, C. (2017). A revival of Indian summer monsoon rainfall since 2002. *Nature Climate Change*, *7*(8), 587–594. https://doi.org/10.1038/nclimate3348

Joseph, L., Skliris, N., Dey, D., Marsh, R., & Hirschi, J. (2024). Increased Summer Monsoon Rainfall Over Northwest India Caused by Hadley Cell Expansion and Indian Ocean Warming. *Geophysical Research Letters*, *51*(16), e2024GL108829. https://doi.org/10.1029/2024GL108829

Kalnay, E., Kanamitsu, M., Kistler, R., Collins, W., Deaven, D., Gandin, L., Iredell, M., Saha, S., White, G., Woollen, J., Zhu, Y., Leetmaa, A., Reynolds, R., Chelliah, M., Ebisuzaki, W., Higgins, W., Janowiak, J., Mo, K. C., Ropelewski, C., … Joseph, D. (1996). The NCEP/NCAR 40-Year Reanalysis Project. *Bulletin of the American Meteorological Society*, *77*(3), 437–471. https://doi.org/10.1175/1520-0477(1996)077%253C0437:TNYRP%253E2.0.CO;2

Karnauskas, K. B., Lundquist, J. K., & Zhang, L. (2018). Southward shift of the global wind energy resource under high carbon dioxide emissions. *Nature Geoscience*, *11*(1), 38–43. https://doi.org/10.1038/s41561-017-0029-9

Keil, P., Schmidt, H., Stevens, B., & Bao, J. (2021). Variations of Tropical Lapse Rates in Climate Models and their Implications for Upper Tropospheric Warming. *Journal of Climate*, 1–50. https://doi.org/10.1175/JCLI-D-21-0196.1

Kendon, E. J., Prein, A. F., Senior, C. A., & Stirling, A. (2021). Challenges and outlook for convection-permitting climate modelling. *Philosophical Transactions of the Royal Society A: Mathematical, Physical and Engineering Sciences*, *379*(2195), 20190547. https://doi.org/10.1098/rsta.2019.0547

Kitoh, A., Endo, H., Krishna Kumar, K., Cavalcanti, I. F. A., Goswami, P., & Zhou, T. (2013). Monsoons in a changing world: A regional perspective in a global context. *Journal of Geophysical Research: Atmospheres*, *118*(8), 3053–3065. https://doi.org/10.1002/jgrd.50258

Knutti, R., & Sedláček, J. (2013). Robustness and uncertainties in the new CMIP5 climate model projections. *Nature Climate Change*, *3*(4), 369–373. https://doi.org/10.1038/nclimate1716

Kripalani, R. H., Oh, J. H., Kulkarni, A., Sabade, S. S., & Chaudhari, H. S. (2007). South Asian summer monsoon precipitation variability: Coupled climate model simulations and projections under IPCC AR4. *Theoretical and Applied Climatology*, *90*(3–4), 133–159. https://doi.org/10.1007/s00704-006-0282-0

Krishnamurthy, V., & Goswami, B. N. (2000). Indian Monsoon–ENSO Relationship on Interdecadal Timescale. *Journal of Climate*, *13*(3), 579–595. https://doi.org/10.1175/1520-0442(2000)013%253C0579:IMEROI%253E2.0.CO;2

Krishnamurti, T. N., & Bhalme, H. N. (1976). Oscillations of a Monsoon System. Part I. Observational Aspects. *Journal of the Atmospheric Sciences*, *33*(10), 1937–1954. https://doi.org/10.1175/1520-0469(1976)033%253C1937:OOAMSP%253E2.0.CO;2

Lau, N.-C., & Nath, M. J. (2000). Impact of ENSO on the Variability of the Asian–Australian Monsoons as Simulated in GCM Experiments. *Journal of Climate*, *13*(24), 4287–4309. https://doi.org/10.1175/1520-0442(2000)013%253C4287:IOEOTV%253E2.0.CO;2

Lau, W. K. M., & Kim, K.-M. (2017). Competing influences of greenhouse warming and aerosols on Asian summer monsoon circulation and rainfall. *Asia-Pacific Journal of Atmospheric Sciences*, *53*(2), 181–194. https://doi.org/10.1007/s13143-017-0033-4

Lau, W. K. M., Kim, K.-M., & Ruby Leung, L. (2017). Changing circulation structure and precipitation characteristics in Asian monsoon regions: Greenhouse warming vs. aerosol effects. *Geoscience Letters*, *4*(1), 28. https://doi.org/10.1186/s40562-017-0094-3

Lee, E., Sacks, W. J., Chase, T. N., & Foley, J. A. (2011). Simulated impacts of irrigation on the atmospheric circulation over Asia. *Journal of Geophysical Research*, *116*(D8), D08114. https://doi.org/10.1029/2010JD014740

Lee, J.-Y., & Wang, B. (2014). Future change of global monsoon in the CMIP5. *Climate Dynamics*, *42*(1–2), 101–119. https://doi.org/10.1007/s00382-012-1564-0

Lehner, F., Deser, C., Maher, N., Marotzke, J., Fischer, E. M., Brunner, L., Knutti, R., & Hawkins, E. (2020). Partitioning climate projection uncertainty with multiple large ensembles and CMIP5/6. *Earth System Dynamics*, *11*(2), 491–508. https://doi.org/10.5194/esd-11-491-2020

Li, B., Zhou, L., Qin, J., Zhou, T., Chen, D., Hou, S., & Murtugudde, R. (2023). Middle east warming in spring enhances summer rainfall over Pakistan. *Nature Communications*, *14*(1), 7635. https://doi.org/10.1038/s41467-023-43463-0

Li, G., Xie, S.-P., He, C., & Chen, Z. (2017). Western Pacific emergent constraint lowers projected increase in Indian summer monsoon rainfall. *Nature Climate Change*, *7*(10), 708–712. https://doi.org/10.1038/nclimate3387

Li, L., Yu, Y., Tang, Y., Lin, P., Xie, J., Song, M., Dong, L., Zhou, T., Liu, L., Wang, L., Pu, Y., Chen, X., Chen, L., Xie, Z., Liu, H., Zhang, L., Huang, X., Feng, T., Zheng, W., … Wei, J. (2020). The Flexible Global Ocean-Atmosphere-Land System Model Grid-Point Version 3 (FGOALS-g3): Description and Evaluation. *Journal of Advances in Modeling Earth Systems*, *12*(9), e2019MS002012. https://doi.org/10.1029/2019MS002012

Li, S., Perlwitz, J., Quan, X., & Hoerling, M. P. (2008). Modelling the influence of North Atlantic multidecadal warmth on the Indian summer rainfall. *Geophysical Research Letters*, *35*(5), 2007GL032901. https://doi.org/10.1029/2007GL032901

Li, X., Xie, S.-P., Gille, S. T., & Yoo, C. (2016a). Atlantic-induced pan-tropical climate change over the past three decades. *Nature Climate Change*, *6*(3), 275–279. https://doi.org/10.1038/nclimate2840

Li, Z., Lau, W. K. -M., Ramanathan, V., Wu, G., Ding, Y., Manoj, M. G., Liu, J., Qian, Y., Li, J., Zhou, T., Fan, J., Rosenfeld, D., Ming, Y., Wang, Y., Huang, J., Wang, B., Xu, X., Lee, S. -S., Cribb, M., … Brasseur, G. P. (2016b). Aerosol and monsoon climate interactions over Asia. *Reviews of Geophysics*, *54*(4), 866–929. https://doi.org/10.1002/2015RG000500

Lindzen, R. S., & Nigam, S. (1987). On the Role of Sea Surface Temperature Gradients in Forcing Low-Level Winds and Convergence in the Tropics. *Journal of the Atmospheric Sciences*, *44*(17), 2418–2436. https://doi.org/10.1175/1520-0469(1987)044%253C2418:OTROSS%253E2.0.CO;2

Liu, J., Wang, B., Cane, M. A., Yim, S.-Y., & Lee, J.-Y. (2013). Divergent global precipitation changes induced by natural versus anthropogenic forcing. *Nature*, *493*(7434), 656–659. https://doi.org/10.1038/nature11784

Lu, J., Vecchi, G. A., & Reichler, T. (2007). Expansion of the Hadley cell under global warming. *Geophysical Research Letters*, *34*(6), 2006GL028443. https://doi.org/10.1029/2006GL028443

Lu, X., McElroy, M. B., & Kiviluoma, J. (2009). Global potential for wind-generated electricity. *Proceedings of the National Academy of Sciences*, *106*(27), 10933–10938. https://doi.org/10.1073/pnas.0904101106

Luo, H., Wang, Z., He, C., Chen, D., & Yang, S. (2024). Future changes in South Asian summer monsoon circulation under global warming: Role of the Tibetan Plateau latent heating. *Npj Climate and Atmospheric Science*, *7*(1), 103. https://doi.org/10.1038/s41612-024-00653-x

Ma, J., & Yu, J. (2014). Paradox in South Asian summer monsoon circulation change: Lower tropospheric strengthening and upper tropospheric weakening. *Geophysical Research Letters*, *41*(8), 2934–2940. https://doi.org/10.1002/2014GL059891

Maher, N., Milinski, S., & Ludwig, R. (2021). Large ensemble climate model simulations: Introduction, overview, and future prospects for utilising multiple types of large ensemble. *Earth System Dynamics*, *12*(2), 401–418. https://doi.org/10.5194/esd-12-401-2021

McDermid, S., Nocco, M., Lawston-Parker, P., Keune, J., Pokhrel, Y., Jain, M., Jägermeyr, J., Brocca, L., Massari, C., Jones, A. D., Vahmani, P., Thiery, W., Yao, Y., Bell, A., Chen, L., Dorigo, W., Hanasaki, N., Jasechko, S., Lo, M.-H., … Yokohata, T. (2023). Irrigation in the Earth system. *Nature Reviews Earth & Environment*, *4*(7), 435–453. https://doi.org/10.1038/s43017-023-00438-5

Mckay, M. D., Beckman, R. J., & Conover, W. J. (2000). A Comparison of Three Methods for Selecting Values of Input Variables in the Analysis of Output From a Computer Code. *Technometrics*, *42*(1), 55–61. https://doi.org/10.1080/00401706.2000.10485979

Meehl, G. A., & Arblaster, J. M. (2003). Mechanisms for projected future changes in south Asian monsoon precipitation. *Climate Dynamics*, *21*(7–8), 659–675. https://doi.org/10.1007/s00382-003-0343-3

Mehta, P., Siebert, S., Kummu, M., Deng, Q., Ali, T., Marston, L., Xie, W., & Davis, K. F. (2024). Half of twenty-first century global irrigation expansion has been in water-stressed regions. *Nature Water*, *2*(3), 254–261. https://doi.org/10.1038/s44221-024-00206-9

Mei, R., Ashfaq, M., Rastogi, D., Leung, L. R., & Dominguez, F. (2015). Dominating Controls for Wetter South Asian Summer Monsoon in the Twenty-First Century. *Journal of Climate*, *28*(8), 3400–3419. https://doi.org/10.1175/JCLI-D-14-00355.1

Menon, A., Levermann, A., Schewe, J., Lehmann, J., & Frieler, K. (2013). Consistent increase in Indian monsoon rainfall and its variability across CMIP-5 models. *Earth System Dynamics*, *4*(2), 287–300. https://doi.org/10.5194/esd-4-287-2013

Miao, H., Dong, D., Huang, G., Hu, K., Tian, Q., & Gong, Y. (2020). Evaluation of Northern Hemisphere surface wind speed and wind power density in multiple reanalysis datasets. *Energy*, *200*, 117382. https://doi.org/10.1016/j.energy.2020.117382

Ministry of New and Renewable Energy, Government of India. (2022). *Annual report 2020–21*. Government of India. https://mnre.gov.in/img/documents/uploads/file_f-1618564141288.pdf

Mishra, S. K. (2012). Effects of convective adjustment time scale on the simulation of tropical climate. *Theoretical and Applied Climatology*, *107*(1–2), 211–228. https://doi.org/10.1007/s00704-011-0479-8

Mishra, S. K., Upadhyaya, P., Fasullo, J. T., Keshri, N. P., Salunke, P., Ghosh, A., Sainudeen, A. B., & Kang, I.-S. (2023). A need for actionable climate projections across the Global South. *Nature Climate Change*, *13*(9), 883–886. https://doi.org/10.1038/s41558-023-01778-2

Monerie, P.-A., Wilcox, L. J., & Turner, A. G. (2022). Effects of Anthropogenic Aerosol and Greenhouse Gas Emissions on Northern Hemisphere Monsoon Precipitation: Mechanisms and Uncertainty. *Journal of Climate*, *35*(8), 2305–2326. https://doi.org/10.1175/JCLI-D-21-0412.1

Olonscheck, D., Suarez-Gutierrez, L., Milinski, S., Beobide-Arsuaga, G., Baehr, J., Fröb, F., Ilyina, T., Kadow, C., Krieger, D., Li, H., Marotzke, J., Plésiat, É., Schupfner, M., Wachsmann, F., Wallberg, L., Wieners, K., & Brune, S. (2023). The New Max Planck Institute Grand Ensemble With CMIP6 Forcing and High-Frequency Model Output. *Journal of Advances in Modeling Earth Systems*, *15*(10), e2023MS003790. https://doi.org/10.1029/2023MS003790

Palmer, T. (2011). A CERN for climate change. *Physics World*, *24*(03), 14–15. https://doi.org/10.1088/2058-7058/24/03/24

Pendergrass, A. G., Coleman, D. B., Deser, C., Lehner, F., Rosenbloom, N., & Simpson, I. R. (2019). Nonlinear Response of Extreme Precipitation to Warming in CESM1. *Geophysical Research Letters*, *46*(17–18), 10551–10560. https://doi.org/10.1029/2019GL084826

Popp, A., Calvin, K., Fujimori, S., Havlik, P., Humpenöder, F., Stehfest, E., Bodirsky, B. L., Dietrich, J. P., Doelmann, J. C., Gusti, M., Hasegawa, T., Kyle, P., Obersteiner, M., Tabeau, A., Takahashi, K., Valin, H., Waldhoff, S., Weindl, I., Wise, M., … Vuuren, D. P. V. (2017). Land-use futures in the shared socio-economic pathways. *Global Environmental Change*, *42*, 331–345. https://doi.org/10.1016/j.gloenvcha.2016.10.002

Rajeevan, M., Bhate, J., & Jaswal, A. K. (2008). Analysis of variability and trends of extreme rainfall events over India using 104 years of gridded daily rainfall data. *Geophysical Research Letters*, *35*(18), 2008GL035143. https://doi.org/10.1029/2008GL035143

Rajesh, P. V., & Goswami, B. N. (2022). A New Emergent Constraint Corrected Projections of Indian Summer Monsoon Rainfall. *Geophysical Research Letters*, *49*(8), e2021GL096671. https://doi.org/10.1029/2021GL096671

Rajesh, P. V., & Goswami, B. N. (2023). Climate Change and Potential Demise of the Indian Deserts. *Earth's Future*, *11*(8), e2022EF003459. https://doi.org/10.1029/2022EF003459

Ramanathan, V., & Carmichael, G. (2008). Global and regional climate changes due to black carbon. *Nature Geoscience*, *1*(4), 221–227. https://doi.org/10.1038/ngeo156

Ramanathan, V., Chung, C., Kim, D., Bettge, T., Buja, L., Kiehl, J. T., Washington, W. M., Fu, Q., Sikka, D. R., & Wild, M. (2005). Atmospheric brown clouds: Impacts on South Asian climate and hydrological cycle. *Proceedings of the National Academy of Sciences*, *102*(15), 5326–5333. https://doi.org/10.1073/pnas.0500656102

Reiner Lemoine Institut. (2019). *Wind Turbine Library* [Dataset]. Reiner Lemoine Institut. https://openenergy-platform.org/dataedit/view/supply/wind_turbine_library

Roderick, M. L., Rotstayn, L. D., Farquhar, G. D., & Hobbins, M. T. (2007). On the attribution of changing pan evaporation. *Geophysical Research Letters*, *34*(17), 2007GL031166. https://doi.org/10.1029/2007GL031166

Rodgers, K. B., Lee, S.-S., Rosenbloom, N., Timmermann, A., Danabasoglu, G., Deser, C., Edwards, J., Kim, J.-E., Simpson, I. R., Stein, K., Stuecker, M. F., Yamaguchi, R., Bódai, T., Chung, E.-S., Huang, L., Kim, W. M., Lamarque, J.-F., Lombardozzi, D. L., Wieder, W. R., & Yeager, S. G. (2021). Ubiquity of human-induced changes in climate variability. *Earth System Dynamics*, *12*(4), 1393–1411. https://doi.org/10.5194/esd-12-1393-2021

Rodwell, M. J., & Hoskins, B. J. (2001). Subtropical Anticyclones and Summer Monsoons. *Journal of Climate*, *14*(15), 3192–3211. https://doi.org/10.1175/1520-0442(2001)014%253C3192:SAASM%253E2.0.CO;2

Rowell, D. P. (2012). Sources of uncertainty in future changes in local precipitation. *Climate Dynamics*, *39*(7–8), 1929–1950. https://doi.org/10.1007/s00382-011-1210-2

Roxy, M. K., Ritika, K., Terray, P., Murtugudde, R., Ashok, K., & Goswami, B. N. (2015). Drying of Indian subcontinent by rapid Indian Ocean warming and a weakening land-sea thermal gradient. *Nature Communications*, *6*(1), 7423. https://doi.org/10.1038/ncomms8423

Saha, A., Ghosh, S., Sahana, A. S., & Rao, E. P. (2014). Failure of CMIP5 climate models in simulating post-1950 decreasing trend of Indian monsoon. *Geophysical Research Letters*, *41*(20), 7323–7330. https://doi.org/10.1002/2014GL061573

Saji, N. H., Goswami, B. N., Vinayachandran, P. N., & Yamagata, T. (1999). A dipole mode in the tropical Indian Ocean. *Nature*, *401*(6751), 360–363. https://doi.org/10.1038/43854

Salunke, P., Keshri, N. P., Mishra, S. K., & Dash, S. K. (2023). Future projections of seasonal temperature and precipitation for India. *Frontiers in Climate*, *5*, 1069994. https://doi.org/10.3389/fclim.2023.1069994

Salzmann, M., & Cherian, R. (2015). On the enhancement of the Indian summer monsoon drying by Pacific multidecadal variability during the latter half of the twentieth century. *Journal of Geophysical Research: Atmospheres*, *120*(18), 9103–9118. https://doi.org/10.1002/2015JD023313

Samset, B. H., Lund, M. T., Bollasina, M., Myhre, G., & Wilcox, L. (2019). Emerging Asian aerosol patterns. *Nature Geoscience*, *12*(8), 582–584. https://doi.org/10.1038/s41561-019-0424-5

Sandeep, S., & Ajayamohan, R. S. (2015). Poleward shift in Indian summer monsoon low level jetstream under global warming. *Climate Dynamics*, *45*(1–2), 337–351. https://doi.org/10.1007/s00382-014-2261-y

Sarojini, B. B., Stott, P. A., & Black, E. (2016). Detection and attribution of human influence on regional precipitation. *Nature Climate Change*, *6*(7), 669–675. https://doi.org/10.1038/nclimate2976

Schneider, T., Leung, L. R., & Wills, R. C. J. (2024). Opinion: Optimizing climate models with process knowledge, resolution, and artificial intelligence. *Atmospheric Chemistry and Physics*, *24*(12), 7041–7062. https://doi.org/10.5194/acp-24-7041-2024

Seland, Ø., Bentsen, M., Olivié, D., Toniazzo, T., Gjermundsen, A., Graff, L. S., Debernard, J. B., Gupta, A. K., He, Y.-C., Kirkevåg, A., Schwinger, J., Tjiputra, J., Aas, K. S., Bethke, I., Fan, Y., Griesfeller, J., Grini, A., Guo, C., Ilicak, M., … Schulz, M. (2020). Overview of the Norwegian Earth System Model (NorESM2) and key climate response of CMIP6 DECK, historical, and scenario simulations. *Geoscientific Model Development*, *13*(12), 6165–6200. https://doi.org/10.5194/gmd-13-6165-2020

Shamal, M., & Sanjay, J. (2021). An observational equatorial Atlantic Ocean constraint on Indian monsoon precipitation projections. *Climate Dynamics*, *57*(1–2), 209–221. https://doi.org/10.1007/s00382-021-05703-1

Sharmila, S., Joseph, S., Sahai, A. K., Abhilash, S., & Chattopadhyay, R. (2015). Future projection of Indian summer monsoon variability under climate change scenario: An assessment from CMIP5 climate models. *Global and Planetary Change*, *124*, 62–78. https://doi.org/10.1016/j.gloplacha.2014.11.004

Shen, C., Zha, J., Li, Z., Azorin-Molina, C., Deng, K., Minola, L., & Chen, D. (2022). Evaluation of global terrestrial near-surface wind speed simulated by CMIP6 models and their future projections. *Annals of the New York Academy of Sciences*, *1518*(1), 249–263. https://doi.org/10.1111/nyas.14910

Shepherd, T. G. (2014). Atmospheric circulation as a source of uncertainty in climate change projections. *Nature Geoscience*, *7*(10), 703–708. https://doi.org/10.1038/ngeo2253

Sherman, P., Gao, M., Song, S., Archibald, A. T., Abraham, N. L., Lamarque, J.-F., Shindell, D., Faluvegi, G., & McElroy, M. B. (2021). Sensitivity of modeled Indian monsoon to Chinese and Indian aerosol emissions. *Atmospheric Chemistry and Physics*, *21*(5), 3593–3605. https://doi.org/10.5194/acp-21-3593-2021

Simpson, I. R., McKinnon, K. A., Davenport, F. V., Tingley, M., Lehner, F., Al Fahad, A., & Chen, D. (2021). Emergent Constraints on the Large-Scale Atmospheric Circulation and Regional Hydroclimate: Do They Still Work in CMIP6 and How Much Can They Actually Constrain the Future? *Journal of Climate*, *34*(15), 6355–6377. https://doi.org/10.1175/JCLI-D-21-0055.1

Simpson, I. R., Rosenbloom, N., Danabasoglu, G., Deser, C., Yeager, S. G., McCluskey, C. S., Yamaguchi, R., Lamarque, J.-F., Tilmes, S., Mills, M. J., & Rodgers, K. B. (2023). The CESM2 Single-Forcing Large Ensemble and Comparison to CESM1: Implications for Experimental Design. *Journal of Climate*, *36*(17), 5687–5711. https://doi.org/10.1175/JCLI-D-22-0666.1

Simpson, I. R., Shaw, T. A., Ceppi, P., Clement, A. C., Fischer, E., Grise, K. M., Pendergrass, A. G., Screen, J. A., Wills, R. C. J., Woollings, T., Blackport, R., Kang, J. M., & Po-Chedley, S. (2025). Confronting Earth System Model trends with observations. *Science Advances*, *11*(11), eadt8035. https://doi.org/10.1126/sciadv.adt8035

Singh, D., Ghosh, S., Roxy, M. K., & McDermid, S. (2019). Indian summer monsoon: Extreme events, historical changes, and role of anthropogenic forcings. *WIREs Climate Change*, *10*(2), e571. https://doi.org/10.1002/wcc.571

Singh, D., McDermid, S. P., Cook, B. I., Puma, M. J., Nazarenko, L., & Kelley, M. (2018). Distinct Influences of Land Cover and Land Management on Seasonal Climate. *Journal of Geophysical Research: Atmospheres*, *123*(21). https://doi.org/10.1029/2018JD028874

Singh, R., Jaiswal, N., & Kishtawal, C. M. (2022). Rising surface pressure over Tibetan Plateau strengthens indian summer monsoon rainfall over northwestern India. *Scientific Reports*, *12*(1), 8621. https://doi.org/10.1038/s41598-022-12523-8

Slingo, J., Bates, P., Bauer, P., Belcher, S., Palmer, T., Stephens, G., Stevens, B., Stocker, T., & Teutsch, G. (2022). Ambitious partnership needed for reliable climate prediction. *Nature Climate Change*, *12*(6), 499–503. https://doi.org/10.1038/s41558-022-01384-8

Smith, D. M., Gillett, N. P., Simpson, I. R., Athanasiadis, P. J., Baehr, J., Bethke, I., Bilge, T. A., Bonnet, R., Boucher, O., Findell, K. L., Gastineau, G., Gualdi, S., Hermanson, L., Leung, L. R., Mignot, J., Müller, W. A., Osprey, S., Otterå, O. H., Persad, G. G., … Ziehn, T. (2022). Attribution of multi-annual to decadal changes in the climate system: The Large Ensemble Single Forcing Model Intercomparison Project (LESFMIP). *Frontiers in Climate*, *4*, 955414. https://doi.org/10.3389/fclim.2022.955414

Sooraj, K. P., Terray, P., & Mujumdar, M. (2015). Global warming and the weakening of the Asian summer monsoon circulation: Assessments from the CMIP5 models. *Climate Dynamics*, *45*(1–2), 233–252. https://doi.org/10.1007/s00382-014-2257-7

Sperber, K. R., Annamalai, H., Kang, I.-S., Kitoh, A., Moise, A., Turner, A., Wang, B., & Zhou, T. (2013). The Asian summer monsoon: An intercomparison of CMIP5 vs. CMIP3 simulations of the late 20th century. *Climate Dynamics*, *41*(9–10), 2711–2744. https://doi.org/10.1007/s00382-012-1607-6

Sun, Q., Miao, C., Duan, Q., Ashouri, H., Sorooshian, S., & Hsu, K. (2018). A Review of Global Precipitation Data Sets: Data Sources, Estimation, and Intercomparisons. *Reviews of Geophysics*, *56*(1), 79–107. https://doi.org/10.1002/2017RG000574

Sun, Y., Ding, Y., & Dai, A. (2010). Changing links between South Asian summer monsoon circulation and tropospheric land-sea thermal contrasts under a warming scenario. *Geophysical Research Letters*, *37*(2), 2009GL041662. https://doi.org/10.1029/2009GL041662

Swapna, P., Krishnan, R., & Wallace, J. M. (2014). Indian Ocean and monsoon coupled interactions in a warming environment. *Climate Dynamics*, *42*(9–10), 2439–2454. https://doi.org/10.1007/s00382-013-1787-8

Swart, N. C., Cole, J. N. S., Kharin, V. V., Lazare, M., Scinocca, J. F., Gillett, N. P., Anstey, J., Arora, V., Christian, J. R., Hanna, S., Jiao, Y., Lee, W. G., Majaess, F., Saenko, O. A., Seiler, C., Seinen, C., Shao, A., Sigmond, M., Solheim, L., … Winter, B. (2019). The Canadian Earth System Model version 5 (CanESM5.0.3). *Geoscientific Model Development*, *12*(11), 4823–4873. https://doi.org/10.5194/gmd-12-4823-2019

Tanaka, H. L., Ishizaki, N., & Kitoh, A. (2004). Trend and interannual variability of Walker, monsoon and Hadley circulations defined by velocity potential in the

upper troposphere. *Tellus A: Dynamic Meteorology and Oceanography*, *56*(3), 250. https://doi.org/10.3402/tellusa.v56i3.14410

Tatebe, H., Ogura, T., Nitta, T., Komuro, Y., Ogochi, K., Takemura, T., Sudo, K., Sekiguchi, M., Abe, M., Saito, F., Chikira, M., Watanabe, S., Mori, M., Hirota, N., Kawatani, Y., Mochizuki, T., Yoshimura, K., Takata, K., O'ishi, R., … Kimoto, M. (2019). Description and basic evaluation of simulated mean state, internal variability, and climate sensitivity in MIROC6. *Geoscientific Model Development*, *12*(7), 2727–2765. https://doi.org/10.5194/gmd-12-2727-2019

Teng, H., Leung, R., Branstator, G., Lu, J., & Ding, Q. (2022). Warming Pattern over the Northern Hemisphere Midlatitudes in Boreal Summer 1979–2020. *Journal of Climate*, *35*(11), 3479–3494. https://doi.org/10.1175/JCLI-D-21-0437.1

Tian, Q., Huang, G., Hu, K., & Niyogi, D. (2019). Observed and global climate model based changes in wind power potential over the Northern Hemisphere during 1979–2016. *Energy*, *167*, 1224–1235. https://doi.org/10.1016/j.energy.2018.11.027

Tian, Y., Hu, S., & Deser, C. (2023). Critical role of biomass burning aerosols in enhanced historical Indian Ocean warming. *Nature Communications*, *14*(1), 3508. https://doi.org/10.1038/s41467-023-39204-y

Torralba, V., Doblas-Reyes, F. J., & Gonzalez-Reviriego, N. (2017). Uncertainty in recent near-surface wind speed trends: A global reanalysis intercomparison. *Environmental Research Letters*, *12*(11), 114019. https://doi.org/10.1088/1748-9326/aa8a58

Turner, A. G., & Annamalai, H. (2012). Climate change and the South Asian summer monsoon. *Nature Climate Change*, *2*(8), 587–595. https://doi.org/10.1038/nclimate1495

Ueda, H., Iwai, A., Kuwako, K., & Hori, M. E. (2006). Impact of anthropogenic forcing on the Asian summer monsoon as simulated by eight GCMs. *Geophysical Research Letters*, *33*(6), 2005GL025336. https://doi.org/10.1029/2005GL025336

Ueda, H., Kamae, Y., Hayasaki, M., Kitoh, A., Watanabe, S., Miki, Y., & Kumai, A. (2015). Combined effects of recent Pacific cooling and Indian Ocean warming on the Asian monsoon. *Nature Communications*, *6*(1), 8854. https://doi.org/10.1038/ncomms9854

Upadhyaya, P., Mishra, S. K., Fasullo, J. T., & Kang, I.-S. (2024). Attributing the recent weakening of the South Asian subtropical westerlies. *Npj Climate and Atmospheric Science*, *7*(1), 283. https://doi.org/10.1038/s41612-024-00777-0

Vautard, R., Cattiaux, J., Yiou, P., Thépaut, J.-N., & Ciais, P. (2010). Northern Hemisphere atmospheric stilling partly attributed to an increase in surface roughness. *Nature Geoscience*, *3*(11), 756–761. https://doi.org/10.1038/ngeo979

Vecchi, G. A., Soden, B. J., Wittenberg, A. T., Held, I. M., Leetmaa, A., & Harrison, M. J. (2006). Weakening of tropical Pacific atmospheric circulation due to anthropogenic forcing. *Nature*, *441*(7089), 73–76. https://doi.org/10.1038/nature04744

Voldoire, A., Saint-Martin, D., Sénési, S., Decharme, B., Alias, A., Chevallier, M., Colin, J., Guérémy, J. -F., Michou, M., Moine, M. -P., Nabat, P., Roehrig, R., Salas Y Mélia, D., Séférian, R., Valcke, S., Beau, I., Belamari, S., Berthet, S., Cassou, C., … Waldman, R. (2019). Evaluation of CMIP6 DECK Experiments With CNRM-CM6-1. *Journal of Advances in Modeling Earth Systems*, *11*(7), 2177–2213. https://doi.org/10.1029/2019MS001683

Wang, B., Biasutti, M., Byrne, M. P., Castro, C., Chang, C.-P., Cook, K., Fu, R., Grimm, A. M., Ha, K.-J., Hendon, H., Kitoh, A., Krishnan, R., Lee, J.-Y., Li, J., Liu, J., Moise, A., Pascale, S., Roxy, M. K., Seth, A., … Zhou, T. (2021a). Monsoons Climate Change Assessment. *Bulletin of the American Meteorological Society*, *102*(1), E1–E19. https://doi.org/10.1175/BAMS-D-19-0335.1

Wang, B., Jin, C., & Liu, J. (2020). Understanding Future Change of Global Monsoons Projected by CMIP6 Models. *Journal of Climate*, *33*(15), 6471–6489. https://doi.org/10.1175/JCLI-D-19-0993.1

Wang, B., Liu, J., Kim, H.-J., Webster, P. J., Yim, S.-Y., & Xiang, B. (2013). Northern Hemisphere summer monsoon intensified by mega-El Niño/southern oscillation and Atlantic multidecadal oscillation. *Proceedings of the National Academy of Sciences*, *110*(14), 5347–5352. https://doi.org/10.1073/pnas.1219405110

Wang, Z., Lin, L., Xu, Y., Che, H., Zhang, X., Zhang, H., Dong, W., Wang, C., Gui, K., & Xie, B. (2021b). Incorrect Asian aerosols affecting the attribution and projection of regional climate change in CMIP6 models. *Npj Climate and Atmospheric Science*, *4*(1), 2. https://doi.org/10.1038/s41612-020-00159-2

Webster, P. J., Magaña, V. O., Palmer, T. N., Shukla, J., Tomas, R. A., Yanai, M., & Yasunari, T. (1998). Monsoons: Processes, predictability, and the prospects for

prediction. *Journal of Geophysical Research: Oceans*, *103*(C7), 14451–14510. https://doi.org/10.1029/97JC02719

World Bank. (2021). *Variable renewable energy locational study (Pakistan Sustainable Energy Series*. World Bank. https://openknowledge.worldbank.org/entities/publication/4cac8dcf-207e-5178-be66-f38a97185d9a

Wu, J., Zha, J., Zhao, D., & Yang, Q. (2018). Changes in terrestrial near-surface wind speed and their possible causes: An overview. *Climate Dynamics*, *51*(5–6), 2039–2078. https://doi.org/10.1007/s00382-017-3997-y

Wu, T., Lu, Y., Fang, Y., Xin, X., Li, L., Li, W., Jie, W., Zhang, J., Liu, Y., Zhang, L., Zhang, F., Zhang, Y., Wu, F., Li, J., Chu, M., Wang, Z., Shi, X., Liu, X., Wei, M., … Liu, X. (2019). The Beijing Climate Center Climate System Model (BCC-CSM): The main progress from CMIP5 to CMIP6. *Geoscientific Model Development*, *12*(4), 1573–1600. https://doi.org/10.5194/gmd-12-1573-2019

Xiang, B., Xie, S.-P., Kang, S. M., & Kramer, R. J. (2023). An emerging Asian aerosol dipole pattern reshapes the Asian summer monsoon and exacerbates northern hemisphere warming. *Npj Climate and Atmospheric Science*, *6*(1), 77. https://doi.org/10.1038/s41612-023-00400-8

Xie, S.-P., Deser, C., Vecchi, G. A., Collins, M., Delworth, T. L., Hall, A., Hawkins, E., Johnson, N. C., Cassou, C., Giannini, A., & Watanabe, M. (2015). Towards predictive understanding of regional climate change. *Nature Climate Change*, *5*(10), 921–930. https://doi.org/10.1038/nclimate2689

Yang, Q., Hannah, W. M., & Leung, L. R. (2022). Convective Momentum Transport and Its Impact on the Madden-Julian Oscillation in E3SM-MMF. *Journal of Advances in Modeling Earth Systems*, *14*(11), e2022MS003206. https://doi.org/10.1029/2022MS003206

Yukimoto, S., Kawai, H., Koshiro, T., Oshima, N., Yoshida, K., Urakawa, S., Tsujino, H., Deushi, M., Tanaka, T., Hosaka, M., Yabu, S., Yoshimura, H., Shindo, E., Mizuta, R., Obata, A., Adachi, Y., & Ishii, M. (2019). The Meteorological Research Institute Earth System Model Version 2.0, MRI-ESM2.0: Description and Basic Evaluation of the Physical Component. *Journal of the Meteorological Society of Japan. Ser. II*, *97*(5), 931–965. https://doi.org/10.2151/jmsj.2019-051

Zeng, Z., Ziegler, A. D., Searchinger, T., Yang, L., Chen, A., Ju, K., Piao, S., Li, L. Z. X., Ciais, P., Chen, D., Liu, J., Azorin-Molina, C., Chappell, A., Medvigy, D., &

Wood, E. F. (2019). A reversal in global terrestrial stilling and its implications for wind energy production. *Nature Climate Change*, *9*(12), 979–985. https://doi.org/10.1038/s41558-019-0622-6

Zhang, S., Stier, P., Dagan, G., Zhou, C., & Wang, M. (2023). Sea surface warming patterns drive hydrological sensitivity uncertainties. *Nature Climate Change*, *13*(6), 545–553. https://doi.org/10.1038/s41558-023-01678-5

Zhou, T., Lu, J., Zhang, W., & Chen, Z. (2020). The Sources of Uncertainty in the Projection of Global Land Monsoon Precipitation. *Geophysical Research Letters*, *47*(15), e2020GL088415. https://doi.org/10.1029/2020GL088415

Ziehn, T., Chamberlain, M. A., Law, R. M., Lenton, A., Bodman, R. W., Dix, M., Stevens, L., Wang, Y.-P., & Srbinovsky, J. (2020). The Australian Earth System Model: ACCESS-ESM1.5. *Journal of Southern Hemisphere Earth Systems Science*, *70*(1), 193–214. https://doi.org/10.1071/ES19035

List of Publications

Mishra, S. K., **P. Upadhyaya**, J. T. Fasullo, N. P. Keshri, P. Salunke, A. Ghosh, et al. 2023. "A Need for Actionable Climate Projections across the Global South." Nature Climate Change 13(10): 883–86. https://doi.org/10.1038/s41558-023-01778-2.

Upadhyaya, P., S. K. Mishra, J. T. Fasullo, and I. S. Kang. 2024. "Attributing the Recent Weakening of the South Asian Subtropical Westerlies." npj Climate and Atmospheric Science 7(1): 283. https://doi.org/10.1038/s41612-024-00777-0.

Upadhyaya, P., S. K. Mishra, D. P. Bhuyan, J. T. Fasullo, J. Tribbia, and I. S. Kang. (n.d.). "Warming Seas, Uncertain Rains: The Fragile Link between SST and Precipitation." (Manuscript submitted for publication)

Upadhyaya, P., S. K. Mishra, and J. T. Fasullo. (n.d.). "A Projected Increase in South Asian Wind Energy Potential due to Aerosol Emission Reductions." (Manuscript under review in Communications Sustainability).

Bhuyan, Debi P., **P. Upadhyaya**, R. Pathak, P. Namdev, P. Salunke, A. Anand, et al. 2026. "Advancing Climate Services in South Asia: The SARCI Framework for Actionable Climate Information and Regional Capacity Building." Bulletin of the American Meteorological Society 107(3): E564–E584. https://doi.org/10.1175/BAMS-D-25-0172.1

Narang, U., K. Juneja, **P. Upadhyaya**, P. Salunke, T. Chakraborty, S. K. Behera, S. K. Mishra, and A. D. Suresh. 2023. "Artificial Intelligence Predicts Normal Summer Monsoon Rainfall for India in 2023." Scientific Reports 14(1): 1495. https://doi.org/10.1038/s41598-023-44284-3.

Upadhyaya, P., S. K. Mishra, 2023: Zonal Momentum Balance in South Asian Summer Monsoon: Forces and Changing Winds. EGU General Assembly Conference Abstracts, EGU23-12313. (Poster)

Biographical Sketch



Pankaj Upadhyaya was born and raised in Assam, India. He completed his Bachelor of Science in Physics from Gauhati University, Guwahati, in 2016, and went on to pursue a Master of Science in Ocean and Atmospheric Sciences at the University of Hyderabad. His master's thesis examined the variability of the Indian summer monsoon during the mid-Holocene using PMIP3 simulations, marking the beginning of his interest in atmospheric modelling and science.

His doctoral research at IIT Delhi, supported by the DST INSPIRE Fellowship, investigates the changing character of winds and precipitation over South Asia, combining observational analysis, climate model experiments, and detection–attribution approaches to understand the mechanisms driving regional circulation changes and to examine the limitations of current climate projections in representing them.

Over the course of his doctoral research, he has authored and co-authored several peer-reviewed publications in journals such as *npj Climate and Atmospheric Science*, *Nature Climate Change*, *Bulletin of the American Meteorological Society*, and *Scientific Reports*. His research interests span regional climate modelling, detection and attribution of climate change, monsoon dynamics, wind energy potential, and the development of actionable climate information for the Global South.